

Single particle and collective dynamics in periodic potentials



The University of
Nottingham

Mark Thomas Greenaway, MSci

Thesis submitted to the University of Nottingham
for the degree of Doctor of Philosophy

February 2010

Abstract

In this thesis, we describe, both semiclassically and quantum mechanically, the single-particle and collective dynamics of electrons and ultracold atoms moving through periodic potentials.

Firstly, we explore collective electron dynamics in superlattices with an applied voltage and tilted magnetic field. Single electrons in this system exhibit non-KAM chaotic dynamics. Consequently, at critical field values, coupling between Bloch and cyclotron motion causes delocalisation of the electron orbits, resulting in strong resonant enhancement of the drift velocity. We show that this dramatically affects the collective electron behaviour by inducing multiple propagating charge domains and, consequently, GHz-THz current oscillations with frequencies ten times higher than with no tilted field.

Secondly, we study the effect of applying an acoustic wave to the superlattice and find that we can induce high-frequency single electron dynamics that depend critically on the wave amplitude. There are two dynamical regimes depending on the wave amplitude and the electron's initial position in the acoustic wave. Either the electron can be dragged through the superlattice and is allowed to perform drifting periodic orbits with THz frequencies far above the GHz frequencies of the acoustic wave; or, by exerting a large enough potential amplitude, Bloch-like oscillations can be induced, which can cause ultra-high negative differential velocity. We also consider collective electron effects and find that, generally, the acoustic wave drags electrons through the lattice. Additionally, high negative differential drift velocity at the transition between these two single-electron dynamical regimes, induces charge domains in the superlattice that generates extra features in the current oscillations.

Finally, we investigate cold atoms in optical lattices driven by a moving potential wave, directly analogous to acoustically-driven superlattices. In this case, we find the same dynamical regimes found in the acoustically driven superlattice. In addition, there are a number of sharp resonant features in the velocity of the atom at critical wave amplitudes and speeds. This could provide a flexible mechanism for transporting atoms to precise locations in a lattice.

List of Publications

- Magnetic-field-induced miniband conduction in semiconductor superlattices. D. Fowler, D. P. A. Hardwick, A. Patanè, **M. T. Greenaway**, A. G. Balanov, T. M. Fromhold, L. Eaves, M. Henini, N. Kozlova, J. Freudenberger, and N. Mori. *Phys. Rev. B* **76**, 245303 (2007)
- Semiconductor charge transport driven by a picosecond strain pulse. D. R. Fowler, A. V. Akimov, A. G. Balanov, **M. T. Greenaway**, M. Henini, T. M. Fromhold, and A. J. Kent. *Appl. Phys. Lett.* **92**, 232104 (2008)
- Using sound to create THz electron dynamics in superlattices. **M. T. Greenaway**, A. G. Balanov, D. Fowler, A. J. Kent, and T. M. Fromhold. arXiv:0803.2193v1 (2008) Accepted for publication in Physical Review B.
- Using sound to generate ultra-high-frequency electron dynamics in superlattices. **M. T. Greenaway**, A. G. Balanov, D. Fowler, A. J. Kent, and T. M. Fromhold. *Microelectron. J.* **40**, 725 (2009) *Conference Proceedings (ICSNN 2008)*
- Controlling and enhancing terahertz collective electron dynamics in superlattices by chaos-assisted miniband transport. **M. T. Greenaway**, A. G. Balanov, E. Schöll, and T. M. Fromhold. *Phys. Rev. B* **80**, 205318 (2009)
- Effects of Dissipation and Noise on Chaotic Transport in Superlattices. A. G. Balanov, **M. T. Greenaway**, and T. M. Fromhold. *Acta Phys. Pol. A* **116**, 733 (2009) *Conference Proceedings (4th Workshop on Quantum Chaos and Localisation Phenomena)*
- Dynamics of ultracold sodium atoms in moving optical lattices. **M. T. Greenaway**, A. G. Balanov, and T. M. Fromhold, in preparation for Physical Review Letters.

Acknowledgements

Firstly I would like to thank my supervisor, Mark Fromhold, for his help, support and advice over the years. I feel privileged to be able to gain from his seemingly inexhaustible condensed matter physics knowledge, incisive clarity, patience guidance, and enthusiasm for the beauty of physics.

I would also like to thank Sasha Balanov, my second supervisor in all but name, for all of the encouragement along the way, and advice on all things non-linear. But also for generosity and hospitality, especially the enjoyable afternoons of drinking coffee, eating biscuits and doing physics.

I am fortunate too in being able to learn from Professor Schöll at TU, Berlin, the visit kick-starting the development of the drift diffusion model. Also thanks to Tony Kent, Dave Fowler, Lawrence Eaves and Amalia Patanè for helpful discussions.

Thanks to Tom Judd, for being a great friend, and also to all my fellow office mates in C19 who have shared in the ups and downs of doing a PhD.

Thanks to all my family, especially my parents for their constant love and always believing in me.

Lastly, thanks to my wonderful wife and best friend, Ruth, for all her love and support.

Contents

| | | |
|----------|--|-----------|
| 1 | Periodic potentials | 1 |
| 1.1 | Band theory | 1 |
| 1.1.1 | Brief introduction to bands in solid state physics | 1 |
| 1.1.2 | The nuts and bolts of the theory | 3 |
| 1.2 | Semiclassical model of electron dynamics | 7 |
| 1.2.1 | Bloch oscillations | 9 |
| 1.3 | Superlattices | 10 |
| 1.3.1 | Models for electrons in superlattices | 13 |
| 1.3.2 | Superlattice structures used in this thesis | 15 |
| 1.3.2.1 | Semiclassical model for electron dynamics | 18 |
| 1.3.2.2 | Quantum mechanical model for electron dynamics | 19 |
| 1.3.3 | Electron scattering | 22 |
| 1.3.4 | Esaki-Tsu formulation of drift velocity | 24 |
| 1.3.5 | Basic charge domain formation in superlattices | 27 |
| 1.4 | Optical lattices | 31 |
| 1.4.1 | Interaction of alkali atoms with an optical lattice | 32 |
| 1.4.2 | Model for atom dynamics in optical lattices | 34 |
| 2 | Magnetic field induced chaotic electron dynamics in superlattices | 37 |
| 2.1 | Superlattice electron dynamics in a tilted magnetic field | 39 |
| 2.1.1 | Electron trajectories | 43 |
| 2.1.2 | Electron drift velocity | 45 |
| 2.2 | Experimental and theoretical $I(V)$ curves | 49 |

| | | |
|----------|---|------------|
| 3 | Controlling charge domain dynamics in superlattices | 52 |
| 3.1 | Model of charge domain dynamics | 53 |
| 3.2 | Results NU2293 | 58 |
| 3.2.1 | Current-voltage characteristics for $\theta = 0^\circ, 25^\circ$ and 40° | 59 |
| 3.2.2 | $I(t)$ curves for $\theta = 0^\circ, 25^\circ$ and 40° | 61 |
| 3.2.3 | Charge dynamics for $\theta = 0^\circ, 25^\circ$ and 40° | 64 |
| 3.2.4 | Stability and power of $I(t)$ oscillations for $0^\circ < \theta < 90^\circ$ | 73 |
| 3.2.5 | Frequency of $I(t)$ for $0^\circ < \theta < 90^\circ$ | 75 |
| 4 | Using sound to control THz electron dynamics in superlattices | 78 |
| 4.1 | Acoustic waves | 78 |
| 4.1.1 | Acoustic wave model | 81 |
| 4.2 | Semiclassical mechanics of an electron in a superlattice driven by an acoustic wave | 83 |
| 4.2.1 | Drift velocity characteristics | 84 |
| 4.2.2 | Electron trajectory in the wave dragging regime | 85 |
| 4.2.3 | Electron trajectory in the Bloch oscillation regime | 90 |
| 4.2.4 | Fourier analysis | 93 |
| 4.2.5 | Analysis of drift velocity | 97 |
| 4.3 | Wavepacket analysis | 100 |
| 4.3.1 | The effect of phase | 103 |
| 4.3.2 | Quantum mechanical electron dynamics and transport | 109 |
| 4.4 | Charge dynamics | 112 |
| 4.4.1 | Current versus acoustic wave amplitude, $I(U)$, curve | 114 |
| 4.4.2 | $I(t)$ curves | 114 |
| 4.4.3 | Spatio-temporal electron density in the superlattice | 115 |
| 5 | Dynamics of ultracold sodium atoms in moving optical lattices | 120 |
| 5.1 | Moving optical lattice | 120 |
| 5.2 | Semiclassical dynamics | 121 |
| 5.2.1 | Time averaged velocity | 123 |
| 5.2.2 | Trajectories in the linear dispersion regime | 125 |
| 5.2.3 | Trajectory in the wave dragging regime | 129 |
| 5.2.4 | Trajectory in the Bloch oscillation regime | 130 |
| 5.2.5 | Average velocity with colour map | 134 |

| | | |
|----------|---|------------|
| 5.2.6 | Non zero initial position | 136 |
| 5.3 | Wavepacket analysis | 140 |
| 5.3.1 | Quantum velocity | 144 |
| 6 | Conclusion | 147 |
| 6.1 | Future work | 148 |
| A | Calculation of dispersion curves and Bloch states for a particle in a periodic potential | 150 |
| B | Experimental measurement of current and the role of contacts | 153 |
| | References | 165 |

Chapter 1

Periodic potentials

The following chapter is an introduction to some of the tools that are used in this thesis when considering the effect of periodic potentials on the motion of quantum particles. Two types of systems where quantum particles experience periodic potentials are introduced, electrons in semiconductor superlattices (see section 1.3) and cold atoms in optical lattices (see section 1.4). Also explored in this chapter are some of the well studied effects relating to the dynamics of these particles in the periodic potentials.

1.1 Band theory

Band theory is able to predict the motion of quantum particles through periodic potentials. It was originally devised to describe the motion of electrons through solids and is the basis of solid state physics. More recently, though, it has also been employed in describing the motion of atoms in optical lattices. In this thesis both the motion of electrons through artificial lattices and atoms through optical lattices shall be considered. However, it is helpful to put the fundamental physics behind this thesis into context by describing some of the basic features of band theory in relation to solid state physics.

1.1.1 Brief introduction to bands in solid state physics

Quantum theory tells us that electrons in single atoms occupy quantised orbits and thus form a set of discrete energy levels. However, when the atoms are brought together to form a molecule, the energy of the atomic orbitals splits, forming a number of molecular orbitals proportional to the number of atoms in the molecule. Ultimately,

when we form a solid (or crystal lattice) with a large number of atoms we obtain a very large number of orbitals and the separation of adjacent energy levels becomes very small. Therefore, in solids, we tend to think that the allowed energy levels of electrons form continuous *bands*. Band theory predicts that these allowed bands occupied by the electrons can be separated by regions in energy, called *band gaps*, where no spatially extended electron wavefunctions exist. The structure of these bands is defined by the properties of the atoms in the crystal and determine the transport properties of electrons within the solid.

The properties and interactions between two bands, the *valence* and *conduction* bands, effectively describe the electronic properties of a solid. The valence band is the highest energy band which is occupied at absolute zero. In an insulator, this band is completely filled (the number of electrons in the band is equal to the number of states up to the top of the valence band) and there is a band gap above the top of the band. Therefore, when an electric field is applied to the crystal the electrons cannot, as a whole, accelerate as there are no unoccupied states within the valence band. However, there is the possibility of some conduction as some of the electrons can be thermally excited across the band gap into the next band, the conduction band, where there are available states and therefore can be accelerated by the electric field. The electron leaves behind a “hole” or a point of positive charge which can also conduct electricity. In a metal, the valence and conduction bands overlap effectively creating a single energy band which is partially filled (around 10% to 90%), so that when applying an electric field there are plenty of available states and the electron can move through the lattice with high conductivity.

Crystals where the band gap between the valence and conduction bands is smaller than in an insulator, but not overlapping like a metal, are semiconductors. In these solids a significant number of electrons are thermally excited into the conduction band, which enables the crystal to carry a current. Uniquely it is possible to engineer the band structures of semiconductors, opening a huge number of possibilities for tailoring the electronic properties of these materials. For example, in the p-n junction two different types of semiconductor are brought together, n-type and p-type. N-type semiconductors have been doped with atoms that will increase the number of free electrons in the structure, effectively adding states into the conduction band and decreasing the energy of the bottom of the conduction band. Conversely, p-type semiconductors have been doped to increase the number of holes in the material,

thus increasing the position of the top edge of the valence band. By bringing these two types of semiconductor together the mismatch in their band levels causes band “bending” across the junction of the device. The effect of which is to let electric current travel in one direction and not in the opposite direction; a diode. Using similar principles it is possible to construct transistors which are the backbone of the semiconductor industry.

In this thesis, the transport of electrons in artificial crystals and also the transport of cold atoms in optical lattices will be studied, in particular the effect of various external applied fields. Crucial for understanding the dynamics of particles in these devices is band theory. In the following section band theory will be derived mathematically to determine some of the model equations used throughout this thesis.

1.1.2 The nuts and bolts of the theory

The spatial lattice created by a periodic potential, $V(\mathbf{r})$, generated by atoms in a solid or by counter propagating lasers in an optical lattice, can be described by the *primitive lattice vectors* \mathbf{a}_1 , \mathbf{a}_2 and \mathbf{a}_3 . Using these vectors, the position of each lattice point (the atoms in the case of a solid or the peaks in laser intensity in an optical lattice) can be described relative to any other point using the *lattice vector*, \mathbf{R} , given by

$$\mathbf{R} = u\mathbf{a}_1 + v\mathbf{a}_2 + w\mathbf{a}_3 \quad (1.1)$$

where u , v , and w are integers. Bloch theory states that, since the potential the quantum particle experiences is periodic, all the measurable properties of its wavefunction must follow the translational symmetry of the lattice. Therefore, the probability of finding the particle at point \mathbf{r} must have the property

$$|\psi(\mathbf{r} + \mathbf{R})|^2 = |\psi(\mathbf{r})|^2 \quad (1.2)$$

it follows then that

$$\psi(\mathbf{r} + \mathbf{R}) = e^{i\alpha(\mathbf{R})}\psi(\mathbf{r}) \quad (1.3)$$

where $\alpha(\mathbf{R})$ is a real, dimensionless, arbitrary function of \mathbf{R} . Imagining the effect of a second translation we find that

$$\psi(\mathbf{r} + \mathbf{R}_1 + \mathbf{R}_2) = e^{i\alpha(\mathbf{R}_1 + \mathbf{R}_2)}\psi(\mathbf{r}) \quad (1.4)$$

or

$$\psi(\mathbf{r} + \mathbf{R}_1 + \mathbf{R}_2) = e^{i\alpha(\mathbf{R}_1)}\psi(\mathbf{r} + \mathbf{R}_2). \quad (1.5)$$

It follows then that

$$\alpha(\mathbf{R}_1 + \mathbf{R}_2) = \alpha(\mathbf{R}_1) + \alpha(\mathbf{R}_2), \quad (1.6)$$

Consequently, α is a linear function of \mathbf{R} and thus can be defined by the following equation

$$\alpha(\mathbf{R}) = k_x R_x + k_y R_y + k_z R_z = \mathbf{k} \cdot \mathbf{R} \quad (1.7)$$

where \mathbf{k} is the wavevector of the wavefunction with the components k_x , k_y and k_z .

Substitution of equation (1.7) into (1.3) results in the following statement of *Bloch's theorem* [1; 2]

$$\psi(\mathbf{r} + \mathbf{R}) = e^{i\mathbf{k} \cdot \mathbf{R}}\psi(\mathbf{r}). \quad (1.8)$$

Further algebra [2] reveals the following alternative statement of Bloch's theorem

$$\psi_{\mathbf{k}}(\mathbf{r}) = e^{i\mathbf{k} \cdot \mathbf{r}}u_{\mathbf{k}}(\mathbf{r}), \quad (1.9)$$

where $u(\mathbf{r})$ is a function with the periodicity, and also the translational symmetry, of the lattice. A second, important, property to note is that independent states only exist within a range of \mathbf{k} . This can be shown to be true by letting $\mathbf{k} = \mathbf{k}' + \mathbf{K}$ where \mathbf{K} is the *reciprocal lattice vector*. \mathbf{K} is analogous to the lattice vector \mathbf{R} , and has the components \mathbf{b}_1 , \mathbf{b}_2 and \mathbf{b}_3 . These are the *primitive reciprocal lattice vectors*, which generate the *reciprocal lattice* (in the same way that \mathbf{a}_1 , \mathbf{a}_2 and \mathbf{a}_3 generate the real lattice). The region defined by the primitive reciprocal lattice vectors is called the *1st Brillouin zone*. The primitive lattice and reciprocal lattice vectors satisfy the following equation

$$\mathbf{b}_i \cdot \mathbf{a}_j = 2\pi\delta_{i,j}. \quad (1.10)$$

The effect of this condition can be shown by substituting $\mathbf{k} = \mathbf{k}' + \mathbf{K}$ into equation (1.9)

$$\psi(\mathbf{r} + \mathbf{R}) = e^{i\mathbf{k}' \cdot \mathbf{R}} e^{i\mathbf{K} \cdot \mathbf{R}} \psi(\mathbf{r}). \quad (1.11)$$

The definition of the reciprocal lattice given in equation (1.10) leads to the relation $\mathbf{K} \cdot \mathbf{R} = 2\pi n$, where n is an integer; therefore

$$e^{i\mathbf{K} \cdot \mathbf{R}} = 1 \quad (1.12)$$

so

$$\psi(\mathbf{r} + \mathbf{R}) \equiv e^{i\mathbf{k}' \cdot \mathbf{R}} \psi(\mathbf{r}). \quad (1.13)$$

Comparing equations (1.13) and (1.8) one finds that

$$e^{i\mathbf{k} \cdot \mathbf{R}} \equiv e^{i\mathbf{k}' \cdot \mathbf{R}} \quad (1.14)$$

so \mathbf{k}' is exactly equivalent to \mathbf{k} and thus the only independent values of \mathbf{k} are in the 1st Brillouin zone. Consequently, only wave vectors in the 1st Brillouin zone need to be considered. The form of the 1st Brillouin zone, even in one dimension, is generally complex. However, if it is assumed that its centre lies at the origin in reciprocal space, then its extreme edges lie at $\mathbf{k} = \mathbf{b}_1/2$ and at $\mathbf{k} = -\mathbf{b}_1/2$. Therefore, using equation (1.10), we find that the range of possible values of k_x is

$$\frac{-\pi}{d} \leq k_x \leq \frac{\pi}{d} \quad (1.15)$$

where d is the periodicity of the lattice.

For completeness, it is possible to calculate the number of \mathbf{k} states in each band by applying a periodic boundary condition known as the *Born-Von Karman boundary condition* to Bloch's theorem, which, in one dimension, states that

$$\psi(x + N_x d) = \psi(x) \quad (1.16)$$

where N_x is the number of lattice points along the x -axis of the lattice [3]. Therefore, substituting this condition into Bloch's theorem we find that

$$e^{ik_x(x+N_x d)} u(x + N_x d) = e^{ik_x x} u(x). \quad (1.17)$$

$u(x + N_x d) = u(x)$ since it has the periodicity of the lattice, therefore

$$e^{ik_x(x+N_x d)} = e^{ik_x x}, \quad (1.18)$$

which implies that

$$k_x = 0, \pm \frac{2\pi}{dN_x}, \pm \frac{4\pi}{dN_x}, \pm \frac{6\pi}{dN_x}, \dots, \pm \frac{\pi}{d}. \quad (1.19)$$

Therefore there is one allowed k_x state per length $2\pi/dN_x$, so the total number of states in the band is given by

$$\frac{2\pi}{d} \frac{dN_x}{2\pi} = N_x. \quad (1.20)$$

Consequently, each band consists of N_x allowed k_x -states. This analysis can be repeated for a three dimensional lattice, to find that each lattice point contributes one k -state to the band.

The Bloch wavefunctions for a particle of energy E and wavefunction ψ can be determined by solving the time independent Schrödinger equation [4; 5; 6]

$$\hat{\mathcal{H}}\psi = E\psi \quad (1.21)$$

where the Hamiltonian operator, $\hat{\mathcal{H}}$, for a infinitely large periodic potential is given by

$$\hat{\mathcal{H}} = -\frac{\hbar^2}{2m}\nabla^2 + V(\mathbf{r}). \quad (1.22)$$

In equation (1.22), $\hbar = h/2\pi$ where $h = 1.054 \times 10^{-34}$ J s⁻¹ is Plank's constant, m is the mass of the quantum particle and $V(\mathbf{r})$ is the periodic potential determined from the lattice properties. There are a many techniques, analytical and numerical, to solve this equation for a Bloch wavefunction of the form given in equation (1.8). For example, in appendix A, the relatively straightforward cellular technique is described (for more information on this and other methods see, for example, [3]).

The solution to equation (1.21) reveals that there are an infinite number of solutions for a given value of \mathbf{k} . Therefore each wavefunction with a particular \mathbf{k} is assigned a quantum number, n , and has a corresponding energy $E^n(\mathbf{k})$, where the function $E^n(\mathbf{k})$ is known as the *dispersion relation*. Figure 1.1 shows schematically how this dispersion relation depends on n and k_x in a one dimensional lattice. This particular diagram is shown in the *reduced zone scheme* as beyond the Brillouin zone

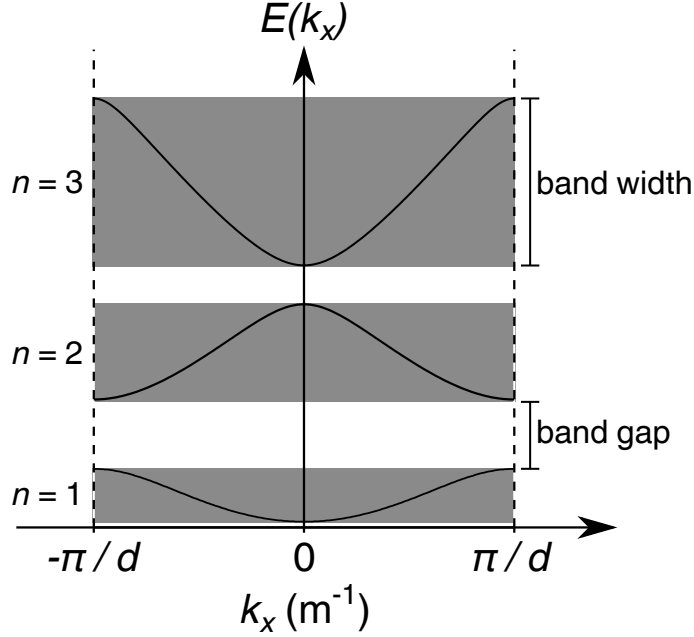


Figure 1.1: A typical dispersion relation $E^n(k_x)$ of the first three bands ($n = 1, 2$ and 3) for a quantum particle in a one dimensional lattice with lattice period d . Grey shaded regions highlight the individual bands with band width and band gap labelled.

boundary (vertical dashed line) the plot simply repeats. However, in the following chapters the *extended zone scheme* will also be considered. The plot shows that the energy of the electron is constrained within a set of *bands* highlighted in grey in the figure and labelled by the quantum number n known as the *band index*. These energies are representative of the allowed, propagating, states of the electron and have a *band width* (labelled in the figure). Outside these allowed energies there exists a region of disallowed states resulting in a *band gap* between the bands (also labelled in the figure). As explained in the previous section, the size of the band gap determines the type of crystal lattice. In this thesis we consider lattices with a large band gap, and how to manipulate these lattices and their *band structure* to generate and control the particle dynamics.

1.2 Semiclassical model of electron dynamics

The basic assumption of the semiclassical model for the dynamics of quantum particles is that they are considered to behave as a classical particle. However, in a periodic

1.2 Semiclassical model of electron dynamics

lattice the quantum particle is not considered to be a free particle, rather its dispersion relation, $E(\mathbf{k})$, is determined from quantum mechanical band structure calculations, see appendix A. This mixture of the classical and quantum allows the analysis of the dynamics of quantum particles within periodic lattices under the effect of slowly varying external fields, providing an important insight into their dynamics in complex systems. There are disadvantages, though, in the semiclassical models presented in this thesis. In particular, the particles are assumed to only populate the lowest energy band and we neglect transitions between the bands¹. The model also does not take into account any effect additional fields may have on the band structure of the system. Therefore the model should be used carefully and, if possible, particle dynamics should be checked for consistency with the quantum mechanical solutions.

We start derivation of the model by assuming that the particle velocity is equal to the group velocity of its corresponding wave packet, which, in three dimensions can be shown to be

$$\mathbf{v} = \frac{1}{\hbar} \nabla_{\mathbf{k}} E(\mathbf{k}). \quad (1.23)$$

This formulation can be proved using the general form of Bloch's theorem and perturbation theory [2]. It is clear that this gives rise to very well defined particle trajectories. Therefore it is important to note that scattering events are not included in this model, although their effect will be included later.

The work, δW , done on an electron by a force, \mathbf{G} , generated by some potential energy field, in the time interval, δt , is given by

$$\delta W = \mathbf{G} \cdot \mathbf{v} \delta t. \quad (1.24)$$

So noting it is possible to write $\delta W = (dW/d\mathbf{k})\delta\mathbf{k}$ and using equation (1.23) we find that

$$\hbar \frac{d\mathbf{k}}{dt} = \mathbf{G}. \quad (1.25)$$

This is a relation that can cause confusion. In free space, the momentum of a quantum particle is defined by Newton's second law of motion $m(d\mathbf{v}/dt) = \hbar(d\mathbf{k}/dt) = \mathbf{G}$. In

¹As stated in section 1.1, it is clearly possible to move between energy bands. However, in the experimental systems presented here the band gaps are large and the effect of transitions between bands is negligible. It should be noted that interband band hopping has been modelled successfully for band structures with narrow band gaps in the semiclassical model, see [7; 8]

a periodic potential however, the particle is subject to forces from the lattice as well as any external force and thus $\hbar\mathbf{k}$ is called the crystal momentum but is not equal to $m(d\mathbf{v}/dt)$. To find the actual momentum we must take into account the *total* force applied, including the contribution due to the periodic potential.

1.2.1 Bloch oscillations

Consider a particle in the lowest energy band subject to a force, G_x , applied along the x direction of a lattice. We know from equation (1.25) that

$$\hbar \frac{dk_x}{dt} = G_x \tag{1.26}$$

It is clear from equation (1.26) that the k_x value of a Bloch particle increases linearly with time. The lowest (solid) curve in figure 1.1 shows qualitatively how the energy varies with increasing k_x for a particle in the lowest energy band of the lattice. We assume that the electron is initially in state where $k_x = 0$ so application of the force results in an increase in k_x towards the Brillouin zone boundary at $k_x = \pi/d$ (right hand vertical dashed line in figure 1.1). Consequently, the gradient of the dispersion curve becomes increasingly positive and the particle starts to accelerate and increase its velocity in real space in the x direction. The velocity is maximal when dE/dk_x is maximal, and then starts to decrease as the particle approaches the Brillouin zone boundary. Eventually when it reaches the Brillouin zone boundary, $dE/dk_x = 0$ and the particle comes to a standstill. We know from the previous section that due to the periodicity of the lattice, a wavevector outside the first Brillouin zone has an equivalent wavevector within the range $\pm\pi/d$. We imagine, therefore, that a particle reaching the edge of the Brillouin zone at $k_x = \pi/d$ will reappear at the opposite boundary at $k_x = -\pi/d$ and, thereafter, its k_x value will continue to increase at a constant rate. However, the gradient of the dispersion curve is now negative and thus the particle will start to move in the negative direction in real space. This process is called *Bragg reflection*. The particle will continue to accelerate in the negative direction, attaining a maximum negative speed when $|dE/dk_x|$ is maximal. Thereafter, the particle slows until $k_x = 0$ where it reaches a standstill at its starting position in real space. The process, known as a *Bloch oscillation*, then repeats.

The amplitude, A_B and the frequency, ω_B , of these oscillations can be easily obtained from integration of equations (1.23) and (1.25) to find

$$A_B = \frac{\Delta}{G_x} \quad (1.27)$$

and

$$\omega_B = \frac{G_x d}{\hbar} \quad (1.28)$$

where Δ is the band width of the dispersion curve (see figure 1.1).

This concept seems to suggest that all electrons in a perfect conductor would perform Bloch oscillations under the influence of a static field, which implies that biasing a perfect conductor would result in an oscillating current with no net current flow along the device. The period of these oscillations can be found using equation (1.28). For an electron in copper in a typical field, this period is $\sim 2 \times 10^{-8}$ s. However, of course, there are no perfect conductors and the scattering time¹ in copper at room temperature is $\sim 10^{-13}$ s. Therefore the possibility of an electron being anywhere near the Brillouin zone edge before being scattered is practically zero. However, in the rest of this thesis, two systems will be described which can exhibit Bloch oscillations. The first system, examined in chapters 2, 3 and 4, is a *semiconductor superlattice*. As explained in the following section, in a superlattice the large effective lattice period greatly increases the frequency of the Bloch oscillations thereby allowing the electron to Bloch oscillate before scattering. Finally, in chapter 5 we will also investigate an atom in an optical lattice where there are no scattering events, allowing the atom to Bloch oscillate. This has been verified in recent experiments where a cloud of Sodium atoms has been shown to perform up to 20,000 Bloch oscillations [9].

1.3 Superlattices

The semiconductor superlattice was first proposed by Leo Esaki and Raphael Tsu in their seminal paper *Superlattice and Negative Differential Conductivity* [10] in 1970², as a device which would exhibit *Bloch oscillations* (see section 1.2.1) and also *negative differential conductivity* (see section 1.3.4). They suggested a device which consisted of a number (typically 10s) of periodic layers. Each period of the structure consisted

¹The scattering time is defined as τ , where dt/τ is the probability of a scattering event occurring in time dt (see section 1.3.3)

²It was encouraging to learn that an original version of this paper sent to Physical Review was rejected [11], the paper having now gone on to receive over 2000 cites!

of at least two layers of semiconductor (or insulator) with similar lattice constants, but having different band gaps as a consequence of differing alloy composition or density of impurities. The differing bandwidths between the materials leads to an offset in the conduction band at the point of contact between the two different materials, resulting in a periodic variation of the conduction band edge similar to that of a natural crystal structure, but with a much larger lattice constant in one direction only. Correspondingly, a band structure is formed in the superlattice in the same way as for a semiconductor crystal lattice. However, the lattice period of the superlattice is much larger than a conventional semiconductor¹ (typically an order of magnitude larger). Consequently, the Brillouin zones for the superlattice are much smaller than that a conventional semiconductor and are therefore known as *minizones*. The energy width of the superlattice bands are also much smaller than a conventional band and are therefore known as *minibands*.

The manufacture of these structures was made possible by the development of growth techniques such as molecular beam epitaxy. During this process, pure elements are heated so that they sublime. The resulting gas is then allowed to condense on a substrate to form a layer of the constituent atoms of that element. The process, crucially, is slow (around a monolayer per second) so it is possible to precisely control the constituent atomic layers of a device, therefore allowing the crystal to be tailored for specific experiments and applications. For more information on the growth of superlattices see, for example, [12].

Figure 1.2 shows the schematic diagram of a typical semiconductor superlattice. The x -axis of the superlattice is defined as being in the growth direction of the superlattice layers and the y and z -axes are parallel to the plane of the layers. The superlattice samples are typically grown on a heavily doped GaAs substrate ($n_D \approx 10^{24} \text{ m}^{-3}$) which is 100s of micrometers thick. Onto this substrate a highly doped ($n_D \approx 10^{23} \text{ m}^{-3}$) GaAs layer is grown, with a thickness of the order of 100s of nanometres, to form an Ohmic emitter contact (labelled in figure 1.2). The superlattice region is then grown on to this contact region and consists of periodic alternating layers of different semiconductor materials. Depending on their relative bandgaps the semiconductor materials result in either a “quantum well” region or a “barrier” region in the conduction band edge of the device, creating a periodic variation in the potential energy for an electron in the superlattice. Generally, the superlattice region is grown so that

¹Hence the name!

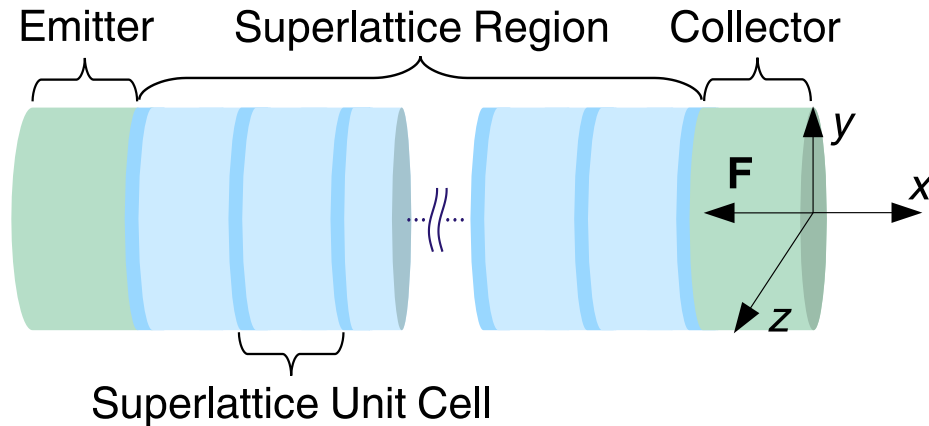


Figure 1.2: Schematic diagram of a typical semiconductor superlattice. Green regions show emitter and collector regions. The superlattice unit cell consists of a quantum well (light blue) enclosed by barriers (dark blue). The x -axis is orientated along the growth direction of the superlattice with the y and z -axes parallel to the layers. The sample is biased via an electric field, $\mathbf{F} = (-F, 0, 0)$, orientated in the opposite direction to the x -axis.

it starts and ends with a barrier layer and has doping levels that are significantly less than the emitter region ($n_D \approx 10^{22} \text{ m}^{-3}$). To ensure that calculations for an infinite lattice apply to a real superlattice, the superlattice region generally consists of more than ~ 10 layers. The structure is then capped by the collector region, a second highly doped region (labelled in figure 1.2). The reason for the highly doped contact regions is to provide a “sea of charge” from which electrons can be transferred into the lightly doped superlattice region. The lower doping levels of the superlattice region ensures that electron mobility is not overly decreased by scattering from the ionised dopants.

Esaki and Tsu’s original idea for a superlattice was to make a device where the miniband structure enables electrons to perform Bloch oscillations. However, the original experiments were on superlattices where minibands were not formed [13]. Therefore, it is important at this point to describe the difference between *weakly coupled* and *strongly coupled* superlattices. Weakly coupled superlattices have relatively thick barriers separating the quantum wells, so the decay length of the electron wavefunction is small. Consequently, the quantum wells are essentially isolated from each other and transport between them takes place via resonant tunnelling. The electronic properties of the superlattice are therefore described by calculating the sub-

band structure of the isolated quantum well and then determining the probability of tunnelling between the wells. For more information on weakly coupled superlattices, or on the formulation of various other superlattice models, the author recommends the 2002 review, *Semiconductor superlattices: a model system for nonlinear transport* by A. Wacker [14]. The reviews by E. Schöll [15] and by L.L. Bonilla and H.T. Grahn [16] also come highly recommended.

In this thesis, however, we concentrate on the strongly coupled superlattice which, in contrast with weakly coupled superlattices, has thin barriers. The electron wavefunctions in these structures are allowed to extend over several periods of the superlattice, like Bloch wavefunctions in conventional semiconductors, and thus the transport properties can be described using the band model defined in section 1.1.2. The semiclassical model for electrons in band structures predict that Bloch oscillations (see section 1.2.1) and other related effects such as negative differential conductivity (see the later section 1.3.4) will be induced in such structures, since the lattice period is larger than a conventional crystal and the electron is allowed to traverse a whole minizone before scattering. However, it is important to note that when the applied electric field is large (i.e. $eFd \gtrsim \Delta$), the band structure breaks down and a ladder structure, known as a Wannier-Stark ladder, of energy levels is formed in the quantum wells. In this regime, electron transport now occurs via phonon assisted hopping between the rungs of each ladder. Here though, we consider only regimes where the band structure of the superlattice is intact and electron transport can be successfully modelled by semiclassical band models.

1.3.1 Models for electrons in superlattices

The dynamics of electrons in a superlattice can be found by either solving the time-dependent Schrödinger equation or by using a semiclassical analysis of the electron trajectories. However, before deriving these models, we must first consider the relatively rapidly varying potential created by the crystal structure which makes up the superlattice layers. To do this we can employ the effective mass approximation, which takes into account the effect of the crystal lattice without including it explicitly in the model.

The effective mass is the mass that a free particle would have if it would respond to applied forces in the same way as a particle in a Bloch state. Consider the case of

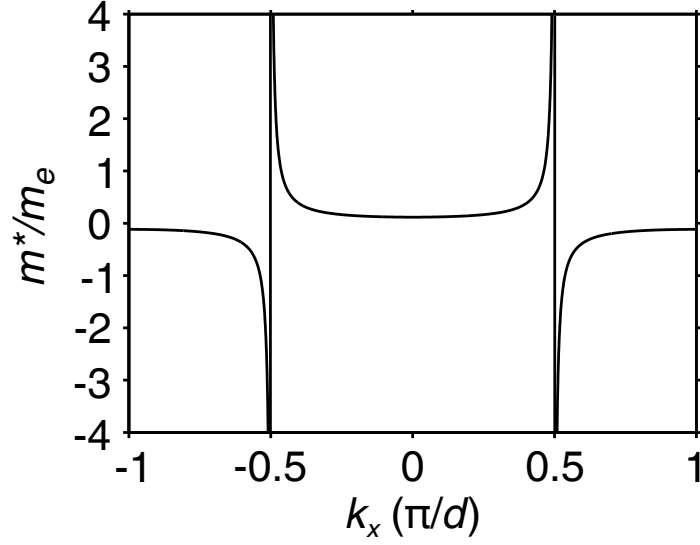


Figure 1.3: Plot showing the typical variation of the effective electron mass within the first Brillouin zone of GaAs.

an electron, with an effective mass of m^* , in an isotropic band; then according to the semiclassical model its response to an external electric field will be given by

$$G_x = eF = m^* \frac{dv_x}{dt} = \frac{m^*}{\hbar} \frac{d^2 E}{dt dk_x} = \frac{m^*}{\hbar} \frac{d^2 E}{dk_x^2} \frac{dk_x}{dt}. \quad (1.29)$$

So, substituting equation (1.26) into equation (1.29) and rearranging, we find that

$$m^* = \hbar^2 \left[\frac{d^2 E}{dk_x^2} \right]^{-1}. \quad (1.30)$$

Figure 1.3 shows the typical variation of the effective mass with the wavevector of the electron. We note that m^* in the underlying material of the structure (for example GaAs), is effectively constant around $k_x = 0$, and also that, due to scattering, the electron will remain near the centre of the Brillouin zone of the crystal lattice (see section 1.2.1). We therefore assume that m^* is constant with varying k_x .

Thus, for an electron in a superlattice we replace the mass of the electron with the effective mass to include the effect of the underlying crystal lattice. Note that m^* will also vary spatially due to the different materials used in the superlattice barriers and quantum wells. However, in the devices considered in this thesis GaAs makes up the bulk of the device so we assume that m^* is constant through out the device and is equal to $0.067m_e$, the effective mass of an electron in GaAs. Therefore,

taking the effective mass approximation into account, the following time-independent Schrödinger equation for an electron in the one-dimensional superlattice potential $V_{SL}(x)$ is obtained ¹

$$-\frac{\hbar^2}{2m^*} \frac{\partial^2}{\partial x^2} \psi + V_{SL}(x)\psi = E\psi. \quad (1.31)$$

1.3.2 Superlattice structures used in this thesis

In this thesis we will consider two superlattice structures. The first sample is a structure that has been used in previous experimental and theoretical work [18] and is known as sample NU2293. This sample will be used in chapters 2 and 3 so comparisons can be made with experimental work. The unit cell of NU2293 is shown in figure 1.4(a) and consists of three layers rather than the usual two layer superlattice. The first layer is AlAs, which has a relatively large bandgap generating a barrier region (see left hand edge of figure 1.4(b)). There is then the GaAs quantum well. At the well centre is an InAs layer, which has a relatively small bandgap (see figure 1.4(b)). NU2293 has a total period of $d_{SL} = 8.241$ nm (details given in the figure) and consists of 14 quantum wells. The band width for the 1st miniband of NU2293 is $\Delta_{SL} = 19.1$ meV.

The band structure for the superlattice is calculated using the method described in appendix A and is shown in figure 1.4(c). The unusual feature of this superlattice is the InAs notch at the centre of the quantum well. This occurs at the antinode of the groundstate wavefunction and consequently lowers the energy of the first miniband. This ensures that the miniband edge is close to the Fermi level of the emitter contact, thus facilitating electron injection. Since the notch occurs at the node of the second miniband (see figure 1.4(c)) it has little effect on this band and therefore the energy gap between the bands is very large (~ 240 meV). Consequently, tunnelling between the first and second miniband is substantially suppressed compared to a conventional superlattice.

In chapter 4 we consider a superlattice, known as sample 7MEV, which is based on a recently investigated experimental superlattice [7]. Figure 1.5(a) shows a schematic diagram of the potential energy variation in one unit cell of the structure. This superlattice consists of a barrier region of AlGaAs and then a well region of GaAs. The lattice period of $d_{SL} = 12.5$ nm and first miniband width of $\Delta_{SL} = 7$ meV were

¹For a more detailed explanation of this approximation then the reader is encouraged to read [17].

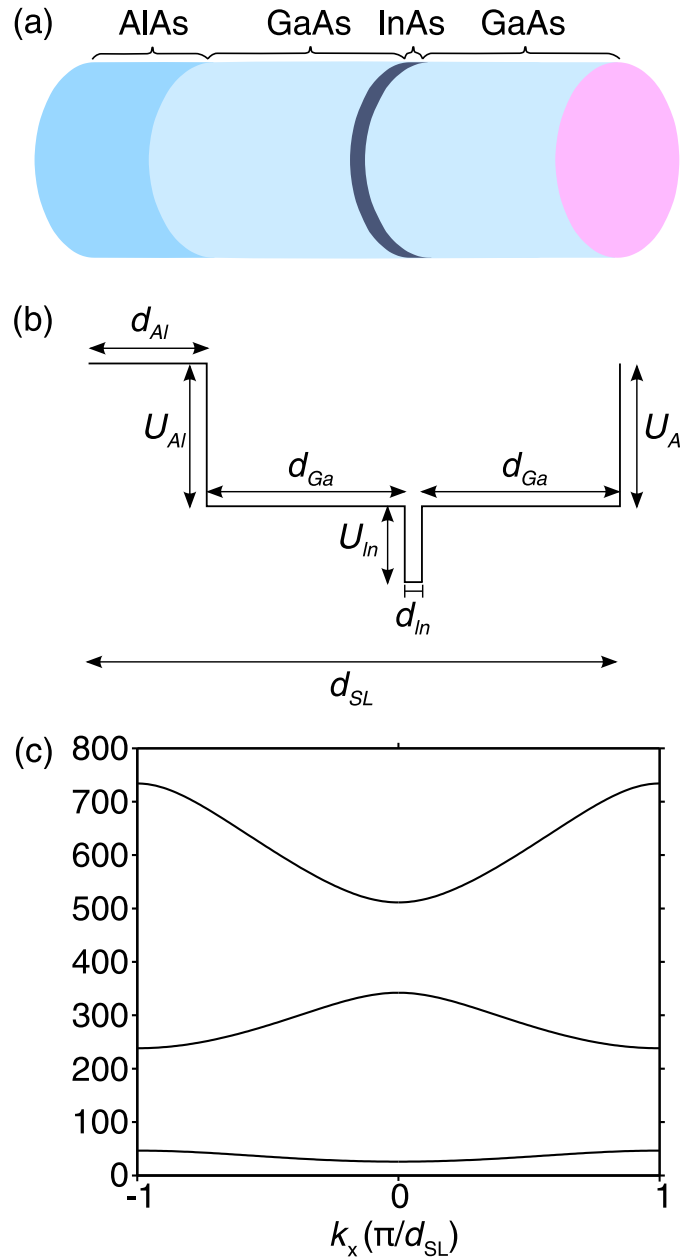


Figure 1.4: Not to scale (a) Physical structure of superlattice sample NU2293. (b) Superlattice potential arising from the variation in the conduction band edge between the different materials, where $U_{Al} = 1064$ meV, $U_{In} = -698$ meV, $d_{Al} = 10$ Å, $d_{Ga} = 35$ Å, and $d_{In} = 2.41$ Å. (c) Dispersion relation of the first three minibands calculated for the unit cell shown in (b) by solving equation (1.31) (see appendix A)

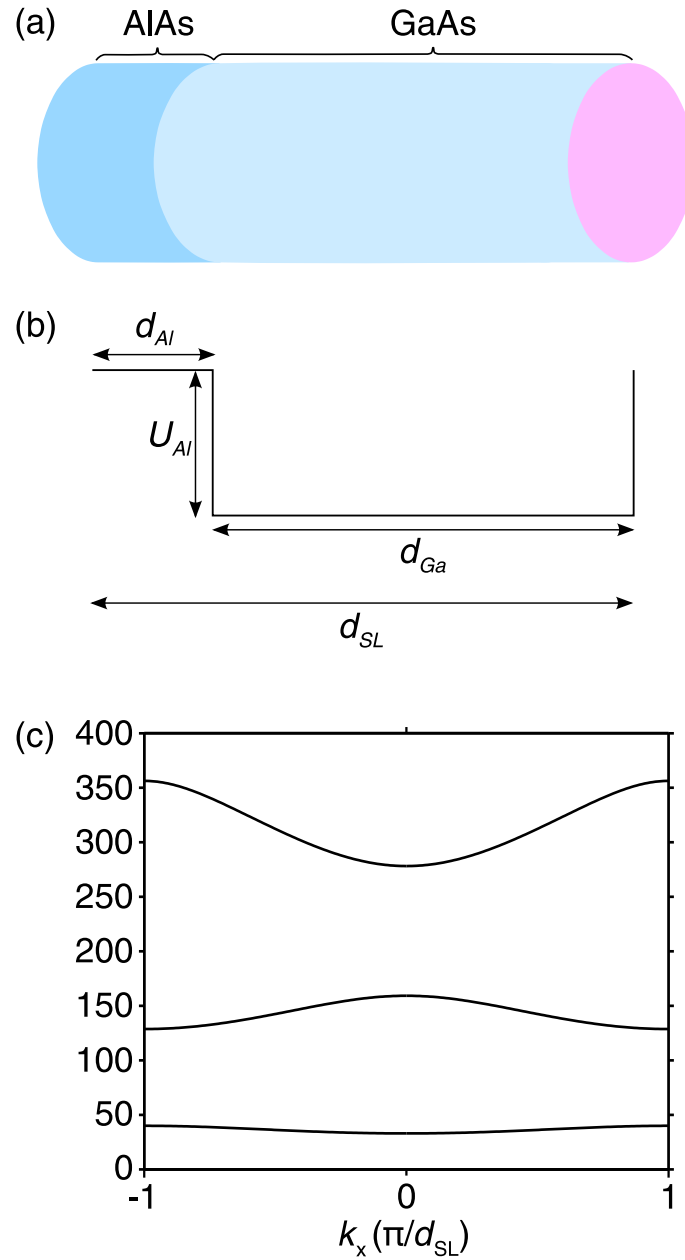


Figure 1.5: (a) Physical structure of superlattice sample 7MEV. (b) Superlattice potential within a unit cell due to the variation in the conduction band edge where $U_{Al} = 409$ meV, $d_{Al} = 25$ Å and $d_{Ga} = 100$ Å. (c) Dispersion relation of the first three minibands obtained from the potential defined in (b).

chosen to allow exploration of effects requiring a lower miniband width than NU2293 but still within experimental ranges.

1.3.2.1 Semiclassical model for electron dynamics

We have already suggested that the dynamics of electrons in a superlattice can be described by the band model, where the band structure is calculated from the potential defined by the superlattice structure, $V_{SL}(x)$. To find the form of the minibands, we must solve a Schrödinger equation of the form given in equation (1.22).

This equation can be solved numerically, using the technique outlined in appendix A, to obtain the Bloch wavefunctions and the resulting dispersion relation $E(k_x)$ for the electron along the x -axis. Once the dispersion relations are known it is possible to construct the corresponding semiclassical Hamiltonian for the electron in the first miniband (see section 1.2)

$$\mathcal{H} = E(p_x) + \frac{p_y^2}{2m^*} + \frac{p_z^2}{2m^*} \quad (1.32)$$

where $\mathbf{p}(p_x, p_y, p_z) = \hbar\mathbf{k}(k_x, k_y, k_z)$ is the momentum of the electron¹. The dispersion relation $E(p_x)$ (see section 1.3.2 for an example) for the first miniband in a given superlattice may be described by following Fourier series,

$$E(p_x) = \frac{\Delta_{SL}}{2} \left(a_0 - \sum_{n=1}^{\infty} a_n \cos\left(\frac{np_x d_{SL}}{\hbar}\right) \right) \quad (1.33)$$

where Δ_{SL} is the width of the first miniband, d_{SL} is the superlattice period, and a_n are the Fourier coefficients². This exact form of the dispersion curve is used in this thesis whenever an exact calculation of the electron dynamics is required. However, noting that $a_1 = 1$ and $a_{n>1} \ll 1$, to get a qualitative idea of the dynamics it is possible to make the following approximation for $E(p_x)$

$$E(p_x) = \frac{\Delta_{SL}}{2} \left(1 - \cos\left(\frac{p_x d_{SL}}{\hbar}\right) \right). \quad (1.34)$$

The electron dynamics can now be obtained using Hamilton's equations, which are equivalent to the semiclassical equations of motion described in section 1.2 and will be explored in later sections of the thesis.

¹Note that the kinetic energy of the electron in the y and z directions is simply the kinetic energy of a free particle with mass m^* .

²The method to obtain the Fourier coefficients can be found in [17].

1.3.2.2 Quantum mechanical model for electron dynamics

The electron dynamics can also be obtained by evolving the electron's wavefunction, $\psi(x, t)$, in time using the time-dependent Schrödinger equation [6]

$$i\hbar \frac{\partial \psi(x)}{\partial t} = \hat{\mathcal{H}}(x, t)\psi(x) \quad (1.35)$$

where the Hamiltonian is given by

$$\hat{\mathcal{H}} = -\frac{\hbar^2}{2m^*} \frac{\partial^2}{\partial x^2} + V_{SL}(x) + V_{ex} \quad (1.36)$$

where V_{ex} , is the potential generated by an applied field. Due to the discontinuities of the superlattice potential, $V_{SL}(x)$, it is difficult to obtain an analytical solution to the Schrödinger equation in this system, and thus it needs to be solved numerically. Here we use the *Crank-Nicolson* scheme, a powerful method used extensively in wave packet analysis. A general introduction to this method is given in Numerical Recipes [19]. However, a more detailed description of this technique with a focus on its application to the Schrödinger equation can be found in the theses by R.G. Scott [20], S. Naylor [21], or T.E. Judd [22].

The initial wavefunction of the system at $t = 0$, ψ_0 , is an important factor when trying numerically to solve equation (1.35). It affects many of the transport properties of the electron since it determines which of the system's minibands will be populated. The starting point for the initial form for the wavefunction is a simple, normalised, Gaussian defined by the following equation

$$\psi(x) = \sqrt{\frac{1}{2\pi\sigma_x}} \exp\left(\frac{-(x - x_c)^2}{2\sigma_x^2}\right) \quad (1.37)$$

where x_c ($= 0$ in this thesis) is the point on the x -axis around which the Gaussian is centred and

$$\sigma_x = f_x/2\sqrt{2 \ln 2} \quad (1.38)$$

is the standard deviation of the Gaussian in the x direction, where f_x is the Full-Width Half-Maximum (FWHM) of the Gaussian. In the following simulations f_x is chosen to be a multiple of the superlattice period. Figure 1.6(a) shows the form of an initial Gaussian wavefunction, as defined in equation (1.37), for the superlattice sample 7MEV (see section 1.3.2). Here the FWHM (f_x in equation (1.38)) of the

initial wavefunction was chosen to span several superlattice periods so the electron would show semiclassical band like dynamics. In the simulations presented here $f_x = 6d_{SL}$. To investigate the effect of using a Gaussian initial wavefunction, the time-dependent Schrödinger equation was solved when only a static electric field is applied to the superlattice, where according to Bloch theory we would expect the electron wavepacket to Bloch oscillate. In this static field regime the applied potential is given by $V_{ex} = V_F(x) = -eFx$, where F is the applied electric field. The Hamiltonian is therefore

$$\hat{\mathcal{H}} = -\frac{\hbar^2}{2m^*} \frac{\partial^2}{\partial x^2} + V_{SL}(x) + V_F(x). \quad (1.39)$$

The plot in figure 1.6(b) shows the evolution in time of the probability density profile, $|\psi(x, t)|^2$, corresponding to the initial wavefunction shown in figure 1.6(a). The simulation was performed for a relatively low field, $F = 2 \times 10^5 \text{ V m}^{-1}$. The wavefunction appears to split into two parts, which oscillate at the same frequency, the Bloch frequency defined in equation (1.28), but have significantly different spatial amplitudes. The splitting is a result of the wavefunction populating two different minibands, revealed when we recall the equation for the amplitude of the Bloch oscillations in a given miniband, index mb , (see equation (1.27)),

$$A_B = \frac{\Delta_{SL}^{mb}}{eF} \quad (1.40)$$

depends on the width of the miniband. Analysis of the differing amplitudes of the oscillations show that the electron resides in the first miniband and the third miniband [21; 23]. The fact that multiple minibands are populated should come as no surprise when we consider that by defining a Gaussian wavefunction for the whole system we ignore the tendency of electrons to reside in the low energy wells in the potential. This also explains why the second band is not populated. The height of the barriers coincides with the position of the third miniband (compare (b) and (c) in figure 1.5) which means that parts of the electron wavepacket in the barriers are forced in the third miniband. Note that ω_B does not depend on the miniband width, and thus the two parts of the wavefunction oscillate at the same frequency.

To ensure that the quantum dynamics are analogous to the semiclassical results, which only consider electron dynamics in the first miniband, the initial wavefunction must also be chosen to only populate the first miniband of the superlattice. The population of a single miniband will also simplify the results of simulations, since

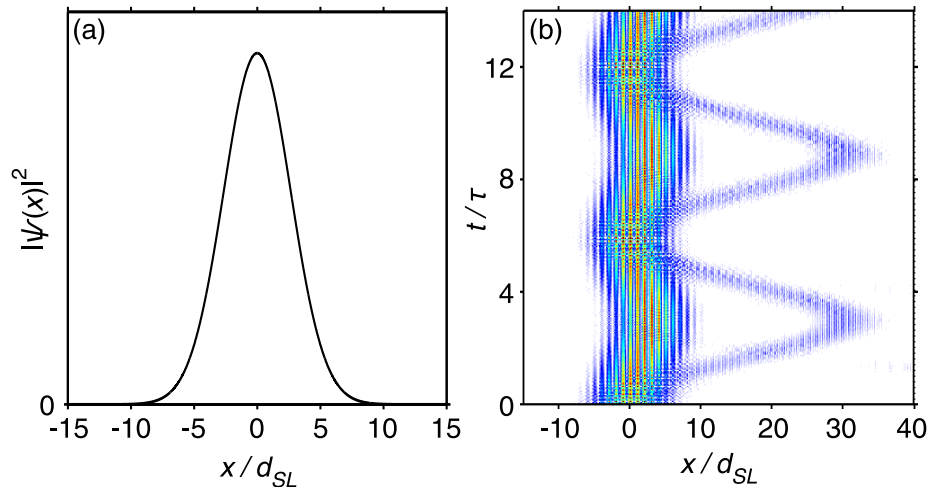


Figure 1.6: (a) Plot showing the form of an initial Gaussian wavefunction as defined in equation 1.37 for $f_x = 6d_{SL}$. (b) Colour map showing the variation of the probability density function, $|\psi(x,t)|^2$ as a function of time and position for the initial wavefunction shown in (a). In the colour map blue represents low values, yellow middle values, and red high values.

the population of multiple bands induces a complex mixture of electron dynamics from the different bands, making analysis of the results difficult. Also, any apparent population of higher order minibands will signify tunnelling of the electron out of the first miniband. Formally, to obtain the wave function of an electron in the first miniband, it is necessary to find the Wannier states of the electron by solving the time-independent Schrödinger equation given in equation (1.31) using a method such as the one outlined in [8].

The determination of the Bloch states is difficult. Fortunately, though, there is a numerical ‘trick’, the imaginary time technique [20], which takes into account the fact that the electron in the first miniband is also in the lowest energy state, the ground state, of the system. In this technique time, t , in equation (1.35) is replaced by $-it$, where $i = \sqrt{-1}$. Then, by solving the equation numerically any reasonable initial guess for the ground state will converge to the actual ground state of the system.

We can understand this technique by considering an initial guess, $\Psi_{guess}(x,t)$ for the ground state, defined as a sum of the eigenfunctions of the electron in the superlattice, ψ_n ,

$$\Psi_{guess}(x, t) = \sum_n c_n \psi_n(x) e^{\frac{iE_n t}{\hbar}}, \quad (1.41)$$

where E_n is the energy of the eigenstate ψ_n , and c_n is the weighting factor determining the contribution of ψ_n to Ψ_{guess} . To evolve Ψ_{guess} in imaginary time we replace t by $-it$ therefore equation (1.41) becomes

$$\Psi_{guess}(x, t) = \sum_n c_n \psi(x)_n e^{-\frac{E_n t}{\hbar}}. \quad (1.42)$$

By making this substitution, the magnitude of each term of the summation is now decaying exponentially in time. However, the state with the lowest energy, within the first miniband, will decay slower than states with higher energies. Therefore, evolving the wavefunction in imaginary time for a long time will eventually result in only the ground state making up the complete wavefunction. Note that, of course, the ground state is also decaying in time so to avoid the wavefunction tending to zero, the wavefunction must be normalised after each time step. The plot in figure 1.7(a) shows the electron wavefunction for an electron in the first miniband with an initial guess defined by the Gaussian in equation (1.37) with $f_x = 6d_{SL}$ (see figure 1.6(a)), evolved in imaginary time for 10 fs. Immediately it is apparent that the wavefunction makes more sense with the probability of the electron being in the barriers of the superlattice tending to zero¹. The plot in figure 1.7(b) shows the evolution of the wavefunction in time corresponding to the initial wavefunction shown in figure 1.7(a). It is clear that the wavefunction does not fragment, implying that it remains in the first miniband, and thus the initial wavefunction determined by the imaginary time method only populates the first miniband.

1.3.3 Electron scattering

Up to this point we have only considered the dynamics of electrons in perfect conductors. However, to get a realistic idea of electron conduction it is necessary to consider the effect of scattering on transport. In fact, as was demonstrated in section 1.2.1, without scattering there would be no electrical conduction in solids. Clearly, the main influence on an electron in a solid is the ions which make up that solid. The effect of these ions on the electron transport is included in Bloch theory. However, perfect

¹Note that the centre of the quantum wells are at $x = 0, d_{SL}, 2d_{SL}...$

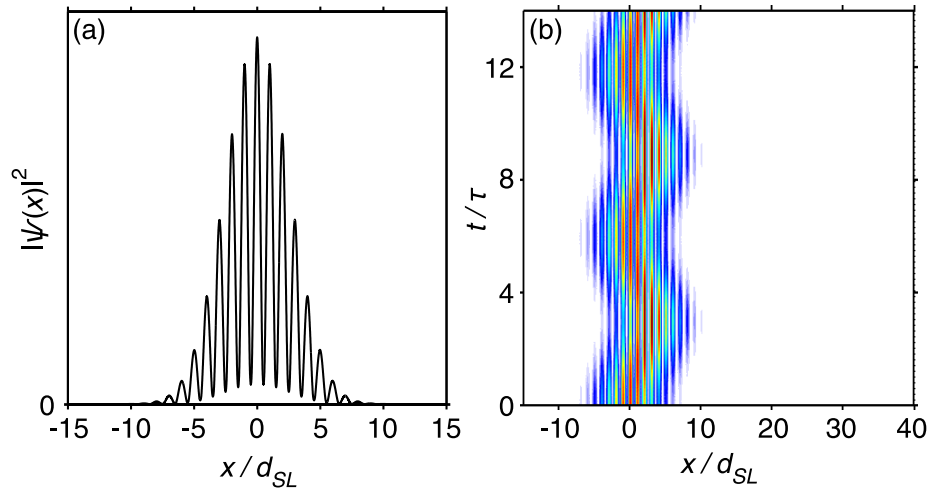


Figure 1.7: (a) Plot showing the form of an initial wavefunction within the first miniband, calculated using the imaginary time method with $f_x = 6d_{SL}$. (b) Colour map showing the variation of the probability density function, $|\psi(x,t)|^2$ as a function of time and position for the initial wavefunction shown in (a). In the colour map blue represents low values, yellow middle values, and red high values.

lattices of ions do not exist in reality and we must consider the effect of imperfect lattices on electron transport. There are two major causes of scattering that remove us from the perfect semiconductor lattice.

The first are scattering events that occur as a result of imperfections in the structure of the semiconductor crystal. Such imperfections include impurities in the structure and deformations in the lattice structure, which both disrupt the periodicity of the lattice. In the fabrication of nanostructures such as superlattices by molecular beam epitaxy the likelihood of defects forming in the structure can be minimised by controlling the deposition process. However, there is also an additional lattice defect associated with the interface between two types of semiconductor material (known as a heterojunction). This interface roughness can occur in the deposition process, outlined previously, but can also arise if the adjoining semiconductor materials have different lattice constants which stretches or compresses the two layers when they contact. This can lead to electron scattering events.

The second type of imperfection is due to external factors such as mechanical deformations or thermal vibrations of the lattice, which again disrupt the periodicity of the crystal and can lead to electron-phonon scattering events. These vibrations occur

at all temperatures of the lattice but their significance decreases as the temperature decreases.

The mechanics of the scattering events are separated into two groups: *inelastic* and *elastic* scattering. During inelastic scattering, deviations in the electron's trajectory occur due to scattering events where both the energy and momentum of the electron are allowed to change. These mostly arise from electron-phonon interactions. During elastic scattering only the momentum of the electron is allowed to change and the energy remains constant as, for example, in a scattering event between the electron and a defect in the lattice.

To include scattering in the transport model of a superlattice we introduce the concept of the scattering time, τ , where dt/τ is the probability of a scattering event occurring in time dt ($\ll \tau$). If we only consider *inelastic* and *elastic* scattering then, as discussed in references [24] and [14], A single effective scattering time,

$$\tau_{eff} = \tau_i \sqrt{\frac{\tau_e}{\tau_i + \tau_e}}, \quad (1.43)$$

can be introduced where τ_i is the inelastic scattering time and τ_e is the elastic scattering time (both can be found from experiment). If the effective scattering time is used, the drift velocity must be scaled by a factor $\delta = \tau_{eff}/\tau_i$ when calculating the current [24].

1.3.4 Esaki-Tsu formulation of drift velocity

To investigate how semiclassical electron transport along the x -axis of the superlattice will be affected by scattering events, we consider transport in the *relaxation time approximation* [10]. In this approximation it is assumed that an electron after a scattering event has no 'memory' of its behaviour prior to the event. We also assume that the scattering time is constant in time and space.

To calculate the drift velocity of electrons in a superlattice, we begin by estimating the number of electrons that remain unscattered at time t , $N(t)$. We know from the previous section (section 1.3.3) that the probability of an electron scattering in time dt is dt/τ where τ was the scattering time. It follows then that the number of electrons scattered in time dt is equal to

$$N(t) \frac{dt}{\tau}. \quad (1.44)$$

Therefore the number of electrons unscattered by time $t + dt$ is

$$N(t + dt) = N(t) - N(t)\frac{dt}{\tau}. \quad (1.45)$$

This implies that the rate of change of unscattered electrons can be found by

$$\frac{dN}{dt} = \frac{N(t + dt) - N(t)}{dt} = -\frac{N(t)}{\tau}. \quad (1.46)$$

By integrating equation (1.46) we find that the number of unscattered electrons at time t is

$$N(t) = N_0 e^{-t/\tau} \quad (1.47)$$

where $N_0 = N(t = 0)$ is the number of electrons at $t = 0$. The probability of an electron scattering in time dt is given by the number of electrons that scatter in time dt , equation (1.44), divided by the total number of electrons

$$P(t)dt = \frac{N(t)dt}{\tau} \frac{1}{N_0}. \quad (1.48)$$

Then by substituting equation (1.47) into equation (1.48) we obtain

$$P(t)dt = \frac{1}{\tau} e^{-t/\tau} dt. \quad (1.49)$$

We note that electrons that have been scattered do not ‘remember’ their behaviour before the scattering event. Therefore, only the behaviour of electrons after their scattering event at time t will contribute to the average electron velocity at time t . So the component of the electron drift velocity at time t is given by

$$v_d(t) = v_x(t)P(t)dt \quad (1.50)$$

i.e. the velocity of the electrons at time t multiplied by the proportion of electrons scattered at time t . We now find the total drift velocity of the system by integrating equation (1.50) over all t to find

$$v_d = \int_0^\infty v_x(t)P(t)dt \quad (1.51)$$

so with substitution of equation (1.49) into (1.51) we find that

$$v_d = \frac{1}{\tau} \int_0^\infty v_x(t)e^{-t/\tau} dt \quad (1.52)$$

which is the general form for the drift velocity of an electron in a superlattice. This equation will be used in following chapters of this thesis. However, as noted above, v_d will be scaled by the factor δ when we use the effective scattering time (see section 1.3.3, equation (1.43)) to calculate current.

With the expression for the drift velocity derived we can now make an analytical prediction for the drift velocity of an electron in a superlattice. From equation (1.23) we know that for the one dimensional superlattice the velocity of the electron in the x direction is

$$v_x = \frac{\partial E}{\partial p_x} \quad (1.53)$$

where the dispersion relation may be approximated by the following expression (see equation (1.34))

$$E(p_x) = \frac{\Delta_{SL}}{2} \left(1 - \cos \left(\frac{p_x d_{SL}}{\hbar} \right) \right). \quad (1.54)$$

Therefore, by substitution of equations (1.53) and (1.54) into equation (1.52) we find the following expression for the drift velocity

$$v_d = \frac{\Delta_{SL} d_{SL}}{2\hbar} \frac{1}{\tau} \int_0^\infty \sin \left(\frac{p_x d_{SL}}{\hbar} \right) e^{-t/\tau} dt. \quad (1.55)$$

If we consider an electron initially at the bottom of the miniband i.e. $p_x(0) = 0$, and we assume that there is an electric field $\mathbf{F} = (-F, 0, 0)$ applied along the superlattice, then according to equation (1.26)

$$p_x(t) = eFt. \quad (1.56)$$

Substituting equation (1.56) into (1.55) and then integrating by parts we find the following expression for the drift velocity

$$v_d = \frac{\Delta_{SL} d_{SL}}{2\hbar} \left(\frac{\omega_B \tau}{1 + \omega_B^2 \tau^2} \right) \quad (1.57)$$

where $\omega_B = eFd_{SL}/\hbar$ is the frequency of the Bloch oscillations. This drift velocity field relation is known as the Esaki-Tsu curve [10], which is plotted in Figure 1.8. Differentiation of the Esaki-Tsu equation reveals that the maximum in the drift velocity occurs when $\omega_B = 1/\tau$. When $\omega_B \ll 1/\tau$ then the drift velocity curve is linear, typical of an ohmic current-voltage relation. In this regime the electrons are scattered before

they are allowed to progress very far along the dispersion curve and the superlattice performs as a regular conductor. At $\omega_B = 1/\tau$ the electron is allowed to traverse roughly half the Brillouin zone before scattering and here the drift velocity is at its maximum. However, when $\omega_B > 1/\tau$ we see a surprising phenomenon whereby the transport of the electron appears to be suppressed with increasing field - known as a region of *negative differential velocity* or *negative differential conductance*. In this region many electrons are allowed to reach the Brillouin zone edge before scattering, are Bragg reflected and allowed to Bloch oscillate. The electrons are localised while undergoing Bloch oscillations thus suppressing transport. As the field is increased further, ω_B increases, further suppressing the electron transport and generating the region of negative differential velocity shown in Figure 1.8.

Negative differential conductance in superlattices was first seen in experiment by Esaki and Chang in 1974 [13] who showed that the conductance of the superlattice exhibited a sequence of dips, reaching negative values as the bias voltage was increased. However, the superlattice used was weakly coupled and these dips are attributed to resonant tunnelling between the wells. It was 20 years after Esaki and Tsu first suggested Bloch oscillation induced negative differential conductance in 1970, that it was first observed in experiment by F. Beltram *et. al.* [25] in 1990. They found direct evidence of negative differential conductance due to electric-field-induced localisation of the wavefunction, and demonstrated it was physically equivalent to the mechanism described above for a strongly coupled superlattice.

It should be noted here that the drift velocity characteristic presented by the Esaki-Tsu relation is true for an electron in the first miniband. However, when $\omega_B \gg 1/\tau$ the electron can tunnel into higher energy minibands [7], which causes the velocity of the electron to increase, so generating a large increase in drift velocity. This type of behaviour is known as an N-shaped drift velocity.

In the following section, we will show that when we consider the collective behaviour of the electrons, negative differential velocity in the drift velocity curve triggers the formation of static and travelling domains, the latter inducing self generating current oscillations.

1.3.5 Basic charge domain formation in superlattices

The semiclassical model of electron transport, described previously in this chapter, is effective in describing the behaviour of a single electron in an infinite superlattice

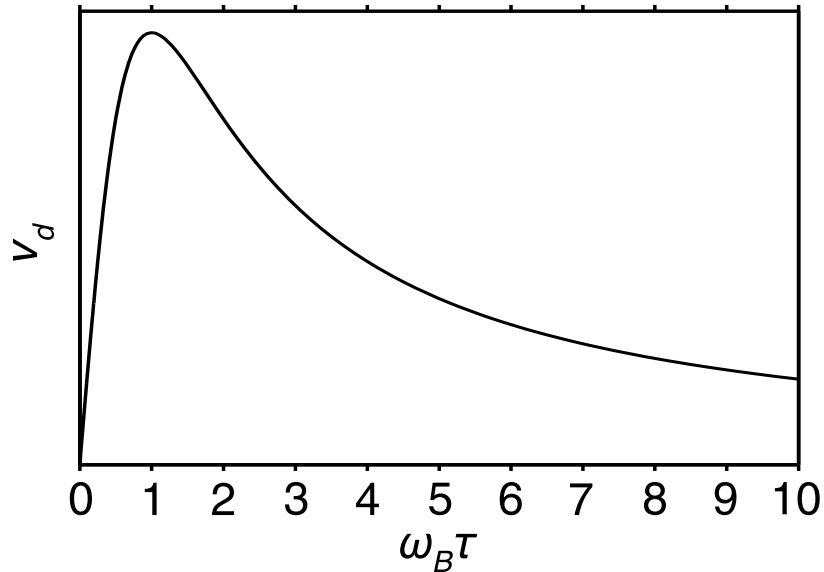


Figure 1.8: Plot showing the form of of the Esaki-Tsu curve, calculated using equation (1.57).

under the influence of electric and magnetic fields. The drift velocity analysis takes into account scattering, within a relaxation time approximation and, also, by averaging over many starting conditions, it can take into account thermal broadening. However, the drift velocity does not include the effect of collective electrostatic effects and dynamics on the transport of electrons, and thus does not produce any experimentally measurable predictions for doped superlattice systems. Note that there are recent experiments, which enable the drift velocity of the electron to be obtained directly using a three-terminal superlattice where the superlattice layers were undoped [26]. However, the experiment is difficult and requires specialised fabrication and measurement techniques.

The localisation of the electron trajectories, due to Bloch oscillations, as the electric field (or voltage) is increased, causes a region of negative differential velocity, and thus induces charge and field domains in the device. Negative differential velocity has been shown to cause charge and field domain formation in various devices (for example the Gunn diode [27; 28]). Thus domain formation was proposed for superlattices [29] and verified experimentally [30]. It was found that the frequency and amplitude of the charge domain oscillations could be varied by changing the form of the drift velocity curve or the length of the superlattice [31; 32; 33], leading to the observation of frequencies over 100GHz [34].

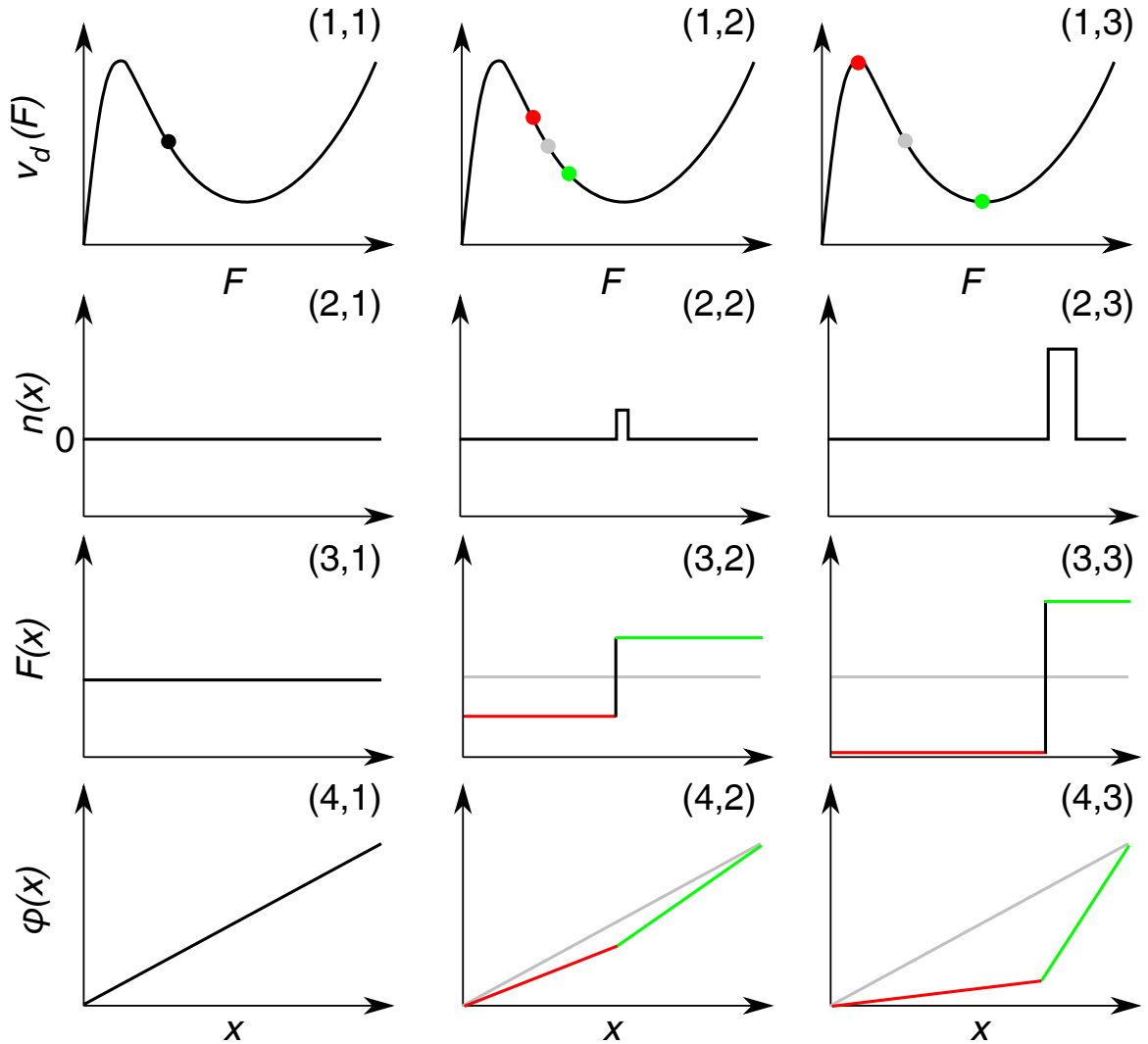


Figure 1.9: Schematic diagram [with individual panels labelled as (i,j) where i (j) is row (column) index] showing the formation of a charge domain in a superlattice. In each column, the panels, from top to bottom, show $v_d(F)$, $n(x)$, $F(x)$ and $\phi(x)$. Left-hand, centre and right-hand columns correspond, respectively, to the system in equilibrium, with a small charge accumulation that destroys the equilibrium, and the subsequent evolution of that charge accumulation. Red lines and dots show low field regions. Green lines and dots show high field regions. In centre and right-hand columns grey lines and dots show the system in equilibrium (as in the left-hand column) to allow comparison.

To understand how charge domains form and propagate in superlattices (and indeed in any doped device exhibiting negative differential velocity) it is useful to consider the behaviour of a general superlattice with a local N-type drift velocity characteristic (one that exhibits a region of negative differential velocity followed by a sharp increase in drift velocity (see figure 1.9(a))) and an external voltage, V , applied along the x axis of the device¹. In such a system, Gauss's law tells us that the electric field, $\mathbf{F}(x)$, at position x , has the following relationship with the corresponding volume electron density at position x , $n(x)$, [36]

$$\nabla \cdot \mathbf{F}(x) = \frac{-e}{\varepsilon_r \varepsilon_0} n(x) \quad (1.58)$$

where ε_r is the relative permittivity of the material of the device and $\varepsilon_0 = 8.8541 \times 10^{-12} \text{ F m}^{-1}$ is the vacuum permittivity. The initial state of the system is homogeneous so that the charge density of electrons is constant across the device (see figure 1.9(b)) and is equal to the doping density n_D . The field therefore is also constant across the system and its value depends on the electric potential $\phi(x)$, so that

$$\mathbf{F}(x) = -\nabla\phi(x). \quad (1.59)$$

This implies that the potential rises linearly through the superlattice with the total increase always equal to the voltage applied, V , which determines the value of the electric field in the homogeneous case, see left-hand column of figure 1.9. It is assumed that the voltage is chosen such that the field in the superlattice lies on the negative differential velocity part of the drift velocity curve, as shown by the filled circle in panel (1,1) of figure 1.9. We now consider the effect of adding a small charge accumulation somewhere in the system. In most cases this would come from current injected into the superlattice region from the emitter. However, for clarity, here we imagine the effect of a small charge accumulation half way along the superlattice region [37]. According to equation (1.58), the charge accumulation produces an abrupt change in the electric field so that the left hand region of the superlattice has a low field, (coloured red in the centre column of figure 1.9), and the right hand region has a high field (coloured green in the centre column of figure 1.9). The value of v_d in the low field region (green circle in figure 1.9(1,2)) is higher than

¹The behaviour explained in the rest of this section is representative not only of superlattices, but also of other semiconductor structures with similar drift velocity characteristics such as Gunn diodes [27] and dilute nitride structures [35].

that in the high field region (red circle in figure 1.9(1,2)). Therefore electrons enter the charge accumulation zone much faster from the red region than they can leave through the green region. Consequently, the small charge accumulation grows, and, since the electrons in the charge accumulation are moving through the superlattice at a velocity determined by the local field, it moves through the superlattice (see right-hand column of figure 1.9). The process continues until the difference in velocities of electrons entering and exiting the charge accumulation no longer increases (see figure 1.9(1,3)), at which point the charge accumulation stops growing and continues to move through the lattice until it reaches the collector. Generally, however, the charge accumulation continues to grow as it traverses the superlattice. Although, if the voltage applied to the superlattice is sufficient to access a region of positive differential conductivity, e.g. for the N-type v_d curve considered here, then as the field in the green region increases, the drift velocity exiting the charge domain will increase and, consequently, the charge accumulation will shrink.

Charge domain formation and propagation is somewhat more complex than the simple explanation given here. Further details are given in reference [15].

Additional to the DC field case considered here, domain formation has also been studied in superlattices under the influence of AC fields [14; 38; 39] and perpendicular and parallel magnetic fields [40; 41; 42; 43]. However, not until the paper by T.M. Fromhold *et. al.* [18] have the effects of a tilted magnetic field on *static* domain formation been considered. In chapter 3 it will be shown that a tilted magnetic field can drastically modify the *dynamics* of charge domain formation and propagation in superlattices.

1.4 Optical lattices

The optical lattice is an incredibly versatile tool which allows the exploration of the dynamics of ultra-cold ($\leq 1 \mu\text{K}$) alkali atoms in periodic potentials. An optical lattice is simply a set of standing waves generated by counter propagating laser beams. The electric field induced by these standing waves interact with the atoms so that they effectively see a periodic potential defined by the wavelength and intensity of the lasers. Therefore, atoms in optical lattices are a direct analogue to an electron in solid, sharing many of the same properties. Thus their dynamics can be investigated with many of the tools found in solid state physics.

Optical lattices offer many advantages to the experimentalist wanting to study fundamental physics of particles in periodic potentials. The lattice parameters can be easily altered, simply by changing the wavelengths and intensity of the laser beams, this in comparison with building a new superlattice in the case of electrons. The initial momentum of the atom cloud can be well defined around a chosen value allowing control over initial conditions. The optical lattice is clear from defects and also from lattice vibration so scattering is not a significant consideration. The time scale for atoms is much longer than electron dynamics (milliseconds compared to picoseconds) due to their greater size and mass, and also because the lattice periods are significantly larger, allowing easier measurement of their dynamics. It is also possible to image the atom within the lattice. Finally it is possible to turn off the optical lattice giving an extra degree of control over system and enabling atoms' momenta to be measured directly

1.4.1 Interaction of alkali atoms with an optical lattice

To understand how alkali atoms interact with the optical lattice we start by considering the effect of a static electric field on an a single atom. In an electric field, ϵ , an atom will acquire an electric dipole moment, \mathbf{d} , resulting in a shift of its energy levels. The expectation value of the dipole moment is directly proportional to the electric field [44] and is given by,

$$\langle \mathbf{d} \rangle = \alpha \epsilon \tag{1.60}$$

where α is the *polarisability* of the atom and is the measure of the tendency of its electron cloud to be distorted by an external electric field. The following expression gives the resulting change in the energy of an atom's state with a small change, $d\epsilon$, in the electric field

$$dE = -\langle \mathbf{d} \rangle \cdot d\epsilon. \tag{1.61}$$

It follows then, by integration, that the contribution of energy by the electric field is

$$\Delta E = - \int \alpha \epsilon \cdot d\epsilon = -\frac{1}{2} \alpha \epsilon^2. \tag{1.62}$$

This equation is generalised by considering an oscillating field, $\epsilon(t) = \epsilon_0 \cos(\omega t)$, with frequency ω , and electric field amplitude ϵ_0 , to obtain,

$$\Delta E = -\frac{1}{2}\alpha'(\omega)\langle\epsilon(\mathbf{r}, t)^2\rangle_t \quad (1.63)$$

where the energy shift is now a function of the frequency dependent, *dynamical polarisability*, $\alpha'(\omega)$, and $\langle\cdots\rangle_t$ is the time average over the period of an oscillation.

This analysis is applied to the case of an optical lattice where there are two counter propagating laser beams of wavelength, λ , with electric fields given by,

$$\epsilon_1(x, t) = \frac{\epsilon_0}{2}e^{i(kx-\omega t)} \quad (1.64)$$

and

$$\epsilon_2(x, t) = \frac{\epsilon_0}{2}e^{i(-kx-\omega t)}. \quad (1.65)$$

where $k = 2\pi/\lambda$. Taking the sum of equations (1.64) and (1.65) we obtain the following standing wave equation

$$\epsilon(x, t) = \epsilon_1(x, t) + \epsilon_2(x, t) = \epsilon_0 \cos(kx)e^{(-i\omega t)}, \quad (1.66)$$

the real part of which is

$$\Re\{\epsilon(x, t)\} = \epsilon_0 \cos(kx) \cos(\omega t). \quad (1.67)$$

Substituting of equation (1.67) into equation (1.63) we find the following expression for the energy shift of the atom and, consequently, the effective periodic potential that the atom will experience in the optical lattice

$$\Delta E = -\frac{1}{2}\alpha'(\omega)\epsilon^2 \cos^2(kx) \langle\cos^2(\omega t)\rangle_t = V_0 \cos^2(kx), \quad (1.68)$$

where V_0 is given by

$$V_0 = -\frac{1}{4}\alpha'(\omega)\epsilon^2. \quad (1.69)$$

Using the trigonometric identity, $\cos^2 A = (1 + \cos(2A))/2$, in equation (1.68) and substituting $k = 2\pi/\lambda$ we find

$$\Delta E = \frac{V_0}{2} + \frac{V_0}{2} \cos\left(2\pi\frac{x}{\lambda/2}\right), \quad (1.70)$$

showing that the period of the optical lattice, d_{OL} , is $\lambda/2$.

1.4.2 Model for atom dynamics in optical lattices

It was shown previously that the potential felt by an atom in an atomic trap is given by equation (1.70). The effective potential energy that the atom experiences in the optical lattice, $V_{OL}(x)$, can be defined as

$$V_{OL}(x) = V_0 \sin^2 \left(\frac{\pi x}{d_{OL}} \right), \quad (1.71)$$

where V_0 is the amplitude of the lattice potential (see equation 1.69), and d_{OL} is the period of the optical lattice. Then the full quantum mechanical Hamiltonian of the atom in the optical lattice is given by

$$\hat{\mathcal{H}} = -\frac{\hbar^2}{2m_a} \frac{\partial^2}{\partial x^2} + V_{OL}(x), \quad (1.72)$$

where m_a is the mass of the atom.

In the simulations presented in chapter 5, we consider a neutral sodium (^{23}Na) atom [45; 46] in a one dimension optical lattice such as the one discussed in the previous section. This is experimentally equivalent to a low-density cloud of cold atoms where the interactions between the atoms have been turned off [9]. For sodium, $m_a = 23/N_A$ where $N_A = 6.022 \times 10^{26} \text{ kmol}^{-1}$ is Avogadro's constant. A clear advantage of using an optical lattice to study periodic potentials is that it is possible to relatively easily tailor the band structure of the lattice, simply by changing the frequencies and intensities of the laser beams. However, it is important to ensure that the laser frequencies are detuned from any atomic resonances that might cause excitation in the atom. Therefore, here, the optical lattice parameters were chosen from experiment [46], so $d_{OL} = 294.5 \text{ nm}$ and $V_0 = 562.52 \text{ peV}$. Substituting equation (1.72) into the time-independent Schrödinger equation (see equation (1.21)) and then solving using a method such as the one in appendix A, one can find the band structure for the sodium atom in the optical lattice. Figure 1.10 shows the form of V_{OL} and the related band structure for the optical lattice.

It is now possible to explore the dynamics of the atom in the optical lattice both semiclassically (see section 1.2); where we assume the dispersion relation of the first energy band has the form

$$E(p_x) = \frac{\Delta_{OL}}{2} \left(1 - \cos \left(\frac{p_x d_{OL}}{\hbar} \right) \right), \quad (1.73)$$

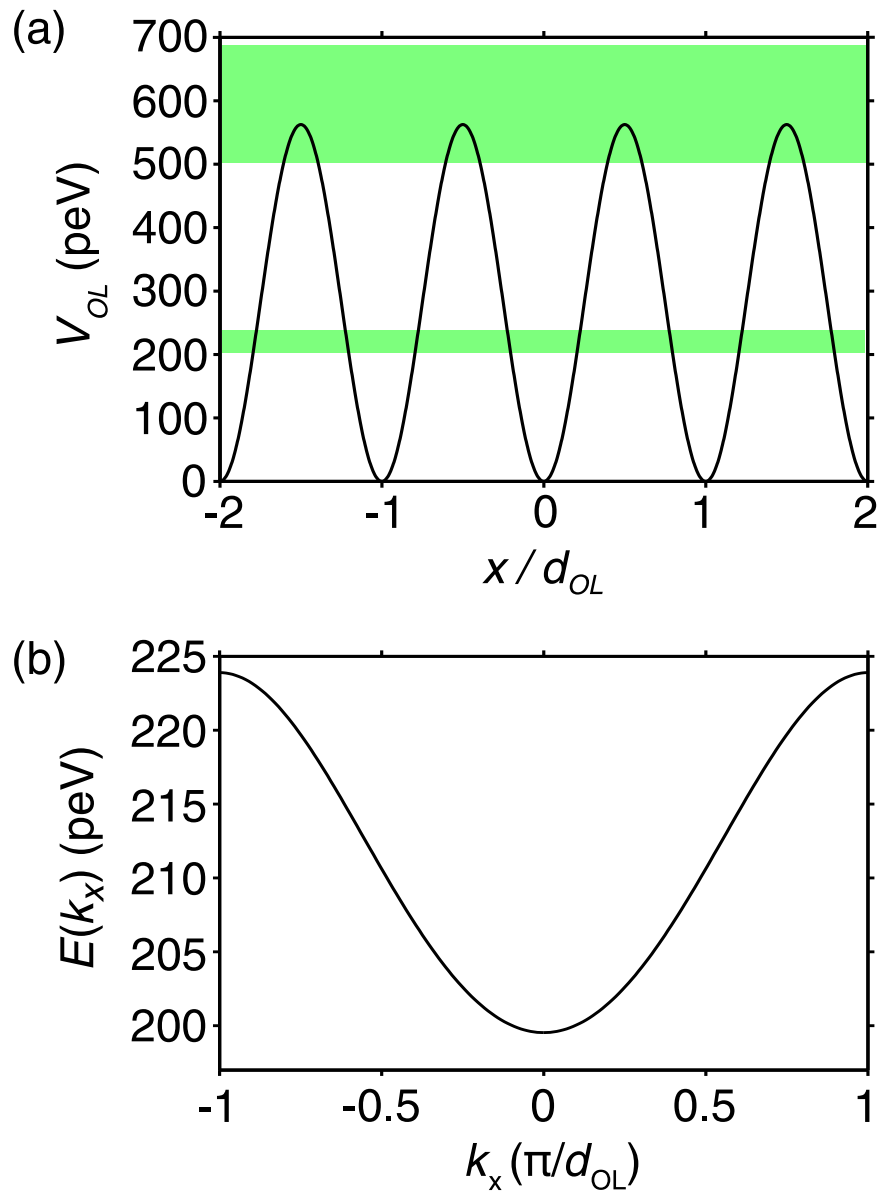


Figure 1.10: (a) Plot showing the potential energy of the optical lattice, $V_{OL}(x)$ (see equation (1.71)). The first and second energy bands occupy yellow shaded regions. (b) Dispersion relation of the first band of the optical lattice.

with a band width $\Delta_{OL} = 24.35$ peV; and also by solving the time dependent Schrödinger equation. In chapter 5 both of these regimes will be explored for a sodium atom in a stationary optical lattice with an additional moving optical potential applied.

Chapter 2

Magnetic field induced chaotic electron dynamics in superlattices

In this chapter, we consider the effect of a tilted magnetic field on the motion of an electron in a strongly coupled, biased, superlattice. It will introduce the work of T.M. Fromhold *et. al.* on chaotic dynamics in superlattices [18; 47]. In section 2.1 we demonstrate that when a magnetic field is applied, an electron's motion in a biased superlattice can be described by a one-dimensional simple harmonic oscillator, driven by time dependent plane waves [18; 47]. This type of system is potentially intrinsically chaotic as there are fewer constants of motion than degrees of freedom¹. In fact, in later sections we will show that this type of oscillator exhibits two types of chaos, both KAM and non-KAM chaos [18; 47; 48].

The Kolmogorov-Arnold-Moser (KAM) theorem explores what happens when an integrable Hamiltonian system is perturbed. The KAM theorem says that as the amplitude of the perturbation to the integrable system is increased, then the transition to chaos occurs by the gradual destruction of the stable periodic orbits in the parameter space. The system then evolves from fully stable motion, to mixed stable-chaotic behaviour (where there are islands of stable orbits in co-ordinate space, enclosed by a chaotic sea) to, eventually, being strongly chaotic where no stable orbits exist. KAM theory is very successful in describing the route to chaos in many nonlinear systems. However, KAM theory requires that the system's unperturbed Hamiltonian, $\mathcal{H}_0(\mathbf{I})$, to be non-degenerate, i.e. each system state has unique frequency, such that:

¹For more detail on Hamiltonian Chaos the author suggests *Chaos in Dynamical Systems* by E. Ott [48].

$$\left| \frac{\partial^2 \mathcal{H}_0(\mathbf{I})}{\partial I_i \partial I_j} \right| \neq 0 \quad (2.1)$$

where the Hamiltonian is expressed in terms of the generalised (action) momenta, \mathbf{I} , corresponding to angles, θ . In the case of a superlattice with a tilted magnetic field, the underlying, driven, one-dimensional oscillator is degenerate (since the oscillation frequency is independent of the system energy) and, consequently, KAM theory cannot be used to explain the types of chaos present in this system [49].

Non-KAM chaos, in contrast to KAM chaos, switches on and off abruptly at critical values of the perturbation frequency; in our particular case when the natural frequency of the simple harmonic oscillator is commensurate with the frequency of the driving term. This type of system is well known in the literature and was first explored by G.M. Zaslavsky and co-workers in the late 1980s and 1990s [49; 50; 51; 52; 53; 54; 55]. As well as being seen in the system presented in this chapter, non-KAM chaos also has implications for the dynamical theory of many other physical systems such as in plasma physics [52; 56] and therefore tokamak fusion [57], turbulence [50; 53; 55], ion traps [58], dynamics of ultra cold atoms in optical lattices [59; 60; 61] and the transmission of light through photonic crystals [62]. However, until the recent experimental work at the University of Nottingham it had not been realised in experiment [18; 63].

Non-KAM chaos presents itself in the phase space of the superlattice as a stochastic web. This web structure allows the electron to follow unbounded orbits through the superlattice, thereby significantly enhancing the current flow through the structure. Therefore we find that as we increase the strength of the perturbation, the strength of the chaos also increases, as expected from KAM theorem. However, at certain critical values the stochastic web ‘turns on’ abruptly enhancing current flow. This mechanism allows us to control and enhance the conductivity of the superlattice to the extent that the switching between the two different types of chaos could provide a sensitive ‘switch’ that could have applications in photonics [62] and electronics [64].

2.1 Superlattice electron dynamics in a tilted magnetic field

In this section we derive the equations of motion that describe the dynamics of an electron within a periodic potential with an applied magnetic field. We begin by deriving the semiclassical Hamiltonian for the electron and then use Hamilton's equations to derive the equations of motion. In section 1.3.2.1 we derived an expression for the Hamiltonian of an electron in the first miniband of a superlattice. By including an electric field, F , applied along the x direction of the superlattice we find that,

$$\mathcal{H} = E(p_x) + \frac{p_y^2}{2m^*} + \frac{p_z^2}{2m^*} - eFx, \quad (2.2)$$

where $\mathbf{p}(p_x, p_y, p_z)$ is the generalised momentum, and the dispersion equation for the electron $E(p_x)$ is given by equation (1.33). The effect of applying a magnetic field is to change the direction of the motion of the electron but not to change the total energy of the system. Therefore the effects of a magnetic field on the electron are included by making substitution [6; 65]

$$\mathbf{p} \rightarrow \mathbf{p} + e\mathbf{A} = \mathbf{q}, \quad (2.3)$$

where $\mathbf{q} = m^*\mathbf{v}$ is the linear momentum ($\mathbf{v} = d\mathbf{r}/dt$) and \mathbf{A} is the magnetic vector potential defined by

$$\mathbf{B} = \nabla \times \mathbf{A} \quad (2.4)$$

in which \mathbf{B} is the magnetic field vector. In the system considered here, \mathbf{B} lies in the x, z plane and is tilted at an angle θ to the x axis, i.e.

$$\mathbf{B} = (B \cos \theta, 0, B \sin \theta). \quad (2.5)$$

The simplest choice for \mathbf{A} , which ensures that equation (2.4) is consistent, and that satisfies the Coulomb gauge condition ($\nabla \cdot \mathbf{A} = 0$), can be shown to be [18; 47]

$$\mathbf{A} = (0, B(x \sin \theta - z \cos \theta), 0). \quad (2.6)$$

Therefore with reference to equation (2.3), we find that

2.1 Superlattice electron dynamics in a tilted magnetic field

$$\begin{aligned}
 q_y &= p_y + e\mathbf{A}(x, z) \\
 &= p_y + eB(x \sin \theta - z \cos \theta).
 \end{aligned}
 \tag{2.7}$$

Therefore, the Hamiltonian for a superlattice electron in a magnetic field is equal to

$$\mathcal{H} = E(p_x) + \frac{q_y^2}{2m^*} + \frac{p_z^2}{2m^*} - eFx.
 \tag{2.8}$$

The equations of motion can now be found from the Hamiltonian using Hamilton's equations. Hamilton's equations define the equations of motion for a particle governed by a particular Hamiltonian with the position coordinates $\mathbf{r}(x, y, z)$ and momentum coordinates $\mathbf{p}(p_x, p_y, p_z)$, and are given by

$$p_i = -\frac{\partial H(t, \mathbf{p}, \mathbf{r})}{\partial r_i}
 \tag{2.9}$$

and

$$r_i = \frac{\partial H(t, \mathbf{p}, \mathbf{r})}{\partial p_i}
 \tag{2.10}$$

where the degrees of freedom are indexed by $i = x, y$ or z . Therefore Hamilton's equation for this system are

$$\dot{x} = \frac{\partial H}{\partial p_x}, \quad \dot{p}_x = -\frac{\partial H}{\partial x}
 \tag{2.11}$$

$$\dot{y} = \frac{\partial H}{\partial p_y}, \quad \dot{p}_y = -\frac{\partial H}{\partial y}
 \tag{2.12}$$

$$\dot{z} = \frac{\partial H}{\partial p_z}, \quad \dot{p}_z = -\frac{\partial H}{\partial z}
 \tag{2.13}$$

where $\dot{}$ represents the time derivative. Evaluating equation (2.11) for the Hamiltonian in equation (2.8) results in the following expressions for the position of the electron in x, y and z

2.1 Superlattice electron dynamics in a tilted magnetic field

$$\dot{x} = v_x = \frac{\Delta_{SL} d_{SL}}{2\hbar} \sum_{n=1}^{\infty} n a_n \sin\left(n \frac{d_{SL} p_x}{\hbar}\right) \quad (2.14)$$

$$\dot{y} = v_y = \frac{q_y(p_y, x, z)}{m^*} \frac{\partial q_y(p_y, x, z)}{\partial p_y} = \frac{q_y(p_y, x, z)}{m^*} \quad (2.15)$$

$$\dot{z} = v_z = \frac{p_z}{m^*}. \quad (2.16)$$

where a_n are the miniband Fourier coefficients (see equation (1.33)). This reveals that \dot{x} is dependent on p_x making this set of equations non-linear. Equation (2.15) shows that $q_y = m^* v_y$, meaning that q_y is the linear momentum of the electron along the y axis (which is expected from the definition in equation (2.3)). It is important to note that these equations are consistent with the semiclassical equation of motion given in equation (1.23) where $\mathbf{v} = \partial E(\mathbf{p})/\partial \mathbf{p}$. Hamilton's equations can be used again with the Hamiltonian to find the following expressions for p_x , p_y and p_z

$$\dot{p}_x = eF - \frac{q_y(p_y, x, z)}{m^*} \frac{\partial q_y(p_y, x, z)}{\partial x} = eF - q_y \omega_c \sin \theta \quad (2.17)$$

$$\dot{p}_y = 0 \quad (2.18)$$

$$\dot{p}_z = -\frac{q_y(p_y, x, z)}{m^*} \frac{\partial q_y(p_y, x, z)}{\partial x} = q_y \omega_c \cos \theta \quad (2.19)$$

where $\omega_c = eB/m^*$ is the angular frequency of cyclotron oscillations caused by the magnetic field. Note that since $\dot{p}_y = 0$ and that q_y is dependent on p_y , x and z only; electron motion in the y -direction is separated from motion in the x - z plane. This implies that for investigation of electron transport along the x axis, only electron dynamics in the x and z directions need to be considered. However, if the position of the electron in y is required then we use the following expression for \dot{q}_y derived from equation (2.7)

$$\dot{q}_y = eB (\dot{x} \sin \theta - \dot{z} \cos \theta) \quad (2.20)$$

where \dot{x} and \dot{z} are given by equations (2.14) and (2.16), thus,

$$\dot{q}_y = eB \left(\sin \theta \frac{\Delta_{SL} d_{SL}}{2\hbar} \sum_{n=1}^{\infty} n a_n \sin\left(n \frac{d_{SL} p_x}{\hbar}\right) - \frac{p_z}{m^*} \cos \theta \right). \quad (2.21)$$

These equations can be shown to be consistent with the semiclassical equations of motion; equation (1.25) showed that $\dot{\mathbf{p}} = \mathbf{G}$ (noting that $\mathbf{p} = \hbar \mathbf{k}$) where \mathbf{G} is

2.1 Superlattice electron dynamics in a tilted magnetic field

the force on the electron due to the magnetic and electric fields given by the Lorentz equation

$$\dot{\mathbf{p}} = -e(\mathbf{F} + \mathbf{v} \times \mathbf{B}). \quad (2.22)$$

resulting in the same equations of motion found in equations (2.17) to (2.20).

With knowledge that this system of equations is independent of motion in the y direction, it can be manipulated to reduce to a single, second-order differential equation dependent on p_z [18; 47]. First, equation (2.19) is differentiated with respect to t and then the expression for \dot{q}_y is substituted from equation (2.20) to obtain

$$\ddot{p}_z = m^* \omega_c^2 \cos \theta (\dot{x} \sin \theta - \dot{z} \cos \theta) \quad (2.23)$$

then, inserting the expressions for \dot{x} and \dot{z} from equations (2.14) and (2.16), the following expression is obtained

$$\ddot{p}_z + (\omega_c \cos \theta)^2 p_z = \frac{m^* \omega_c^2 \Delta_{SL} d_{SL} \sin \theta \cos \theta}{2\hbar} \sum_{n=1}^{\infty} n a_n \sin \left(n \frac{dp_x}{\hbar} \right). \quad (2.24)$$

This expression now defines p_z in terms of p_x . However, by combining equations (2.17), (2.19) and (2.21) the following expression is derived

$$\dot{p}_x = eF - \dot{p}_z \tan \theta. \quad (2.25)$$

Then integrate to find

$$p_x(t) = p_x(t=0) + eFt - (p_z(t) - p_z(t=0)) \tan \theta. \quad (2.26)$$

We can now use this expression to obtain the following highly non-linear equation for p_z

$$\ddot{p}_z + (\omega_c \cos \theta)^2 p_z = -\frac{m^* \omega_c^2 \Delta_{SL} d_{SL} \sin \theta \cos \theta}{2\hbar} \sum_{n=1}^{\infty} n a_n \sin (n (K p_z - \omega_B t - \phi)). \quad (2.27)$$

This equation corresponds to a one-dimensional simple harmonic oscillator with natural frequency $\omega_{\parallel} = \omega_c \cos \theta$ (the cyclotron frequency corresponding to the component of \mathbf{B} along the x axis), driven by time-dependent plane waves with frequency $n\omega_B$, wave vector nK , and phase $n\phi$, where $K = -d_{SL} \tan \theta / \hbar$ and $\phi =$

2.1 Superlattice electron dynamics in a tilted magnetic field

$d [p_x(t=0) + p_z(t=0) \tan \theta] / \hbar$. All the dynamical variables of the system can now be determined from equation (2.27) using equations (2.14), (2.16), and (2.26). The general form of this system, a harmonic oscillator driven by a monochromatic plane wave, is well known in the theoretical literature as a chaotic system which exhibits very rich and intricate phase space patterning [47; 50; 53; 54; 55; 56; 57; 58; 66; 67; 68]. Also, these types of system are known to not obey the KAM theorem (non-KAM) [65] because the harmonic oscillator is degenerate, since the oscillation frequency, $\omega_c \cos \theta$, is independent of the energy of the system. This type of non-KAM chaos generally turns on when the natural frequency of the oscillator is commensurate with the frequency of the driving term, in this case when $\omega_B = r\omega_{\parallel}$ where r is an integer, and characterises itself as a stochastic web in phase space.

2.1.1 Electron trajectories

To show the effect of the magnetic field on the electron dynamics, we can consider the electron trajectories in the x - z plane, found by numerically integrating equations (2.17) - (2.20) using a scheme such as the 4th order Runge-Kutta algorithm [19].

The traces in figure 2.1 show the electron trajectories starting from rest ($p_x(0) = p_y(0) = p_z(0) = x(0) = y(0) = z(0) = 0$) for electric and magnetic field strengths of $F = 1.57 \times 10^6 \text{ V m}^{-1}$ and $B = 15 \text{ T}$ respectively. The superlattice parameters used correspond with the superlattice sample NU2293 (see section 1.3.2). Figure 2.1(a) shows the electron trajectory when $\theta = 0^\circ$, we find that in this case the plane wave has zero amplitude (note the $\sin \theta$ term on the right hand side of equation (2.27)), thus the motion in the x and z directions is separable. Since the trajectories are starting from rest there is only motion in the x direction and the electron performs Bloch oscillations along the line shown in the figure¹. When $\theta = 30^\circ$, see figure 2.1(b), there is only a small increase in the driving term of the harmonic oscillator and thus the oscillations remain stable and regular, reminiscent of the case when $\theta = 0^\circ$, albeit now tilted by the magnetic field. Increasing θ to 45° , figure 2.1(c), the plane wave term is now at its maximum, and consequently drives the electron's motion chaotic allowing the electron to traverse a large, though finite, number of superlattice periods. However, we find that when $\theta = 60^\circ$, figure 2.1(c), corresponding to the case when

¹If the electron does not start from rest then we find that the electron performs cyclotron oscillations about the direction of the magnetic field, and Bloch oscillations in the x direction (see section 1.2.1), which add to produce regular motion reminiscent of a Lissajous figure, see [65].

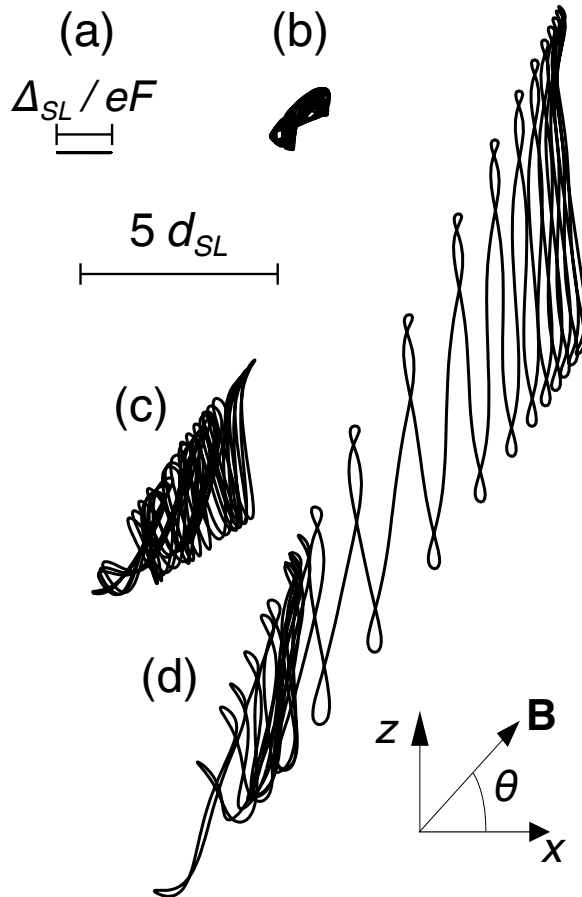


Figure 2.1: Electron trajectories in the x - z frame (axes inset) corresponding to $B = 15$ T and $F = 1.57 \times 10^6$ V m $^{-1}$ with $\theta =$ (a) 0° , (b) 30° , (c) 45° and in (d) 60° , for which $r = 1$. Upper and lower horizontal bars show respectively the width of the Bloch oscillations in (a) and scale for all panels.

$r = 1$, the electron orbits are not bounded at all and are allowed to extend arbitrarily far through the superlattice.

To understand this drastic increase in the length of the trajectory, Poincaré sections when $F = 1.57 \times 10^6$ V m $^{-1}$ and $B = 15$ T (corresponding to the trajectories in figure 2.1) are presented in figure 2.2. The sections shown in this figure are constructed by plotting q_y and p_z at regular time intervals, t_{sec} , equal to the period of the harmonic oscillator, $t_{sec} = 1/\omega_{||}$. Figure 2.2(a) shows the stroboscopic Poincaré section when $\theta = 30^\circ$. The electron trajectory is clearly localised to the tori defined by the initial conditions, shown as regular rings in the figure. Increasing θ to 45° , see figure 2.2(b), we find electron trajectories with low momenta (in the centre of the

plot) are within a ‘sea of chaos’, the formation of which is typical of normal KAM chaos. This allows the electron trajectory to extend much further in momentum space than when $\theta = 0$, where the electron motion in the z direction is completely localised and characterised by a simple harmonic oscillator. However this *delocalised* motion is limited to electron trajectories that lie within the chaotic sea. Orbits that are outside this region are again localised to periodic tori. Figure 2.2(c) shows the Poincaré section when $\theta = 60^\circ$ corresponding to $r = 1$. The phase space is now patterned with a *stochastic web* where the filaments of the web structure (highlighted by the yellow boxes) are extensions of the chaotic sea in the centre of the section. Figure 2.2(d) is when $\theta = 60^\circ$ but with an electric field corresponding to $r = 3$. In this case, there are 6 filaments radiating from the centre of the web, (again highlighted by yellow boxes). These web filaments extend to infinity through the entirety of the phase space of the electron.

In [47] and [18] it was shown that the effect of these stochastic webs patterns is to enhance the extent of the electron orbits in real space. As the electron moves through the superlattice the kinetic energy of the electron, gained from the potential energy gradient caused by the electric field, \mathbf{F} , is transferred into the y - z plane by the tilted magnetic field. In fact, the distance of each point in the web to the centre of web is approximately proportional to \sqrt{x} . Consequently p_z and q_y increases and the electron moves along one of the filaments in the stochastic web, also enhancing x . The webs extend to infinity and thus the chaotic electron orbit is unbounded, both in momentum and real space, resulting in a drastic increase in the current. The web like structure and thus unbounded orbits only occur when r is an integer. Only slightly off resonance the web structure is immediately destroyed, localising the electron orbits and suppressing current. This mechanism may give the opportunity to use the superlattice as a sensitive switch which only allows electron transport when r is an integer [64].

2.1.2 Electron drift velocity

As discussed previously in this thesis, the drift velocity of the electrons is calculated to understand the effect of the electron trajectories on the transport of electrons through the superlattice. The drift velocity is calculated using equation (1.52) derived in section 1.3.4 and restated here for clarity:

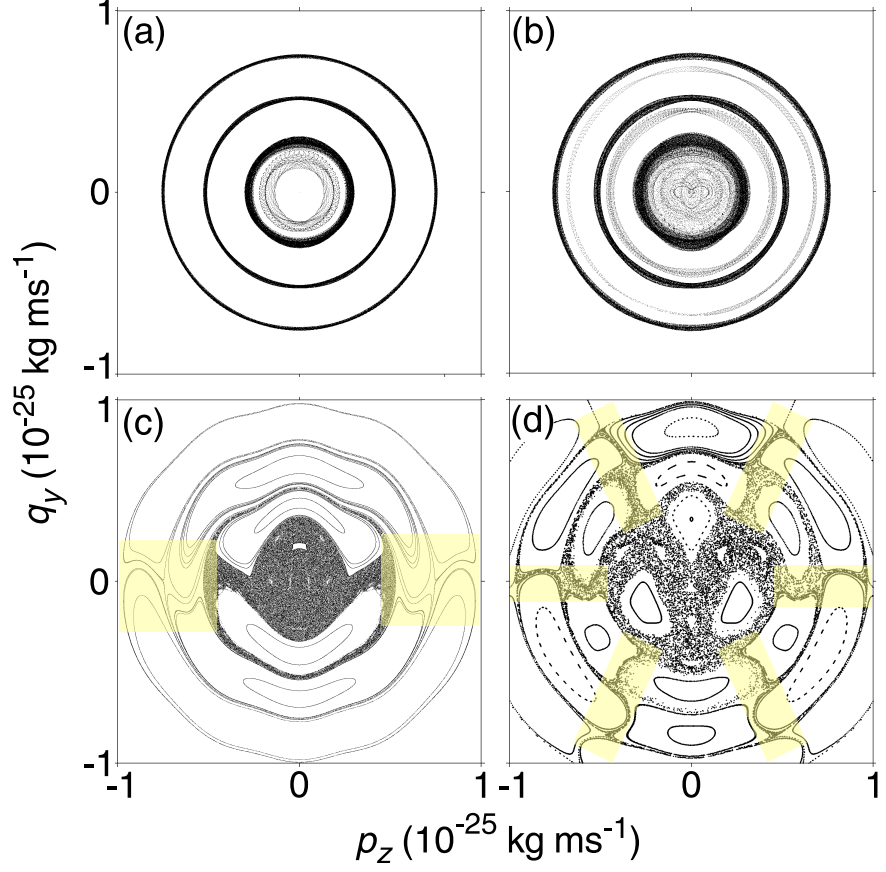


Figure 2.2: Poincaré sections showing the phase space structure of the electron when $B = 15\text{T}$. (a) $\theta = 30^\circ$ and $F = 1.57 \times 10^6 \text{ V m}^{-1}$, (b) $\theta = 45^\circ$ and $F = 1.57 \times 10^6 \text{ V m}^{-1}$, (c) $\theta = 60^\circ$ and $F = 1.57 \times 10^6 \text{ V m}^{-1}$ ($r = 1$) (d) $\theta = 60^\circ$, $F = 4.71 \times 10^6 \text{ V m}^{-1}$ ($r = 3$). Yellow, semi-opaque, overlays highlight the stochastic web filaments.

2.1 Superlattice electron dynamics in a tilted magnetic field

$$v_d = \frac{1}{\tau} \int_0^\infty v_x(t) e^{-t/\tau} dt, \quad (2.28)$$

where, in this section, we take the scattering time, τ , to be 250 fs determined from experiment [69], and $v_x(t)$ is determined from equation (2.14). The drift velocity was averaged over ~ 2500 initial conditions with a maximum energy of 10 meV. This energy consists of a thermal component $k_B T \sim 0.4$ meV and a kinetic energy component, imparted by the electric field $\approx \Delta_{SL}/2 \sim 10$ meV. The initial conditions were linearly spaced over a sphere of initial momenta in p_x , q_y , and p_z with a radius equal to the defined maximum energy of the system. This naïve method of defining the thermal distribution was explored in [8] and has shown good correspondence with experimental results [8; 18]. Figure 2.3 shows $v_d(F)$ curves calculated for $\theta = 0^\circ$ (bottom trace) to 90° (top trace) in 5° intervals.

When $\theta = 0^\circ$ (lower curve in figure 2.3) we see a curve (corresponding to the Esaki-Tsu curve shown in figure 1.8) with a single peak labelled ‘ET’ in yellow. This peak is caused by the interplay between scattering induced current, which begins to be suppressed when $\omega_B \tau > 1$ by induced Bloch oscillations (for more detail see section 1.3.4). When $\theta = 90^\circ$ (upper curve in figure 2.3), the cyclotron and Bloch oscillations are decoupled and the drift velocity curve has a similar shape to when $\theta = 0^\circ$, however now the ‘Esaki-Tsu’ peak is shifted to a higher field value. This shift occurs because the magnetic field shifts bends the electron trajectory away from the x axis, reducing the electron’s velocity in the x direction, thus requiring a higher electric field to reach the peak in drift velocity [8; 47].

Significantly though, by increasing θ from 0° to 55° additional peaks occur in the drift velocity plot corresponding to field values when $\omega_B = r\omega_{\parallel}$ where $r = 1$ (labelled in purple) and $r = 2$ (labelled in green). When this resonance condition is satisfied the stochastic web structure is ‘switched on’ (see figure 2.2(c) and (d)), and the electron is allowed to follow unbounded chaotic electron trajectories through the superlattice (see figure 2.1(d)) which results in the enhancement of the drift velocity for these field values. Note that for $\theta \gtrsim 30^\circ$, there is also a peak in drift velocity when $r = 0.5$ (labelled in blue). This is not caused by delocalisation of the electron orbits facilitated by a stochastic web (only expected when r is an integer). Instead, here we see the typical enhancement of chaotic motion when the driving and natural frequency of a driven oscillator are resonant [8].

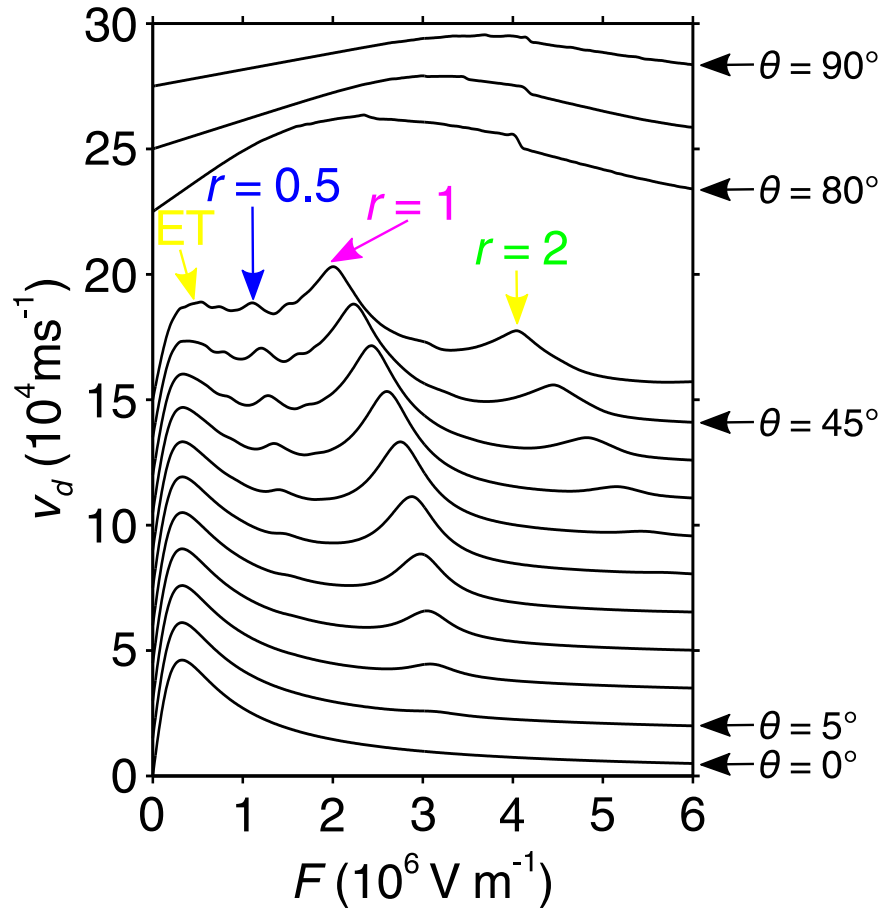


Figure 2.3: $v_d(F)$ curves for superlattice sample NU2293 with $B = 15\text{T}$ and $\theta = 0^\circ$ (bottom trace) to 90° (top trace) at 5° intervals. Arrows mark the Esaki-Tsu peak (yellow) (see section 1.3.4), and also the chaos assisted resonance peaks at $r = 0.5$ (blue), $r = 1$ (purple) and $r = 2$ (green).

This has a very interesting consequence that by changing both the field and angle of the magnetic field it is possible to tailor the shape of the drift velocity curve for a given superlattice. This has implications for controlling and increasing the frequency and power of the dynamic charge domain dynamics, explored in chapter 3 and in [70].

2.2 Experimental and theoretical $I(V)$ curves

In the previous section, we showed how stochastic webs affect the dynamics of a *single* electron within a biased superlattice with an applied magnetic field. To understand how this affects the current of electrons, which depends on *collective* electron effects, in this section we show the effect of a magnetic field on the experimental and theoretical current voltage, $I(V)$, curves. Here, the experimental $I(V)$ curves are compared to a theoretical *static* model for charge domain formation in superlattices (first presented in [18]). The results shown in this section are a review of paper [18], which represents the first experimental study of the effect of tilted magnetic fields on the current-voltage curves, and the first time that the signature of non-KAM chaos has been seen in an experimental system. The theoretical calculations involve solving the Poisson and current continuity equations (see section 1.3.5) using the $v_d(F)$ curves to determine the drift of electrons and assuming that the current density of the electrons is constant throughout the device [8; 18].

Figure 2.4 shows experimental and theoretical curves of $I(V)$ and $G(V) = dI(V)/dV$ calculated for superlattice sample NU2293, with $B = 11$ T and for a range of θ . It is apparent after comparing figures 2.4(a) and (b) that the theoretical results agree well with the experimental results. When $\theta = 0^\circ$ and 90° , the current increases linearly and then flattens when the voltage across the superlattice is large enough to reach the Esaki-Tsu peak in the $v_d(F)$ curve. In this static theoretical model there is no drop in current for large V , in contrast to the pronounced negative differential velocity seen in $v_d(F)$. This is because electrons accumulate towards the collector contact of the device causing F to increase and v_d to decrease. This increase in the electron number compensates for the drop in their v_d keeping I constant.

Increasing θ from 0° to $\approx 55^\circ$, causes both the theoretical and experimental current to increase for all θ until $V \approx 250$ mV. When $V \approx 250$ mV there is a region of enhanced current which results in a strong resonant peak in the $G(V)$ curves, highlighted by the grey shaded regions for both the theoretical (figure 2.4(c)) and

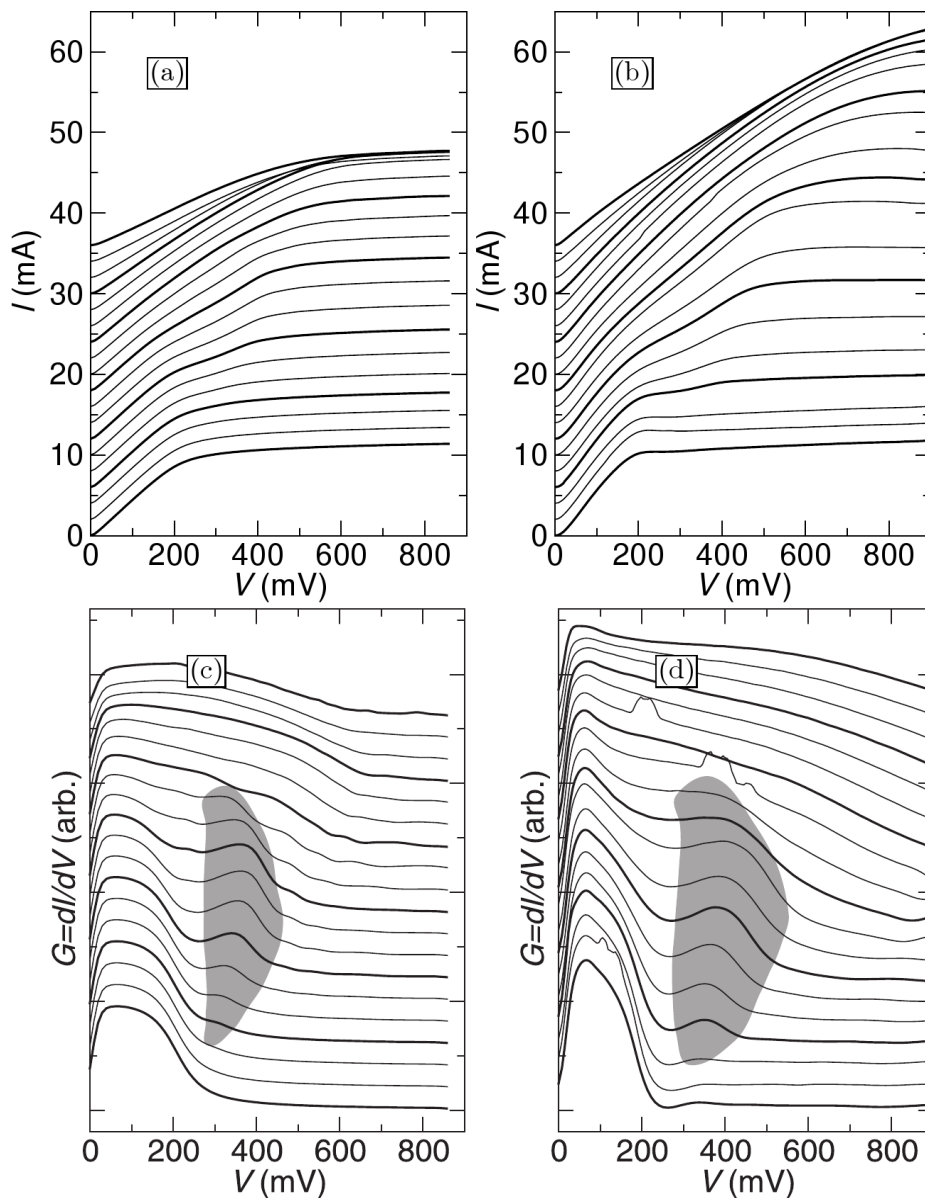


Figure 2.4: Figure reproduced from [8]. (a) and (b) are $I(V)$ curves, (c) and (d) are $G(V) = dI(V)/dV$ curves calculated theoretically, (a) and (c), and experimentally, (b) and (d) for superlattice sample NU2293 with $B = 11$ T and $\theta = 0^\circ$ (bottom trace) to 90° (top trace) at 5° intervals. Curves are vertically offset for clarity. In (c) and (d), the grey shaded regions, highlight the $r = 1$ resonance. Note that these curves are also shown in [18].

experimental (figure 2.4(d)) cases. The amplitude of this resonant peak decreases until $\theta = 0^\circ$, where it disappears completely. This resonant peak is explained purely by semiclassical miniband transport model, which determines the shape and magnitude of the $I(V)$ curves in the theoretical model. The resonant peak in both the experimental and theoretical results occurs close to the voltage for which $\omega_B = \omega_{\parallel}$ which, according analysis of the single electron dynamics, is where the phase space is threaded with a stochastic web.

It is apparent that although there is good agreement with the position and size of the resonant enhancement in the $G(V)$ curves, there is not a huge increase in the current at the resonance condition. If the field in the superlattice was constant throughout the sample then there would be very strong resonant peaks in the $I(V)$ curve ($\propto v_d(F)$) which would be of the same form as those seen in the drift velocity calculations. However, in fact, the field is not constant in the device and, due to the N shape of the drift velocity versus field curves, charge accumulates, compensating for the effects of the resonant v_d peaks, and so smoothing the $I(V)$ curve.

The theoretical model here is a *static* model, which assumes that the current is constant throughout the device. Therefore, the presence of this charge build up weakens the experimental manifestation of stochastic-web induced resonances because it reduces the effect of the current enhancement [8]. In the following chapter, a dynamical model of charge in the superlattice will be developed, building on the static model. It will be shown there that, far from being a hindrance, the build up of charge actually improves the performance of the superlattice as a frequency generator.

Chapter 3

Controlling charge domain dynamics in superlattices

In this chapter, it will be shown that a tilted magnetic field can be used to manipulate the structure and dynamics of charge domains in a biased semiconductor superlattice. The multiple regions of negative differential conductivity in the drift velocity curve, caused by strong, chaotically-induced, resonant enhancement of the electron trajectories (see chapter 2) generate extra charge domain filaments in the superlattice, which increase the frequency and amplitude of the self sustained current oscillations.

The collective dynamics of electrons in superlattices, and the resulting fields and charge densities, have been studied extensively and a number of interesting phenomena have been observed and studied. For a complete review of these models refer to [14] and [16]. However, not until the 2004 investigation by T.M. Fromhold *et. al.* have the effects of tilted magnetic fields on the collective behaviour of electrons in superlattices been considered. In [18] the authors used a model which calculated the *static* (unstable) solution for the field and charge profiles and found good correspondence with the experimental $I(V)$ curves confirming the non-KAM chaos induced electron dynamics (see section 2.2). In this chapter, we will consider a *dynamic* model of charge and field domains for superlattices in tilted magnetic fields, and predict that the magnetic field not only changes the shape of the $I(V)$ curve, but also significantly modifies the charge dynamics.

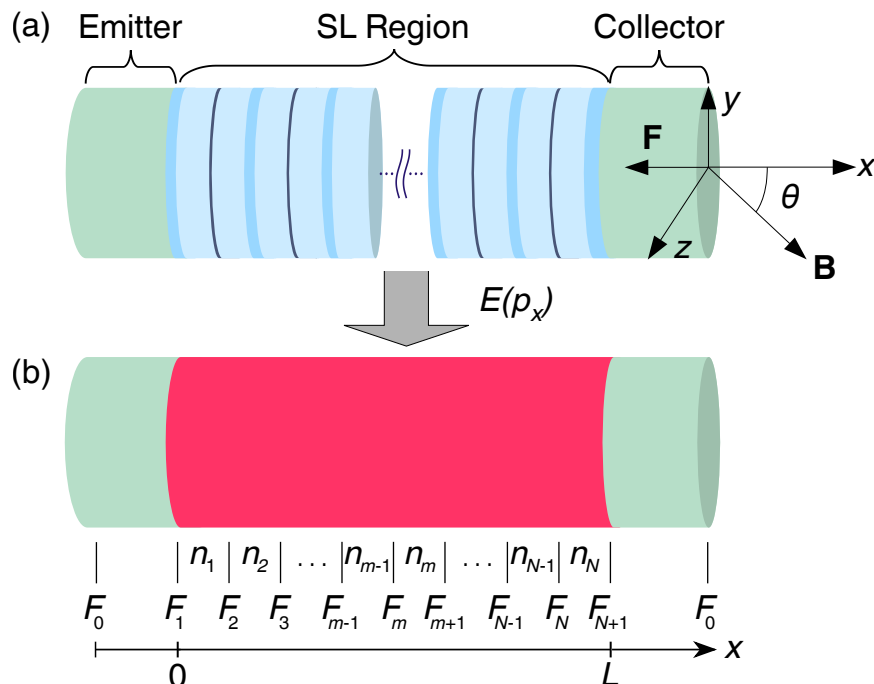


Figure 3.1: Schematic diagram showing how the superlattice structure (a) can be described by a continuum (b) where electron transport is defined by the miniband dispersion relation $E(p_x)$. The continuum is discretised into N layers where in the m^{th} layer the electron density is n_m . The fields at the left- and right-hand edges of the layer are F_m and F_{m+1} respectively, and F_0 is the field at the left- and right-hand edges of the device. The coordinate axes show the orientation of \mathbf{F} and \mathbf{B} .

3.1 Model of charge domain dynamics

To investigate the collective behavior of the electrons, the current-continuity and Poisson equations were solved self-consistently throughout the device by adapting a model, used previously to describe inter-well transitions in superlattices [14; 37; 71], for miniband transport. This allows us to investigate how the electron density, $n(x, t)$ and electric field, $F(x, t)$ in the superlattice vary spatially and temporally.

Figure 3.1(a) shows a schematic diagram of the superlattice device NU2293 which consists of the layered, central, superlattice region, of length L , with emitter and collector contacts, of length l , on the left and right hand edges respectively. The system was simulated by assuming that it can be modelled as a continuum (depicted in figure 3.1(b)) where electron transport is described by the miniband model introduced in chapter 2. In the calculations, the superlattice region of the device was discretised

into $N = 480$ layers with width $\Delta x = L/N = 0.24$ nm, which, after analysis of the results, was shown to be small enough to approximate a continuum¹. The volume electron density of electrons in the m^{th} layer is n_m and the field values at the left- and right-hand edge of the layer (see the vertical lines in figure 3.1(b)) are F_m and F_{m+1} respectively.

The dynamical equation that describes the evolution of the charge density in each layer is given by the following current continuity equation,

$$e\Delta x \frac{dn_m}{dt} = J_{m-1} - J_m \quad m = 1 \dots N, \quad (3.1)$$

where $e > 0$ is the electron charge and J_m is the current density ($\text{C s}^{-1} \text{ m}^{-2}$) of electrons moving from the m^{th} into the $m + 1^{\text{th}}$ layer. This equation is integrated numerically using a fourth order Runge-Kutta scheme [19]. Note that in this analysis, diffusion of electrons is neglected, as in previous models [18; 37], since for systems with bias applied its effect is small compared to electron drift. J_m depends on the local drift velocity of electrons in layer m , v_d^m , and is given by

$$J_m = en_m v_d^m, \quad m = 1 \dots N. \quad (3.2)$$

Thus J_m depends directly on the single electron orbits and therefore we can expect that the features of the single electron transport will have an effect on the collective electron dynamics². The Esaki-Tsu approach outlined in section 1.3.4 was used to calculate the drift velocity for a field corresponding to the average field in layer m , $\overline{F_m}$, so that,

$$v_d^m = v_d(\overline{F_m}, B, \theta). \quad (3.3)$$

where,

$$v_d(\overline{F_m}, B, \theta) = \sum \frac{\delta}{\tau} \int_0^\infty v_x(\overline{F_m}, B, \theta, t) e^{-t/\tau} dt. \quad (3.4)$$

In this equation, we use the effective scattering time from equation (1.43) such that

¹The model is considered to approximate a continuum when the field in the device varies on a spatial scale $\ll \Delta x$

²Note that the scattering time, τ , is less than the characteristic time scale of the domain dynamics allowing us to assign a local drift velocity.

3.1 Model of charge domain dynamics

$$\tau = \tau_i \sqrt{\frac{\tau_e}{\tau_i + \tau_e}} \quad (3.5)$$

where τ_i is the inelastic scattering time and τ_e is the elastic scattering time. Since we are using this expression for τ , the drift velocity is modified by the coefficient, $\delta = \tau/\tau_i$ [24].

In these simulations, we average the drift velocity over ~ 2500 initial energies determined by the average temperature of the electrons. For a lattice temperature of 4 K, we consider a range of initial electron energies up to 10 meV. This energy consists of a thermal component $k_B T \sim 0.4$ meV (where k_B is Boltzmann's constant) and also a contribution due to voltage heating i.e. kinetic energy imparted by the electric field, $\approx \Delta_{SL}/2 \sim 10$ meV. The initial conditions were linearly spaced over a 'sphere' of initial momenta in p_x , q_y , and p_z with a radius equal to the defined maximum energy of the system. This naïve method of defining the thermal distribution was explored in [8] and has shown good correspondence with experimental results [8; 18].

When the drift diffusion model is considered, in the case of a weakly coupled superlattice, the electron density and electric fields are discrete variables specified within, and at the edges of, each well. However, in a strongly coupled superlattice where electron dynamics is governed by miniband transport, the model of charge transport must approximate a continuum¹. In this model it is assumed, therefore, that the field an electron experiences at a particular point must be an average of the field values surrounding it. In particular, to create a smooth field profile the field was averaged over a distance of one superlattice period². Therefore we use the average field at point x , $\overline{F(x)}$, which is defined as

$$\overline{F(x)} = \frac{1}{d_{SL}} \int_{-d_{SL}/2}^{d_{SL}/2} F(x) dx. \quad (3.6)$$

After discretisation, this average field is given by

$$\overline{F}_m = \frac{1}{N_{FA}} \sum_{m-N_{FA}/2}^{m+N_{FA}/2} F_m, \quad (3.7)$$

where $N_{FA} = d_{SL}/\Delta x$ is the number of discretisation layers in one quantum well.

¹Equivalent to models describing charge in Gunn diodes [28].

²Which has physical sense if we consider the wavefunction of the electron to have its maximum across a single quantum well.

In each layer, F_m obeys the discretised version of Poisson's equation (see equation (1.58))

$$F_{m+1} = \frac{e\Delta x}{\epsilon_0\epsilon_r} (n_m - n_D) + F_m \quad m = 1 \dots N, \quad (3.8)$$

where $\epsilon_0 = 8.85 \times 10^{-12} \text{ F m}^{-1}$ and $\epsilon_r = 12.5$ are, respectively, the absolute and relative permittivities, and $n_D = 3 \times 10^{22} \text{ m}^{-3}$ is the n-type doping density in the superlattice layers.

To properly simulate the charge domain dynamics of a system, it is very important to consider the boundary conditions of the system, i.e. the physical properties of the contact regions. There have been many theoretical works that investigate the effect of the boundary conditions on the dynamics of the charge in the superlattice [15; 72]. The choice of the boundary conditions has been shown to induce stationary charge domains, and also moving charge domains which give rise to both periodic [73] and chaotic currents [72]. In this investigation, however, we wish to compare these numerical results with experimental data. Therefore the contact regions are modelled using a realistic picture of the contact doping profiles, in order to obtain good correspondence between theory and experiment.

Ohmic boundary conditions [14] are used to determine the current injected into the superlattice region from the emitter, which is

$$J_0 = \sigma F_1 \quad (3.9)$$

where σ ($\Omega^{-1} \text{ m}^{-1}$) is the electrical conductivity given by [8; 18],

$$\sigma = \frac{n_0 e^2 \tau_c}{m^*} \quad (3.10)$$

where n_0 and τ_c are, respectively, the doping density and scattering time in the contact regions. The voltage applied to the system is the global constraint. It is determined from the sum of the potential dropped across each discrete superlattice layer and across the contact regions. In fact, most of the field is dropped across the contact regions and any external resistance (e.g. measuring equipment) that is in series with the superlattice, so these regions must be considered rigorously. In the contact, just to the left of the superlattice layers, we assume that there is a charge accumulation layer. Applying Gauss's law to this layer we find that

$$F_1 - F_0 = \frac{en_L}{\epsilon_0\epsilon_r} \quad (3.11)$$

where n_L is the areal density of electrons in the accumulation layer, which modelled as a delta function sheet of negative charge at distance $l - s$ from the left hand edge of the device, and F_0 is the field at the left hand edge of the device. The electric field, F_{N+1} , at the right hand edge of the superlattice region is screened by a depletion layer of length q and electron density n_0 , which ensures that the fields at the left- and right-hand edge of the *device* are equal, which implies that

$$F_0 = F_{N+1} - \frac{en_0q}{\epsilon_0\epsilon_r}. \quad (3.12)$$

The potential drop across the collector contact is found by spatial integration of the electric field

$$V_C = \int_0^q F(x)dx = \int_0^q \left(F_{N+1} - \frac{en_0x}{\epsilon_0\epsilon_r} \right) dx.$$

Therefore the voltage dropped across the depletion region is

$$V_C = F_{N+1}q - \frac{en_0q^2}{2\epsilon_0\epsilon_r}. \quad (3.13)$$

The voltage drop across the entire device, V , can be found by assuming that the field in the remaining sections of the superlattice is constant across each layer so that

$$V = F_0(l - s) + F_0(l - q) + F_1s + V_C + \frac{\Delta x}{2} \sum_{m=1}^N (F_m + F_{m+1}) + \sigma F_0 A R_{ext} \quad (3.14)$$

where R_{ext} is the resistance that describes the physical contacts to the device and the remaining circuit of the experimental system, and A is the cross sectional area of the device. In this system of equations, V is the global constraint that determines the dynamics of each n_m and F_m .

We define the global current density, $J(t)$, in the layers of the superlattice region as

$$J(t) = \frac{1}{(N + 1)} \sum_{m=0}^N J_m. \quad (3.15)$$

The corresponding current is then

$$I(t) = J(t)A. \quad (3.16)$$

The relation between the current in the superlattice layers ($I(t)$) and that in the Ohmic contacts and remaining circuit ($\sigma F_0 A$) is discussed in appendix B. The system of equations (3.1)-(3.16) can now be solved self consistently (ensuring that the voltage dropped across the device is constant and equal to the applied voltage) to obtain $n(x, t)$, $F(x, t)$ and, therefore, $I(t)$.

It should be noted here that there are three assumptions made for this model:

- For a given voltage across the device the electric field is constant in the ends of the device and is equal to F_0 , which corresponds to the device remaining overall neutral.
- The width of the superlattice sections, Δx , is small enough that the changes in electric field and charge density in the sections are negligible.
- Rigorously, the proportion of ionised donors will depend exponentially on the local electric field [18]. However if this is applied for collective dynamics in a magnetic field, the model is numerically unstable. Therefore, here we assume that all donors are ionised.

3.2 Results NU2293

In this section, we consider the electron dynamics for the GaAs/AlAs/InAs superlattice (NU2293) described in section 1.3.2. We consider a semiclassical formulation for electrons in the first miniband of the superlattice, using the method described in section 2.1, to obtain the electron velocity along the x axis, v_x , in the equation for drift velocity (3.4). The drift velocity was calculated by averaging over 2500 electron trajectories corresponding to a lattice temperature of 4K (see previous section). The experimentally obtained (and verified [8; 18]) parameters for superlattice NU2293 are summarised in following table.

| Parameter | Symbol | Value |
|--------------------------------|--------------|-------------------------------------|
| Mean doping density of layers | n_D | $3 \times 10^{22} \text{ m}^{-3}$ |
| Effective scattering time | τ_{eff} | 250 fs |
| Drift velocity correction | δ | 1/8.5 |
| External resistance | R_{ext} | 17 Ω |
| Contact length | l | 500 \AA |
| Contact doping density | n_0 | $1.0 \times 10^{23} \text{ m}^{-3}$ |
| Contact scattering time | τ_c | 90 fs |
| Position of accumulation layer | s | 150 \AA |
| Diameter of superlattice mesa | D_{SL} | 25 μm |

These parameters are used in the system of equations derived in section 3.1 to calculate the charge domain dynamics for superlattice NU2293. In the simulations we solved equations (3.1)-(3.16) self consistently, solving the current continuity equation, equation (3.1), using the fourth order Runge - Kutta method [19]. Initially the density of electrons in the layers is equal to the doping density ($n_m(t = 0) = N_D$) and the fields in the layers are given a nominal value to avoid divisions by 0 ($F_m(t = 0) = 1 \times 10^3 \text{ V m}^{-1}$). In this analysis we only consider the case when $B = 15 \text{ T}$. The results are presented in the following sections.

3.2.1 Current-voltage characteristics for $\theta = 0^\circ, 25^\circ$ and 40°

In this section we consider the $I(V)$ curves for the superlattice. Generally, following the initial transient behaviour, the current-time characteristics reaches a constant value or performs self sustained oscillations between the maximum and minimum current, I_{min} and I_{max} respectively. The behaviour of the current oscillations depends strongly on V , B , and θ . Figure 3.2 shows the current-voltage characteristics for values of $\theta = 0^\circ, 25^\circ$ and 40° when $B = 15 \text{ T}$, offset for clarity. The plot shows that for all values of theta the current is single valued at low V and then at some critical voltage, V_{crit} , the current becomes double valued (the upper line showing I_{max} and the lower line I_{min}), denoted by the shaded region in the plot. At low voltages the current-voltage curve is approximately linear and has a stationary solution, showing similar characteristics to bulk semiconductor material. This ohmic part of the $I(V)$ curve corresponds to the approximately linear region in the drift velocity characteristic. At the critical value, V_{crit} (the value of which depends on field and θ), the stationary state loses its stability via Hopf bifurcation and starts to oscillate between I_{max} and I_{min} , corresponding to the nonlinear region of the drift velocity characteristic.

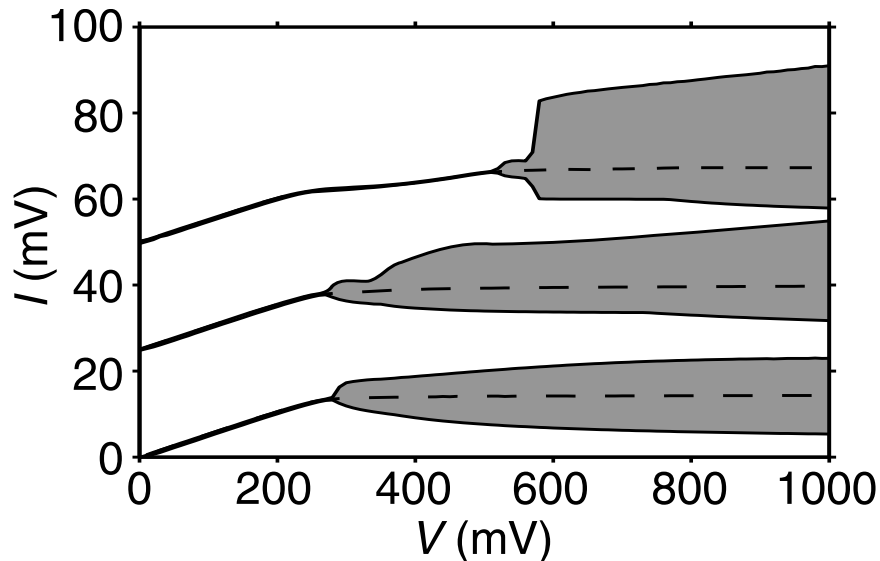


Figure 3.2: $I(V)$ characteristics calculated for (from bottom to top) $\theta = 0^\circ$, 25° , and 40° . For clarity, curves are vertically offset by 15 mA. Current oscillations occur within the shaded regions, whose upper [lower] bounds are $I_{\max}(V)$ [$I_{\min}(V)$]. Dashed curves show I values corresponding to the unstable steady state solution of equation (3.1).

With further increase of V , the size of the oscillations $I_a = I_{\max} - I_{\min}$ and, consequently, their power grows for all θ (in the range of voltages presented here). However, as clearly shown in figure 3.2, the presence of a tilted magnetic field ($\theta \neq 0$) can also increase the amplitude of the current oscillations, e.g. their maximum size in the voltage range 0 - 1V for $\theta = 0^\circ$ is ≈ 18 mA compared to ≈ 24 mA for $\theta = 25^\circ$, and ≈ 33 mA for $\theta = 40^\circ$.

The dashed curves in figure 3.2 show the static solution to the dynamical equations obtained by setting equation (3.1) to 0. Such static solutions have been shown previously to closely correspond to experimental DC $I(V)$ measurements (see section 2.2 and [18]). For low voltages (in the stationary regime), the full time-dependent solution of the equations of motion correspond exactly to the static solutions. When $\theta = 40^\circ$, features corresponding to the $r = 1$ resonance are visible between 200 mV and 400 mV. In the current oscillation regime, the static current effectively bisects the extremal values, I_{\min} and I_{\max} , of the dynamical solution showing that even when we enter the oscillating regime, the two solutions are still broadly consistent with each other also suggesting good correspondence with experimental results.

3.2.2 $I(t)$ curves for $\theta = 0^\circ, 25^\circ$ and 40°

In this section the $I(t)$ curves and how they vary with the applied voltage, V and magnetic field, B and θ are considered in detail. We consider θ values of 0° , 25° and 40° because the drift velocity curves have a simple form with, respectively, only 1, 2 and 3 resonant features, see figure 2.3. The traces shown in the left hand column of figure 3.3 are the $I(t)$ characteristics for $\theta = 0^\circ$ when $V = 290$ mV and 490 mV. Figure 3.3(a) is for $V = 290$ mV; a value close to the critical voltage $\approx V_c$. The $I(t)$ curve exhibits very periodic oscillations whose frequency ~ 37 GHz corresponds to the single dominant peak in the Fourier power spectrum shown in figure 3.3(b). The sparsity of the power spectrum confirms the periodicity of the current oscillations at the Hopf bifurcation. Increasing V to 490 mV has little qualitative effect on the shape of the current oscillations (see figure 3.3(c)). However, the fundamental frequency of the oscillations falls to ~ 12 GHz. In addition, the peaks in $I(t)$ sharpen and also increase in amplitude. These effects combine to strengthen the higher frequency harmonics in the Fourier power spectrum (see figure 3.3(d))

The plots in figure 3.4 shows the $I(t)$ curves and comparative Fourier power spectra when $\theta = 25^\circ$ for different V values. The $I(t)$ curve and frequency spectrum calculated for $\theta = 25^\circ$ and $V = 290$ mV $\approx V_c$ (see figure 3.4(a) and (b)) are very similar to those for $\theta = 0^\circ$ (see figure 3.3(a) and (b)). However we find in figure 3.4(c) that when V increases to 490 mV, the current-time characteristics for $\theta = 25^\circ$ differ markedly from those for $\theta = 0^\circ$, see figure 3.4(c). Comparison of the figures reveals that, in particular, tilting \mathbf{B} almost doubles the fundamental frequency (compare figures 3.3(d) and 3.4(d)) and also introduces new features in $I(t)$ (arrowed in figure 3.4(c)) which are absent when $\theta = 0^\circ$. These features originate from the $r = 1$ resonance in the drift velocity curve, as explained in the next section. Compared with the case when $\theta = 0^\circ$, the arrowed features in the $I(t)$ curve strongly enhance the high frequency components in the Fourier power spectrum: see figure 3.4(d), which reveals a dominant 3^{rd} harmonic at 54 GHz and also strengthened harmonics for frequencies > 0.2 THz. Increasing V further to 690 mV (figure 3.4(e)) induces stronger resonant features in the $I(t)$ curve and also strengthens the high frequency components of the spectra (figure 3.4(f)).

Increasing θ to 40° , we find that when $V = 540$ mV $\approx V_c$ the shape of the $I(t)$ curve (figure 3.5(a)) and the Fourier power spectrum (figure 3.5(b)), which is dominated by the fundamental peak, do not significantly alter from the case when $\theta = 0^\circ$ and

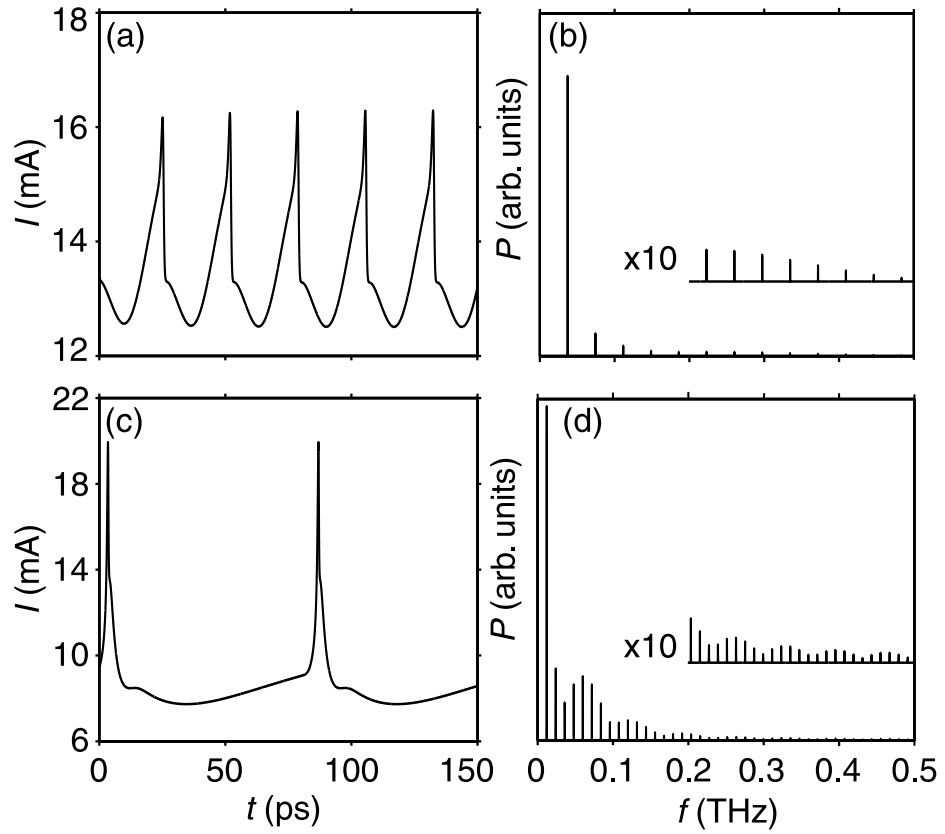


Figure 3.3: $I(t)$ oscillations calculated when $\theta = 0^\circ$ for (a) $V = 290$ mV and (c) $V = 490$ mV. The corresponding Fourier power spectra of $I(t)$ are given in (b) and (d) for $V = 290$ mV and $V = 490$ mV respectively, with a common vertical scale in arb. units. Inset within the Fourier power spectra are $\times 10$ magnifications of the spectra for $f > 0.2$ THz.

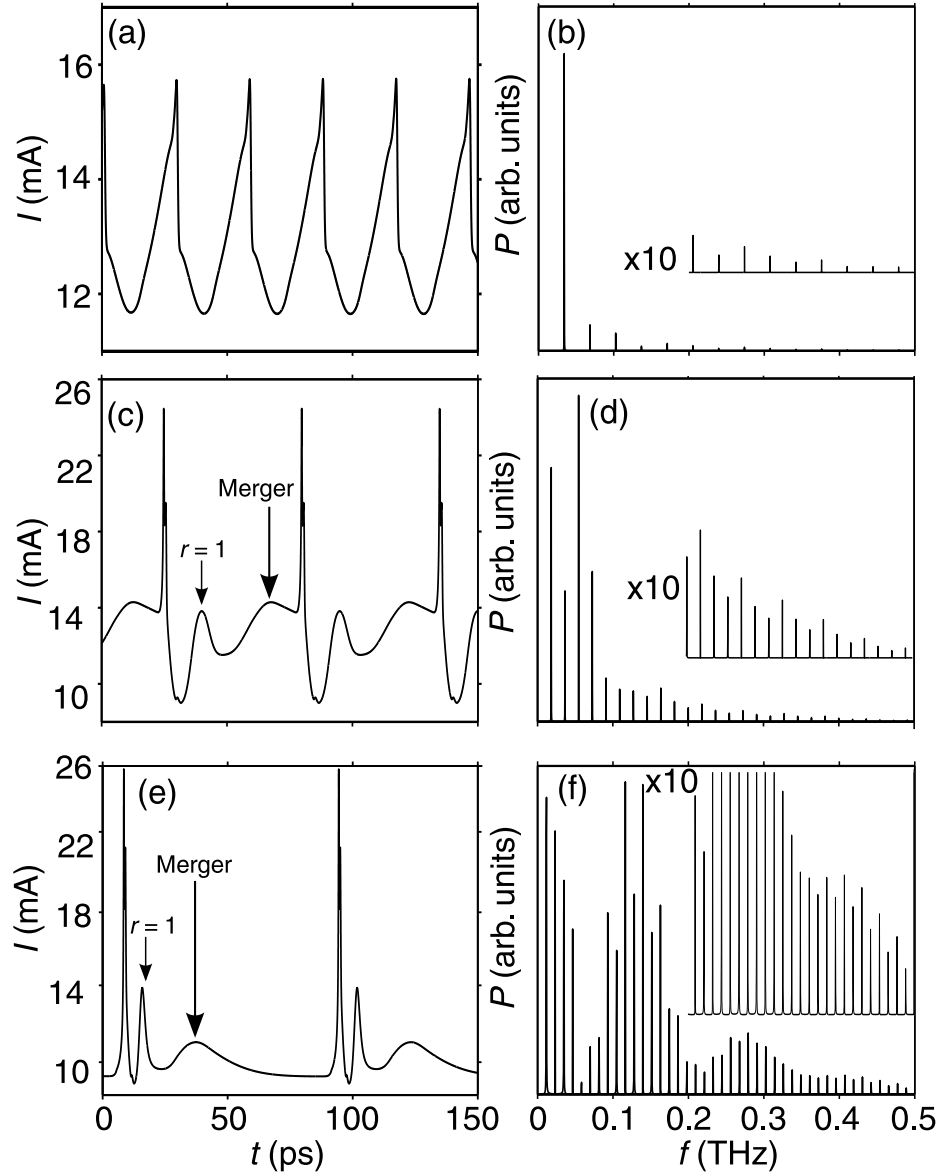


Figure 3.4: $I(t)$ oscillations calculated when $\theta = 25^\circ$ for (a) $V = 290$ mV, (c) $V = 490$ mV and (e) $V = 690$ mV. The corresponding Fourier power spectra of $I(t)$ are given in (b), (d) and (f) for $V = 290$ mV, 490 mV and 690 mV respectively, with a common vertical scale in arb. units. Inset within the Fourier power spectra are $x10$ magnifications of the spectra for $f > 0.2$ THz.

25°. However, the frequency of the fundamental peak does increase substantially to 56 GHz compared to 37 GHz and 34 GHz when $V \approx V_c$ for $\theta = 0^\circ$ and $\theta = 25^\circ$ respectively. In contrast, increasing the voltage to $V = 610$ mV when $\theta = 40^\circ$ (see figure 3.5(c)) induces complex $I(t)$ fluctuations that are both stronger and richer than for comparable voltages at $\theta = 0^\circ$ (see, for example, figure 3.3(c)) and $\theta = 25^\circ$ (see, for example, figure 3.4(c)). Consequently, the high frequency peaks in the Fourier power spectrum (figure 3.5(d)) are further enhanced, with the 5th harmonic at 92 GHz being the strongest. Increasing V to 740 mV (figure 3.5(e)) we find a similar $I(t)$ plot to when $V = 610$ mV. However, in the fourier power spectrum (figure 3.5(f)) the fundamental frequency is decreased compared to when $V = 610$ mV, consistent with other θ considered in this section. Note that there is also no significant enhancement of the high frequency components seen after increasing V from 490 mV to 690 mV when $\theta = 25^\circ$ (compare figure 3.4(d) and (f)). This suggests that the mechanism of frequency enhancement is complex. The general dependence of θ and V on frequency will be considered in section 3.2.5.

3.2.3 Charge dynamics for $\theta = 0^\circ, 25^\circ$ and 40°

To understand how $I(t)$ varies with V and θ , in this section we consider how these parameters affect the underlying spatio-temporal electron charge dynamics. The charge dynamics of the system depend strongly on the drift velocity characteristics of electrons in the system. So, for clarity, the drift velocity - field characteristics for $\theta = 0^\circ, 25^\circ$ and 40° (the angles considered in this and the previous section) are shown in figure 3.6. When $\theta = 0^\circ$ we clearly see only one maximum in the drift velocity curve (yellow arrow labelled ET) corresponding to the Esaki-Tsu peak (see section 1.3.4). However, when $\theta = 25^\circ$, in addition to the Esaki-Tsu peak there is an $r = 1.0$ resonance. Increasing θ to 40° we find that there are now 4 resonant peaks corresponding to the Esaki-Tsu and $r=0.5, 1$ and 2 resonances. It was shown in chapter 2 that the origin of these peaks are extended chaotic electron trajectories facilitated by stochastic webs formed in electron phase space. In this section, it will be shown that via the resonances that they produce in the drift velocity curves, the single electron chaotic trajectories can drastically alter the electron charge dynamics.

The grey-scale plot in figure 3.7(a) shows n_m calculated versus t and x for $\theta = 0^\circ$ and $V = 290\text{mV} \approx V_{crit}$. The plot in figure 3.7(b) shows the corresponding three dimensional visualisation of the natural log of the charge density. These figures show

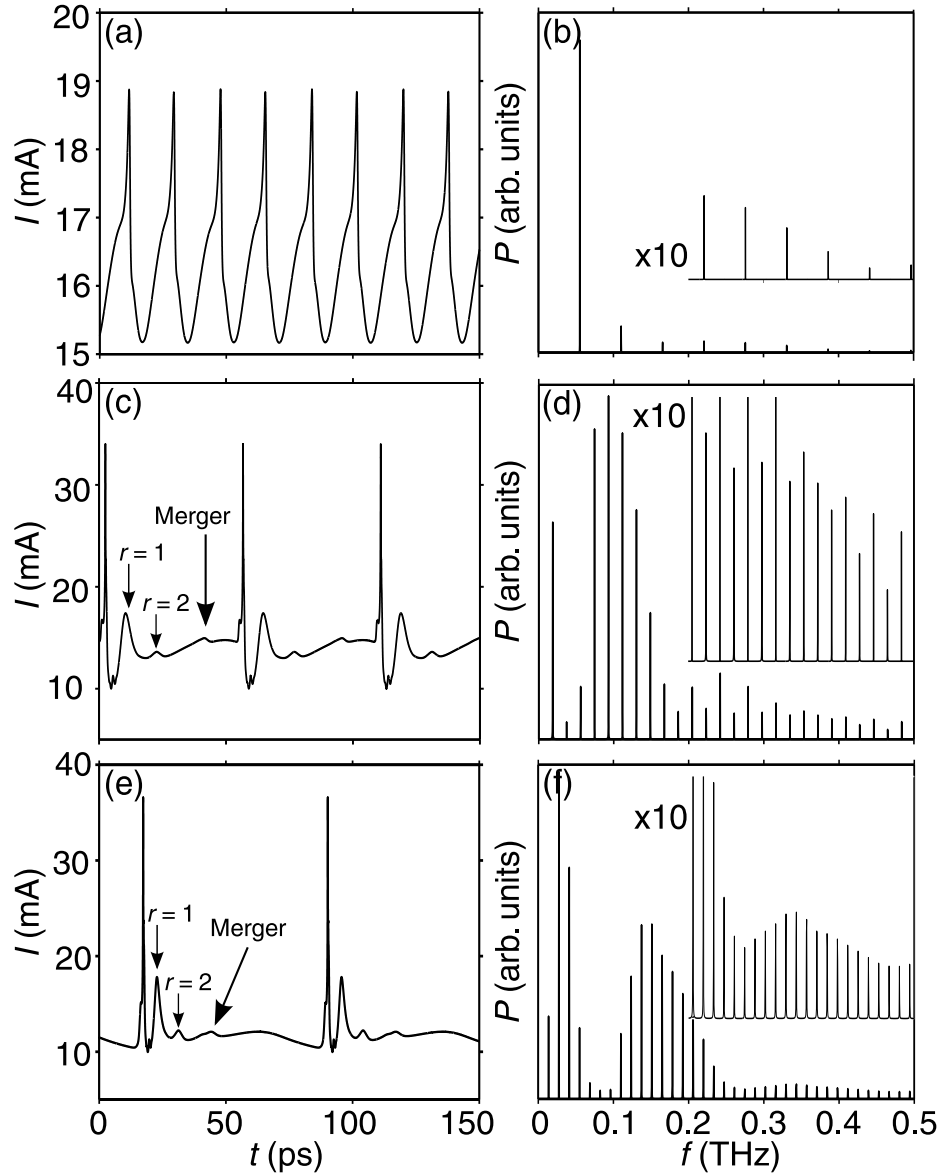


Figure 3.5: $I(t)$ oscillations calculated when $\theta = 40^\circ$ for (a) $V = 540$ mV, (c) $V = 610$ mV and (e) $V = 740$ mV. The corresponding Fourier power spectra of $I(t)$ are given in (b), (d) and (f) for $V = 540$ mV, 610 mV and 740 mV respectively, with a common vertical scale in arb. units. Inset within the Fourier power spectra are $\times 10$ magnifications of the spectra for $f > 0.2$ THz.

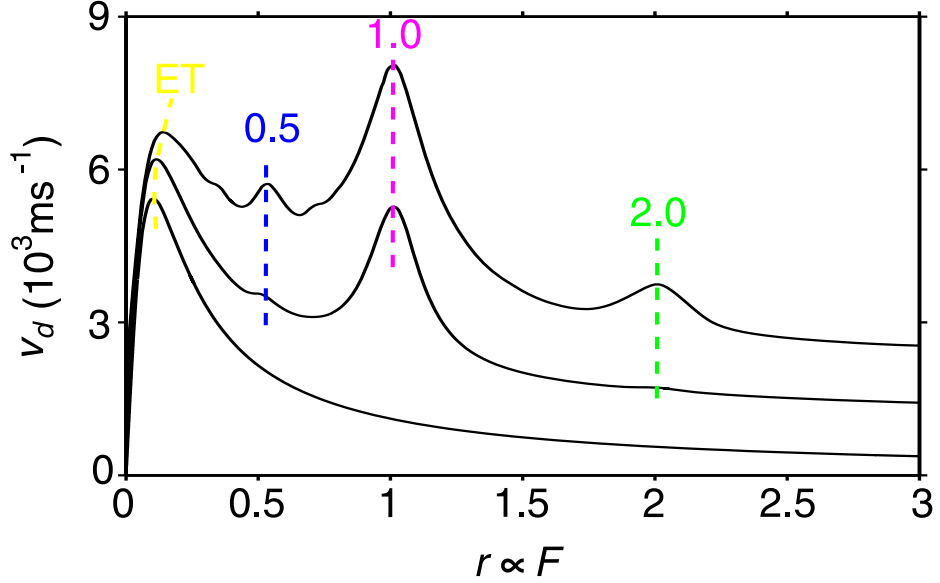


Figure 3.6: (b) v_d versus $r \propto F$ curves calculated for $B = 15$ T with (from bottom to top) $\theta = 0, 25^\circ$ and 40° . For clarity, curves are offset vertically by 10^3 ms^{-1} . The dashed coloured lines show the positions of the Esaki-Tsu (ET) peak (yellow), the $r=0.5$ peak (blue), the $r=1$ peak (purple) and the $r=2$ peak (green).

that for any given x , the local charge density oscillates periodically as a function of t . This is due to the negative differential velocity in the corresponding $v_d(F)$ curve (see lower plot in figure 3.6) as we now explain.

To demonstrate the influence of the negative differential velocity region, the dashed yellow curve in figure 3.7(a) shows the (t, x) locus along which F is fixed at the value corresponding to the ET peak in the lower curve of figure 3.6. As x passes beyond this locus, the electrons, due to the negative differential velocity, slow thereby increasing the local values of both n_m and F_m (see section 1.3.5). This further decreases v_d and, so, increases n_m , making the electrons accumulate in a charge domain (shown light gray in figure 3.7(a) and as a large peak in the $n(x, t)$ surface in figure 3.7(b)). Note that the condition for forming the charge domain requires electrons to be in the negative differential velocity regime throughout a sufficiently extended region of the superlattice and also a large enough injection current to ‘seed’ a charge domain [14; 15; 37; 74] (see section 1.3.5).

As the domain propagates through the superlattice it strengthens as the difference in drift velocity between the low and high field regions increases (see section 1.3.5). Also, due to the resulting local increase of field in the high field region and the

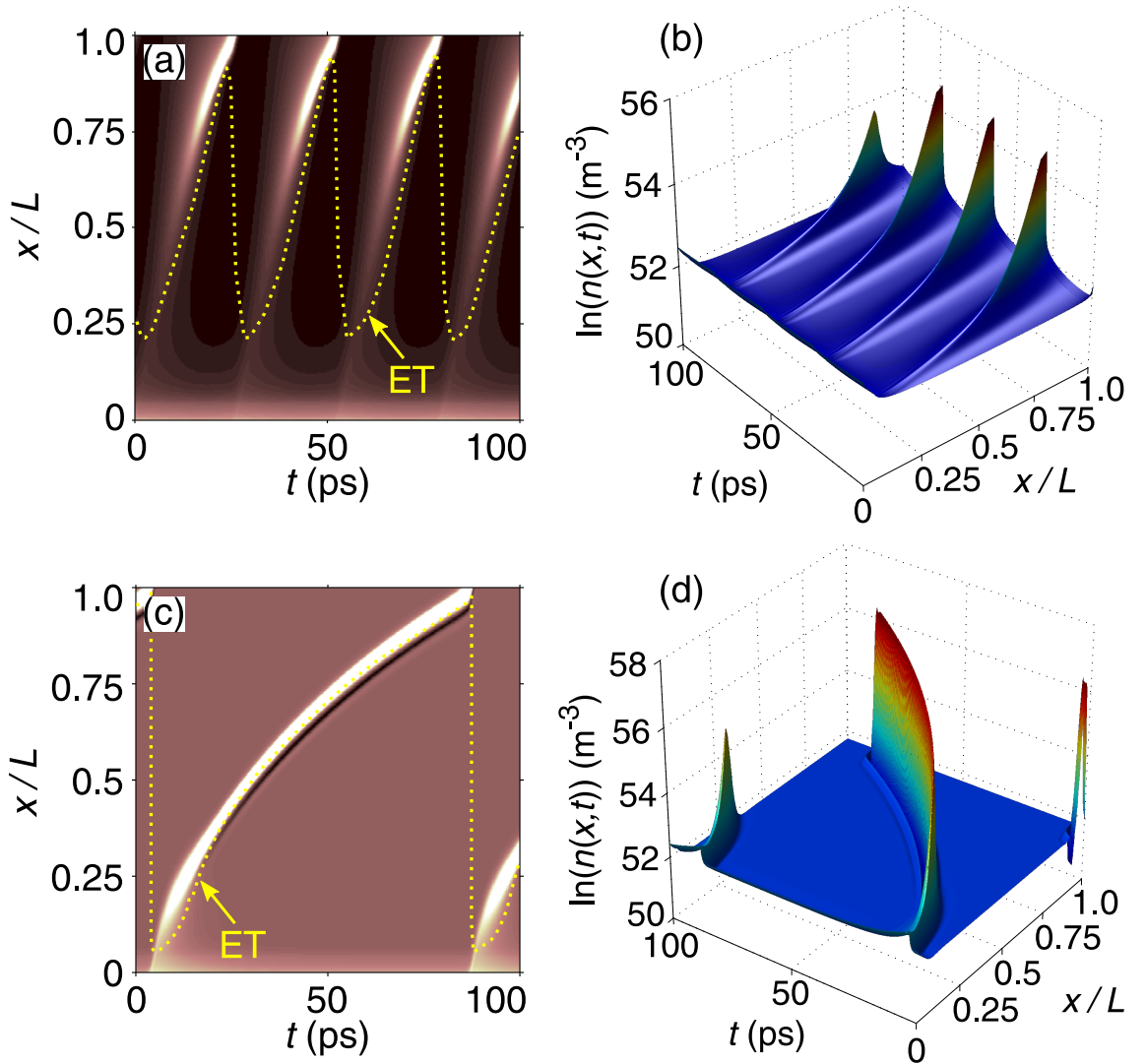


Figure 3.7: Grey scale (left-hand column) and surface plots (right-hand column) of $n_m(t, x)$ calculated for $\theta = 0^\circ$. (a-b) are for $V = 290$ mV and (c-d) are for $V = 490$ mV. In figures (a) and (c) charge densities $> 10^{23} \text{ m}^{-3}$ appear white. Yellow curves are loci of constant F values corresponding to the Esaki-Tsu (ET) drift velocity peak (see figure 3.6).

corresponding reduction in drift velocity, the domain slows (both effects are clearly shown in figure 3.7(a) and (b)).

When the domain approaches the collector ($x = L$), the high field region immediately beyond the domain narrows. Consequently, to keep V constant, the electric field in that region increases, which requires the charge within the domain to also increase. When this domain reaches the collector contact, it therefore produces a sharp peak in $I(t)$ (figure 3.3). Immediately, a new charge domain forms near the emitter, due to an increase in field at the left hand edge of the superlattice and the propagation process repeats, so producing self sustained $I(t)$ oscillations [14; 30; 33].

For larger V , (see figures 3.7(c) and (d) when $V = 490$ mV) similar domain dynamics occur. But now there is a higher mean field in the layers of the superlattice. Consequently, the Esaki-Tsu locus (dashed yellow line in figure 3.7(c)) is closer to the emitter compared to when $V = 290$ mV. As a result the charge domain forms closer to the emitter and, as t increases, traverses the entire superlattice. Increasing V also increases the difference between the field values in the high and low field regions. This requires more charge to accumulate in the domain, which raises the amplitude of the $I(t)$ oscillations and, since v_d falls at higher fields, decreases the frequency of the oscillations (see $I(t)$ curve in figure 3.3(c)).

When $V = 290$ mV $\approx V_c$, increasing θ from 0° (figure 3.7(a)) to 25° (figure 3.8(a)) produces little qualitative change in the charge domain dynamics. This is because V is low enough to ensure that $r < 1$ throughout the superlattice: a regime where the $v_d(r)$ curves for $\theta = 25^\circ$ and $\theta = 0^\circ$ have similar shapes (compare the bottom two curves in 3.6) .

This picture changes qualitatively when V and, consequently, some F_m values become high enough to ensure that, locally, $r \geq 1$. Figures 3.8(c) and (d) illustrates this for $V = 490$ mV and $\theta = 25^\circ$. The yellow and purple curves in (c) show the (t, x) loci along which F equals the values corresponding, respectively, to the leftmost Esaki-Tsu and $r = 1$ v_d peaks in figure 3.6. When $t \approx 25$ ps, negative differential velocity associated with the Esaki-Tsu peak creates a high density charge domain for x just beyond the yellow locus, as in low voltage case. However, when t increases to ≈ 50 ps, a second charge accumulation region appears above the purple locus. This domain originates from the negative differential velocity region just beyond the $r = 1$ drift velocity peak. Its appearance produces an additional peak, labeled ' $r = 1$ ', in the $I(t)$ trace in figure 3.4(c). The two charge domains merge when $t \approx 65$ ps,

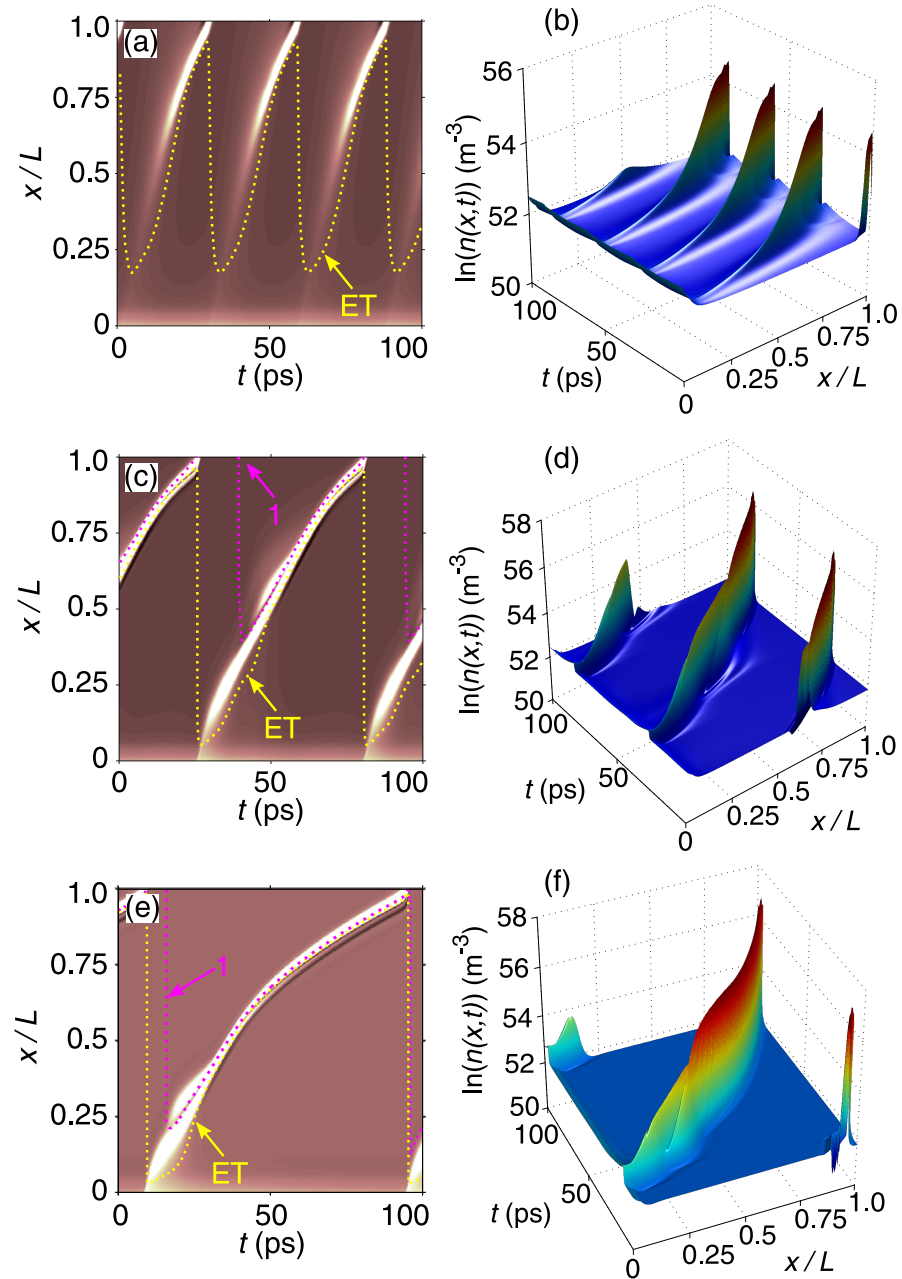


Figure 3.8: Grey scale (left-hand column) and surface plots (right-hand column) of $n_m(t, x)$ calculated for $\theta = 25^\circ$. In figures (a-b) $V = 290$ mV, (c-d) $V = 490$ mV and (e-f) $V = 690$ mV. Charge densities $> 10^{23}$ m^{-3} appear white in figures (a,b and c). Yellow and purple curves are loci of constant F values corresponding, respectively, to the Esaki-Tsu (ET) and $r = 1$ drift velocity peaks (see figure 3.6).

thereby inducing an additional peak in $I(t)$, labeled ‘Merger’ in figure 3.4(c). After merger, the charge within the single domain is almost twice that for $\theta = 0^\circ$. In addition, the presence of the large $r = 1$ v_d peak increases the mean electron drift velocity compared with $\theta = 0^\circ$, thus also raising the domain propagation speed. These two factors increase both the frequency and amplitude of the $I(t)$ oscillations (compare figure 3.3(c) to figure 3.4(c)). The appearance of the extra ‘Merger’ peak in $I(t)$ further strengthens the high-frequency harmonics in the Fourier power spectrum (compare figure 3.3(d) and 3.4(d)).

Increasing V to 690 mV produces in higher fields in the superlattice, which reduces the spatial distance between the (t, x) loci corresponding to the Esaki-Tsu and $r = 1$ drift velocity peaks (see figure 3.8(e)). Therefore the charge domain associated with $r = 1$ peak is generated closer to the emitter (when $x/L \approx 0.25$) and thus closer, both spatially and temporally, to the generation of the ‘Esaki-Tsu’ domain. Additionally the charge domain grows much quicker than for lower voltages (compare figures 3.8(d) and 3.8(f)). The combination of these factors causes the $r = 1$ and merger peaks in the $I(t)$ trace for $V = 690$ mV (see arrowed peaks in figure 3.4(e)) to occur at lower t and also be much sharper than when $V = 490$ mV (see arrowed peaks in figure 3.4(c)). In turn, this makes the high frequency components in the Fourier power spectra stronger for $V = 690$ mV than for 490 mV (compare figures 3.4(d) and 3.4(f)).

Note that higher voltages do not necessarily achieve higher frequency Fourier components. In fact, as the system approaches $V \approx 1$ V the effect of the $r = 1$ v_d peak on the charge density profile, and thus the $I(t)$ curve, is negated because the $r = 1$ domain occurs closer to the Esaki-Tsu domain.

Increasing θ to 40° further enriches the charge domain patterns, see figure 3.9. Now the $r = 0.5, 1$ and 2 resonances are stronger (see upper curve in figure 3.6) and occur for smaller F , meaning that their effect on the domain dynamics is apparent even for V very close to V_c . Figure 3.9(a) is the charge density plot when $V = 540$ mV $\approx V_c$ for $\theta = 40^\circ$. it reveals charge domains near the yellow, blue and purple loci along which F coincides, respectively, with the Esaki-Tsu, $r = 0.5$ and $r = 1$ v_d peaks. It is interesting to note that the $r = 0.5$ locus effectively splits the domain induced by the Esaki-Tsu negative differential velocity (see blue curve in figure 3.9(a)), which clearly demonstrates the effect of the multiple drift velocity peaks on the charge domain dynamics. The shape of these domains are clearly shown in the three dimensional plot in figure 3.9(b).

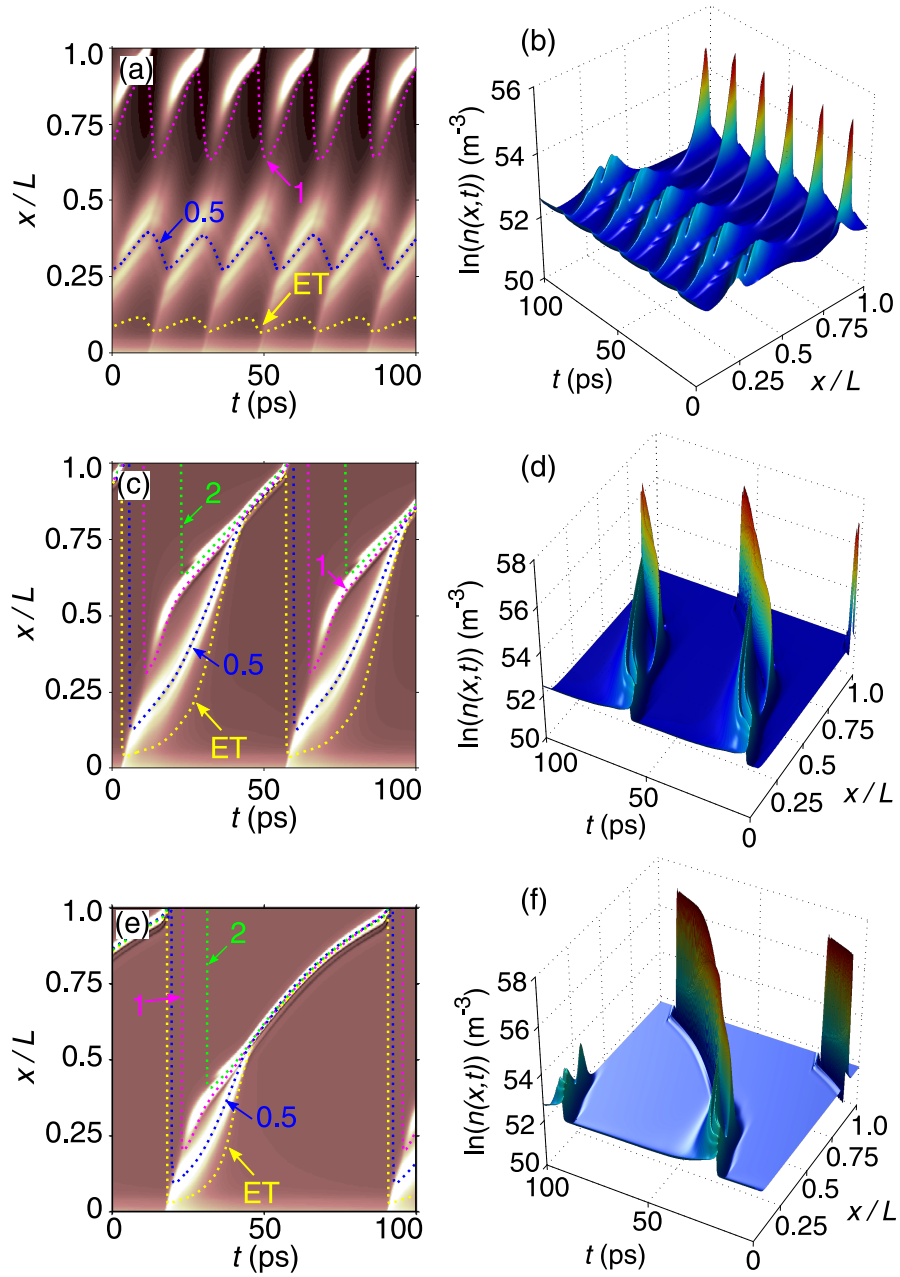


Figure 3.9: Grey scale (left-hand column) and surface plots (right-hand column) of $n_m(t, x)$ calculated for $\theta = 40^\circ$. In figures (a-b) $V = 540$ mV, (c-d) $V = 610$ mV and (e-f) $V = 740$ mV. Charge densities $> 10^{23} \text{ m}^{-3}$ appear white in figures (a,b and c). Yellow, blue, purple and green curves are loci of constant F values corresponding, respectively, to the Esaki-Tsu (ET) and $r = 0.5$, $r = 1$ and $r = 2$ drift velocity peaks (see figure 3.6).

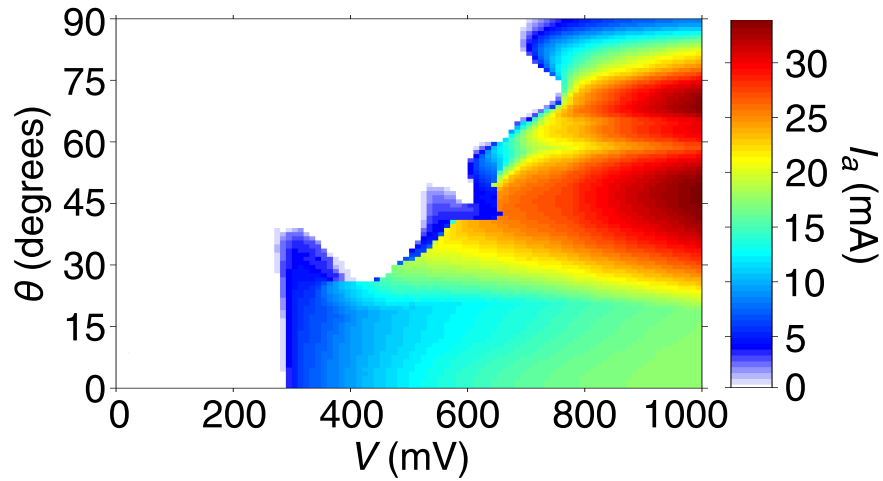


Figure 3.10: Colour map of $I_a = I_{max} - I_{min}$ (scale right) calculated for $B = 15$ T.

In the left hand region of the superlattice, between the left-hand quantum well and the domain, the local field lies in the region of negative differential velocity where $r < 1$ in the v_d curve. As x increases, the local field increases and enters the region of positive differential velocity. This stops the domain progressing further through the superlattice. For $x > 2L/3$, the local fields lie within the $r > 1$ region of negative differential velocity and a second domain is formed. The coexistence, and in phase oscillation, of these multiple domains doubles both the amplitude and frequency of the $I(t)$ oscillations (see figure 3.5(a)) in the $V \approx V_c$ regime compared to when $\theta = 0^\circ$ (see figure 3.3(a)) and $\theta = 25^\circ$ (see figure 3.4(a)).

When V reaches 610 mV, see figures 3.9(c) and (d), a new domain associated with the $r = 2$ resonance (green locus) appears. When $t = 40$ ps the domains with $r = 0.5, 1$ and 2 resonant peaks all merge. At this voltage the various domains produce multiple peaks in $I(t)$, as shown in figure 3.5(c) where the labels mark peaks arising from the formation of the ET, $r = 0.5, 1$ and 2 domains and their eventual merger, resulting in strong high-frequency components in the power spectrum, figure 3.5(d)

By increasing the voltage to 740 mV, figures 3.9(e) and (f), it is clear that this causes the domains to bunch. This ‘blurs’ the shape of the $I(t)$ curve, figure 3.5(e), so reducing the high frequency components in the power spectrum, figure 3.5(f).

3.2.4 Stability and power of $I(t)$ oscillations for $0^\circ < \theta < 90^\circ$

In this section, we consider how the stability, strength, and frequency of the current oscillations change over a wide range of θ and V .

Figure 3.10 is a colour map showing the variation of $I_a = I_{max} - I_{min}$ for a range of V up to 1 V and for $0^\circ < \theta < 90^\circ$. The plot effectively maps the boundary between low V regimes (left-hand white area), where the current does not oscillate, and high V regimes where oscillations do occur. The colour scale gives a measure of the power of the current oscillations at high V . It is clear that for all θ there are no current oscillations ($I_a = 0$) for $V \lesssim 280$ mV, corresponding with the position of the Esaki-Tsu peak when $\theta = 0^\circ$ (see figure 3.6). Generally, as θ increases, the critical voltage above which the system has current oscillations ($I_a > 0$), V_c , increases. At first glance this may seem surprising since, as we increase θ , the resonances in the $v_d(F)$ shift to lower F suggesting we might expect V_c decrease with increasing θ . However, altering θ also changes the strength of the resonant features, which makes V_c depend in a complicated way on the shape of the $v_d(F)$ curve.

To understand the cause of the complex variation of V_c with θ , it is useful to recap how the drift velocity varies with F and θ . Figure 3.11 is a colour map showing the variation of $v_d(F, \theta)$. The resonant features due to the Esaki-Tsu peak when $\omega_B\tau = 1$ (yellow dotted line), and the features due to the Bloch and cyclotron resonances $r = 0.5$ (blue dotted line), 1 (purple), and 2 (green) peaks are clearly visible. The resonant features become more pronounced as θ is increased to 45° , because the coupling between the cyclotron and Bloch oscillations strengthens (increasing the amplitude of the driving term in equation 2.27). Increasing θ beyond 45° weakens the resonant peaks as the cyclotron and Bloch oscillations decouple. In addition, the resonances all occur at lower field values resulting in ‘bunching’ of the drift velocity peaks, clear for $60^\circ < \theta < 80^\circ$. When $\theta > 80^\circ$ the Esaki-Tsu peak again dominates as the resonance effects diminish. Now though, we find that the Esaki-Tsu peak occurs at a higher F values as θ approaches 90° . This shift occurs because the magnetic field deflects the electron away from the x -axis toward the z -axis, thus reducing the drift velocity and increasing the electric field required to obtain the maximum drift velocity [17].

The form of the $v_d(F, \theta)$ map shown in figure 3.11 enables us to explain the variation of V_c , with θ . For values of $\theta \lesssim 27^\circ$, figure 3.11 reveals that the Esaki-Tsu peak is dominant in v_d and, consequently, V_c is constant (figure 3.10), with current

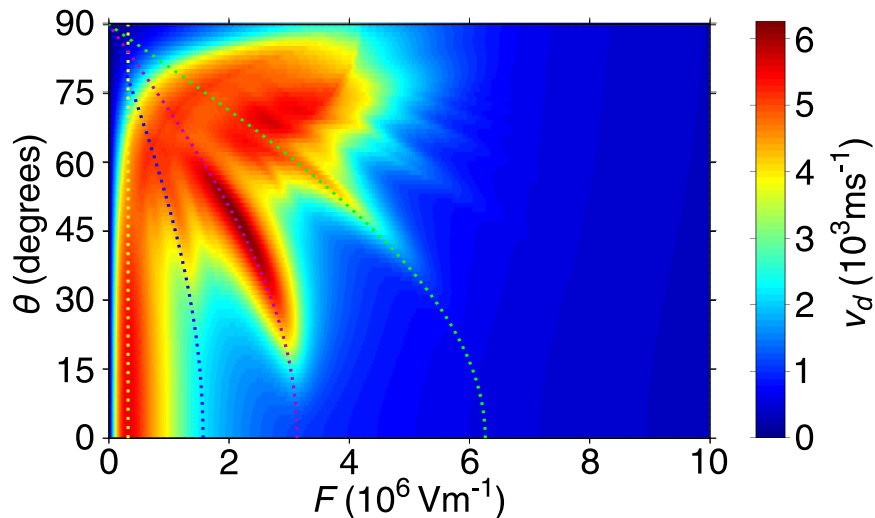


Figure 3.11: Colour map of $v_d(F, \theta)$ (scale right) calculated for $B = 15$ T.

oscillations being induced by the region of negative differential velocity immediately following the Esaki-Tsu peak. When $40^\circ \gtrsim \theta \gtrsim 60^\circ$ the $r = 1$ peak is dominant in figure 3.11, and, correspondingly, V_c jumps to a higher voltage ≈ 600 mV corresponding to the region of high negative differential velocity following the $r = 1$ peak. For $60^\circ \lesssim \theta \lesssim 75^\circ$, figure 3.11 shows that the region of negative differential velocity occurs at increasingly high F as θ increases and, correspondingly, V_c also increases. For $75^\circ \gtrsim \theta \gtrsim 85^\circ$ the amplitude of the higher order resonant peaks in the drift velocity diminish and, correspondingly, V_c decreases. When $\theta \gtrsim 85^\circ$ the Esaki-Tsu peak dominates and, since at high θ its position occurs with increasing F , we find a slight increase in V_c .

An interesting case occurs when $28^\circ \lesssim \theta \lesssim 35^\circ$, in this regime the initial “switch-on” of current oscillations when $V \approx 290$ mV, there is a second stationary current region that begins between ≈ 350 and 400 mV (depending on θ), and then sustained current oscillations for $V \gtrsim 500$ mV. Analysis of figure 3.11 reveals that in this regime the $r = 1$ resonance is well defined and well separated from the Esaki-Tsu peak (for example at $\theta = 30^\circ$ the separation of the peaks is $\approx 2.5 \times 10^6$ V m $^{-1}$). Therefore, for sufficiently low voltages, the system can only access the Esaki-Tsu negative differential velocity region and the system will behave as if $\theta = 0^\circ$. But increasing the voltage allows the fields in the superlattice to access the region of positive differential velocity corresponding to the $r = 1$ peak, which suppresses the charge domains and so kills

the current oscillations. Increasing V to the second critical voltage ensures that $r > 1$ in a substantial part of the superlattice region and so current oscillations are again induced by the associated negative differential velocity region.

The surface plot of I_a in figure 3.10, also gives an estimate of the power of the current oscillations. When $\theta \lesssim 20^\circ$ we find that the current oscillations are relatively weak, although increasing the voltage from V_c to 1 V raises the amplitude of the oscillations by ≈ 15 mA (from ≈ 5 mA to 18 mA when $\theta = 0^\circ$). The increase in the oscillatory amplitude can again be attributed to the shape of the drift velocity curve. Increasing the voltage across the device enhances the field difference between the low and high field regions in the superlattice and, hence, the difference in the drift velocity between the high and low field regions. This allows more charge to be injected into the charge domain, thereby enhancing the current oscillations. At higher voltages the low and high field regions (corresponding to high and low velocity regions) are both larger, which allows the domain to form and grow more quickly and so increase the amount of charge in the domain.

As θ increases so that the $r = 1$ resonance strengthens in $v_d(F)$, there is a gradual increase in the amplitude of the current oscillations until $\theta = 45^\circ$. because increasing the peak drift velocity in $v_d(F)$ also increases the associated negative differential velocity (see figure 3.11). The enhanced velocity injects more charge into the domains and the larger negative differential velocity allows the domain to form quicker and thus “collect” more charge. In addition, there are new domain filaments formed by the extra features in the drift velocity curve, which carry more charge through the superlattice. These effects combine to increase the amplitude of the current oscillations.

Increasing θ beyond 45° leads to the appearance of a second region of enhanced current oscillations in figure 3.10 when $\theta \approx 70^\circ$, where a large number of resonant domains are induced in the superlattice. Further increasing θ to 90° generally decreases I_a until $\theta = 90^\circ$ when I_a has qualitatively the same form as when $\theta = 0^\circ$

3.2.5 Frequency of $I(t)$ for $0^\circ < \theta < 90^\circ$

In sections 3.2.2 and 3.2.3 it was shown that by inducing extra charge domain filaments it was possible to significantly increase the power and frequency of the current oscillations: especially when $\theta = 40^\circ$ and $V = 610$ mV, where the dominant component in the frequency spectrum was the 5th harmonic with a frequency of 92 GHz.

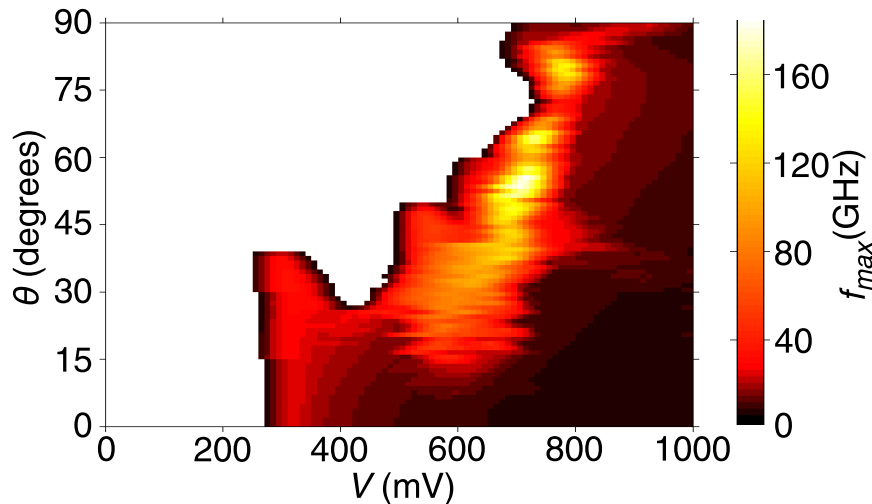


Figure 3.12: Colour map of $f_{max}(V, \theta)$ (scale right) calculated for $B = 15$ T.

To explore this further, figure 3.12 shows a colour map of the dominant harmonic in the $I(t)$ frequency spectrum, f_{max} , versus θ and V . The figure reveals a startling increase in the characteristic frequency of the system when a tilted magnetic field is applied to the superlattice. Generally for low $\theta \lesssim 5^\circ$ $f_{max} \approx 25$ GHz when $V \approx V_c$, but decreases with increasing $V > V_c$. This is because increasing V raises the electric field in the superlattice, thereby reducing the drift velocity and, hence, the frequency of the oscillations in $I(t)$ (see figures 3.3).

However, as soon as a resonant peak appears in the drift velocity curve when $\theta \approx 15^\circ$ (see figure 3.11) there is an immediate increase in the frequency of the current oscillations to approximately 40 GHz (see figure 3.12) as extra charge domains are induced in the superlattice. Again increasing the voltage causes a decrease in the frequency of the $I(t)$ oscillations because the fields in the superlattice increase, thus diminishing the effect of the resonant features. The optimum voltage for the maximum frequency output occurs when, throughout the superlattice, the electric fields encompass the resonances in $v_d(F)$ so that all the charge domains contribute to the features in the $I(t)$ curve.

As θ increases, the power of the higher harmonics in the frequency spectra increases due to the creation of extra charge domains until, at $\theta \approx 57^\circ$, the frequency of the highest powered peak is, astonishingly, at ≈ 180 GHz: an order of magnitude increase in the frequency of the dominant peak when $\theta = 0^\circ$.

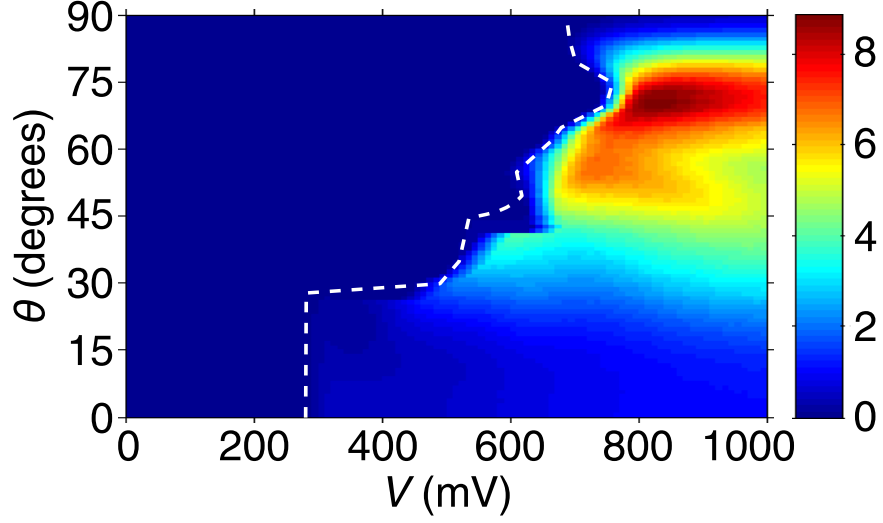


Figure 3.13: Colour map of $P_{int}(V, \theta)$ (scale right in arbitrary units) calculated for $B = 15$ T. Dashed curve: variation of V_c with θ

Recent experimental results [75; 76] show successfully that, by using backward wave oscillators, it is possible to take advantage of the higher harmonics of frequency generators such as superlattices. Therefore, to quantify the overall power of the high frequency components we calculate $P_{int} = \langle P(f) \rangle$, where $\langle \cdot \rangle$ denotes integration over $f > 0.2$ THz. Figure 3.13 shows a colour map of P_{int} in the $V - \theta$ plane. For $V < V_c$ (left of the dashed curve in figure 3.13), $P_{int} = 0$ because there are no charge domain oscillations (see also figure 3.10).

As for the case of f_{max} , P_{int} generally increases with increasing θ as extra charge domains are formed in the superlattice. We find there is a maximum in P_{int} (dark red region) when $V \approx 800$ mV and $\theta \approx 70^\circ$. In this regime, P_{int} is an order of magnitude higher than for $\theta = 0^\circ$ due to the formation of multiple propagating charge domains.

Chapter 4

Using sound to control THz electron dynamics in superlattices

In this chapter, we will show that an acoustic wave propagating through a semiconductor superlattice can induce a charge current even when no static electric field is applied. There are two distinct dynamical regimes, depending on whether the energy amplitude of the acoustic wave is greater, or less, than a critical value which depends on the superlattice parameters. When the energy amplitude of the acoustic wave is less than the critical value, we find the electron is dragged through the superlattice by the acoustic wave causing strong resonant enhancement of electron transport, accompanied by very high frequency, almost periodic, oscillations of the electron orbits (in our present samples ≈ 20 times larger than the applied wave). For phonon wave amplitudes higher than the critical value, the electrons perform Bloch-like oscillations, which dramatically suppresses electron transport. Consequently, we see that driving the electrons with GHz sound waves, rather than a static electric field, greatly increases both the peak value of v_d and the magnitude of the negative differential velocity. Since high-frequency superlattice oscillators require high values of both parameters [14; 32], acoustic driving could strongly enhance the performance of such devices.

4.1 Acoustic waves

Traditionally considered a limiting factor in the performance of condensed matter devices (due to the effect of scattering processes), the use of phonons as a method

of controlling and enhancing such devices is emerging as a powerful new tool [77; 78]. Advances in femtosecond laser technology have resulted in the development of experimental techniques to generate coherent picosecond acoustic waves. Since the 1980s, it has been known that by fast thermoelastic deformation of a thin metal film it is possible to produce a coherent strain pulse which has a well defined spectral component of frequencies in the range 100-200 GHz [79; 80; 81; 82; 83]. The strain pulse propagates through the material at a speed equal to the speed of sound for the particular substance. This technique has been used to probe the acoustic properties of a wide range of materials, see for example [84] and [85]. However, recently it was shown that a pulse of this type can be used to drive an electric current through both a layer of bulk GaAs and also through a semiconductor superlattices in the absence of an external electric field [69]. Figure 4.1 shows the schematic diagram for generating of a coherent acoustic pulse in a GaAs substrate. One side of the GaAs substrate is polished flat and has a thin layer of aluminium deposited onto it. This film is then excited using pulses from a femtosecond laser focused onto a spot opposite the contact region. The current is then measured by amplifying changes in the voltage across the top and bottom of the contact region. It was shown in [69] that a sharp current response related to the coherent acoustic wave was observed after a delay corresponding to the time of flight for the acoustic pulse across the GaAs substrate. This is clear evidence of ‘phonon drag’ phenomena [86; 87] in this material where the phonons are able to exert momentum on electrons (and holes) via a *deformation potential*. This deformation potential is the effective electric potential experienced by an electron in a solid caused by the local deformation of a crystal lattice. In this paper the experiment was also extended to use a semiconductor superlattice in place of the GaAs substrate where similar evidence of phonon drag was found.

One of the most promising directions in the control of acoustic waves in condensed matter is the SASER or “Sound Amplification by Stimulated Emission of Radiation” device [88; 89; 90; 91]. The SASER works in a very similar way to the LASER. The semiconductor version of the SASER consists of a semiconductor superlattice enclosed within an acoustically reflective chamber. Consider such a superlattice with a lattice period d and an electric field, F , applied along the device so that the potential energy dropped across a quantum well, eFd , is much larger than the miniband width of the superlattice. This effectively destroys the band structure of the superlattice since

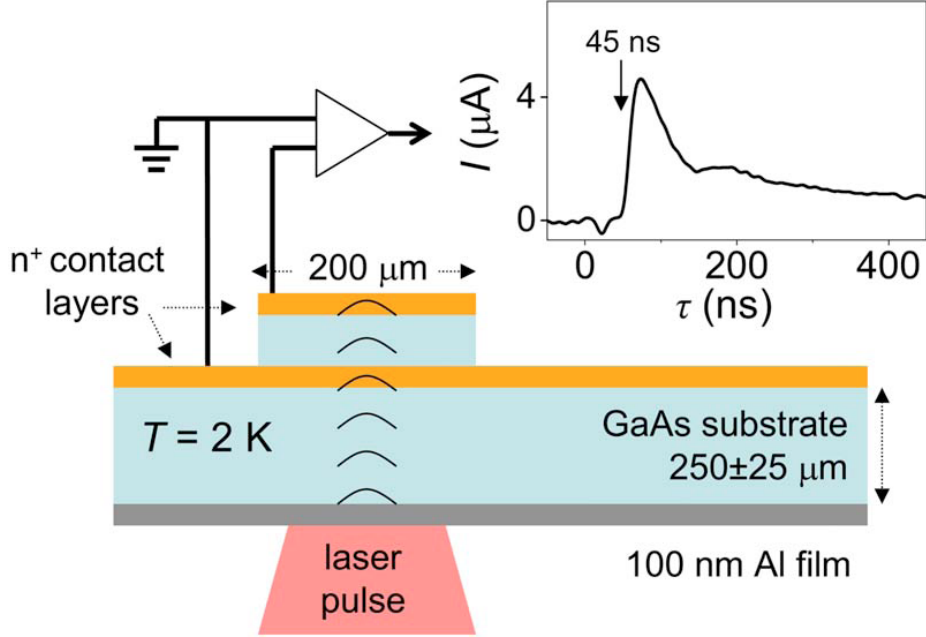


Figure 4.1: Figure reproduced from [69] showing an experimental schematic of an acoustic pulse incident on bulk GaAs. Inset shows a typical $I(t)$ signal from the device after an incident laser pulse at $t = 0$.

electron states in adjacent wells can no-longer be considered to be isoenergetic¹. In this regime, we find a series of electron states in each quantum well known as a Wannier Stark ladder forming a periodic sequence of energy levels with a separation equal to eFd [14]. The horizontal red lines in figure 4.2 represent the Wannier Stark ladder formed within the potential energy landscape of the superlattice (black lines). In this model, charge transport is achieved by electrons tunnelling through the superlattice barriers as they “hop” between states in adjacent quantum wells. Disregarding the possibility of photon assisted transitions, conservation of momentum and energy tells us that the hopping between wells is facilitated either by defect scattering, with the realted emission of phonons, or by inelastic phonon-assisted tunnelling, see figure 4.2. Therefore a phonon with energy $\hbar\omega_{in} = eFd$, incident on an electron in a particular

¹Note that although the band model starts to become invalid in this regime, we can still use a semiclassical model provided that the width of the Bloch oscillations, A_B , is of the order, or larger than the lattice period, i.e.

$$A_B = \frac{\Delta}{eF} \gtrsim d. \quad (4.1)$$

quantum well, can cause it to hop into a lower energy state in the next quantum well. In reference [88] it was shown that this transition is indirect in momentum space, and therefore results in a phonon with energy $\hbar\omega_{em} < eFd$ being emitted; and also that the transition occurs from an initial state with higher population than that of the final state. Implying that, in this case, population inversion can be achieved in a similar way to a LASER. The generated phonons will then bounce off the interfaces between the layers causing more electron transitions, increasing the population of phonons with the same energy. Then careful design of the superlattice structure can result in the synchronisation of the phonons to produce a narrow beam of coherent, high frequency ‘sound’, otherwise known as a coherent acoustic wave.

Preliminary experimental demonstration of the semiconductor SASER in the terahertz regime [90; 91] suggests potential applications including imaging of nano-sized structures and the manipulation of electrons in semiconductors, perhaps leading to the development of terahertz computer processors.

The development of the acoustic devices, particularly the SASER device, opens new opportunities for studying electron dynamics in superlattices. Previously, control of electron transport in superlattices has been via static or oscillating electric fields [14] or with a magnetic field, explored in chapters 2 and 3. However, the potential energy fields generated by acoustic waves propagating through the structure, at the speed of sound of the material, are much slower, and fundamentally different from those previously considered potentials. In the following chapter it will be shown that the use of acoustic waves opens new possibilities in the control of electron dynamics (and thus charge transport) in superlattices.

4.1.1 Acoustic wave model

In this investigation, we consider a longitudinal coherent acoustic wave, such as the one generated by the SASER device¹, propagating along the x -axis of the superlattice, and its effect on the electron dynamics and charge transport.

In the model, we can assume that the acoustic wave generates a deformation potential, which results in the periodic variation of the conduction band edge of the superlattice, first justified by Bardeen and Shockley in the effective mass approximation in 1950 [92]: see also [78; 93; 94; 95; 96].

¹The model could also be applied to an acoustic pulse generated by fast excitation of a thin film [69].

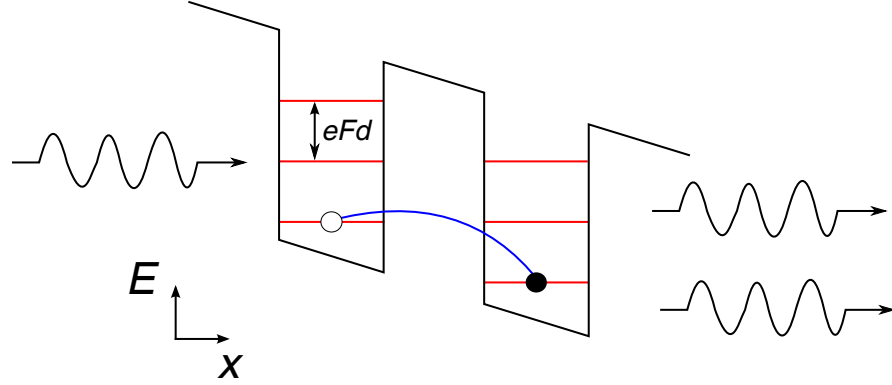


Figure 4.2: Figure adapted from reference [90] illustrating electron transport by hopping induced by an acoustic pulse (shown, schematically, by sine waves with arrows) incident on bulk GaAs.

Note that in our analysis we consider an acoustic wave with a frequency in the GHz range. Also, since the strain wave travels along the principle growth axis of the superlattice piezoelectric coupling is zero [95]. Consequently the main mechanism of electron-phonon interaction is the deformation potential and any piezo-electric potential effects are negligible [88].

In the semiclassical model the potential energy due to a strain of the lattice, S , is given by

$$V_S = DS \quad (4.2)$$

where D is the electron-phonon coupling constant, which has been measured experimentally to be ~ 10 eV [69; 78; 94; 95; 97]: the value used in this thesis. Note that here we are considering the interaction between a coherent acoustic wave and an electron; *not* electron-phonon scattering. Consequently, the strength of interaction does not depend on the eigenfunctions of the electrons. The strain, $S(x, t)$, generated by the coherent acoustic wave travelling along the x -axis of the superlattice is given by

$$S = -S_0 \sin(k_S x + \omega_S t), \quad (4.3)$$

where $S_0 < 0.5\%$ is the maximum strain generated by the wave. Here, k_S is the wave number of the acoustic wave, which we take to lie within the first half of the superlattice minizone. This allows us to assume a linear dispersion relation for

4.2 Semiclassical mechanics of an electron in a superlattice driven by an acoustic wave

the frequency of the acoustic wave, $\omega_S = v_S k_S$ where $v_S = 5000 \text{ m s}^{-1}$ is the speed of sound in GaAs [90]. The maximum strain can be written as

$$S_0 = k_S A \quad (4.4)$$

where A is the mechanical displacement amplitude of the wave, i.e. the physical displacement of the lattice generated by the acoustic wave. Equation (4.4) reveals that S_0 depends functionally on the wavelength, $\lambda_S = 2\pi/k_S$. However, as we are only concerned with the magnitude of S_0 , the dependence of S_0 on k_S is not relevant to the analysis of the system and is only included here for completeness. Using equations (4.2), (4.3), and (4.4) we can rewrite the potential energy generated by the acoustic wave as

$$V_S(x, t) = -U \sin(k_S x - \omega_S t), \quad (4.5)$$

where $U = DS_0$ is the wave amplitude. Note that in this simplest case the phase of the wave is chosen so that the force, $-\partial V_S/\partial x$, is maximal when x and t is 0, which would correspond to the propagation of an acoustic pulse. Initially, we will consider the case when $x(t=0) = 0$, but later we will also consider electron trajectories not starting at the origin.

4.2 Semiclassical mechanics of an electron in a superlattice driven by an acoustic wave

In the previous section we derived an expression for the potential energy, V_S , generated by the acoustic wave. Therefore, following arguments given in section 1.2, the semiclassical Hamiltonian of the system, which is equal to the sum of the kinetic energy and potential energy is given by

$$\mathcal{H}(x, p_x, t) = E(p_x) + V_S(x, t) \quad (4.6)$$

where we use the simplified version of the dispersion relation

$$E(p_x) = \frac{\Delta_{SL}}{2} \left(1 - \cos\left(\frac{p_x d}{\hbar}\right) \right). \quad (4.7)$$

In the following simulations we consider the superlattice described in section 1.3, with $\Delta_{SL} = 7 \text{ meV}$ and $d_{SL} = 12.5 \text{ nm}$. These parameters were chosen to correspond to an

4.2 Semiclassical mechanics of an electron in a superlattice driven by an acoustic wave

ongoing experiment [69]. It should be noted, though, that similar results are obtained for a wide range of superlattice parameters.

The semiclassical Hamilton's equations of electron motion, obtained from the Hamiltonian in equation (4.6), are

$$v_x = \frac{dx}{dt} = \frac{\partial \mathcal{H}}{\partial p_x} = \frac{\Delta d}{2\hbar} \sin\left(\frac{p_x d}{\hbar}\right) \quad (4.8)$$

$$\frac{dp_x}{dt} = -\frac{\partial \mathcal{H}}{\partial x} = k_S U \cos(k_S x - \omega_S t). \quad (4.9)$$

We solve equations (4.8) and (4.9) numerically using a 4th order Runge-Kutta algorithm¹, taking $x = p_x = 0$ when $t = 0$, to determine the electron trajectories in the absence of scattering.

4.2.1 Drift velocity characteristics

The solid curve in figure 4.3 shows the variation of v_d as a function of U for an acoustic wave with $\omega_S = 4 \times 10^{11}$ rad s⁻¹, calculated using the following Esaki-Tsu formulism (see section 1.3.4)

$$v_d = \frac{1}{\tau} \int_0^\infty v_x(U, t) \exp(-t/\tau) dt. \quad (4.10)$$

taking the scattering time $\tau = 280$ fs from experiment [7]. To make a comparison with previous results, the dashed curve in 4.3 shows the usual Esaki-Tsu drift velocity [10] calculated for an electron accelerated by a *static* electric field of magnitude $k_S U/e$. As discussed previously, in section 1.3.4, the Esaki-Tsu $v_d(U)$ curve is linear for small U , attains a maximum when $U = U_{ET} = \hbar/\tau \approx 2.4$ meV, and thereafter decreases with increasing U as more electrons complete spatially-localised Bloch oscillations before scattering. Comparing the two curves it would appear for low U ($\lesssim 1$) meV and high U ($\gtrsim 18$) meV, the curves generated by the static and propagating fields converge implying similar transport mechanisms. However, for intermediate values of U there are two significant differences in the shape of the curves. Firstly, not only do we get significant transport of electrons generated by only an acoustic wave, but the peak drift velocity is significantly higher than the peak found for the Esaki-Tsu curve. Secondly, the acoustic wave produces a far steeper region of negative drift

¹For details of this numerical method see the highly recommended *Numerical Recipes* [19].

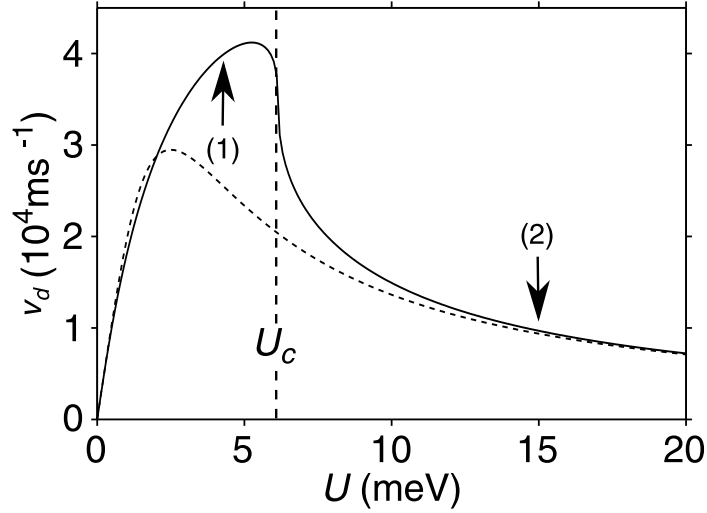


Figure 4.3: (a) Solid curve: v_d versus U calculated for a miniband electron driven by an acoustic wave only. Dashed curve is v_d versus U calculated for a miniband electron accelerated by a *constant* electric field, $k_S U/e$ only. The dashed vertical line shows the position of U_c , the transition between the two dynamical regimes. Arrows (1) and (2) show the positions of $U = 4$ and 15 meV respectively

velocity (factor ≈ 13) in comparison with the Esaki-Tsu curve. The rapid suppression of transport at a critical value of the energy of the acoustic wave, U_c , suggests a transition between distinct dynamical regimes.

To explain the differences in the drift velocity curves, the electron trajectories calculated in the absence of scattering will be explored in the following two sections. We will see in section 4.2.2 that for $U < U_c$, the acoustic wave drags the electron through the superlattice enhancing the drift velocity. However, it will be shown in section 4.2.3 that for U_c , the acoustic wave induces Bloch oscillations, thereby dramatically suppressing transport via a similar mechanism to that found in the static field case.

4.2.2 Electron trajectory in the wave dragging regime

Figure 4.4(a) shows the $x(t)$ trajectory obtained numerically from equations (4.8) and (4.9), when $\omega_S = 4 \times 10^{11}$ rad s $^{-1}$ and taking $U = 4$ meV (marked by arrow (1) in figure 4.3) to the left of the peak drift velocity in the $v_d(U)$ curve. The trajectory consists of regular, almost sinusoidal, oscillations superimposed on a linear background of

4.2 Semiclassical mechanics of an electron in a superlattice driven by an acoustic wave

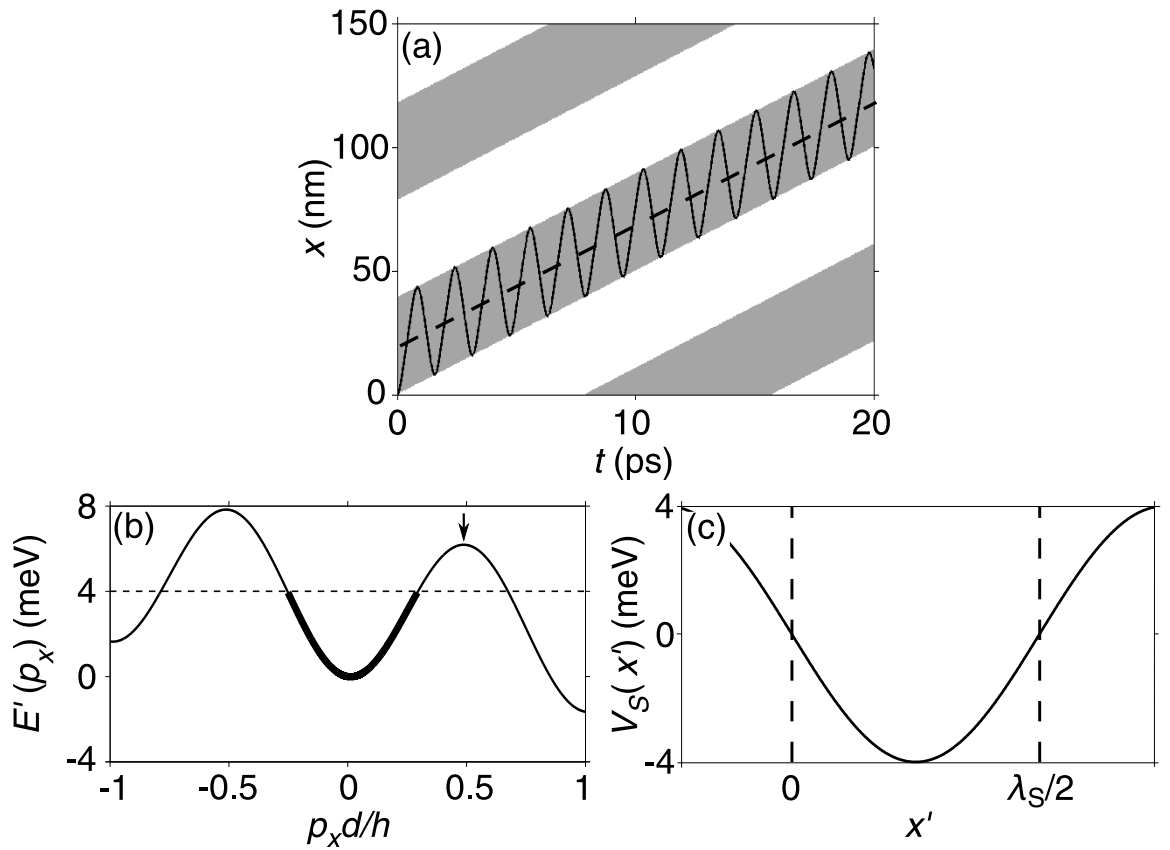


Figure 4.4: (a) Solid curve: electron trajectory, $x(t)$, calculated for $U = 4$ meV. Within the white regions, $V_S(x, t) > 0$ and in the gray regions $V_S(x, t) < 0$. Dashed line has gradient v_S . (b) is $E'(p_x)$ where the dotted line shows when $U = 4$ meV. At the arrowed peak, $E'(p_x) = U_c$. (c) shows $V_S(x')$, where dotted lines mark turning points of orbit in (a).

4.2 Semiclassical mechanics of an electron in a superlattice driven by an acoustic wave

gradient v_S . The amplitude of the oscillations equals half the wavelength, λ_S , of the acoustic wave. To illustrate this, the dashed line in figure 4.4(a) shows the function

$$\langle x(t) \rangle = v_S t + \frac{\lambda_S}{4}. \quad (4.11)$$

This clearly suggests that the electron is being dragged through the lattice by the acoustic wave, as in previous studies of phonon drag in 2D electron gases [86; 87], and bulk GaAs [69].

To understand further the trajectory in the acoustic wave dragging regime, we can study the electron motion within the *rest frame* of the acoustic wave. To make this coordinate transformation we start with the Hamiltonian in the rest frame of the superlattice, as defined in equation (4.6). This gives the total energy of the electron. Note, however, that due to the explicit time dependence of the acoustic wave potential (equation (4.5)), it is not a constant of motion.

To assist the transformation from the lab (x, y, z) frame to the rest frame (x', y, z) of the acoustic wave, we define the Lagrangian corresponding to the Hamiltonian in equation (4.6). The Lagrangian is an explicit function of generalised coordinates, in this case the position coordinates and the generalised velocities. Using the Legendre transform¹ the Lagrangian, \mathcal{L} , is

$$\mathcal{L}(x, \dot{x}, t) = \dot{x} p_x[\dot{x}] - \mathcal{H}(x, p_x[\dot{x}], t) \quad (4.12)$$

$$= \dot{x} p_x[\dot{x}] - E(p_x) - V_S(k_S x - \omega_S t) \quad (4.13)$$

where $p_x[\dot{x}]$ is the dependence of the canonical momentum on $\dot{x} = \partial \mathcal{H} / \partial p_x$. We make the co-ordinate transformation of $x(t)$ into the moving frame of the acoustic wave $x'(t)$ with the following substitution

$$x'(t) = x(t) - v_S t \quad \Rightarrow \quad \dot{x}'(t) = \dot{x}(t) - v_S, \quad (4.14)$$

therefore, the transformed Lagrangian, \mathcal{L}' is

$$\mathcal{L}'(x'(t), \dot{x}'(t)) = (\dot{x}' + v_S) p_x[\dot{x}' + v_S] - E(p_x[\dot{x}' + v_S]) - V_S(x'). \quad (4.15)$$

¹For an introduction to classical mechanics the author recommends Goldstein's *Classical Mechanics* [65].

4.2 Semiclassical mechanics of an electron in a superlattice driven by an acoustic wave

The electron in the acoustic wave frame therefore experiences a *static*, i.e. time independent, potential energy and thus the acoustic wave potential in equation (4.5) becomes (noting that $\omega_S = v_S k_S$)

$$V_S(x') = -U \sin(k_S x'). \quad (4.16)$$

We can now calculate the generalised momentum in the moving frame, p'_x , remembering that $\dot{x}'(t) = \dot{x}(t) - v_S$,

$$p'_x = \frac{\partial \mathcal{L}}{\partial \dot{x}'} = p_x [\dot{x}' + v_S] = p_x \quad (4.17)$$

showing that the canonical momentum is the same in both reference frames. This implies that the Hamiltonian function in the moving frame, $\mathcal{H}'(x', p'_x) = \mathcal{H}'(x', p_x)$. Therefore we find that the Hamiltonian in the moving frame, via the Legendre transformation, is given by

$$\mathcal{H}'(x', p_x) = \dot{x}' p_x - \mathcal{L}' = E(p_x) - v_S p_x + V_S(x') \quad (4.18)$$

\mathcal{H}' is therefore time independent and a constant of the motion, however it should be emphasised that it is *not* the total energy of the system, \mathcal{H} . In the moving frame, we therefore have a modified dispersion relation for the system given by

$$E'(p_x) = E(p_x) - v_S p_x, \quad (4.19)$$

and \mathcal{H}' can be written as the summation of the kinetic and potential energy

$$\mathcal{H}' = E'(p_x) + V_S(x'). \quad (4.20)$$

The corresponding equations of motion in the frame of the acoustic wave can be found using Hamilton's equations and are equal to

$$v'_x = v_x - v_S = \frac{dx'}{dt} = \frac{\partial \mathcal{H}'}{\partial p_x} = \frac{\Delta d}{2\hbar} \sin\left(\frac{p_x d}{\hbar}\right) - v_S, \quad (4.21)$$

$$\frac{dp_x}{dt} = -\frac{\partial \mathcal{H}'}{\partial x'} = k_S U \cos(k_S x'). \quad (4.22)$$

Initially, we simulate electron trajectories starting at rest, so that $x(t=0) = p_x(t=0) = x'(t=0) = 0$. Therefore at $t=0$, $\mathcal{H}' = 0$. Since \mathcal{H}' is a constant of motion it therefore is equal to 0 for all t . This implies that

4.2 Semiclassical mechanics of an electron in a superlattice driven by an acoustic wave

$$E'(p_x) = -V_S(x'). \quad (4.23)$$

and therefore $E'(p_x)$ can only take values between $\pm U$, determined by amplitude $V_S(x')$.

Figure 4.4(b) is a plot of the effective dispersion curve, $E'(p_x)$ versus p_x , for $U = 4$ meV corresponding to the trajectory in figure 4.4(a). The horizontal dotted line and the lower axis in the figure mark ± 4 meV i.e. the maximum and minimum values that $E'(p_x)$ can possibly obtain. The dotted line reveals that the electron can only access the almost parabolic region of the $E'(p_x)$ curve, around $p_x = 0$, shown as a thick curve in figure 4.4(b). Since the minimum value of $E'(p_x)$ that the electron can attain is ≈ 0 , its maximum potential energy is also ≈ 0 . The electron is therefore confined within a single potential well in the acoustic wave and oscillates back and forth across this well between turning points at $x' = 0$ and $\lambda_S/2$ (see vertical dashed lines in figure 4.4(c)), where $\lambda_S = 2\pi/k_S \approx 6d_{SL}$ is the acoustic wavelength. Since the electron remains within the almost parabolic region of $E'(p_x)$, where its effective mass is constant, $x'(t)$ is an almost harmonic function of t . Consequently, as we see clearly in figure 4.4(a), the electron trajectory can be approximated by

$$x(t) \approx v_S t + \frac{\lambda_S}{4} (1 - \cos(\omega_R t)), \quad (4.24)$$

where ω_R is the frequency for motion to and fro across the potential well. The gray bands in figure 4.4(a) represent the region where $V_S(x, t) \lesssim 0$ showing the electron trapped within the well. The well then propagates through the lattice dragging the electron through the SL at a mean speed equal to v_S *in the absence of scattering*.

Increasing U above 4 meV initially has no qualitative effect on the electron orbits. They continue to be dragged through the superlattice and are of the form $x(t) = v_S t + f(t)$. However, as the value of U (represented by the upper dotted line in figure 4.4(b)) increases, the electron can access the nonparabolic regions of $E'(p_x)$. Consequently the trajectory becomes less periodic and its Fourier transform has stronger high frequency components (see later in the chapter).

When U reaches the critical value, U_c , equal to the local maximum of $E'(p_x)$, marked by the arrow in figure 4.4(b), the electron is no longer trapped within the acoustic wave. The electrons can now reach the edge of the first minizone, and their trajectories change abruptly from closed to open orbits in p_x that can traverse several minizones. The value of U_c can be estimated analytically by analysing equation (4.18).

The local maximum of $E'(p_x)$, see equation (4.19), occurs when

$$\frac{dE(p_x)}{dp_x} = v_S \quad (4.25)$$

i.e. when

$$\sin\left(\frac{p_x d_{SL}}{\hbar}\right) = \frac{2\hbar v_S}{\Delta_{SL} d_{SL}}. \quad (4.26)$$

It follows, using small-angle approximations and remembering that the Brillouin zone extends for a distance of $\hbar\pi/d_{SL}$, that the local maximum arrowed in figure 4.4(b) occurs when

$$p_x \approx \frac{\hbar\pi}{d_{SL}} - \frac{2\hbar^2 v_S}{\Delta_{SL} d_{SL}^2}. \quad (4.27)$$

Substitution of equation (4.27) into equation (4.18) for \mathcal{H}' , reveals the following, simplified¹, expression for U_c ,

$$U_c \approx \Delta_{SL} - \frac{v_S \hbar \pi}{d_{SL}}. \quad (4.28)$$

The vertical dashed line in the drift velocity plot in figure 4.3, shows the position of $U_c = 6.2$ meV defined by equation (4.28) for the parameters used in the calculation of the curve. This estimate shows good correspondence with the position of the negative differential velocity, expected since the suppression of transport results from a transition to the localised Bloch oscillation regime.

This abrupt onset of the acoustically-driven Bloch oscillations contrasts with the gradual switch on produced by increasing a *static* force [10; 14; 98]. Since the onset occurs when the $-v_S p_x$ term in \mathcal{H}' pulls the local maximum in $E'(p_x)$ marked by the arrow in figure 4.4(b) below U , it is somewhat analogous to vortex shedding in a superfluid, which happens when an obstacle passes through the superfluid fast enough to pull the roton minimum below a critical energy (the Landau criterion) [44].

4.2.3 Electron trajectory in the Bloch oscillation regime

Figure 4.5(a) shows $x(t)$ calculated for $U = 15$ meV $> U_c$ (≈ 6.2 meV). The trajectory shows high frequency oscillations (within brackets) interrupted by jumps (arrowed) in the negative x direction. We find that the bursts of high-frequency fluctuations in $x(t)$ are Bloch oscillations driven by the acoustic wave. The jumps in $x(t)$ occur

¹A more exact expression for U_c includes a second order term. However, it is omitted here as it is negligibly small.

4.2 Semiclassical mechanics of an electron in a superlattice driven by an acoustic wave

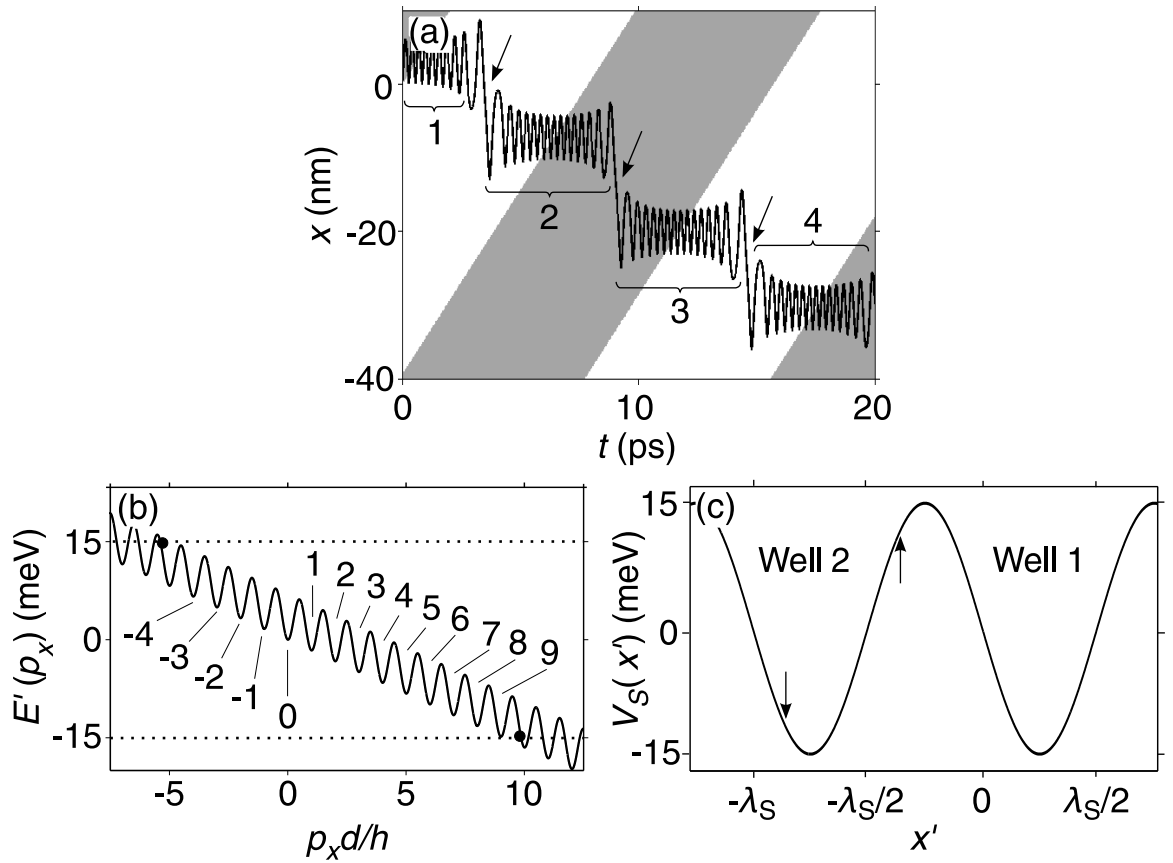


Figure 4.5: (a) Solid curve: electron trajectory, $x(t)$, calculated for $U = 15$ meV. Within the white regions, $V_S(x, t) > 0$ and within the gray regions $V_S(x, t) < 0$. Bloch oscillation bursts, within numbered brackets, are separated by sudden jumps (arrowed). (b) is $E'(p_x)$ where dotted lines mark $\pm U$ when $U = 15$ meV. The left and right hand filled circles mark where $E'(p_x) = U$ and $-U$ respectively. Numbers label different minizones. (c) shows adjacent energy wells (1 and 2) in $V_S(x')$, with arrows discussed in text.

4.2 Semiclassical mechanics of an electron in a superlattice driven by an acoustic wave

when V_S is maximal (at the centres of the white and gray stripes in figure 4.5(a)) and, consequently, when the acoustic force is temporarily too weak (zero) to induce Bloch oscillations.

To fully explain the form of the trajectory in figure 4.5(a), we consider the variation of $E'(p_x)$ and $V'(x)$ in the rest frame of the acoustic wave, shown respectively in figures 4.5(b) and 4.5(c). Initially, the electron is at $x' = 0$ where the high gradient of $V_S(x')$ (see figure 4.5(c)) causes p_x to rapidly increase up to the edge of the first minizone (labelled 0 in figure 4.5(b)), thus reversing v_x and also v'_x . After crossing the minizone boundary, the electron continues to experience a large positive force, which increases p_x through minizones 1-9 in figure 4.5(b), thus generating the Bloch oscillations within Bracket 1 in figure 4.5(a). We see in figure 4.5(c) that as p_x increases, the average value of $E'(p_x)$ decreases and thus $V_S(x')$ increases (to keep \mathcal{H}' in equation (4.18) = 0) as the electron moves up the left-hand side of Well 1 in figure 4.5(c). As the electron climbs the well wall, $|dV_S(x')/dx'|$ decreases, thus reducing the frequency of the Bloch oscillations and increasing their amplitude, see section 1.2.1 or [10; 14; 98], as shown by the $x(t)$ curve within Bracket 1 in figure 4.5(a).

When the electron reaches the top of Well 1 (see figure 4.5(c)), so that $V_S(x') = U$, $E'(p_x)$ attains its lowest possible value of $-U$ (lower dotted horizontal line in figure 4.5(b)) and so p_x can no longer increase. Instead, since the acoustic force is instantaneously zero, p_x is temporarily pinned at the intersection (right hand filled circle in figure 4.5(c)) between $E'(p_x)$ and the lower dotted line. The large negative velocity at this intersection, $dE'/dp_x \approx -5.6 \times 10^4$ m s $^{-1}$, makes the electron jump backwards along the section of the $x(t)$ curve marked by the left hand arrow in figure 4.5(a). This jump transfers the electron to the position marked by the right hand arrow in Well 2 (figure 4.5(c)). At this position, the acoustic wave exerts a large negative force on the electron, which causes p_x to decrease, so inducing another burst of Bloch oscillations [within Bracket 2 in figure 4.5(a)], until $E'(p_x)$ reaches its maximum value (upper dotted line in figure 4.5(b)) and $V_S(x')$ attains its minimum value of $-U$ in Well 2. Then, the electron again jumps backwards, along the $x(t)$ trajectory marked by the central arrow in figure 4.5(a), with velocity $\approx -6.8 \times 10^4$ m s $^{-1}$, approximately equal to dE'/dp_x at the intersection (left hand filled circle in figure 4.5(b)) between $E'(p_x)$ and the upper dotted line. This jump transfers the electron to the position marked by the left hand arrow in Well 2 [figure 4.5(c)], where a large positive force causes p_x rapidly to increase, triggering the Bloch oscillation

4.2 Semiclassical mechanics of an electron in a superlattice driven by an acoustic wave

burst within Bracket 3 in figure 4.5(a). Thereafter, the cycle repeats, with the electron jumping backwards after each Bloch oscillation burst.

The number of Bloch oscillations within each burst, N_{BO} , equals the number of distinct minizones that the electron can traverse. On dividing the possible energy range of the applied acoustic wave, $2U$, by the slope of the effective dispersion curve, $2v_S\hbar\pi/d$, we find that

$$N_{BO} \approx 2U \frac{d_{SL}}{v_S \hbar}. \quad (4.29)$$

When $U = 15$ meV, $N_{BO} \approx 14$, corresponding to crossing the minizones labeled -4 to 9 in figure 4.5(b).

4.2.4 Fourier analysis

Figure 4.6(a) shows a colour map of the Fourier power¹, $S(\omega)$, of $v_x(t)$ ² trajectories calculated for a range of U at fixed $\omega_S = 4 \times 10^{11}$ rad s⁻¹. The spectra clearly abruptly changes its form at $U = U_c$ (arrowed), due to the transition from the wave-dragging to Bloch oscillation regimes.

Figure 4.6(b) shows a typical Fourier power spectrum for the dragging regime $U = 4$ meV $< U_c$ corresponding to the trajectory shown in figure 4.4(a). We see that $S(\omega)$ has a single sharp peak at the frequency, ω_R (labelled in figure 4.6(b)), due to the almost periodic motion across the potential well (see section 4.2.2 and figure 4.4(b)). When $U = 4$ meV, ω_R is approximately an order of magnitude ($\omega_R \approx 17\omega_S$) larger than the frequency of the acoustic wave, ω_S . Therefore, since we have almost periodic oscillations, we can consider this mechanism to be frequency multiplication of the applied acoustic wave, but again emphasise that this is in the absence of scattering and neglects any effects that collective electron dynamics might have.

In figure 4.6(a), we see that initially ω_R increases with increasing U as the electron accelerates more rapidly across the confining potential well. For values of $U > 3$ meV, three higher harmonics become visible, but their power is orders of magnitude lower than the fundamental frequency (see figure 4.6(b)). The appearance of these peaks is a result of the system now being able to access the non-parabolic part of the dispersion

¹The Fourier transform was calculated using a Fast Fourier Transform method. For more information on this powerful technique see [19].

²We calculated the Fourier Transform of $v_x(t) = \dot{x}(t)$ rather than $x(t)$, since the former has no ‘drift’ component. Note, however, that $v_x(t)$ and $x(t)$ have the same non-zero Fourier components.

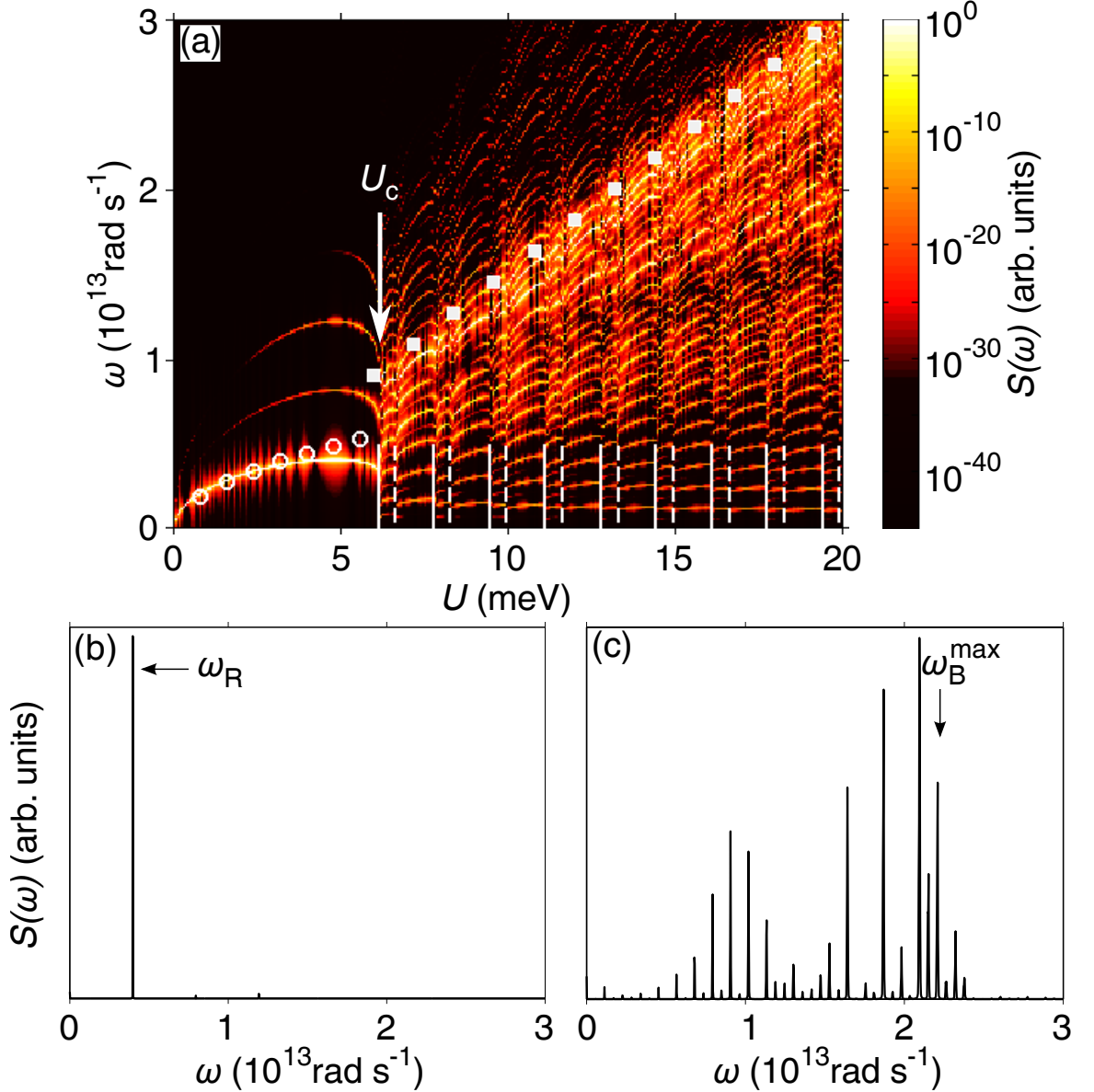


Figure 4.6: (a) Fourier power spectrum, $S(\omega)$ of $v_x(t)$ trajectories calculated for a range of U at fixed $\omega_S = 4 \times 10^{11}$ rad s $^{-1}$. Arrow is at $U = U_c$. Open circles [filled squares]: analytical estimates of ω_R [ω_B^{max}] in the phonon-drag [Bloch oscillation] regimes. Solid and dotted white lines mark U values where closely-spaced spectral peaks shift abruptly to lower ω . (b) Fourier power spectrum for the electron trajectory in figure 4.4(a), which lies in the wave-dragging regime with $U = 4$ meV. (c) Fourier power spectrum for the trajectory in figure 4.5(a) corresponding to the Bloch oscillating regime with $U = 15$ meV.

4.2 Semiclassical mechanics of an electron in a superlattice driven by an acoustic wave

curve. For higher U , the electron is allowed to reach the highly nonparabolic part of $E'(p_x)$, which causes its average speed and, hence, ω_R to decrease.

In the regime where we have almost periodic motion of the electron, an estimate of ω_R can be found using the approximation for $x(t)$ given in equation (4.24). Therefore we substitute equation (4.24) into equation (4.9) and, knowing that $k_S = \omega_S/v_S$, we find

$$\frac{\partial p_x}{\partial t} \approx k_S U \cos\left(\frac{\pi}{2} - \frac{\pi}{2} \cos(\omega_R t)\right). \quad (4.30)$$

We can then make the following approximation

$$\cos\left(\frac{\pi}{2} - \frac{\pi}{2} \cos(\omega_R t)\right) \approx \cos(\omega_R t), \quad (4.31)$$

which is valid for all t and ω_R , resulting in the following simplification of equation (4.30)

$$\frac{\partial p_x}{\partial t} \approx k_S U \cos(\omega_R t). \quad (4.32)$$

Integrating equation (4.32) with respect to t , for the initial conditions $p_x(t=0) = x(t=0) = 0$, we then derive the following approximation for p_x

$$p_x \approx \frac{k_S U}{\omega_R} \sin(\omega_R t). \quad (4.33)$$

Equation (4.33) is then substituted into equation (4.8) to derive the following approximation for $\partial x/\partial t$

$$\frac{\partial x}{\partial t} \approx \frac{\Delta_{SL} d_{SL}}{2\hbar} \sin\left(\frac{k_S U}{\omega_R} \sin(\omega_R t) \frac{d_{SL}}{\hbar}\right). \quad (4.34)$$

Equation (4.24) is differentiated to derive an analytical expression for the velocity in the x direction, and is equated to (4.34) to find

$$v_S + \frac{\lambda_S \omega_R}{4} \sin(\omega_R t) \approx \frac{\Delta_{SL} d_{SL}}{2\hbar} \sin\left(\frac{k_S U}{\omega_R} \sin(\omega_R t) \frac{d_{SL}}{\hbar}\right). \quad (4.35)$$

Note that

$$v_S \ll \frac{\lambda_S \omega_R}{4} \quad (4.36)$$

therefore

4.2 Semiclassical mechanics of an electron in a superlattice driven by an acoustic wave

$$\frac{\lambda_S \omega_R}{4} \sin(\omega_R t) \approx \frac{\Delta_{SL} d_{SL}}{\hbar} \sin\left(\frac{k_S U}{\omega_R} \sin(\omega_R t) \frac{d_{SL}}{\hbar}\right). \quad (4.37)$$

A further approximation can be made;

$$\sin\left(\frac{k_S U}{\omega_R} \sin(\omega_R t) \frac{d_{SL}}{\hbar}\right) \approx \sin(\omega_R t) \sin\left(\frac{k_S U}{\omega_R} \frac{d_{SL}}{\hbar}\right). \quad (4.38)$$

Using this with equation (4.37) and noting that $\lambda_S = 2\pi v_S/\omega_S$, we obtain the following transcendental equation

$$\frac{\omega_R}{\omega_S} \approx \frac{\Delta_{SL} d_{SL}}{\pi \hbar v_S} \sin\left(\frac{k_S U}{\omega_R} \frac{d_{SL}}{\hbar}\right). \quad (4.39)$$

Then, using the small angle approximation, and noting that $k_S = \omega_S/v_S$ we find

$$\omega_R \approx \alpha \omega_S \quad (4.40)$$

where

$$\alpha = \left(\frac{U \Delta_{SL}}{\pi}\right)^{1/2} \frac{d_{SL}}{\hbar v_S}. \quad (4.41)$$

The open circles in figure 4.6(a) show approximate ω_R value obtained from equation (4.40), which agree well with the numerically-calculated spectrum. There is deviation between numerical values and analytical approximation as U approaches U_c since $x(t)$ becomes increasingly quasi-periodic. To achieve better correlation, higher order harmonics of ω_R could be included in equation (4.24). However, the analytical expression in equation (4.40) is accurate enough to give an idea of parameters to change when designing optimum superlattices.

When U exceeds U_c , the bandwidth of $S(\omega)$ increases and the peaks become much more dense. Figure 4.6(c) shows a typical Fourier power spectrum of the trajectory in figure 4.5(a), which lies in the Bloch oscillation regime when $U = 15$ meV. We see a complex spectrum with a broad range of frequency peaks. The high frequency components are a result of the induced Bloch oscillations and the low frequency components originate from the acoustic wave oscillation. The broad range of peaks is induced by the complex interaction between these two mechanisms. The maximum frequency peak in the spectrum can be estimated by using Carson's rule [99], which states that nearly $\sim 98\%$ of the power of the frequency modulated signal lies within a bandwidth, $\Delta\omega$, which, in this model, is given by

4.2 Semiclassical mechanics of an electron in a superlattice driven by an acoustic wave

$$\Delta\omega = 2(\omega_B^{max} + \omega_S). \quad (4.42)$$

Since the central frequency of the bandwidth is 0 and $\omega_B^{max} \gg \omega_S$, we find that the maximum frequency in the power spectrum can be approximated by

$$\omega_B^{max} = \frac{k_S U d}{\hbar}, \quad (4.43)$$

where ω_B^{max} is the maximum possible frequency of the Bloch oscillations induced by the acoustic wave [10; 14; 98]. The value of ω_B^{max} for $U = 15$ meV is shown by the labelled arrow in figure 4.6(c). The open squares in figure 4.6(a) show ω_B^{max} versus U obtained from equation (4.43). These values are in good correspondence with the maximum frequencies in the numerical spectra, confirming that the high frequency oscillations in the trajectory in figure 4.5(a) are indeed induced Bloch oscillations.

The spectrum shown is broad band because the Bloch frequency changes continuously throughout each burst since the force on the electron varies with its position in the acoustic wave. The series of abrupt jumps (arrowed in figure 4.5(a)) between Bloch oscillation bursts generates the low-frequency ($\omega \lesssim 0.3 \times 10^{13}$ rad s⁻¹) peaks in $S(\omega)$ and their harmonics. These peaks shift abruptly to lower ω as U increases (most easily seen for $\omega \lesssim 10^{13}$ rad s⁻¹). Two distinct series of jumps, each with a period of ≈ 1.7 meV, occur at U values marked by the solid and dashed white lines in Fig. 4.6(a). Their origin can be understood by considering figure 4.5(b). As U increases, the upper dotted line moves upwards through the $E'(p_x)$ curve. At the U values marked by the solid white lines in figure 4.6(a), the upper dotted line in figure 4.5(b) passes above a local maximum in $E'(p_x)$. This enables the electron to enter a new minizone, so adding an additional Bloch oscillation to each burst (within brackets in figure 4.5(a)). As a result, the repeat frequency of the bursts decreases abruptly, thus red-shifting the corresponding spectral peaks in $S(\omega)$. Similar shifts occur at U values marked by the dashed white lines in figure 4.6(a), when the lower dotted line in figure 4.5(b) passes below a local minimum in $E'(p_x)$.

4.2.5 Analysis of drift velocity

Knowing the form and underlying physics of the electron trajectories, we can now better understand the shape of the $v_d(U)$ curves shown in figure 4.3. In the limit that $U \rightarrow 0$, $\omega_R \propto U^{1/2} \rightarrow 0$, which means that the electron scatters when $x' \approx 0$

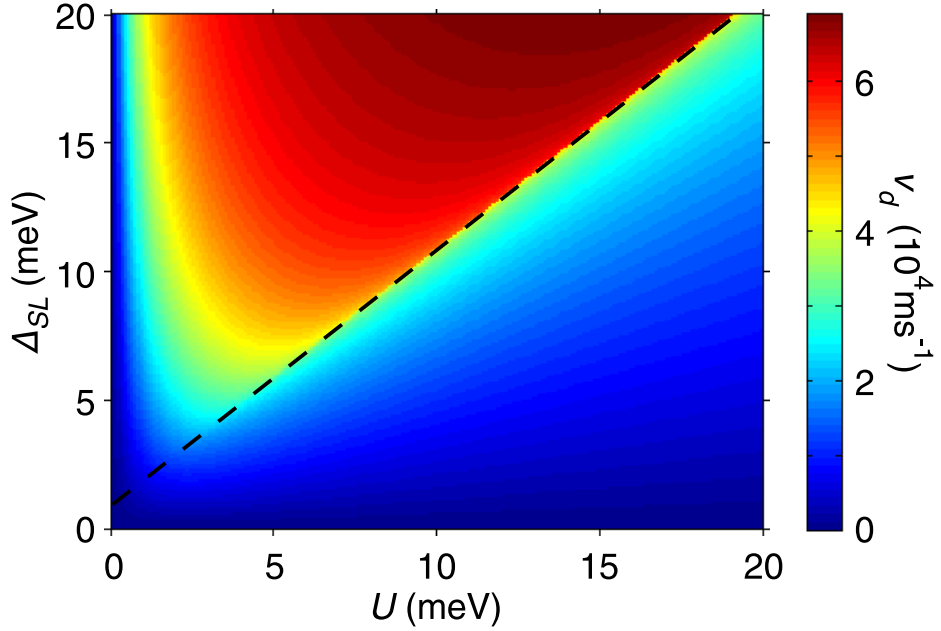


Figure 4.7: Colour map of v_d versus U and Δ_{SL} . Dashed line shows U_c versus Δ_{SL} . $\omega_S = 4 \times 10^{11}$ rad s $^{-1}$.

and will experience an almost constant force equal to $k_S U$. Consequently, in figure 4.3, the v_d curve for the acoustic wave (solid line) converges to the Esaki-Tsu curve (dashed line) for an electron accelerated by a constant electric field, $k_S U/e$. The two curves also converge when $U \gg U_c$ since in this region most Bloch oscillations created by the acoustic wave occur near $x' = 0$, where the force is almost constant. Since $U_c > U_{ET}$ (see figure 4.3) the v_d curve produced by the acoustic wave overshoots that generated by a static force and so causes far higher peak drift velocity and also maximal negative differential velocity, D_V .

Figure 4.7 shows a colour map of v_d calculated versus U and Δ_{SL} . When $U = U_c \approx \Delta_{SL}$ (dashed line), v_d decreases abruptly due to the sudden onset of Bloch oscillations. Figure 4.7 reveals that the velocity overshoot and, hence, D_V , both increase rapidly with increasing Δ_{SL} . When $\Delta_{SL} = 20$ meV, $D_V \approx 60$ times higher than produced by a static force.

We can make an estimate of the maximum possible drift velocity attained by the electron by considering the sinusoidal approximation for $x(t)$ in the wave dragging regime. Therefore by differentiating equation (4.24) and substituting the result into the drift velocity equation (4.10), we find

4.2 Semiclassical mechanics of an electron in a superlattice driven by an acoustic wave

$$v_d = \frac{1}{\tau} \int_0^\infty \left(v_S + \frac{\lambda_S \omega_R}{4} \sin(\omega_R t) \right) e^{-t/\tau} dt, \quad (4.44)$$

which can be separated to find

$$v_d = \frac{v_S}{\tau} \int_0^\infty e^{-t/\tau} dt + \frac{\lambda_S \omega_R}{4\tau} \int_0^\infty \sin(\omega_R t) e^{-t/\tau} dt. \quad (4.45)$$

Then, by integrating equation (4.45), we find that

$$v_d^S = v_S + \frac{\lambda_S}{4} \left(\frac{\tau \omega_R^2}{\tau^2 \omega_R^2 + 1} \right). \quad (4.46)$$

This result is, unsurprisingly, similar to the Esaki-Tsu expression for the drift velocity (equation (1.57)) induced by a static field, F . This correspondence becomes clear when we note that the Esaki-Tsu equation can be rewritten as

$$v_d^B = \frac{A_B}{2} \left(\frac{\tau \omega_B^2}{\tau^2 \omega_B^2 + 1} \right) \quad (4.47)$$

where $A_B = \Delta_{SL}/eF$ is the magnitude of the induced Bloch oscillations. Therefore, the drift velocity of a Bloch oscillating electron at frequency ω_B and magnitude A_B corresponds to that calculated for an electron oscillating in the acoustic wave potential at frequency ω_R and magnitude $\lambda_S/2$. Note, though, that the additional term, v_S , in equation (4.46) enhances the acoustic wave-induced drift velocity. It should be noted that although there is clear correspondence between v_d^B and v_d^S , the amplitude of the Bloch oscillations depends inversely on the frequency of the Bloch oscillations, causing v_d^B to decrease as F increases. By contrast the amplitude of the oscillations derived from v_d^S is independent of ω_R and therefore does not reflect the drift velocity characteristics seen in figure 4.3. This is expected since v_d^S is only calculated in the wave dragging regime. It is possible to make a analytical estimate of the maximum possible drift velocity for the electron, $\max(v_d^S)$, in the wave dragging regime by noting from figure 4.3, that $\max(v_d^S)$ occurs when $U \approx U_c$. Therefore substituting U_c into equation (4.40), we find

$$\omega_R(U_c) = \omega_S \left(\frac{U_c \Delta_{SL}}{\pi} \right)^{1/2} \frac{d_{SL}}{\hbar v_S}. \quad (4.48)$$

Then substituting $\omega_R(U_c)$ into equation (4.46) we find the following expression for $\max(v_d^S)$

$$\max(v_d^S) = \frac{(2d_{SL}^2 \Delta_{SL} \tau^2 v_S \omega_S^2 + d^2 \Delta_{SL} \pi \tau v_S \omega_S) U_c + 2\hbar^2 \pi v_S^3}{2d_{SL}^2 \Delta_{SL} \tau^2 \omega_S^2 U_c + 2\hbar^2 \pi v_S^2}. \quad (4.49)$$

The plot in figure 4.8 shows $\max(v_d^S)$ versus Δ_{SL} , calculated numerically (solid line), and using equation (4.49) (dashed line). The analytical result compares well with the numerical result. Although equation (4.49) does overestimate the maximum drift velocity, one can understand this by referring to the Fourier analysis of electron dynamics. In figure 4.6(a), it is clear that close to the transition between the wave dragging and Bloch oscillation regimes, ω_R starts to dip as the electron starts to oscillate in the non-parabolic part of the dispersion curve and thus slows down. This effect is not considered in the estimate of ω_R in equation (4.40), where we assume that the electron always oscillates sinusoidally when $U < U_c$ (see equation (4.24)). This results in the continuous overestimate of the drift velocity shown in figure 4.8. The estimate does show, however, that for a given d_{SL} there is an optimum Δ_{SL} beyond which one does not significantly increase $\max(v_d^S)$.

Note that the analysis predicts strong acoustic enhancement of the peak v_d value for all superlattices with $\omega_B \tau = \frac{k_S U d_{SL}}{\hbar} \gtrsim 1$ when $U \approx U_c$. This ensures that v_d^{max} is close to the mean speed ($\approx \alpha v_S$) that the electron attains during one traversal of the potential well within the acoustic wave (see figure 4.4), rather than the far slower speed, v_S , corresponding to motion of the well itself

4.3 Wavepacket analysis

It is possible to compare the semiclassical electron trajectories shown in sections 4.2.2 and 4.2.3 with a quantum mechanical wavepacket analysis. It is important to show that the wavepacket analysis of the system corresponds with the semiclassical trajectories since the semiclassical approximation does not take into account any effect the acoustic wave has on the band structure. The one-dimensional time-dependent Schrödinger equation (see equation (1.35) and (1.36)) for an electron wave packet, ψ , in an acoustically driven superlattice is given by

$$i\hbar \frac{\partial \psi(x, t)}{\partial t} = -\frac{\hbar^2}{2m^*} \frac{\partial^2 \psi(x, t)}{\partial x^2} + V_{SL}(x) \psi(x, t) + V_S(x, t) \psi(x, t) \quad (4.50)$$

where V_{SL} is defined by the variation in the conduction band edge of the superlattice, given in section 1.3.2, and V_S is the potential generated by the acoustic wave, see

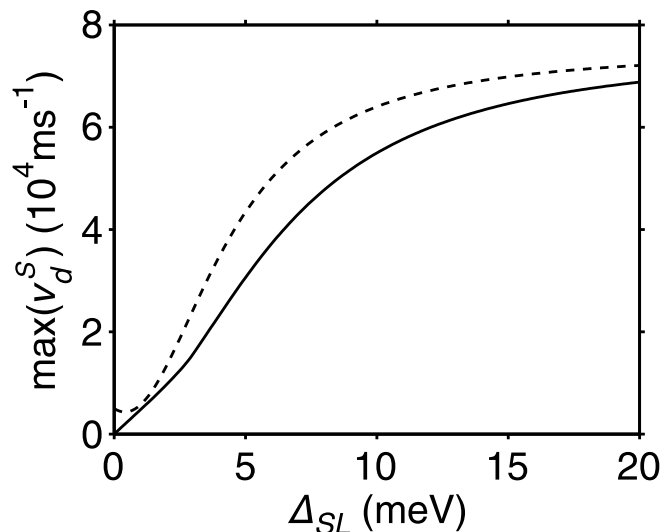


Figure 4.8: Figure showing $\max(v_d^S)$ versus Δ_{SL} calculated numerically (solid line) and analytically (dashed line).

equation (4.5). The initial wavepacket of the electron is determined using the imaginary time method outlined in section 1.3.2.2. It is clear that in the case of acoustic wave driving where the potential varies spatially as well as temporally, then the width of the initial wavepacket is important. If this is too large, then the wavepacket will extend across the acoustic wave potential well and therefore feel a wide range of forces, which is distinct from a semiclassical model with a single initial position. However, making the initial wavepacket too small will result in the electron not ‘feeling’ the band structure of the system and thus not showing any of the characteristics associated with transport in a band. Preliminary investigations revealed that an acceptable compromise between these two extremes is to set the value of the Full Width Half Maximum (FWHM) of the initial wavefunction to $2d_{SL}$, which spans enough quantum wells to allow the wavefunction to follow the band dynamics, as shown below.

The panels in figure 4.9 show the evolution of an electron wavepacket in the superlattice sample 7MEV with $\omega_S = 4 \times 10^{11} \text{ rad s}^{-1}$ corresponding to the semiclassical analysis in section 4.2. Figure 4.9(a) shows the wavepacket evolution for an electron in the wave dragging regime ($U < U_c$) with the acoustic wave amplitude $U = 4 \text{ meV}$ corresponding to the semiclassical trajectory in figure 4.4(a). It is clear that the wavepacket is periodically oscillating while being dragged through the superlattice (see red and yellow high intensity areas in the figure). The dashed curves overlaid on

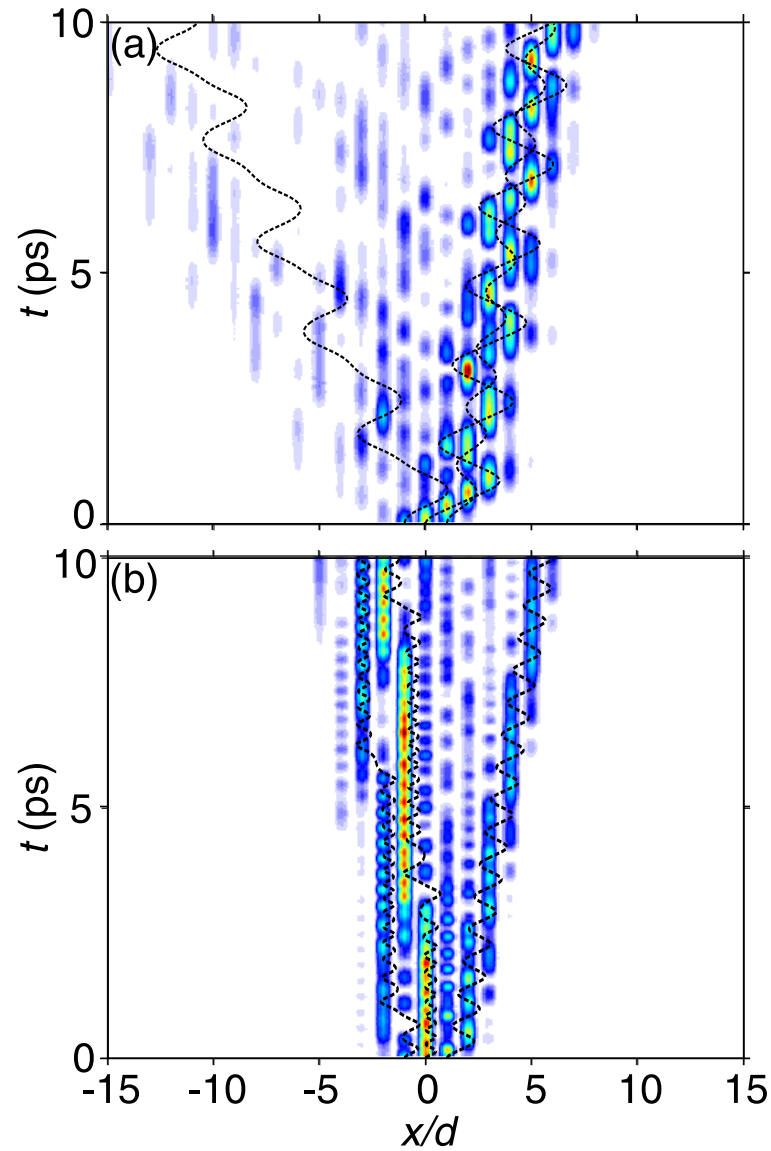


Figure 4.9: Figure showing the evolution of the electron wavepacket calculated using the time-dependent Schrödinger equation. Panel (a) is when $U = 4$ meV (see figure 4.4(a)) and panel (b) is when $U = 15$ meV. The dashed lines in both panels show semiclassical trajectories with, from left to right $x(t = 0) = -d_{SL}$, 0 and d_{SL} . In the colour map, blue represents low values, yellow middle values, and red high values.

the plot are the corresponding semiclassical trajectory when $x(t=0) = -d_{SL}$, 0 and d_{SL} , and show very good comparison with the trajectory of the wave packet. This implies that for $U < U_c$ the electron wavepacket oscillates in the periodic potential generated by the acoustic wave, and is therefore dragged through the superlattice by the wave. There are deviations between the evolution of the quantum and semiclassical trajectories though. This can be expected since in the semiclassical analysis a simplified form of the dispersion curve is used.

Figure 4.9(b) is the wavepacket evolution for $U > U_c$ for an electron in the Bloch oscillation regime with $U = 15$ meV (see figure 4.5(a)). Here the picture is not as clear as for the wave dragging regime. However, a significant fraction of the wavepacket follows the semiclassical trajectory for $x(t=0) = 0$ (central dashed line). Part of the electron wavefunction originating for $x(t=0) \lesssim -d_{SL}$ are also Bloch oscillating with jumps in the negative direction and have the same characteristics as the semiclassical trajectory. However, part of the wave function seen for $x \gtrsim 0$ is not Bloch oscillating and is instead being dragged through the superlattice, and confined within one potential well in the acoustic wave.

We can understand this behaviour when the effect of the phase of the acoustic wave is considered. In the previous, semiclassical, analysis the electron trajectory was treated as a point charge whereas, of course, in the quantum analysis the electron's wavefunction is spatially extended. Therefore it is necessary to consider the initial conditions of the electron (or the phase of the acoustic wave) on its trajectory. Due to the spatial variation of the acoustic wave, different parts of the wavefunction experience different driving forces resulting in the mixed dynamical regimes seen in figure 4.9. This is highlighted when semiclassical trajectories corresponding to electron trajectories starting with $x(t=0) = -d_{SL}$, 0, and d_{SL} (trajectories starting from left to right respectively in figure 4.9) are overlaid. The envelope of these trajectories are in very good correspondence with the dynamics of the wavepacket. Since it is clear from figure 4.9 that the phase of the acoustic wave is very influential on the electron dynamics we now expand the previous analysis to include both the phase of the acoustic wave and the initial position of the electron.

4.3.1 The effect of phase

It is important to consider the effect of phase on the nature of the trajectories of the electron. In the previous analysis of the semiclassical trajectories, we assumed that the

electron started from rest and at $x = 0$, where the potential energy $V_S(x(t = 0)) = 0$. In the following section, we consider the effect of including a phase shift in the range $-\pi < \phi < \pi$ to the acoustic wave potential and also a change in the initial position of the electron so that,

$$V_S(x, t) = -U \sin(k_S x - \omega_S t + \phi). \quad (4.51)$$

Therefore, in the moving reference frame, where $x' = x - v_S t$, the acoustic wave potential becomes

$$V_S(x') = -U \sin(k_S x' + \phi). \quad (4.52)$$

Consequently, the corresponding Hamiltonian of the system in the moving frame of the acoustic wave (see equation (4.18)) is

$$\mathcal{H}' = E'(p_x) - U \sin(k_S x' + \phi) \quad (4.53)$$

where $E'(p_x)$ is the modified dispersion curve, see equation (4.19). Consequently, at $t = 0$, the Hamiltonian in the moving frame $\mathcal{H}'(x', p_x, \phi)$ equates to

$$\mathcal{H}' = \underbrace{E'(p_x(t = 0))}_{=0} - U \sin(k_S x_0 + \phi) = -U \sin(k_S x_0 + \phi). \quad (4.54)$$

where x_0 is the value of x at $t = 0$. Since \mathcal{H}' is a constant of motion then $\mathcal{H}' = -U \sin(k_S x_0 + \phi)$ for all t , thus

$$E'(p_x) + V_S(x') = -U \sin(k_S x_0 + \phi). \quad (4.55)$$

Previously, we showed that for the electron to Bloch oscillate it must attain enough kinetic energy to traverse the first local maxima in the $E'(p_x)$ curve (see arrow in figure 4.4(b)), which occurs when $E'(p_x) \approx \Delta_{SL} - v_S \hbar \pi / d_{SL}$ (see equation (4.28)). Therefore in the Bloch oscillation regime we must have

$$\Delta_{SL} - v_S \frac{\hbar \pi}{d_{SL}} \leq -U \sin(k_S x_0 + \phi) - V_S(x', x_0, \phi). \quad (4.56)$$

The right hand side of this equation is maximal when

$$V_S = -U \sin(k_S(x + x_0) - \omega_S t + \phi) = -U. \quad (4.57)$$

Therefore substituting this condition into equation (4.56), we find that the inequality in equation (4.56) is satisfied at, or above, a critical value of $U = U_c(x_0, \phi)$ given by

$$U_c(x_0, \phi) \approx \frac{1}{1 - \sin(k_S x_0 + \phi)} \left(\Delta_{SL} - \frac{v_S \hbar \pi}{d_{SL}} \right). \quad (4.58)$$

For $U < U_c(x_0, \phi)$, the electron is in the wave dragging regime and for $U \geq U_c(x_0, \phi)$ the electron is allowed to perform Bloch-like oscillations. This has some interesting implications for the electron dynamics, as we discuss below.

We first assume that $x_0 = 0$ as before. In this case, as ϕ approaches $\pi/2$ then $U_c \rightarrow \infty$ implying that when $\phi = \pi/2$ the electron can never perform Bloch oscillations. Also, choosing $\phi < 0$ lowers the value of $U_c(\phi)$, allowing Bloch oscillations at a lower energy than when $\phi = 0$.

We can also consider the effect of a non-zero initial position ($x_0 \neq 0$) on U_c when $\phi = 0$. This is an important consideration for understanding the dynamics of the wavepacket, which spreads over a range of x . Figure 4.10(a) shows the variation of U_c with the initial position of the electron, x_0 . Increasing x_0 from 0 to $\lambda_S/4$ (i.e. increasing $k_S x_0$ from 0 to $\pi/2$) results in an exponential growth of U_c until, at $x_0 = \lambda_S/4$, $U_c(x_0, \phi) \rightarrow \infty$. This can be qualitatively understood by comparing the corresponding variation of $\mathcal{H}'(x_0, t = 0)$ (from equation (4.54)), shown as the dashed line in figure 4.10(a). As x_0 increases from 0, $\mathcal{H}'(t = 0)$ decreases until, when $x_0 = \lambda_S/4$, it reaches its minimum value of $-U$, at which point $E'(p_x)$ must be zero for all t and thus the electron can't perform Bloch oscillations and remains at rest in the rest frame of the acoustic wave. Conversely, by decreasing x_0 from 0 to $-\lambda_S/4$, the value of \mathcal{H}' increases, attaining a maximum value, U , when $x_0 = -\lambda_S/4$. For this x_0 value, U_c is decreased to half its value when $x_0 = 0$.

Figure 4.10(b), shows the electron drift velocity calculated versus U and x_0 for $\phi = 0$, with the dashed line in the figure showing when $U = U_c(x_0)$. Firstly it is important to note that, as expected, the drift velocity characteristics are periodic as a function of x_0 , with the wavelength of the acoustic wave.

We first consider the case when $x_0 = 0$, corresponding to the drift velocity curve shown in figure 4.3. Increasing U from 0 results in an increase in drift velocity in the wave dragging regime (see section 4.2.5) until $U = U_c$ (dashed line) where there is a sharp suppression in v_d (red to yellow regions in the panel) when the electron enters the Bloch regime. This general behaviour is seen for $-\lambda_S/4 \lesssim x_0 \lesssim \lambda_S/8$ where the

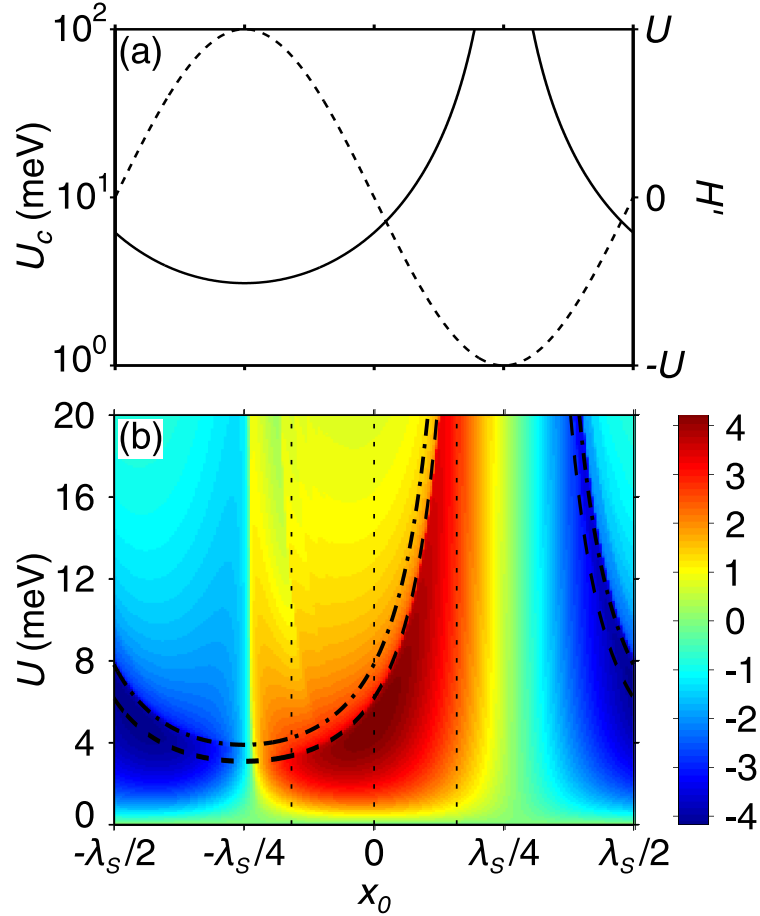


Figure 4.10: Figure showing the effect of changing x_0 on the semiclassical dynamics ($\phi = 0$). In panel (a), the solid line shows the variation of $U_c(x_0)$, and the dashed line is the variation of \mathcal{H}' with x_0 . Panel (b) is a colour map showing the variation of electron drift velocity with U and x_0 . The dashed line shows $U_c(x_0, \phi = 0)$ and the dot-dashed line shows $U'_c(x_0, \phi = 0)$. Vertical dashed lines show when $x_0 = -d_{SL}$, 0 and d_{SL} .

value of U at the suppression of drift velocity corresponds well with U_c , suggesting a transition between the wave dragging and Bloch oscillating regimes.

For $\lambda_S/8 \lesssim x_0 \lesssim 3\lambda_S/8$ the transition to the Bloch from the wave dragging regime occurs beyond the range of U that is experimentally accessible, and there is no associated suppression of v_d in figure 4.10(b). Therefore, in this range, $v_d(U)$ is approximately constant. However, for a given, constant, U we find that increasing x_0 results in a gradual decrease in drift velocity. We understand this by considering the range of possible values of $E'(p_x)$ given (from equation (4.55)) by

$$E'(p_x) = \pm U - U \sin(k_S x_0) \quad (4.59)$$

This implies that increasing x_0 from 0 to $\lambda_S/4$ decreases the maximum attainable value of $E'(p_x)$ (dashed line in figure 4.4(b)). Therefore the electron can no longer access the high gradient regions of $E'(p_x)$ where the magnitude of $v'_x = dE'(p_x)/p_x$ is high. v'_x continues to decrease as x_0 increases until $x_0 \approx \lambda_S/4$ at which point equation (4.59) shows that the maximum value of $E'(p_x) = 0$. The electron cannot oscillate in the potential well and is simply dragged through the lattice, consequently, here, $v_d \approx v_S$.

Increasing x_0 past $\lambda_S/4$ we find the initial force on the electron,

$$-\frac{dV_S(t=0)}{dx} = k_S U \cos(k_S x_0), \quad (4.60)$$

becomes negative. The electron is therefore initially forced in the negative direction in p_x where the gradient of $E'(p_x)$ and also v'_x is negative (see figure 4.4(b)). The electron drift velocity therefore becomes increasingly negative as it starts to access the high (negative) gradient regions of $E'(p_x)$ (see equation (4.59)).

When $x_0 \approx \lambda_S/2$, increasing U from 0 we find that the electron drift velocity initially decreases. However, its magnitude is dramatically suppressed at some critical value of $U = U'_c(x_0, \phi)$, which we find to be close to $U_c(x_0, \phi)$. We might expect that the suppression of drift velocity would occur *exactly* at the transition from dragging trajectories to Bloch trajectories, as seen for the regions where the initial force is positive (see equation (4.60)). However, for $x_0 \approx \lambda_S/2$, the electron is initially forced in the negative direction in momentum space (see equation (4.60)). Therefore, for $U \approx U_c(\phi, x_0)$, the electron is scattered before it can traverse the local maximum in $E'(p_x)$ (arrowed in figure 4.4(b)). Consequently, the transition to the Bloch regime for $x_0 \approx \lambda_S/2$, does not have a signature in the drift velocity curve at $U = U_c$.

Instead the suppression of $|v_d|$ occurs at a value of U slightly larger than U_c . In fact, we find that the suppression of drift velocity in this regime occurs when the electron can Bragg reflect by traversing the local maximum to the left of the origin, i.e. when $E(p_x) = \Delta_{SL} + v_S \hbar \pi / d_{SL}$. Using this condition with the analysis shown in equation (4.56) we find that

$$U'_c(x_0, \phi) \approx \frac{1}{1 - \sin(k_S x_0 + \phi)} \left(\Delta_{SL} + \frac{v_S \hbar \pi}{d_{SL}} \right). \quad (4.61)$$

This is plotted in figure 4.10(b) as a dot-dashed line, and shows good correspondence with the dramatic suppression of $|v_d|$ when $x_0 = \lambda_S/2$. Therefore, when $-\lambda_S/4 \lesssim x_0 \lesssim \lambda_S/4$ and the initial force is positive (see equation (4.60)), $U_c(x_0, \phi)$ is a good estimate for the suppression of v_d . However, when $\lambda_S/4 \lesssim x_0 \lesssim \lambda_S/2$ and $-\lambda_S/2 \lesssim x_0 \lesssim -\lambda_S/4$, then $U'_c(x_0, \phi)$ is a good estimate of the position of v_d suppression. Note that, interestingly, there is a discontinuity between the validity of these conditions when $x_0 = -\lambda_S/4$ and $x_0 = \lambda_S/4$ where the initial force is 0 and the drift velocity is minimal.

The phase dependence of the semiclassical trajectories also has some important consequences for the dynamics of the wave function. In the calculations presented in figure 4.9, the initial wavefunction has a FWHM of $2d_{SL}$. Therefore the peaks in $|\psi(x)|^2$ occur when $x_0 = -d_{SL}$, $x_0 = 0$, and $x_0 = d_{SL}$ (vertical dashed lines in figure 4.10) and the majority of the wavepacket lies within the range $-1.5d_{SL} < x_0 < 1.5d_{SL}$.

Using equation (4.58) we find when $x_0 = -d_{SL}$, $U_c = 3.4$ meV, when $x_0 = 0$ then $U_c = 6.2$ meV and when $x_0 = d_{SL}$ then $U_c = 39$ meV. Figure 4.9(a) shows the evolution of the wavepacket when $U = 4$ meV. In this case most of the spread of the wavefunction (on the right-hand side of the figure) lies within the wave dragging regime. Consequently, we see that most of the wavefunction is indeed dragged through the lattice. Some Bloch oscillations are, however, visible in the left hand side of the figure where $U > U_c(x_0)$.

In contrast, figure 4.9(b) shows the evolution of the same wave packet when $U = 15$ meV. Now all parts of the initial wavepacket with $x_0 \lesssim 7.9$ nm ($\approx 0.6d_{SL}$) i.e. the majority, are allowed to perform Bloch oscillations. This is demonstrated in figure 4.9(b) where most of the wavefunction can perform Bloch oscillations, although a significant fraction is still dragged through the lattice.

This analysis implies that the entire electron wavepacket will be dragged through the lattice when $U \lesssim 3.1$ meV. Thereafter, increasing U results in a *gradual* turn-on

of Bloch oscillations in the wave packet. This is in contrast to the abrupt transition seen in the single electron, semiclassical, analysis, as we show in the next section.

4.3.2 Quantum mechanical electron dynamics and transport

To analyse the wavepacket evolution, we calculate the expectation value of the electron's position along the x -axis:

$$\langle x \rangle = \frac{\int_{-\infty}^{\infty} \Psi^* x \Psi dx}{\int_{-\infty}^{\infty} \Psi^* \Psi dx}. \quad (4.62)$$

Figure 4.11(a,b) shows the variation of $\langle x \rangle$ with time corresponding to the probability density evolutions shown in figure 4.9(a,b). Immediately, it is apparent that the $\langle x \rangle$ versus t curves are significantly different from the corresponding semiclassical trajectories shown in figures 4.4(a) and 4.5(b). Generally, the $\langle x \rangle$ versus t curves represent an average of the semiclassical trajectories with different initial positions. When $U = 4$ meV (figure 4.11(a)) the spread of x_0 is sufficient to span both the dragging and Bloch oscillation regimes, as discussed in section 4.3.1. Consequently, although the wavepacket is still dragged through the lattice, transport is partially suppressed as different parts of the wavepacket oscillate out of phase. In addition, transport is suppressed by the Bloch oscillating region of the wavepacket moving in the opposite (negative) direction (see semiclassical trajectories with $x_0 = -d_{SL}, 0$ and d_{SL} in figure 4.9(a)). We also find that the oscillations in $\langle x \rangle$ versus t are not as sinusoidal as for the semiclassical orbit in figure 4.4(a), although they are approximately periodic.

By comparison, when $U = 15$ meV (figure 4.11(b)) $\langle x \rangle$ versus t is closer to the corresponding semiclassical trajectory. Again, compared with the semiclassical orbits, $\langle x \rangle$ versus t are less periodic (see figure 4.5(b)). This is because although the initial conditions corresponding to the electron wavepacket mostly lie in the Bloch oscillation regime, the quantum electron drifts more slowly in the negative direction since a significant part of the wavepacket is dragged through the lattice by the acoustic wave.

Electron transport through the lattice can be quantified in the quantum regime by differentiating $\langle x \rangle$ to find $\langle \dot{x} \rangle$, and adapting the semiclassical drift velocity formula given in equation (4.10) to give

$$v_d = \frac{1}{\tau} \int_0^{\infty} \langle \dot{x} \rangle \exp(-t/\tau) dt. \quad (4.63)$$

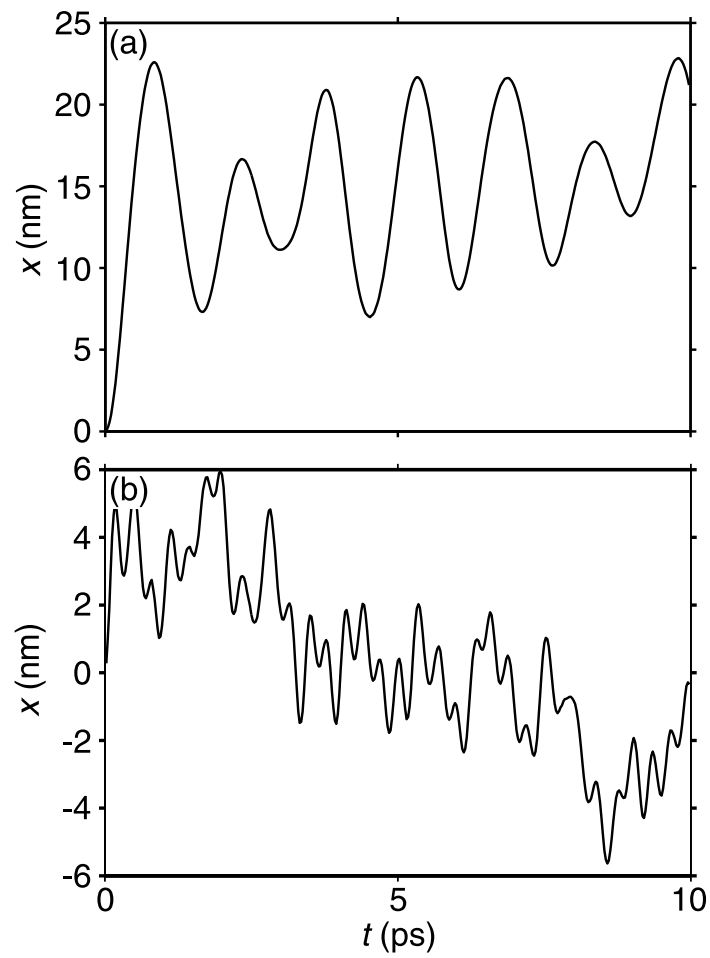


Figure 4.11: Figure showing $\langle x \rangle$ versus t corresponding to the wavepacket evolution shown in figure 4.9 when $U = 4$ meV, (a) and 15 meV (b).

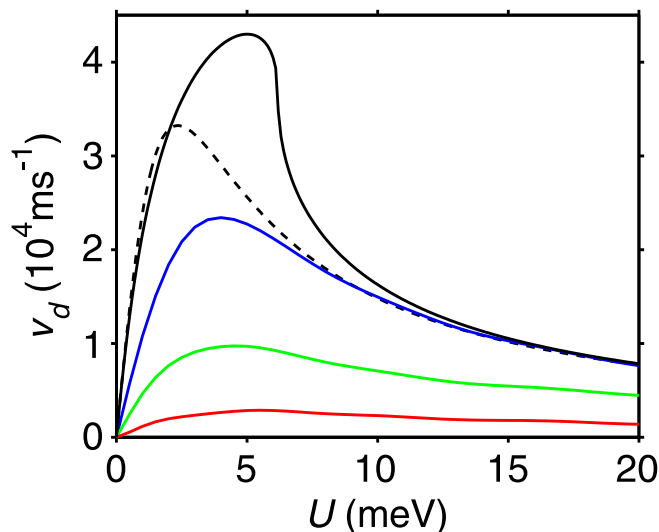


Figure 4.12: Drift velocity versus U characteristics. Blue, yellow and red curves show drift velocity calculated using the quantum mechanical analysis (equation (4.62)) where $f_x = 2d_{SL}$, $4d_{SL}$ and $6d_{SL}$ respectively. Black solid curve shows semiclassical drift velocity and the dashed black curve is the Esaki-Tsu curve (see section 4.2.1).

Figure 4.12 compares the drift velocity, versus U curve calculated from the quantum trajectories and using the semiclassical technique introduced in section 4.2.1. The blue curve is the drift velocity calculated using the trajectories in figure 4.11 corresponding to an initial Gaussian with $f_x = 2d_{SL}$. This curve has a smaller peak value and less pronounced negative differential velocity than the corresponding semiclassical case (black curve in figure 4.12). The peak drift velocity falls because Bloch oscillations are induced in the wavepacket (see figure 4.9) suppressing $\langle x \rangle$. This general smoothing of the $v_d(U)$ curve in the quantum regime occurs because the spread of the initial wavefunction blurs the two different dynamical regimes, making the turn on of Bloch oscillations and the consequent suppression of v_d much more gradual. Increasing the initial spread to $f_x = 4d_{SL}$ (yellow curve in figure 4.12) further reduces the peak $v_d(U)$ value and negative differential velocity. When $f_x = 6d_{SL}$ (red curve in figure 4.12) the wave dragging and Bloch oscillation parts of the trajectory effectively cancel each other out, killing significant electron transport.

These results suggest that the high peak v_d and associated high negative differential velocity seen in the semiclassical case are strongly suppressed in a quantum picture. However, in the following section we consider the collective transport of

charge in an acoustically driven superlattice and show that interesting effects occur even when a spread of electron trajectories is considered.

4.4 Charge dynamics

In this section we show the effect of the single particle dynamics, presented previously in this chapter, on the collective dynamics of electrons in the acoustically driven superlattice. To do this we further develop the model of charge dynamics derived in chapter 3. Again we discretise the superlattice into $N = 480$ layers, where the number density of electrons in the m^{th} layer is n_m and the electric field values at the left hand and right hand edge of the layer are F_m and F_{m+1} respectively (see section 3.1 for further details). The time evolution of n_m is determined by the following charge continuity equation

$$e\Delta x \frac{dn_m}{dt} = J_{m-1} - J_m, \quad m = 1 \dots N, \quad (4.64)$$

and the field values are determined by the discretised version of Poisson's equation (see equation (3.8))

$$F_{m+1} = \frac{e\Delta x}{\varepsilon_0\varepsilon_r} (n_m - n_D) + F_m, \quad m = 1 \dots N. \quad (4.65)$$

All symbols have the same meaning as those introduced in section 3.1. Here, we wish to investigate the effect of acoustic driving only (with no bias voltage applied). Since we have no constant driving force it is important here to include the diffusion of electrons (i.e. transport of electrons from regions of high charge density to low charge density)¹. Therefore we modify the equation for current density, first used in equation (3.2), to

$$J_m = en_m v_d^m(V_S) - eD_E \frac{\partial n_m}{\partial x} \quad m = 1 \dots N, \quad (4.66)$$

where D_E is a field-independent diffusion term which is calculated from the Einstein relation [100] given by

$$D_E = \frac{\mu k_B T}{e}. \quad (4.67)$$

¹In the model discussed in chapter 3, where a constant voltage is applied, we were able to neglect diffusion since, empirically, we found it to have little effect on the domain dynamics [37].

In the Einstein relation μ is the low field mobility, k_B is Boltzmann's constant, and $T = 4\text{K}$ is the temperature. The mobility is given by the ratio of the electron's terminal drift velocity with the corresponding applied force

$$\mu = \frac{v_p}{F_c} \quad (4.68)$$

where $v_p \approx 6 \times 10^3 \text{ m s}^{-1}$ is the peak drift velocity in the Esaki-Tsu curve and $F_c \approx 5 \times 10^5 \text{ V m}^{-1}$ is the field at the peak [2; 32]. The drift velocity of the electrons in each layer is determined from the following semiclassical Hamilton's equations of motion, which depend on the average field in each layer, \overline{F}_m , (see equation (3.7)), the position of the layer in the lattice $x_m = m\Delta x$, and the charge dynamics simulation time t ,

$$\frac{\partial p_x}{\partial t'} = Uk_S \cos(k_S(x + x_m) - \omega_S(t' + t)) + e\overline{F}_m, \quad (4.69)$$

$$\frac{\partial x}{\partial t'} = \frac{\Delta_{SL}d_{SL}}{2\hbar} \sin\left(\frac{p_x d_{SL}}{\hbar}\right). \quad (4.70)$$

where t' is the single electron dynamics simulation time. These equations are numerically solved to obtain $v_x(t')$, from which we determine the drift velocity¹ using the standard Esaki-Tsu formalism

$$v_d^m(t) = \frac{\delta}{\tau} \int_0^\infty v_x(U, \overline{F}_m, x_m, t) e^{-t'/\tau} dt'. \quad (4.71)$$

The boundary conditions and parameters of the system are the same as those derived in section 3.1. The global current density in the superlattice layers can be found using

$$J(t) = \frac{1}{(N+1)} \sum_{m=0}^N J_m. \quad (4.72)$$

and the current is given by

$$I(t) = J(t)A. \quad (4.73)$$

In the results presented in the following sections, we calculate the charge dynamics for a range of U , taking $\omega_S = 4 \times 10^{11} \text{ rad s}^{-1}$ as in the single particle analysis.

¹Note that the scattering time, τ , is less than the characteristic time scale of the domain dynamics allowing us to assign a local drift velocity.

4.4.1 Current versus acoustic wave amplitude, $I(U)$, curve

The plots in figure 4.13(a) show the variation of the current (found from equation (4.73)) in the superlattice with the amplitude of the acoustic wave potential, U . The upper and lower solid lines in 4.13(a) show, respectively, the maximum, I_{max} , and minimum current, I_{min} , for a given U , and therefore indicate the range of values that $I(t)$ oscillates between. The dashed line shows the time averaged current, I_{ave} . Immediately it is apparent that the acoustic wave can induce a current in a superlattice, although the shape of the curve is quite different from that found with a constant bias applied (see figure 3.2). Remarkably, we find that even at low acoustic wave amplitudes there are significant current oscillations. As U increases from 0 to 4 meV, the magnitudes of I_{max} and I_{min} initially increase, with I_{max} attaining a maximum value of ≈ 7.4 mA when $U \approx 4$ meV and I_{min} having a minimum value of ≈ -5.8 mA when $U = 2$ meV. The magnitudes of both I_{max} and I_{min} decrease as U increases beyond 4 meV.

In figure 4.13(b), we show, versus U , $I_a = I_{max} - I_{min}$, which illustrates the magnitude of the current oscillations. This curve resembles the Esaki-Tsu curve since the magnitude of the current oscillations, I_a , initially increases with increasing U until it reaches a maximum of ≈ 11.6 mA when $U \approx 3$ meV and thereafter decreases with increasing U .

The general $I(U)$ characteristics can be understood within our single particle analysis. We found in section 4.3.1 that all electrons follow dragged orbits when $U \lesssim 3.1$ meV. Consequently, increasing U within this regime also increases their drift velocity (see figure 4.3) thereby increasing the magnitude of the current oscillations since $I \propto v_d$. Beyond this critical value of U , Bloch oscillations gradually turn on, initially for electron trajectories starting at the maximum of the acoustic wave potential, but eventually for the majority of electron trajectories, thus suppressing the current oscillations.

4.4.2 $I(t)$ curves

In this section we present and analyse the $I(t)$ curves that underlie the $I(U)$ curves in figure 4.13. Figure 4.14(a) shows the $I(t)$ curve calculated for $U = 1$ meV, well below the peak in I_a , where all of the electrons are within the wave dragging regime (see also figure 4.4(a)). The current oscillations are regular and almost cosinusoidal.

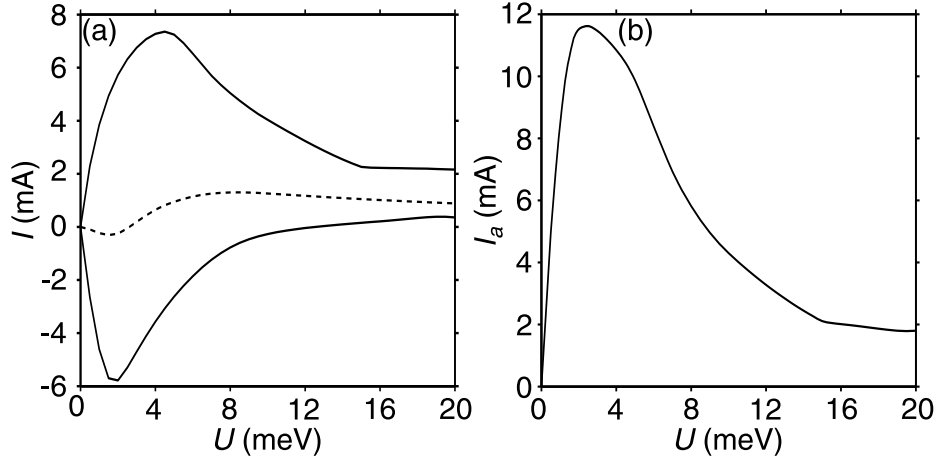


Figure 4.13: (a) Upper [lower] curves shows I_{max} [I_{min}] versus U . Dashed line shows the time averaged current, I_{ave} . (b) variation of $I_a = I_{max} - I_{min}$ with U .

Also, the oscillations appear to be quite smooth in comparison with the ‘spiky’ nature of the current oscillations in the biased superlattice (see figure 3.3).

Figure 4.14(b) shows $I(t)$ calculated when $U = 4$ meV just beyond the peak in I_a (see also figure 4.4(a)). As shown in figure 4.10, when $U = 4$ meV, for some initial conditions the electrons perform Bloch oscillations. However, most of the semiclassical trajectories are in the wave dragging regime. Therefore the qualitative form of the $I(t)$ oscillations is similar to the case when $U = 1$ meV except slightly less symmetrical, and of higher amplitude.

Increasing U to 15 meV causes many of the electrons to perform Bloch oscillations and so induce new features in the $I(t)$ curve (see figure 4.14(c)), in particular the kinks in the descending part of the waveform. Note, however, that the $I(t)$ oscillations are still periodic.

We also find that the frequency of the oscillations is independent of U and is equal to the frequency of the acoustic wave $\omega_S = 4 \times 10^{11}$ rad s^{-1} (≈ 63.7 GHz)

4.4.3 Spatio-temporal electron density in the superlattice

To understand the form of the $I(t)$ characteristics, we now consider the spatio-temporal evolution of electron density in the superlattice shown in figure 4.15. Panel (a) shows a colour map of $n(x, t)$ calculated when $U = 1$ meV. There are multiple high electron density accumulation regions (coloured red in the plot), which travel across the superlattice to the collector and are separated by electron depletion regions

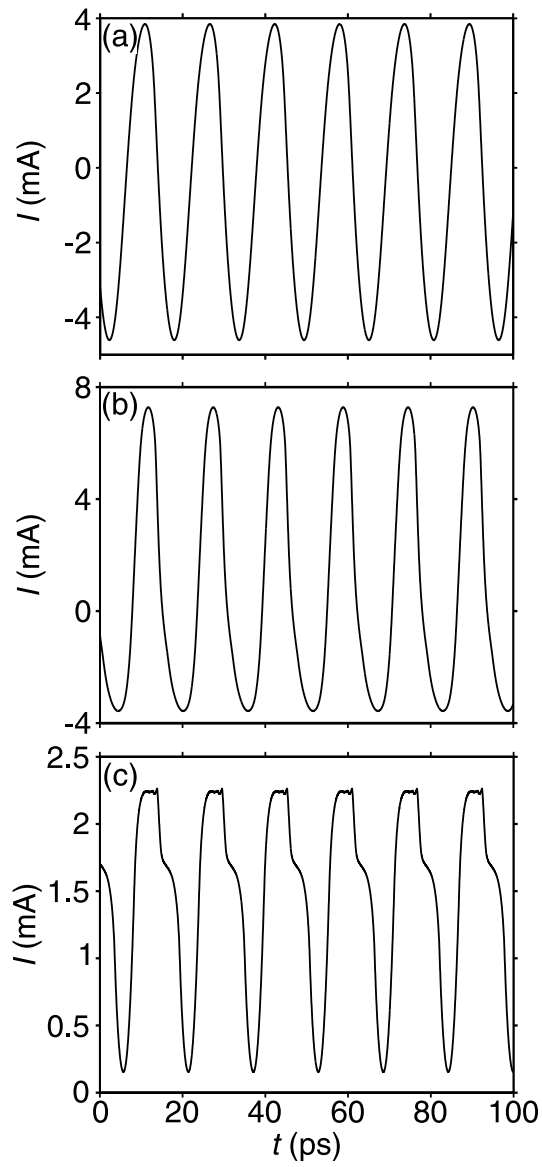


Figure 4.14: $I(t)$ oscillations calculated for $U =$ (a) 1 meV, (b) 4 meV and (c) 15 meV.

(coloured blue in the figure). Each region of charge accumulation originates at the left hand edge of the superlattice layers and travels at almost constant speed across the superlattice. When it reaches the right hand edge of the superlattice it produces a peak in the $I(t)$ curve. The solid curve in figure 4.15(b) is the cross section of the $n(x, t)$ surface along the vertical dotted line in figure 4.15(a) ($t = 35$ ps) when $U = 1$ meV. The dashed curve in figure 4.15(b) shows the corresponding form of V_S . The acoustic wave creates an accumulation of charge (solid arrows in figure 4.15(b)) in the acoustic wave minima (dashed arrows in figure 4.15(b)) and electron depletion at the acoustic wave maxima. Note that this is qualitatively similar to the charge domains formed with an applied bias voltage. However, in the low U acoustic wave case, electron accumulation is driven by the spatial variance of the wave potential rather than by negative differential velocity. Since V_S is propagating through the lattice, in figure 4.15(b) the charge accumulation indicated by the right-hand solid arrow effectively shows the charge accumulation indicated by the left hand arrow at a later time. We note that the accumulation is ‘dragged’ to higher x values as the acoustic wave minima propagate through the superlattice, but with minimal change to its form. Note that since the acoustic wave is propagating through the superlattice lattice from left to right (i.e. along the positive x -direction) the accumulation regions tend to lag slightly behind the position of the local minima as the electrons ‘ride’ up the left hand side of the potential wells in the acoustic wave, due to inertia. In the low U case (figures 4.15(a) and (b)) the amount of accumulation and depletion is similar resulting in the symmetric current oscillations around 0, shown in figure 4.14(a).

Increasing U to $U = 4$ meV (figure 4.15(c)) gives similar dynamics to when $U = 1$ meV, although the regions of electron accumulation are not quite as regular. The charge density - position characteristics for $U = 4$ meV (figure 4.15(d)) are also similar to when $U = 1$ meV. To illustrate this, the solid curve in figure 4.15(d) is the cross-section of the $n(x, t)$ surface along the dotted line in figure 4.15(c), i.e. when $t = 35$ ps. Compared with figure 4.15(b), it is clear that the amount of accumulated charge has increased and there is also an extra kink-like feature in the $n(x)$ curve. The increased amount of charge in the potential well is a result of the well depth increasing. The extra feature in the $n(x)$ curve results from high negative differential velocity between electron trajectories starting in the Bloch oscillation regime and the wave dragging regime (see figure 4.10), causing a region of charge accumulation to form via a similar mechanism to that seen in chapter 3. Figure 4.15(c) reveals that the

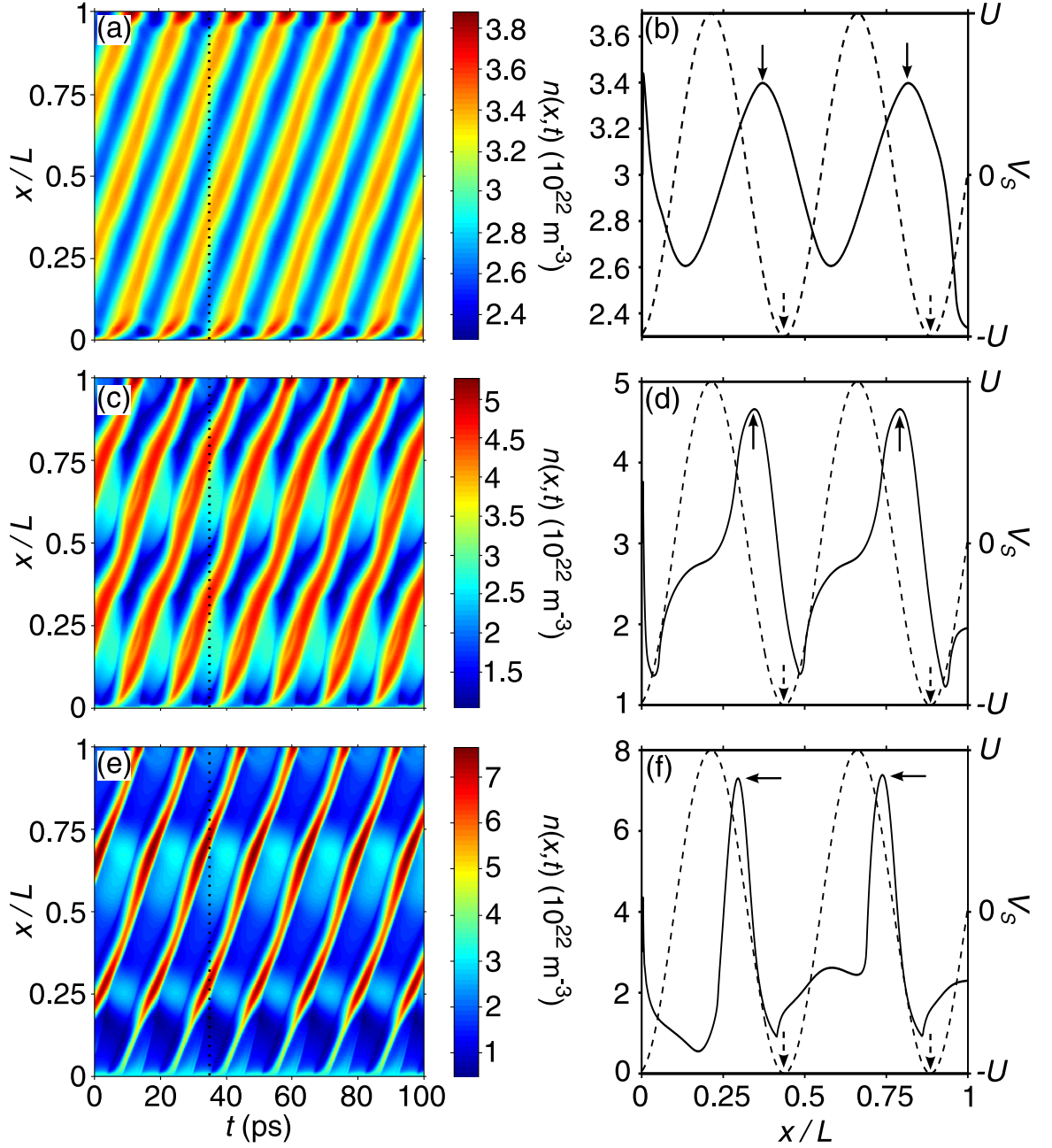


Figure 4.15: Colour surface plots (scale right) of $n(t, x)$, (a, c and e). n versus x (solid curve) and V_S versus x (dashed curve) plots when $t = 35$ ps, (b, d and f) calculated for $U = 1$ meV (a-b), 4 meV (c-d) and 15 meV (e-f). Vertical dotted lines in (a, c and e) show positions of cross sections shown in (b, d and f).

extra kink feature in $n(x)$ moves in the potential well, so producing periodic ‘ripples’ in the accumulation front as it moves through the superlattice. This is manifested in the figure by the width of the accumulation region (red) oscillating as a function of t as it propagates through the superlattice. Note, though, that this extra feature does not significantly affect the shape of the $I(t)$ curve, see figure 4.14(b).

Increasing U to 15 meV (see figure 4.15(e)) preserves the overall structure of the charge domains and dynamics. However, compared to $U = 4$ meV, the amount of charge in each (red) domain is much greater: note scale on right-hand side of panel. Also, the shape of the accumulation front is rather different, appearing spatially much narrower. These changes give rise to the different shapes of the $I(t)$ curves, shown in figure 4.14(c). The solid curves in figure 4.15(f) shows $n(x)$ at $t = 35$ ps (i.e. along the vertical dashed line in figure 4.15(e)). The accumulation front formed towards the left hand side of the superlattice (left-hand solid arrow) is much sharper than those found for smaller U because the onset of Bloch trajectories further suppresses drift velocity, thereby enhancing electron accumulation. The corresponding dramatic decrease in the local electron drift velocity induces a larger charge domain in the same way as for a static field. However, since there are more Bloch oscillating trajectories, each with a low drift velocity, the peak in the $I(t)$ curve ($I \propto v_d$) for $U = 15$ meV (figure 4.14(c)) is smaller than for lower U (figures 4.14(a) and (b)). Since a larger region of the superlattice is in the Bloch oscillating regime, the negative differential velocity-induced domains contain more electrons. This magnifies the extra kinks in $I(t)$, seen on the descending part of the waveform in figure 4.14(c), compared to when $U = 4$ meV (see figure 4.14(b)).

A new charge domain forms each time an acoustic wave minimum arrives at the left hand edge of the superlattice, which occurs at a frequency ω_S . Also, since each domain travels at the speed of sound through the superlattice, we find a new domain (and therefore a peak in $I(t)$) arriving at the right hand edge of the superlattice layers at the acoustic wave frequency.

Chapter 5

Dynamics of ultracold sodium atoms in moving optical lattices

Recently there has been increased experimental interest into the dynamics of atoms in moving optical lattices. These experiments have shown that such systems can be a useful tool for transporting atoms along distances as far as 20 cm [101]. Investigations have also revealed some interesting stochastic resonance effects [102] and band structure properties [103]. What has not yet been investigated, though, is the effect of a moving optical lattice propagating through a *stationary* optical lattice, a direct analogue of the acoustic wave propagation through semiconductor superlattices presented in chapter 4. In the following chapter we shall consider such a system and show that the interaction between the two lattices induces a large number of resonances in the transport characteristics of the atom.

5.1 Moving optical lattice

The moving optical potential is created by counter propagating laser beams whose frequencies are slightly detuned, generating a standing wave optical potential which is moving at a speed determined by the detuning. The following derivations show the resulting potential energy for the atom generated by the detuned laser beams. It was shown in chapter 1 that the addition of two counter-propagating plane waves (equations (1.64) and (1.65)) results in a stationary standing wave (see equation (1.67)). By substituting $x - v_M t$ for x , we effectively create an optical lattice, which is moving at a speed v_M along the x axis and has electric field vector

$$\epsilon_M = \frac{\epsilon_M}{2} e^{i(k(x-v_M t)-\omega t)} + \frac{\epsilon_M}{2} e^{i(-k(x-v_M t)-\omega t)} \quad (5.1)$$

where ϵ_M is the magnitude of the electric field. Making the substitution $kv_M = \delta\omega/2$ and rearranging, we find

$$\epsilon_M = \frac{\epsilon_M}{2} e^{i(kx-(\omega+\delta\omega/2)t)} + \frac{\epsilon_M}{2} e^{i(-kx-(\omega-\delta\omega/2)t)}. \quad (5.2)$$

revealing the relationship between the speed of the optical lattice with the detuning between the two laser beams to be $\delta\omega = 2kv_M$. So, by following the analysis in section 1.4, the potential that will be experienced by the atom in the moving optical lattice, $V_M(x, t)$, is

$$V_M(x, t) = \frac{U_M}{2} - \frac{U_M}{2} \sin(k_M x - \omega_M t), \quad (5.3)$$

where $k_M = 2\pi/\lambda_M$ is the wavenumber of the propagating lattice of wavelength λ_M , $\omega_M = v_M k_M$ is the frequency of the optical lattice, and U_M is the optical lattice amplitude, determined by (see equation (1.69))

$$U_M = -\frac{1}{4} \alpha'(\omega) \epsilon_M^2. \quad (5.4)$$

5.2 Semiclassical dynamics

To investigate the sodium atom dynamics in an optical lattice with an additional moving potential applied, the arguments in chapter 1 are used to derive the following one-dimensional semiclassical Hamiltonian

$$\mathcal{H} = E(p_x) + V_M(x, t), \quad (5.5)$$

where $E(p_x)$ is the dispersion relation of the optical lattice and $V_M(x, t)$ is the moving optical lattice potential. The form of $E(p_x)$ can be found by solving the time independent Schrödinger equation and can be approximated by equation (1.73), restated here for clarity

$$E(p_x) = \frac{\Delta_{OL}}{2} \left(1 - \cos \left(\frac{p_x d_{OL}}{\hbar} \right) \right), \quad (5.6)$$

where Δ_{OL} is the band width of the 1st energy band and d_{OL} is the spatial period of the optical lattice. Substituting equations (5.3) and (5.6) into the Hamiltonian, equation (5.5), gives

$$\mathcal{H} = \frac{\Delta_{OL}}{2} \left(1 - \cos \left(\frac{p_x d_{OL}}{\hbar} \right) \right) + \frac{U_M}{2} (1 - \sin(k_M x - \omega_M t)), \quad (5.7)$$

which is similar to the form of the Hamiltonian given in chapter 4 although the potential energy is always > 0 . In section 4.2.2, the system of equations was transformed into the moving frame of the acoustic wave to gain insight into the electron's trajectory. Therefore, here we make the following transformation into the frame of the propagating potential

$$x'(t) = x(t) - v_M t \quad \Rightarrow \quad \dot{x}'(t) = \dot{x}(t) - v_M. \quad (5.8)$$

In equation (4.20), the Hamiltonian was derived for a miniband electron in the frame of a propagating sound wave. Similarly the corresponding (conserved) Hamiltonian for the semiclassical atom in the frame of the propagating optical potential is given by

$$\mathcal{H}' = E'(p_x) + V_M(x'). \quad (5.9)$$

In this equation, $E'(p_x)$ is the effective dispersion relation for the sodium atom in the moving frame, given by

$$E'(p_x) = E(p_x) - v_M p_x \quad (5.10)$$

and

$$V_M(x') = \frac{U_M}{2} (1 - \sin(k_M x')). \quad (5.11)$$

Assuming that the electron has an initial position of $x(t=0) = x_0$, and starts from rest ($p_x(t=0) = 0$) then

$$\mathcal{H}' = \frac{U_M}{2} (1 - \sin(k_M x_0)) \quad (5.12)$$

for all t . This assumption allows us to make many analytical predictions of the trajectory, which are explored in the next few sections.

The equations of motion for the atom can be found using Hamilton's equations (first used in chapter 2), which, for the Hamiltonian given in equation (5.7), are

$$\frac{\partial p_x}{\partial t} = \frac{U_M}{2} k_M \cos(k_M x - \omega_M t) \quad (5.13)$$

$$\frac{\partial x}{\partial t} = \frac{\Delta_{OL} d_{OL}}{2\hbar} \sin\left(\frac{p_x d_{OL}}{\hbar}\right). \quad (5.14)$$

These equations were integrated numerically using a 4th order Runge-Kutta routine [19] to find the trajectories of the atom.

In the following analysis of this system, we use a stationary optical lattice with a band width of $\Delta_{OL} = 24.35$ peV and lattice period of $d_{OL} = 294.5$ nm taken from experiment [46]. In this optical lattice system there is great flexibility in the speed, the depth and the wavelength of the propagating potential. For example in [101], v_M was shown to vary from 0 to ~ 50 mm s⁻¹, and in [104], optical lattices with periods of ~ 20 μ m ($\sim 70d_{OL}$) have been created.

5.2.1 Time averaged velocity

In previous chapters, we calculated the electron drift velocity in order to determine the measured transport characteristics of electrons in a superlattice. However, when considering the transport of atoms in optical lattices, where the effect of scattering is negligible, it is not relevant to consider v_d . It has also been shown in recent experiments that it is possible to observe ~ 20000 Bloch oscillations with minimal disruption of the atom cloud [9]. Therefore, to gain a general overview of the dynamics of the atom we calculate its average velocity, $\langle v_x \rangle_t$, over many periods of oscillation with no scattering events. The Hamiltonian for the superlattice electron with an acoustic wave applied, and for an atom in an optical lattice with a propagating potential applied, are broadly equivalent so we expect qualitatively similar dynamics. However, the results in this chapter show that $\langle v_x \rangle_t$ reveals resonant features not relevant or apparent in the previous analysis.

Figure 5.1 shows the $\langle v_x \rangle_t$ versus U_M curve calculated for $\lambda_M = 20d_{OL}$ and $v_M = 2.5$ mm s⁻¹ corresponding to a parameter regime similar to that explored in chapter 4. In these and subsequent calculations, v_x was averaged over a time interval of 0.25 s.

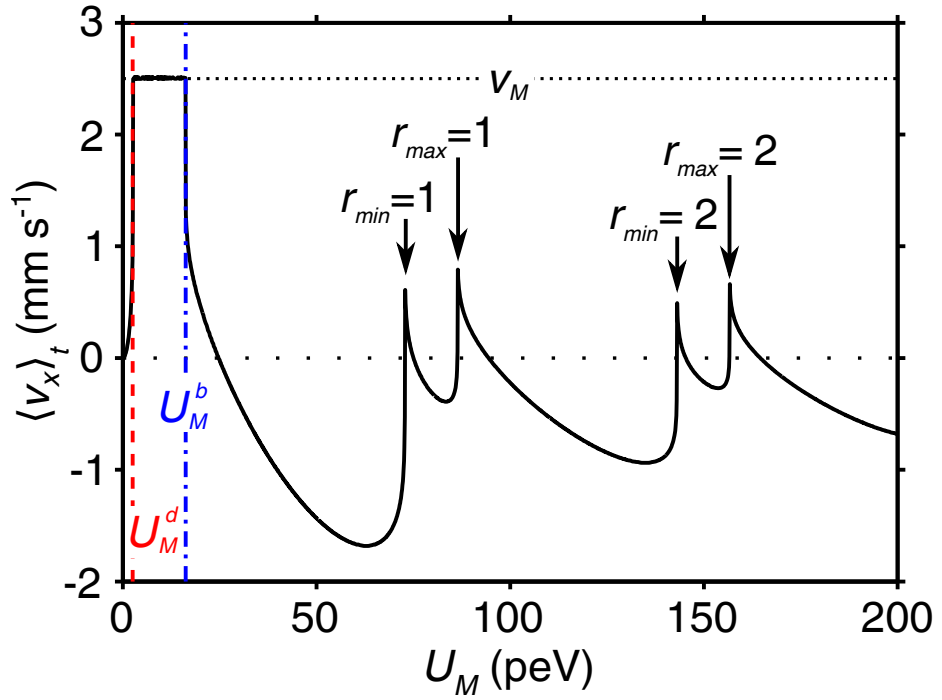


Figure 5.1: Figure showing $\langle v_x \rangle_t$ versus U_M . Vertical red dashed line (labelled U_M^d) shows the position of the onset of atom dragging. Blue dot-dash line (labelled U_M^b) marks the position of the onset of Bloch oscillations. Arrows highlight resonant peaks in $\langle v_x \rangle_t$, explained in the text. For guidance, the upper horizontal dotted line shows $\langle v_x \rangle_t = v_M$ and the lower horizontal dotted line shows $\langle v_x \rangle_t = 0$.

Figure 5.1 reveals that for very low U_M , $\langle v_x \rangle_t$ increases exponentially from 0 with increasing U_M until U_M reaches a critical value $U_M^d \approx 2.5$ peV, at which point $\langle v_x \rangle_t = v_M$. As U_M increases beyond U_M^d , $\langle v_x \rangle_t$ remains pinned at v_M until U_M reaches a second critical value $U_M^b \approx 16$ peV where the average velocity decreases abruptly. Thereafter, increasing U_M gives rise to a series of resonant peaks (arrowed in figure 5.1).

When $U_M \geq U_M^d$, it is possible to understand the form of the $\langle v_x \rangle_t(U_M)$ curve within the analysis made in chapter 4. There are two distinct regimes to consider, when $U_M^d < U_M < U_M^b$, the electron is in the wave dragging regime (see section 4.2.2). The atom is trapped within a potential well generated by the moving optical lattice and is therefore dragged through the stationary optical lattice at an average speed equal to the velocity of the propagating potential. When $U_M > U_M^b$, the electron is within the Bloch oscillation regime and the atom can ‘escape’ a single potential well of the moving optical lattice and, thus has an extended orbit in phase space allowing it to perform Bloch oscillations, resulting in the dramatic suppression of transport observed just to the right of the vertical dot-dashed line in figure 5.1 (see section 4.2.3). The resonant peaks in $\langle v_x \rangle_t$ seen as U_M increases are a result of the atom ratcheting up the modified dispersion curve, with each jump up in the velocity corresponding to the atom being able to access a new Brillouin zone (see figure 4.5(b)). Precisely the same mechanism produces the discontinuities in the surface spectra plot shown in figure 4.6 for electron transport.

5.2.2 Trajectories in the linear dispersion regime

In the following section, we describe the atom’s trajectory in the low U_M regime and show that, here, the atom is confined to a linear region of the effective dispersion curve, $E'(p_x)$.

Figure 5.2(a) shows the atom trajectory (starting from rest $x(t=0) = p_x(t=0) = 0$) within the low field regime when $U_M = 1$ peV ($< U_M^d$ see red dashed line in figure 5.1). The atom demonstrates periodic oscillations with a positive drift imposed on the trajectory. To explain the form of this trajectory, we consider the Hamiltonian in the rest frame of the atom, equation (5.9). Equation (5.12) tells us that for $x_0 = 0$, $\mathcal{H}' = U_M/2$, which implies that

$$E'(p_x) = -V_M + \frac{U_M}{2} = \frac{U_M}{2} \sin(k_S x'). \quad (5.15)$$

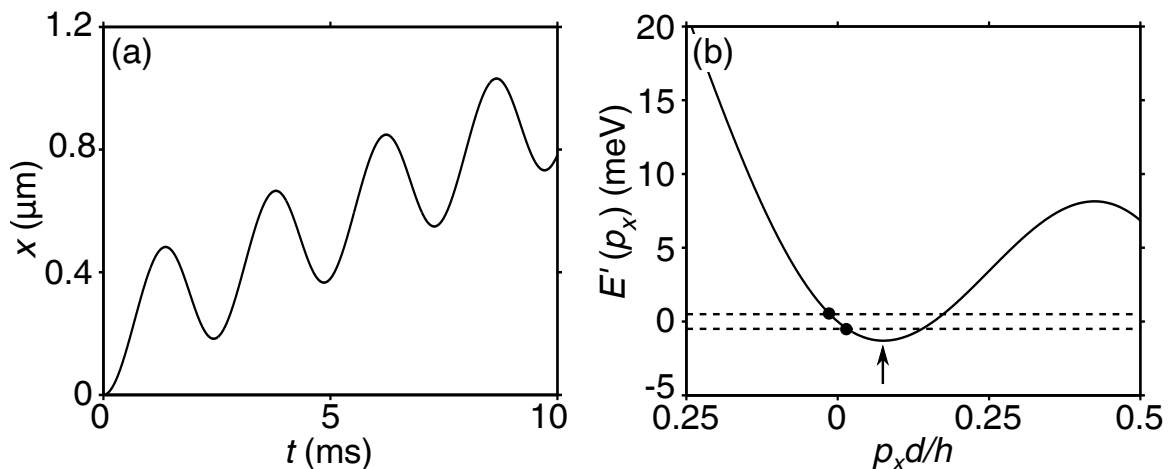


Figure 5.2: Figure showing atom trajectories for $U_M = 1$ peV and $v_M = 2.5$ mm s $^{-1}$. (a) is $x(t)$. (b) is $E'(p_x)$ where horizontal dashed lines show $\pm U_M/2$ and filled circles highlight when $E'(p_x) = \pm U_M/2$ and therefore the extremities of the orbit in p_x .

Consequently, $E'(p_x)$ can only take values between $-U_M/2$ and $U_M/2$. Figure 5.2(b) is a plot of $E'(p_x)$ when $v_M = 2.5$ mm s $^{-1}$. With this combination of Δ_{OL} ($= 24.35$ peV) and v_M , the slope of $E'(p_x = 0)$ is quite steep, resulting in the energy of the local minimum (arrowed in figure 5.2(b)) being significantly less than 0. The horizontal dashed lines in the figure show when $E'(p_x) = \pm U_M/2$, and the filled circles mark the intersection between the $\pm U_M/2$ lines and $E'(p_x)$, revealing that the orbit is very well confined in p_x . Initially, when $t = 0$, the force applied to the atom by the optical wave, $-\partial V_M(x)/\partial x$, is at its maximum and the atom is accelerated in momentum space until $E'(p_x) = -U_M/2$ (see lower filled circle in figure 5.2(b)). At this point, the atom's velocity attains its maximum value, determined by the slope of the dispersion curve ($v_x = \partial E'(p_x)/\partial p_x + v_M$). However, according to equation (5.15), when $E'(p_x) = -U_M/2$, $V_M(x') = U_M$ and thus the atom is at the top of the potential well where the force on the atom is 0. The atom momentarily drifts at the given velocity, until the force on the atom becomes negative ($-\frac{dV_M}{dx} < 0$) whereupon it is then accelerated in the negative direction in p_x . It moves through the origin of $E'(p_x)$ where $v_x = 0$, until $E'(p_x) = U_M/2$ (see upper filled circle in figure 5.2(b)), where the atom has its minimum velocity. The atom is then at the bottom of the potential well, $V_M(x') = 0$. As x' increases further the force on the atom becomes positive, returning it to the origin, causing the cycle to repeat.

In the regime where U_M is small, we can assume that the section of the dispersion

curve that the atoms can access is linear. Consequently, an estimate of the average velocity of the atom in the moving frame of the propagating wave can be found from the slope of this linear dispersion curve. Analysis of figure 5.2(b) reveals that the maximum value of p_x , $\max(p_x)$, occurs when $E'(\max(p_x)) = -U_M/2$, therefore using small angle approximations we find, from equation (5.9), that

$$\frac{\Delta_{OL}d^2}{2\hbar^2} \max(p_x)^2 - 2v_M \max(p_x) + U_M = 0. \quad (5.16)$$

Also, noting that $E'(\min(p_x)) = U_M/2$ where $\min(p_x)$ is the minimum value of p_x then

$$\frac{\Delta_{OL}d_{OL}^2}{2\hbar^2} \min(p_x)^2 - 2v_M \min(p_x) - U_M = 0. \quad (5.17)$$

These equations can be solved analytically by completing the square to find, for the parameters used in figure 5.2(a), that $\max(p_x) = 3.5964 \times 10^{-29} \text{ kg m s}^{-1}$ and $\min(p_x) = -2.9358 \times 10^{-29} \text{ kg m s}^{-1}$. These compare very well with the numerically determined values of $\max(p_x) = 3.5979 \times 10^{-29} \text{ kg m s}^{-1}$ and $\min(p_x) = -2.9413 \times 10^{-29} \text{ kg m s}^{-1}$. An initial estimate, $\langle v'_x \rangle_{t1}$, of the drift speed can be made by calculating the gradient of the effective dispersion curve assuming $E'(p_x)$ is linear around $p_x = 0$ to find

$$\langle v'_x \rangle_{t1} \approx \frac{U_M}{\max p_x - \min p_x}. \quad (5.18)$$

Using the analytical values of $\max(p_x)$ and $\min(p_x)$, we find $\langle v_x \rangle_{t1} = 50.6 \text{ } \mu\text{m s}^{-1}$ which underestimates the numerically calculated value of $75.5 \text{ } \mu\text{m s}^{-1}$. A second estimate can be found by calculating the difference in the magnitude of the maximum and minimum velocities, which occur when $p_x = \max(p_x)$ and $\min(p_x)$ respectively. The velocity of the atom is calculated using Hamilton's equation (5.14) which can be simplified for small p_x to

$$v_x(p_x) \approx \frac{\Delta_{OL}d_{OL}^2}{2\hbar^2} p_x. \quad (5.19)$$

Therefore substituting in the values $\max(p_x)$ and $\min(p_x)$, a second estimate of the average velocity is $\langle v'_x \rangle_{t2} \approx |v'_x(\max(p_x))| - |v'_x(\min(p_x))| = 101 \text{ } \mu\text{m s}^{-1}$. Taking the average of $\langle v'_x \rangle_{t1}$ and $\langle v'_x \rangle_{t2}$ gives $\langle v_x \rangle_t = 75.8 \text{ } \mu\text{m s}^{-1}$: very close to the numerically determined value of $75.5 \text{ } \mu\text{m s}^{-1}$. In figure 5.3 we compare the analytical estimate of

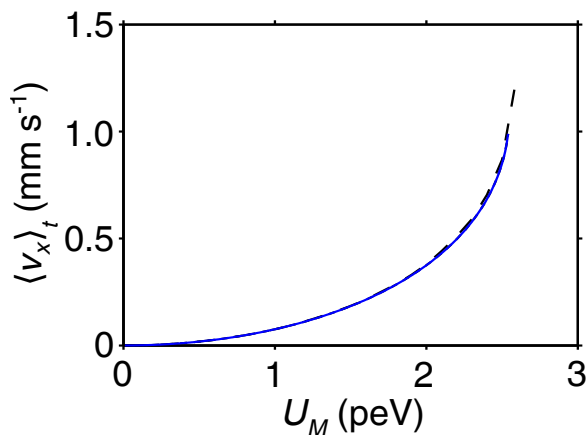


Figure 5.3: Plot showing $\langle v_x \rangle_t(U_M)$ for low U_M calculated both analytically (blue curve) and numerically (black dashed curve).

$\langle v_x \rangle_t$ (blue solid curve) with the numerical evaluation (black dashed curve) and see very good comparison for $U_M \lesssim 2.5$ peV.

Figure 5.2(b) shows increasing U_M from 1 peV, increases the range of accessible p_x values and thus makes the region of the dispersion curve that the atom traverses increasingly nonlinear. Therefore the estimate of $\langle v_x \rangle_t$ deviates from the numerical calculation. As U_M increases further, the extent of the trajectory in p_x drastically increases, when $-U_M/2$ falls below the value of the local minimum in $E'(p_x)$ (arrowed in figure 5.2(b)). Previously, it was found that the local minimum in $E'(p_x)$ (see equation (4.27)) occurs when

$$p_x = \frac{2\hbar^2 v_M}{\Delta_{OL} d_{OL}^2}. \quad (5.20)$$

Substituting this into $E'(p_x)$ (equation (5.15)), we obtain the following estimate for the transition out of the regime where it is possible to only access a linear region of the dispersion curve (with $x_0 = 0$)

$$U_M^d(x_0 = 0) = \frac{4\hbar^2 v_M^2}{\Delta_{OL} d_{OL}^2} - \Delta_{OL} \left(1 - \cos \left(\frac{2\hbar v_M}{\Delta_{OL} d_{OL}} \right) \right). \quad (5.21)$$

For this particular set of parameters, $U_M^d \approx 2.50$ peV (see red dashed line in figure 5.1), which coincides with entering the wave dragging regime, where $\langle v_x \rangle_t = v_M$ in figure 5.1. Note that we could use a small angle approximation for the cos term in equation (5.21) to obtain a simpler expression for U_M^d . However, later in the this

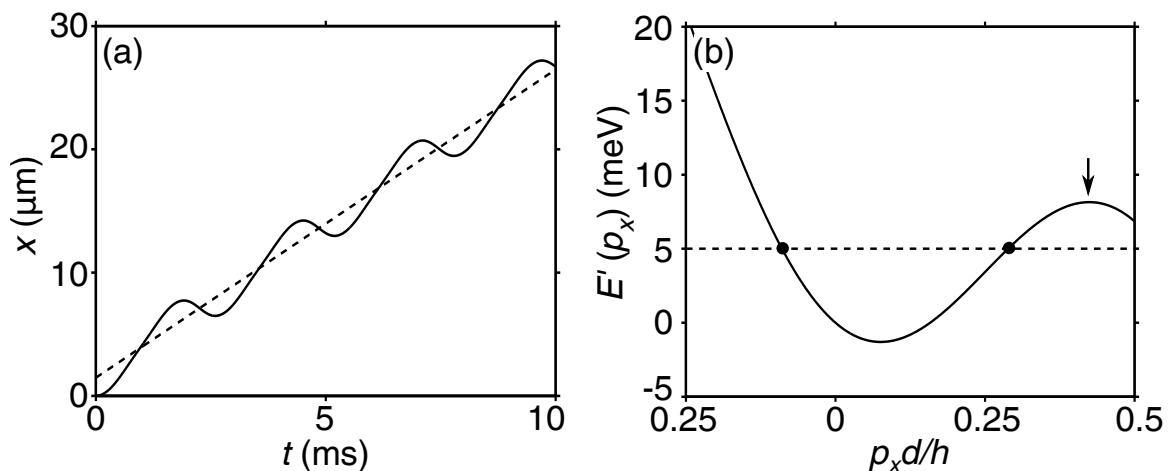


Figure 5.4: Figure showing atom trajectories for $U_M = 10$ peV within the wave dragging regime. (a) is $x(t)$ where the dashed line shows $x(t) = \lambda/4 + v_M t$. (b) is $E'(p_x)$ within which the horizontal dashed line shows $U_M/2$ and filled circles highlight when $E'(p_x) = U_M/2$ and therefore the extent of the orbit in p_x .

chapter we consider larger values of v_M than considered here, where small angle approximations do not apply.

5.2.3 Trajectory in the wave dragging regime

Figure 5.4(a) shows the atom trajectory starting from rest ($x(t=0) = p_x(t=0) = 0$) when $U_M = 10$ peV ($> U_M^d$). The atom's trajectory comprises regular sinusoidal oscillations superimposed on a background drift, with slope equal to v_M . Figure 5.4(b) shows $E'(p_x)$ with the horizontal dashed line showing the maximum possible value for the energy of the atom ($= U_M/2$). The minimum possible potential energy of the atom ($-U_M/2$) is less than the local minimum of $E'(p_x)$. Consequently, the atom can now oscillate in a parabolic region of the effective dispersion curve (between the two filled circles in figure 5.4(b)) where the extent of the trajectory in p_x is defined by the solutions of $E'(p_x) = U_M/2$.

Initially, at $t = 0$ and $p_x = 0$, the force on the atom, $-\partial V_M/\partial x$, is at its maximum, accelerating it along the p_x axis and increasing its velocity until $E'(p_x) = U_M/2$ (right hand filled circle in figure 5.4(b)) where the velocity is maximal. The force on the atom then becomes negative i.e. when $x' = \lambda_M/4$, accelerating the atom in the negative p_x direction, through the origin, at which point the velocity of the atom becomes 0

(when $x' = \lambda_M/2$). The atom continues travelling in the negative p_x direction with increasingly negative velocity until $E'(p_x) = U_M/2$ (left hand filled circle in figure 5.4(b)). Here, the force on the atom become positive and it returns to the beginning of the oscillation. Therefore the atom performs approximately sinusoidal oscillations in x' between 0 and $\lambda_M/2$. Also, since the oscillations in the well of $E'(p_x)$ are almost symmetric, i.e. the turning points (marked by filled circles in figure 5.4(b)) occur at the same energy and similar velocity, the atom's orbit does not drift in the moving frame. Thus, in the rest frame, the atom is dragged with a velocity equal to v_M . For a more detailed analysis of this trajectory see section 4.2.2.

With increasing U_M , the orbit generally keeps the same form, although the oscillations of $x'(t)$ become increasingly non-sinusoidal as the atom accesses the non-parabolic parts of the dispersion curve. However, once the value of $U_M/2$ is greater than the local maximum of the $E'(p_x)$ curve (arrow in figure 5.4(b)), the atom's trajectory changes from being closed to open and can access several Brillouin zones, allowing the atom to Bragg reflect and perform Bloch oscillations. Equation (4.27) implies that the first local maximum of $E'(p_x)$ occurs when

$$p_x \approx \frac{\hbar\pi}{d} - \frac{2\hbar^2 v_M}{\Delta_{OL} d^2}. \quad (5.22)$$

Substituting this into $E'(p_x)$ (equation (5.15)) we find the following estimate for the transition between the dragging and Bloch oscillation regimes (with $x_0 = 0$)

$$U_M^b(x_0 = 0) \approx 2 \left[\Delta_{OL} - \frac{\hbar\pi v_M}{d_{OL}} + \frac{2\hbar^2 v_M^2}{\Delta_{OL} d_{OL}^2} \right]. \quad (5.23)$$

$U_M^b(x_0 = 0)$ is plotted in figure 5.1 by the blue dot-dashed line labelled U_M^b , and shows good correspondence with the onset of suppression of $\langle v_x \rangle_t$ that accompanies the transition to Bloch oscillations.

5.2.4 Trajectory in the Bloch oscillation regime

Figure 5.5(a) shows the atom's trajectory when $U_M = 150$ peV revealing that the atom undergoes fast oscillations (bracketed) interrupted by jumps in the orbit (arrows). This regime is exactly the one found for electron Bloch oscillations driven by an acoustic wave case (see section 4.2.3).

Figure 5.5(b) is the corresponding plot of $E'(p_x)$, with the horizontal lines delimiting the range of $E'(p_x)$ accessible to the atom (between $\pm U_M/2$). Initially, when

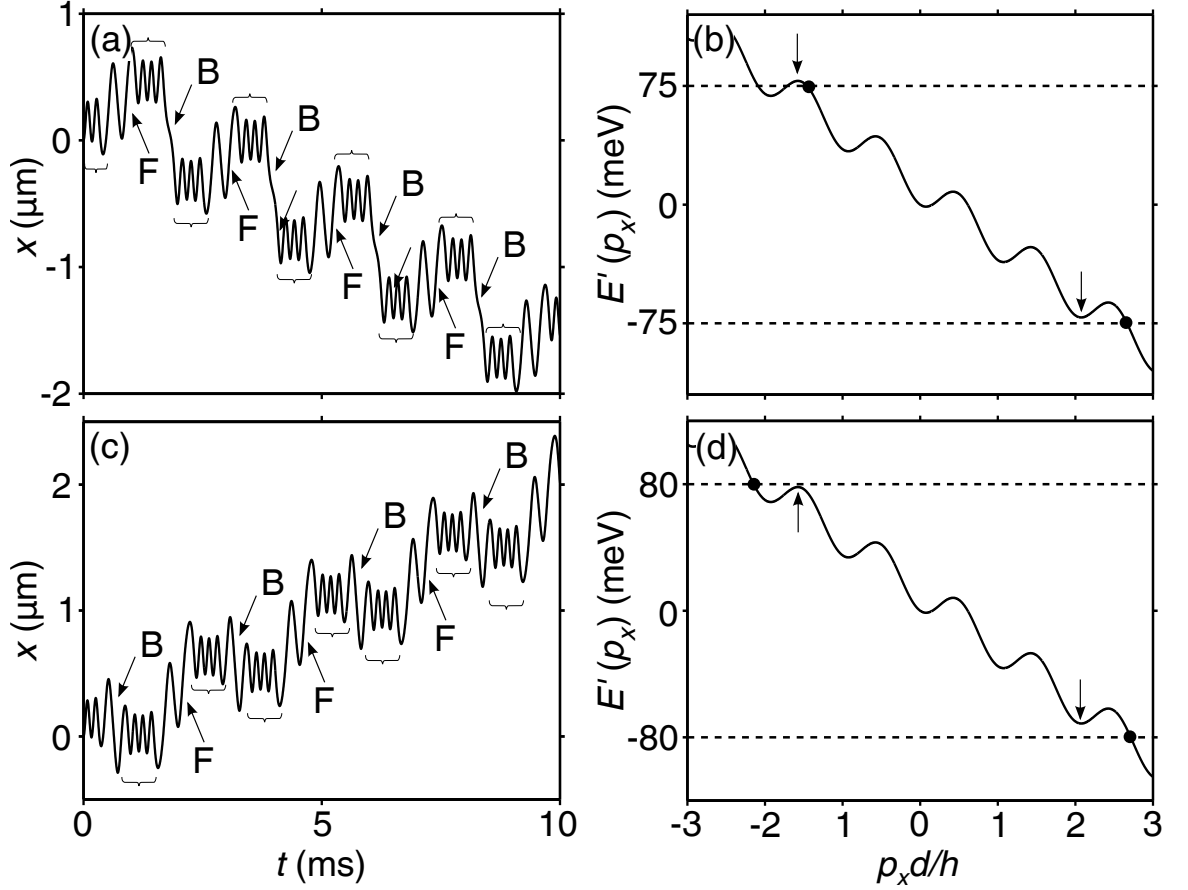


Figure 5.5: Atom trajectories within the Bloch oscillation regime, $U_M = 150$ peV in panels (a) and (b) and $U_M = 160$ peV in panels (c) and (d). (a) and (c) show $x(t)$. (b) and (d) show $E'(p_x)$. Horizontal dashed lines show $\pm U_M/2$. Filled circles mark $E'(p_x) = \pm U_M/2$ and therefore indicate the extent of the orbit in p_x space. Arrows, brackets and labels 'B' and 'F' explained in text.

$t = 0$, $x = p_x = 0$, the driving force on the atom is maximal, so rapidly increasing p_x . The atom traverses the local maxima and minima in $E'(p_x)$, Bragg reflecting and performing Bloch oscillations as it does so (see bracketed region of trajectory in figure 5.5(a)). As $E'(p_x)$ decreases, V'_M increases to keep \mathcal{H}' (see equation 5.9) constant, and thus the force ($|dV'_M/dx'|$) on the atom also decreases, reducing the frequency and increasing the amplitude of the Bloch oscillations (see section 4.2.3). Eventually when $E'(p_x) \approx -U_M/2$, the atom is at the top of the potential well ($V_M(x') = U_M$), and thus the force on the atom is effectively zero. Therefore the atom is temporarily pinned in the region of the dispersion curve where $E'(p_x) \approx -U_M/2$ (right-hand filled circle in figure 5.5(b)). This causes the atom have an almost constant velocity equal to the gradient of the dispersion curve at this point, temporarily stopping Bloch oscillations. The atom continues to drift until the force on the atom is large enough to drive it back up the effective dispersion curve where it again performs Bloch oscillations, passing through the origin, until $E(p_x) \approx U_M/2$. Here the atom is again pinned in momentum space leaving it to drift along the x -axis. The atom is then driven back to beginning of its oscillation.

In section 5.2.2, we showed that the average velocity of the atom is solely determined by the difference in the speed of the atom at the left and right hand edges of the orbit in momentum space. Here, however, the atom can access more of the dispersion curve giving it a more complex $E'(p_x)$ dependence. Consequently, the calculation of the average velocity is more complex. For $U_M = 150$ peV, the minimum possible value of $E'(p_x)$ occurs just below the local minima in the curve marked by the right-hand arrow in figure 5.5(b). Here, the velocity of the atom (at the right-hand filled circle in figure 5.5(b)) is negative, indicating that the atom will move in the negative direction at this point. However, since the force on the atom (and its velocity along p_x) is diminished close to the maximum value of p_x (right-hand filled circle in figure 5.5(b)), the atom spends a considerable amount of time in the region of $E'(p_x)$ where the velocity of the atom is positive (to the right of the right-hand arrow in figure 5.5(b)). Overall the atom spends more time with positive velocity than negative velocity causing the atom to jump *forwards* along the x -axis, (arrows labelled 'F' in figure 5.5(a)) i.e. the second Bloch oscillation burst has a midpoint at a value of $x > x_0 = 0$. Conversely, the maximum possible value of $E'(p_x)$ (upper dashed line in figure 5.5(b)) occurs just below the local maxima in $E'(p_x)$ (left-hand arrow in figure 5.5(b)). Since the force close to the right-hand filled circle is low, the

atom remains in the negative velocity region of $E'(p_x)$ for a long time (to the right of the left hand arrow in figure 5.5(b)). This results in the atom making a massive jump *backwards* along the x -axis (arrows labelled ‘B’ in figure 5.5(a)). We see in figure 5.5 that the atom jumps backward further than it jumps forward, giving the atom an overall negative average velocity.

Figure 5.5(c) is the trajectory for $U_M = 160$ peV. We find that generally the form of the trajectory is similar to when $U_M = 150$ peV (Bloch oscillation bursts interrupted by jumps in the orbit). Now though, that with increased U_M , the atom can access a new peak in $E'(p_x)$ (left-hand arrow in figure 5.5(d)) resulting in an extra Bragg reflection in the trajectory. This allows the atom to access a new region of $E'(p_x)$ where the velocity of the atom is positive (to the left of the left-hand arrow in figure 5.5(d)), close to when the force on the atom is 0 (at the left-hand filled circle). Consequently, the atom jumps *forward* along x when p_x is minimal. This in contrast to when $U_M = 150$ peV, where the atom jumps *backward* along x when p_x is minimal.

Note that when $U_M = 160$ peV the atom can access a larger region of negative velocity in $E'(p_x)$ when p_x is maximal (to the left of the right-hand filled circle in figure 5.5(d)) causing the atom to jump it backward (see arrow labelled ‘B’ in figure 5.5(c)). This in contrast to when $U_M = 150$ peV, where the atom jumps *forward* along x when p_x is maximal. For $U_M = 160$ peV, the forward jump is larger than the backward jump and the average velocity is positive.

This analysis implies that the average velocity will have a resonant peak each time the atom can access a new local maximum, or minimum in $E'(p_x)$, and thus access a new region of $E'(p_x)$ where the gradient and, consequently, v'_x is positive. Equation (5.22) shows that the minima in the dispersion curve occur when

$$p_x(r_{min}) \approx r_{min} \frac{2\pi\hbar}{d_{OL}} + \frac{2\hbar^2 v_M}{\Delta_{OL} d_{OL}^2}, \quad (5.24)$$

where $r_{min} = 1, 2, \dots$ are integers labelling the minima. Correspondingly, equation (5.20) shows that the local maxima occur when

$$p_x(r_{max}) \approx -(2r_{max} - 1) \frac{\pi\hbar}{d_{OL}} - \frac{2\hbar^2 v_M}{\Delta_{OL} d_{OL}^2}, \quad (5.25)$$

where $r_{max} = 1, 2, \dots$ are integers labelling the maxima. Therefore, substituting equations (5.24) and (5.25) into equation (5.15), we find that the local minima and maxima of $E'(p_x)$ occur when $E'(p_x(r_{min})) = -U_M/2$ and $E'(p_x(r_{max})) = U_M/2$ respectively

$$U_M(r_{min}) \approx -\Delta_{OL} \left(1 - \cos \left(\frac{p_x(r_{min})d_{OL}}{\hbar} \right) \right) + 2v_M p_x(r_{min}), \quad (5.26)$$

$$U_M(r_{max}) \approx \Delta_{OL} \left(1 - \cos \left(\frac{p_x(r_{max})d_{OL}}{\hbar} \right) \right) - 2v_M p_x(r_{max}). \quad (5.27)$$

When $r_{min} = 1$ and 2 , $U_M(r_{min}) = 72.6$ peV and 142 peV respectively and when $r_{max} = 1$ and 2 , $U_M(r_{max}) = 86.3$ peV and 156 peV respectively. The positions of these points are shown in figure 5.1 by the labelled arrows, and correspond well with the positions of the resonant peaks in $\langle v_x \rangle_t$.

5.2.5 Average velocity with colour map

Optical lattices provide great freedom and control of the system's parameters. For example, we are able to increase v_M to speeds of ~ 50 mm s⁻¹ [101] and U_M to ~ 500 peV [46]. Figure 5.6 is a colour map showing the variation of the average velocity of the atom, $\langle v_x \rangle_t$ with v_M and U_M . The figure clearly reveals the three dynamical regimes considered in sections 5.2.2, 5.2.3 and 5.2.4. The lower dashed magenta line is the solution of $U_M^d(v_M)$ (see equation (5.21)) showing the onset of the dragging regime. In the region where v_M is small ($\lesssim 3$ mm s⁻¹), U_M^d is also small and therefore trajectories in the regime described in section 5.2.2 occupy a very small region of the plot where $U_M \approx 0$. However, U_M^d depends quadratically on v_M (see equation (5.21)) so for $v_M \gtrsim 3$ mm s⁻¹ we see a clear transition from the regime where the atom accesses only the linear part of the dispersion curve and $\langle v_x \rangle_t \approx 0$ (coloured blue in figure 5.6) to the wave dragging regime where $\langle v_x \rangle_t \approx v_M$. Note that, as explored in section 5.2.2, in this regime $\langle v_x \rangle_t$ increases with increasing U_M .

The black dashed line in figure 5.6 shows U_M^b versus v_M (see equation 5.23) marking the position of the transition of the atom from the dragging regime into the Bloch oscillation regime. The region of the plot below the black dashed line and above the magenta dashed line corresponds to the wave dragging regime where $\langle v_x \rangle_t = v_M$ (appearing in the figure as a linear gradient of colour). With increasing v_M , the atom can still be dragged by the propagating potential, albeit in a smaller region in parameter space, until $v_M = \Delta_{OL}d_{OL}/\hbar\pi = 3.5$ mm s⁻¹, corresponding to when $U_M^d = U_M^b$. Now the tilt of $E'(p_x)$ is large enough that the value of U_M needed for the atom to traverse the local minima in $E'(p_x)$ is the same value, or larger, than required to traverse the local maxima. Therefore the atomic motion changes straight

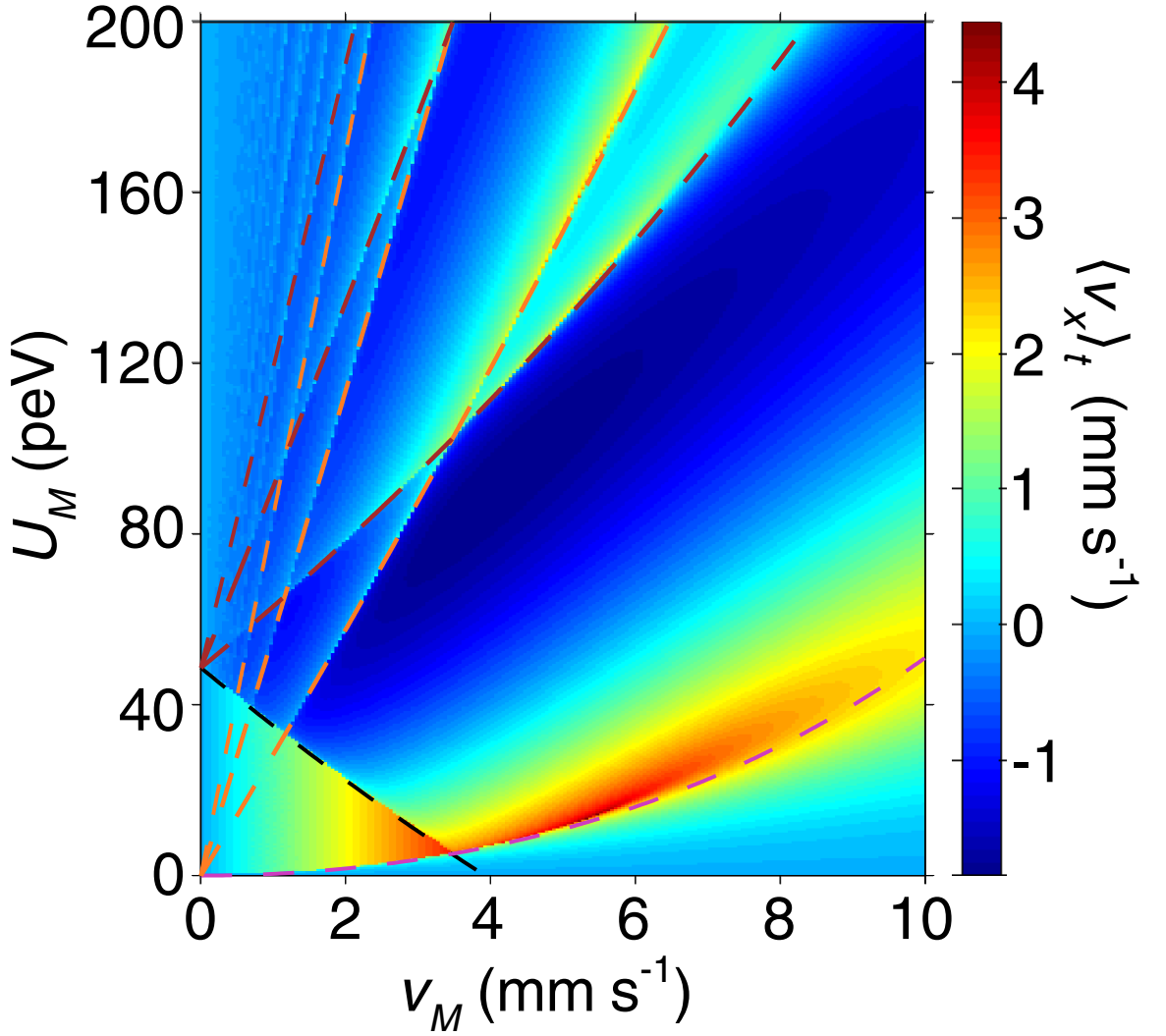


Figure 5.6: Colour map (scale right) showing the variation of the average atom velocity, $\langle v_x \rangle_t$, with v_M and U_M when $\lambda_M = 20d_{OL}$. Magenta dashed line shows U_M^d versus v_M (see equation (5.21)). Black dashed line shows U_M^b versus v_M (see equation (5.23)). Orange dashed lines are the solutions of $U_M(r_{min})$ versus v_M when $r_{min} = 1, 2$ and 3 (see equation (5.26)). Brown dashed lines are the solution for $U_M(r_{max})$ when $r_{max} = 1, 2$ and 3 (see equation (5.27)).

from the linear dispersion regime to the Bloch oscillation regime, which occurs when $U_M \approx U_M^d$.

Following the arguments given in section 5.2.4, we also expect the atom to have its highest average velocity (in the Bloch oscillation regime) when $U_M = U_M^d$ since here the atom spends the most *time* in the region of $E(p_x)$ corresponding to positive velocity. $U_M^d(v_M)$ is shown as the magenta line in figure 5.6 where we see for $v_M > 3.5$ mm s⁻¹, $\langle v_x \rangle_t \sim v_M$ until $v_M \gtrsim 5.5$ mm s⁻¹ at which point $\langle v_x \rangle_t$ begins to decrease as v_M increases. This decrease in velocity occurs when $v_M > \Delta_{OL} d_{OL} / 2\hbar$, i.e when the dragging velocity is larger than the maximum velocity of the atom in the band. At this point the gradient of the effective dispersion curve starts to become significantly deformed compared to when $v_M = 0$. This has the effect of reducing the atom's maximum velocity.

Also included in the plot are orange and brown dashed curves showing respectively $U_M(r_{min})$ and $U_M(r_{max})$ for r_{min} and $r_{max} = 1, 2$ and 3 , see equations (5.26) and (5.27). These show good correspondence with the positions of the resonant peaks in the colour map, which are shown as white/red lines (high $\langle v_x \rangle_t$) within the blue region of the plot (low $\langle v_x \rangle_t$) for $U_M \gtrsim 40$ peV.

5.2.6 Non zero initial position

In this section we consider the effect of the initial position of the atom on its dynamics by setting $x(t = 0) = x_0$ when $v_M = 2.5$ mm s⁻¹ (for which figure 5.6 reveals rich dynamics when $x_0 = 0$) and $\lambda_M = 20d_{OL}$. Figure 5.7 shows a color map of $\langle v_x \rangle_t$ versus U_M and x_0 , which reveals a number of resonant features. A cross section of the plot when $x_0 = 0$ is shown in figure 5.1. The three dynamical regimes are apparent. For very low $U_M \lesssim 3$ peV, the atom is in the linear dispersion regime, yellow in the color map (see section 5.2.2) irrespective of x_0 . Increasing U_M when $x_0 = 0$, induces a transition into the wave dragging regime (when $\langle v_x \rangle_t = v_M$) which appears as the dark red region in the colour map (see section 5.2.3 and figure 5.6). Further increasing U_M , we enter the Bloch oscillation regime where the atom's velocity is dramatically suppressed, indicated by the yellow region of the plot (see section 5.2.4). Within the Bloch regime there are resonances, which correspond to those arrowed in figure 5.1, and occur when the atom is allowed to access a new peak in the $E'(p_x)$ dispersion curve (see section 5.2.5).

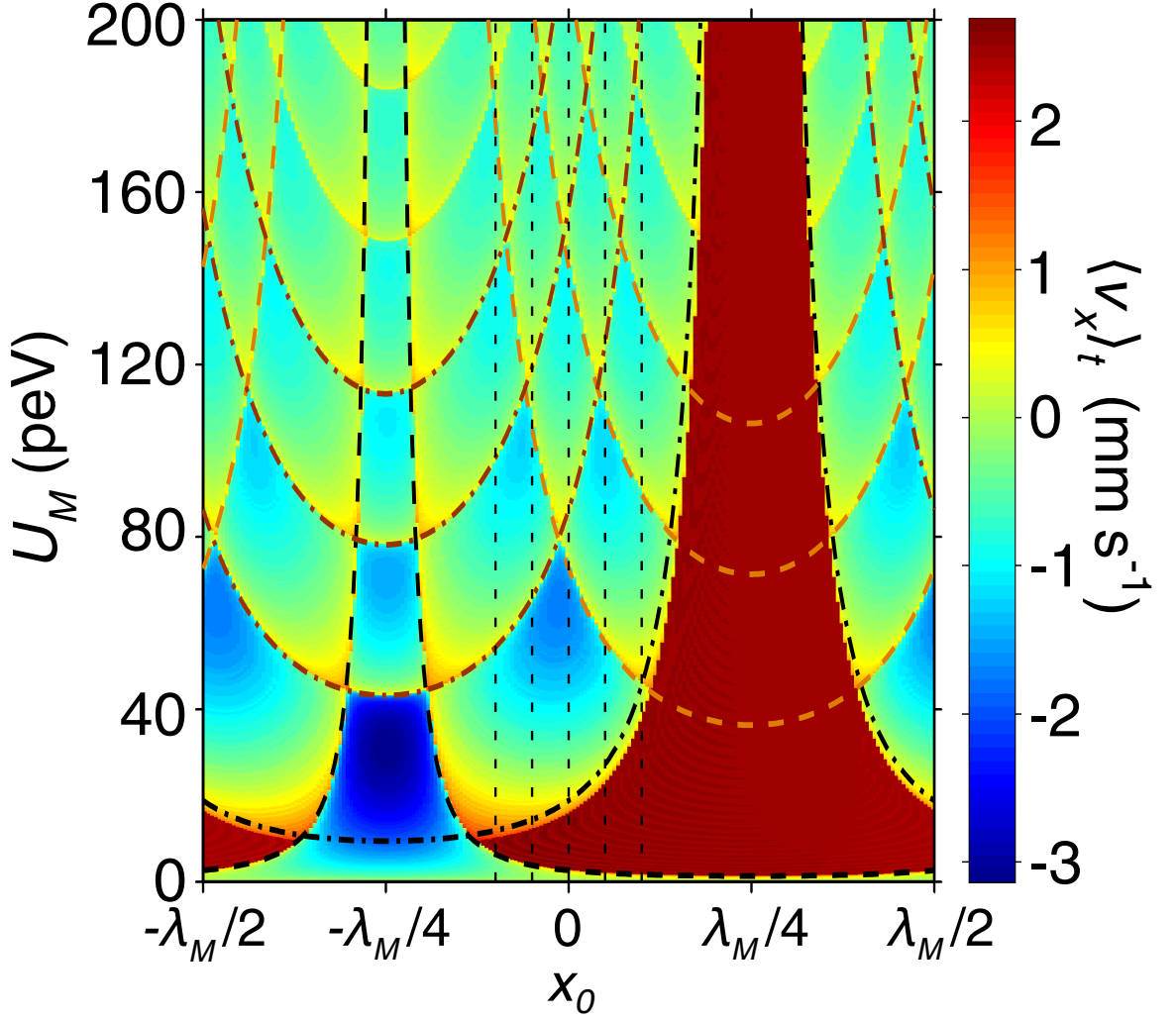


Figure 5.7: Colour map (scale right) showing the variation of the average atom velocity with x_0 and U_M when $\lambda_M = 20d_{OL}$. Black dashed curve shows the value of $U_M^d(x_0)$ representing the onset of dragged atom trajectories (see equation (5.31)). Black dot-dashed line mark the values of $U_M^b(x_0)$ (see equation (5.32)). Orange dashed lines are the solution for $U_M(r_{min}, x_0)$, where $r_{min} = 1, 2$ and 3 (see equation (5.33)). Brown dashed lines are the values of $U_M(r_{max}, x_0)$ where $r_{max} = 1, 2$ and 3 (see equation (5.34)). For guidance, vertical dashed lines show the positions of the centres of 5 wells at $-2d_{OL}$, $-d_{OL}$, 0 , d_{OL} and $2d_{OL}$.

The location of these regimes in figure 5.7 can be understood if we consider the effect of x_0 on the position of the transition between the linear regime and the wave dragging regime (U_M^d) and also on the transition between the wave dragging regime and Bloch oscillation regime (U_M^b). Equation (5.12) implies that, generally,

$$E'(p_x) = \frac{U_M}{2} (\sin k_M x' - \sin k_M x_0). \quad (5.28)$$

Therefore $E'(p_x)$ can take values between

$$E'(p_x) = \frac{U_M}{2} (1 - \sin k_M x_0) \quad (5.29)$$

and

$$E'(p_x) = \frac{U_M}{2} (-1 - \sin k_M x_0). \quad (5.30)$$

Note that, as before, when $x_0 = 0$, $E'(p_x)$ takes values between $U_M/2$ and $-U_M/2$. We know that the atom enters the wave dragging regime when it can traverse the local minimum, close to $p_x = 0$, in $E'(p_x)$ (arrowed in figure 5.2(b)). This causes the atom to have zero average velocity in the rest frame and therefore be dragged through the lattice. Following the analysis in section 4.3.1, we find that the transition from the linear regime to the dragging regime occurs when

$$U_M^d(x_0) = \frac{1}{1 + \sin k_M x_0} \left[\frac{4\hbar^2 v_M^2}{\Delta_{OL} d_{OL}^2} - \Delta_{OL} \left(1 - \cos \left(\frac{2\hbar v_M}{\Delta_{OL} d_{OL}} \right) \right) \right]. \quad (5.31)$$

The variation of $U_M^d(x_0)$, shown as the black dashed curve in figure 5.7, agrees well with the transition from the linear dispersion regime to the wave dragging regime shown in the colour map. Increasing x_0 to $\lambda_M/4$ causes the transition to the wave dragging regime to occur at a decreasing value of U_M , which attains a minimum value of $U_M = 1.3$ peV when $x_0 \approx \lambda_M/4$. For $x > \lambda_M/4$ the value of U_M required to enter the dragging regime increases until $x_0 = \lambda_M/2$, at which point the system is *approximately* equivalent to when $x_0 = 0$.

Decreasing x_0 from 0 we find that the transition to the wave dragging regime from the linear regime occurs at increasing U_M until $x_0 \approx -\lambda_M/8$ after which there is no transition to a wave dragging regime. When $x_0 \approx -3\lambda_M/8$, the wave dragging regime re-emerges and the value of U_M at the transition decreases until $x_0 = -\lambda_M/2$ which is *exactly* equivalent to when $x_0 = \lambda_M/2$.

The analysis in section 5.2.2 showed that as v_M increases $U_M^d(x_0 = 0)$ also increases and therefore the parameter space corresponding to the wave dragging regime is reduced (see figure 5.6). However, interestingly, equation (5.31) shows that as $x_0 \rightarrow -\lambda_M/4$, $U_M^d(x_0) \rightarrow \infty$ implying that for any given v_M and U_M the atom will never enter the wave dragging regime. We understand this in the effective dispersion curve picture by noting, from equations (5.29) and (5.30), that when $x_0 = -\lambda_M/4$, $E'(p_x)$ takes values between U_M and 0. Therefore the atom will not traverse the local minimum in $E'(p_x)$ when $p_x \approx 0$ (arrowed in figure 5.2(b)) and thus will not enter the wave dragging regime.

In section 5.2.4, it was shown that in order for the atom to Bragg reflect, it must traverse the local maximum in $E'(p_x)$ arrowed in figure 5.4(b). Following the analysis in section 4.3.1, this occurs when U_M exceeds $U_M^b(x_0)$, given by

$$U_M^b(x_0) \approx \frac{2}{1 - \sin k_M x_0} \left[\Delta_{OL} - \frac{\hbar \pi v_M}{d_{OL}} + \frac{2\hbar^2 v_M^2}{\Delta_{OL} d_{OL}^2} \right]. \quad (5.32)$$

The solution to this equation, shown as the dot-dashed curve in Figure 5.7, agrees well with the transition from the wave dragging regime (red region in the figure) to the Bloch oscillation regime (yellow or blue region in the colour map). Increasing x_0 from 0, the transition to the Bloch regime occurs at increasing U_M until $x_0 \approx 3\lambda_M/16$ where there is no transition in the range of U_M shown. Equation (5.32) shows that as $x_0 \rightarrow \lambda_M/4$, then $U_M^b \rightarrow \infty$ implying that trajectories with $x_0 = \lambda_M/4$ are not able to Bloch oscillate for any given v_M or U_M . Note that when $x_0 = \lambda_M/4$, according to equations (5.29) and (5.30), $E'(p_x)$ takes values between 0 and $-U_M$ so the atom is not able to traverse the maximum in $E'(p_x)$ and thus cannot Bloch oscillate.

Increasing x_0 past $\lambda_M/4$, we find that the Bloch oscillation regime reappears in the parameter space when $x_0 \approx 5\lambda_M/16$. Then $U_M^b(x_0)$ decreases with decreasing x_0 until $x_0 = \lambda_M/2$, which is equivalent to when $x_0 = -\lambda_M/2$.

As x_0 decreases from 0, the transition to the Bloch regime occurs at decreasing U_M until $U_M^d(x_0) = U_M^b(x_0)$. Thereafter, there is no wave dragging regime and increasing U_M induces a transition straight from the linear regime into the Bloch oscillation regime. However, we note that as x_0 approaches $-\lambda_M/4$ then for any given U_M the atom cannot reach the first local maximum in $E'(p_x)$ and therefore cannot Bloch oscillate since it cannot traverse the local minimum (see black dashed line in figure 5.7). Therefore, the atom will only Bragg reflect when it reaches the peak in $E'(p_x)$ occurring when $p_x \approx -\hbar\pi/d$, resulting in the dramatic change from negative velocity

(blue region in figure 5.7) to positive velocity (yellow region in figure 5.7) when $U_M \approx 45$ peV.

The other resonant features in Figure 5.7 are a result of the atom being able to access new peaks in $E'(p_x)$, as previously discussed in section 5.2.4. These resonances occur when

$$U_M(r_{min}, x_0) \approx \frac{1}{1 + \sin k_M x_0} \left[-\Delta_{OL} \left(1 - \cos \left(\frac{p_x(r_{min}) d_{OL}}{\hbar} \right) \right) + 2v_M p_x(r_{min}) \right] \quad (5.33)$$

and

$$U_M(r_{max}, x_0) \approx \frac{1}{1 - \sin k_M x_0} \left[\Delta_{OL} \left(1 - \cos \left(\frac{p_x(r_{max}) d_{OL}}{\hbar} \right) \right) - 2v_M p_x(r_{max}) \right] \quad (5.34)$$

where $p_x(r_{min})$ and $p_x(r_{max})$ are given by equations (5.24) and (5.25) respectively. $U_M(r_{min}, x_0)$ and $U_M(r_{max}, x_0)$ are plotted in figure 5.7 respectively as orange dashed and brown dot-dashed lines and accurately predict the positions of the resonant features shown in the colour map.

5.3 Wavepacket analysis

This system is one-dimensional because all the potentials acting on the sodium atom are along the x axis. Therefore, the quantum mechanical Hamiltonian for the sodium atom in this system is given by

$$\hat{\mathcal{H}} = -\frac{\hbar^2}{2m_a} \frac{\partial^2}{\partial x^2} + V_{OL} + V_M \quad (5.35)$$

where m_a is the mass of the sodium atom. The potential, V_{OL} , generated by the stationary optical lattice is shown in equation (1.71) and restated here for clarity

$$V_{OL}(x) = V_0 \sin^2 \left(\frac{\pi x}{d_{OL}} \right), \quad (5.36)$$

where $d_{OL} = 294.5$ nm and $V_0 = 563$ peV. The potential $V_M(x, t)$ is generated by the moving optical lattice (see equation (5.3))

$$V_M(x, t) = \frac{U_M}{2} - \frac{U_M}{2} \sin(k_M x - \omega_M t). \quad (5.37)$$

To simulate the motion of a Sodium atom wavepacket in this system the time dependent Schrödinger equation,

$$i\hbar \frac{\partial \psi(x)}{\partial t} = \hat{\mathcal{H}}(x, t)\psi(x), \quad (5.38)$$

was solved using the method described in section 1.3.2.2. Figure 5.8 shows the evolution of the wave packet corresponding to the same parameters used for the semiclassical trajectories explored in the previous section ($v_M = 2.5 \text{ mm s}^{-1}$, $\lambda_S = 20d_{OL}$). Initially the wavepacket is in the 1st miniband of the optical lattice and has a FWHM value of $f_x = 2d_{OL}$.

In panel (a), we show the evolution of the wave packet when $U = 1 \text{ peV}$, corresponding to a semiclassical trajectory in the ‘linear’ dispersion regime (see section 5.2.2). Overlaid are semiclassical trajectories with $x_0 = -2d_{OL}, -d_{OL}, 0, d_{OL},$ and $2d_{OL}$ corresponding to the wells that are spanned by the initial wavefunction. In this case, most of the wavepacket does not follow the semiclassical trajectories (solid curves). Instead most of the wavepacket disperses from the origin with only a small fraction of the wavefunction being dragged through the lattice. Naïvely, from figure 5.7, we would expect all of the wavepacket to be in the linear dispersion regime and, consequently see no dragging of the wavepacket. It is clear, however, that the wavepacket does not follow a semiclassical trajectory. This suggests that for such a low potential, the spreading of the wavepacket, resulting from position-momentum uncertainty, dominates any dynamics expected from the semiclassical analysis. This effect will therefore give a lower limit of U_M on the validity of the semiclassical analysis.

We note also that since the wavepacket under consideration is quite spatially confined its corresponding intrinsic momentum spread is large. The uncertainty principle states $f_x \Delta p_x \approx \hbar$ where Δp_x is the spread of the momentum of the wavepacket. Therefore, the initial energy of the wavepacket in the system can be estimated as $E_{wp} = (1/2m_a)(\Delta p_x)^2$, which, when $f_x = 2d_{OL}$, equals to 2.5 peV. This energy is large enough, when added to the potential energy of the wavepacket, to allow part of the atom to enter the wave dragging regime, resulting in the dragged region of the wavepacket observed in the figure 5.8(a).

Figure 5.8(b) shows the evolution of the wavepacket when $U = 10 \text{ peV}$ corresponding to a semiclassical trajectory in the wave dragging regime (see figure 5.4). The figure reveals that, as predicted, in this regime most of the wavepacket is dragged

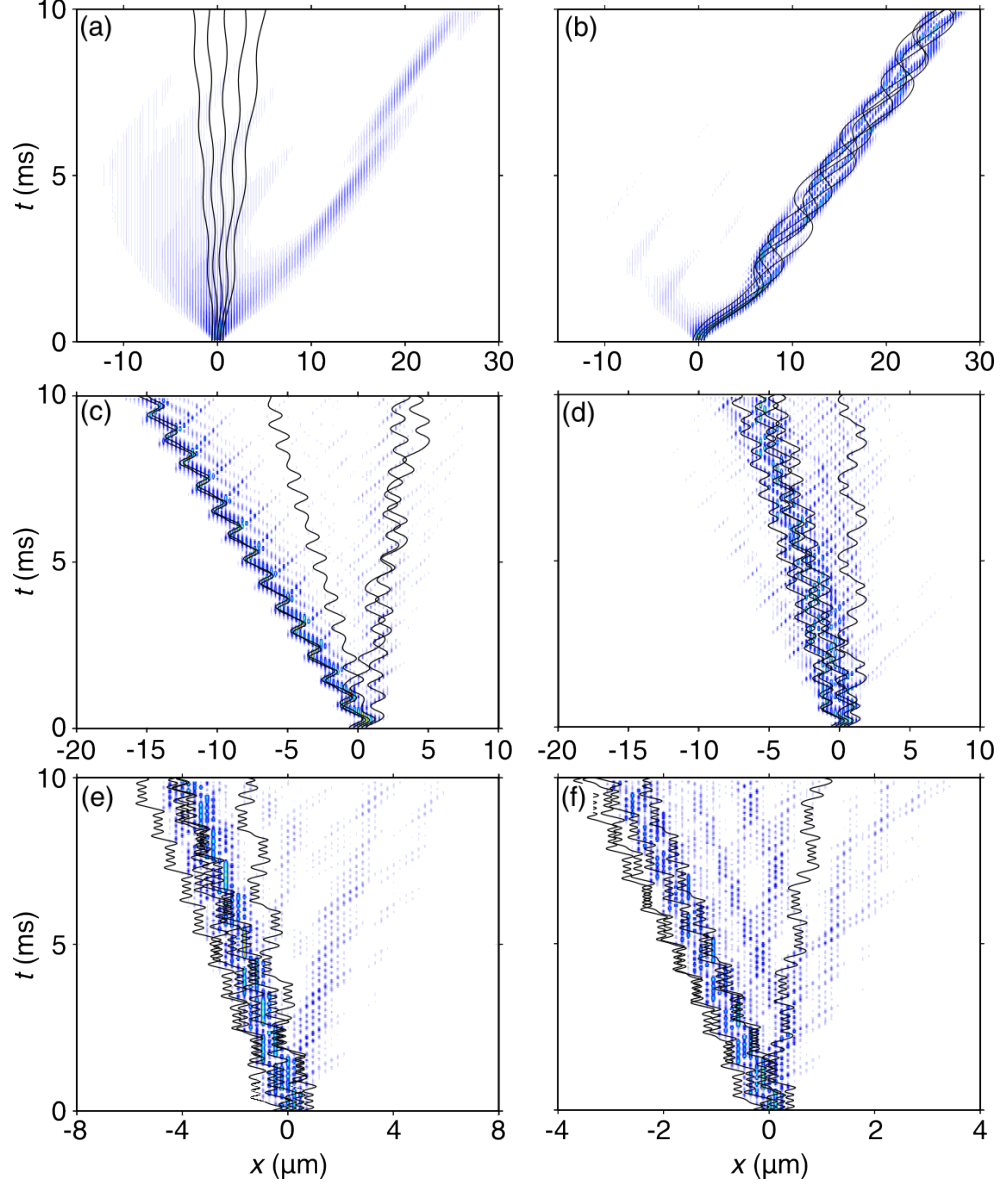


Figure 5.8: Colour maps showing the evolution of the probability density of the electron wave packet. Panel (a) is when $U_M = 1$ peV (linear regime, see figure 5.2), panel (b) is when $U_M = 10$ peV (dragging regime, see figure 5.4) and panels (c-f) are when $U_M = 55, 75, 150$ and 160 peV respectively (Bloch oscillating regime, see figure 5.5). The solid lines in the panels show corresponding semiclassical trajectories with, from left to right, $x_0 = -2d_{OL}, -d_{OL}, 0, d_{OL}$ and $2d_{OL}$. In the colour map blue represents low values, yellow middle values, and red high values.

through the optical lattice by the propagating potential. The shape of the wavepacket is well described by a superposition of the semiclassical trajectories. Note that, in contrast to the dragging regime of electrons in a superlattice, there are no Bloch oscillations in this picture. This is due to the comparatively longer wavelength of the optical potential increasing the spatial ‘window’ of initial conditions where dragging trajectories can originate. This is clear when we consider that for $U_M = 10$ peV the full spread of the wave function (see left- and right- most dashed vertical lines in Figure 5.7) lies within the wave dragging regime.

Figures 5.8(c) and (d) show, respectively, the evolution of wavepackets corresponding to $U_M = 55$ peV and $U_M = 75$ peV: both in the Bloch oscillation regime. In both cases, the wavepacket follows Bloch-like oscillations and the semiclassical trajectories correspond well with the evolution of the quantum wavepacket.

When $U_M = 55$ peV, Figure 5.8(c), the majority of the wavepacket moves in the negative direction following the semiclassical trajectory originating from $x_0 = 0$. However, we also see part of the wavepacket moving with a positive velocity following the semiclassical trajectories originating from $x_0 = -2d_{OL}$ and $2d_{OL}$. This highlights the extreme sensitivity of this system to the initial position. Figure 5.7 shows that when $U_M = 55$ peV, a wavepacket which spreads from $x_0 = -2d_{OL}$ to $x_0 = 2d_{OL}$ crosses two resonant features (see vertical dashed lines in Figure 5.7). Consequently, most of the wavepacket exists in a regime corresponding to negative average velocity (so most of the wavepacket follows this type of trajectory). However, the two edges of the wavepacket (with minimal population) have a positive velocity.

Note also in the left hand part of figure 5.8(c), tunnelling effects are present which, at the turning point of the oscillation, causes a portion of the wavepacket to follow a Bloch oscillation moving in anti-phase with, and having a larger amplitude than, the semiclassical trajectory. This suggests that the atom is allowed to tunnel into the second miniband: unsurprising when we consider that the applied potential (55 peV) is large compared to the width of the 1st miniband (≈ 25 peV).

Increasing U_M to 75 peV, we find that for $x_0 = 0$ the system is close to an intersection between two resonances (see vertical dashed lines in Figure 5.7). Therefore, trajectories close to $x_0 = 0$ follow different (semiclassical) paths resulting in the complex form of the wavepacket dynamics seen in figure 5.8(d). Note that here too we get significant tunnelling of the atom into higher minibands.

Figures 5.8(e) and (f) show the wavepacket evolution for $U_M = 150$ peV and 160 peV corresponding to the Bloch trajectories in figures 5.5(a) and (c). In these plots we see that the semiclassical trajectories quite well predict the evolution of the wavepacket. It appears, though, that for high U_M the wavepacket dynamics start to deviate from the semiclassical paths due to tunnelling and breakdown of the band. This breakdown of the band at high U_M suggests an upper limit to the validity of the previous lowest-band semiclassical analysis.

5.3.1 Quantum velocity

From the evolution of the wavefunction, it is possible to find the expectation value of the atom's position, $\langle x(t) \rangle$ using equation (4.62). Then, after differentiating $\langle x(t) \rangle$ with respect to time, we can find the time-averaged quantum velocity of the atom, $\langle v_x \rangle_t$, which gives insight into the transport of the wavepacket through the lattice with varying v_M and U_M . Figure 5.9(a) is a plot of $\langle v_x \rangle_t$ when $v_M = 2.5$ mm s⁻¹, calculated both quantum mechanically (solid curve) and semiclassically (dashed curve) when $x_0 = 0$. We find that for $U_M \lesssim 50$ peV the quantum calculation shows very good correspondence with the semiclassical curve. However, when more resonances begin to appear in the (x_0, U_M) parameter space (see figure 5.7) the curves start to deviate. In the quantum regime we see the “blurring” of the sharp resonant features, evident in the semiclassical analysis, since the wavepacket spatially spans several dynamical regimes.

Increasing v_M to 5 mm s⁻¹, figure 5.9(b), we see that for low U_M , initially $\langle v_x \rangle_t$ calculated semiclassically, increases with increasing U_M , whereas the quantum mechanical calculation of $\langle v_x \rangle_t$ decreases with increasing U_M . This is due to the spreading of the wavepacket dominating the quantum dynamics, and preventing the atom entering the linear dispersion regime. When $U_M \approx 10$ peV there is a dramatic increase in velocity in both the semiclassical and quantum calculations as the atom enters the Bloch regime. We also see that the wavepacket analysis reveals resonance peaks, in approximately the same place as the semiclassical trajectory, due to the atom accessing new peaks in $E'(p_x)$.

When $v_M = 7.5$ mm s⁻¹, figure 5.9(c), there is very good agreement between the quantum and semiclassical calculations over the full range of U_M considered. We understand this good correspondence when we realise that the resonant peaks in $\langle v_x \rangle_t$ versus U_M become more spaced out as we increase v_M and thus the wavepacket

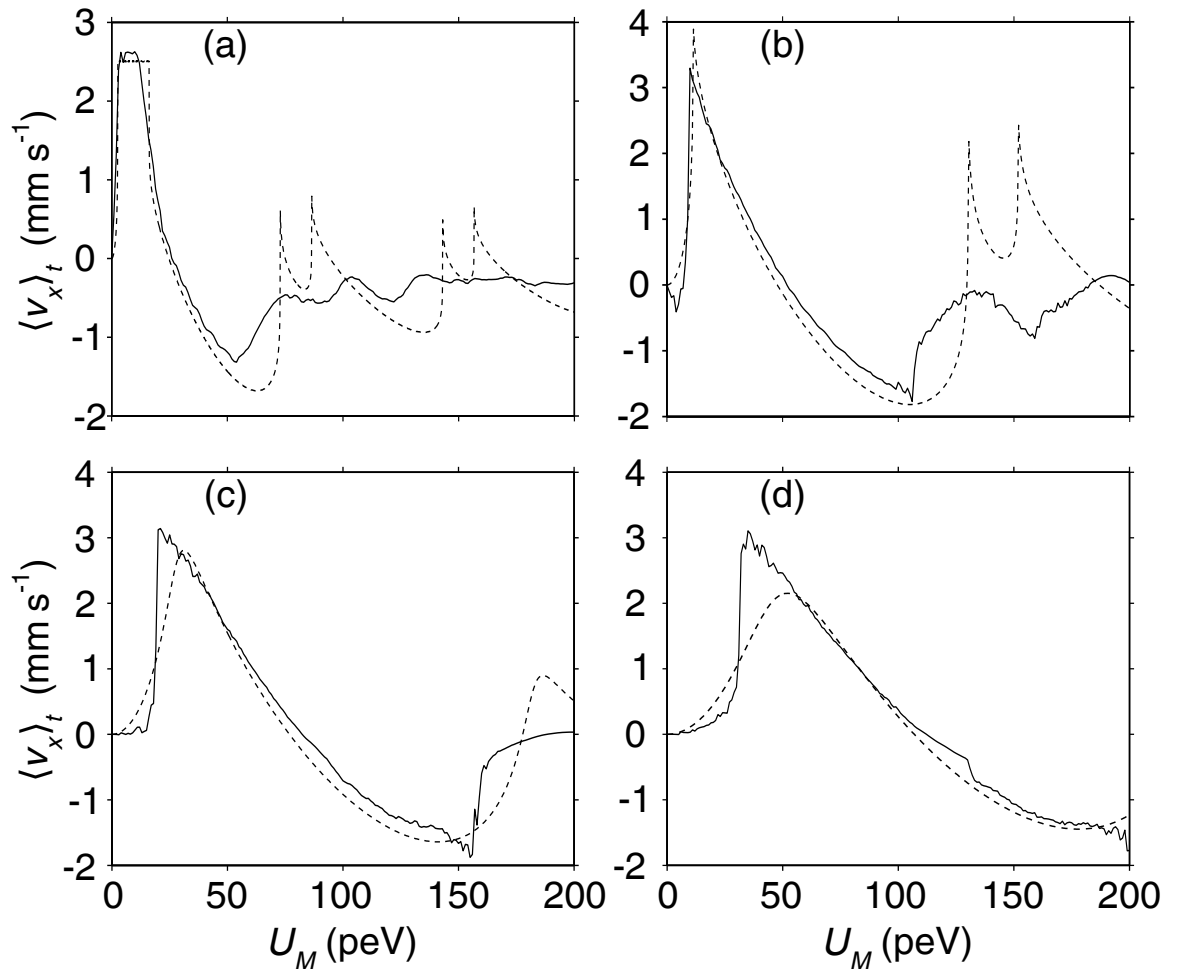


Figure 5.9: Figure showing the quantum calculation of time-averaged velocity, $\langle v_x \rangle_t$, vs. U_M , with $v_M =$ (a) 2.5 mm s^{-1} , (b) 5 mm s^{-1} , (c) 7.5 mm s^{-1} and (d) 10.0 mm s^{-1} . In each panel, the solid curve shows the quantum calculation. For comparison the dashed curve shows the semiclassical calculation when $x_0 = 0$.

spans a single dynamical regime (see figure 5.6). Further increasing v_M to 10 mm s^{-1} , figure 5.9(d), for $U \gtrsim 50 \text{ peV}$ we find improving correspondence between the semiclassical and quantum solutions. However, it is interesting to note that the peak average velocity is greater in the quantum calculation and occurs at a lower U_M than in the semiclassical calculation. This may suggest that in the quantum calculation the dynamics are less affected by large v_M distorting the effective dispersion curve, compared to the semiclassical case (see section 5.2.5).

This analysis suggests that there are limits to the correspondence between the semiclassical and quantum calculations. However, it is clear that some resonant features are retained in the wavepacket analysis and for $v_M = 7.5 \text{ mm s}^{-1}$ and 10 mm s^{-1} we see a dramatic increase of velocity when, respectively $U_M \approx 20 \text{ peV}$ and $\approx 30 \text{ peV}$. This raises the intriguing possibility that a small change in U_M can give rise to a dramatic increase in average velocity.

Chapter 6

Conclusion

In this thesis, three systems were investigated which control and enhance the dynamics of particles in periodic potentials. Firstly, we considered the effect of a tilted magnetic field on the self sustained current oscillations in superlattices. We then investigated the effect of a propagating acoustic wave (generated for example by the new SASER device, recently demonstrated at the University of Nottingham) on the dynamics of single electrons and the charge distribution in superlattices. Finally, we considered the effect of a propagating optical potential on a cold atom cloud in a stationary optical lattice (the cold atom analogue to the superlattice-SASER system).

In chapter 2, and previous publications [18; 47], it was shown that resonant delocalisation of the chaotic single-electron trajectories creates additional maxima in the drift velocity-field curve. Also, previous investigation of transport in superlattices with no tilted magnetic field revealed that negative differential velocity can induce high-frequency self sustained current oscillations. To understand the effect of the tilted magnetic field on the self sustained current oscillations we formulated in chapter 3, a modified drift-diffusion model. Simulations of the collective electron dynamics revealed that the extra negative differential drift velocity regions, caused by the resonant peaks, induce multiple charge domains. These extra domains increase both the amplitude and frequency of the current oscillations: both effects that should be experimentally observable.

In chapter 4, we demonstrated that acoustic waves can create direct current in superlattices, even when no bias voltage is applied, and also induce a transition between two distinct dynamical regimes: the acoustic wave can either drag the electron through the superlattice or induce Bloch oscillations. In the single electron analysis

we found that for small acoustic wave amplitudes, the electrons oscillate at frequencies far greater than the acoustic wave frequency within a single spatial period of the acoustic wave. Consequently, the electrons are dragged through the superlattice with a drift velocity whose peak value, which increases with increasing band width, can greatly overshoot that produced by a *static* field. Increasing the acoustic wave amplitude beyond a well defined critical value triggers bursts of Bloch oscillations, thereby causing very high negative differential drift velocity: an essential characteristic of THz sources [14; 32]. The effect of the single particle dynamics on the collective dynamics of electrons was also considered, and it was shown that the acoustic wave drags charge through the lattice, creating current oscillations. In addition, it generates extra features in the charge distribution due to the high negative differential drift velocity. The results of these simulations are consistent with previous experiments where acoustic waves were shown to drag electrons through superlattices [69]. In future experiments we expect to see negative differential conductivity with increasing wave amplitude, indicating the ‘switch on’ of Bloch oscillating electrons.

In chapter 5, we showed that ultracold atoms in optical lattices exhibit similar dynamics to acoustically driven electrons in superlattices, if additional detuned laser beams are used to simulate the propagating sound wave [102]. We found an abrupt transition between dragging and Bloch-oscillation regimes and also sharp resonant peaks in the velocity of the atom as it interacts with the effective dispersion curve. This gives rise to a rich parameter space of different, well defined resonances where, in some cases, a very small change in potential can cause the atom to move in opposite directions. This could provide a flexible mechanism for transporting atoms to precise locations in a lattice: as required for using cold atoms to simulate condensed matter or as a stepping stone to quantum information processing.

6.1 Future work

Shortly after submission of this thesis an experimental investigation of the frequency output of a superlattice in a tilted magnetic field was undertaken. The analysis encouragingly revealed that there are ‘hot spots’ in the power of the output when the tilt angle is between 45 and 80°, a result that compares well with the analysis in chapter 3, specifically with figure 3.13. However, the oscillation frequencies measured in the experiment are an order of a magnitude less than those predicted by the model

described in chapter 3. It can be shown that by including the effect of an external capacitor and inductor into the model described in chapter 3, good correspondence between the experimental and theoretical results can be obtained. These new results highlight the importance of the role of external circuit elements on frequency measurements, and further work (currently being undertaken) is required to fully understand their effects.

Recently there has been some work on the demonstration of stable THz gain in superlattices using a modulated bias [105] and also with a tilted magnetic field applied [106]. Thus far these studies have focused on the homogeneous field case. It would be interesting to study the gain of superlattices in the non-homogeneous field case to confirm the existence of the high frequency components in the current spectra. Also, our results suggest that it is possible to control the form and *collective* dynamics of charge domains in superlattices by using *single-electron* miniband transport to tailor $v_d(F)$. Multiple v_d maxima can also be created in other ways, for example by applying an AC electric field [107], which could be studied in the context of the model presented in chapter 3.

The influence of a static bias field on the acoustically driven superlattice could have interesting results, especially if we consider the acoustic wave to be a perturbation of a superlattice within the negative differential velocity regime. It is possible that the charge domains induced by the static field will interact with the charge being dragged through the lattice, so producing high frequency current oscillations.

An obvious extension to the work on atoms in moving potentials would be to consider a Bose-Einstein Condensate in the optical lattice where interactions between the atoms become important. The complex form of the potential and the interactions between the atoms could result in the formation of vortices within the atom cloud [108], which could, in turn, influence its motion through the system.

Appendix A

Calculation of dispersion curves and Bloch states for a particle in a periodic potential

The following appendix describes how dispersion curves like those shown in figures 1.4 and 1.5 can be calculated for a given superlattice. The method described below is the relatively simple ‘cellular method’ for solving the Schrödinger equation (1.21) [3]. In this method it is assumed that, because of Bloch’s theorem, equation (1.8), stated here in one dimension,

$$\psi(x + d_{SL}) = e^{ikd_{SL}}\psi(x), \quad (\text{A.1})$$

it is enough to solve the Schrödinger equation in a single primitive cell of the superlattice (of length d_{SL}). Then, using equation (A.1), the electron wavefunction in all other primitive cells in the lattice can be found. We know from equation (1.9) that Bloch theory tells us that, in a period potential, the wavefunction $\psi_k(x)$ has the form

$$\psi_k(x) = e^{ikx}u_k(x) \quad (\text{A.2})$$

where $u_k(x)$ is a function with the periodicity and translational symmetry of the lattice. The time independent Schrödinger equation for the Bloch wavefunction in a one dimensional lattice in energy band n , $\psi_k^n(x)$, is given by

$$\hat{\mathcal{H}}\psi_k^n(x) = E^n(k)\psi_k^n(x), \quad (\text{A.3})$$

where $E^n(k)$ is the energy-wavenumber dispersion relation of the electron in band n and

$$\hat{\mathcal{H}} = -\frac{\hbar^2}{2m^*} \frac{\partial^2}{\partial x^2} + V_{SL}, \quad (\text{A.4})$$

where V_{SL} is the periodic potential with a form such as that shown in figures 1.4(b) or 1.5(b). An additional boundary condition must also be applied, since to obtain a solution to the Schrödinger equation ψ must be continuous as x crosses the superlattice primitive cell boundary. Therefore we impose the following boundary conditions onto the solution of ψ

$$\psi(x) = e^{-ikd_{SL}}\psi(x + d_{SL}) \quad (\text{A.5})$$

and also that

$$\frac{d\psi(x)}{dx} = e^{-ikd_{SL}} \frac{d\psi(x + d_{SL})}{dx}. \quad (\text{A.6})$$

To find the Bloch wavefunctions and the dispersion curve, $E^n(k)$, of the superlattice we turn our attention to determining the form of $u_k^n(x)$ in equation (A.2). Substituting (A.2) into equation (A.3) we find

$$-\frac{\hbar^2}{2m^*} \frac{\partial^2 [e^{ikx} u_k^n(x)]}{\partial x^2} + V_{SL} [e^{ikx} u_k^n(x)] = E^n(k) [e^{ikx} u_k^n(x)]. \quad (\text{A.7})$$

This can be expanded to find that the left hand side is equal to

$$-\frac{\hbar^2}{2m^*} [(u_k^n(x))'' e^{ikx} + 2(u_k^n(x))' ik e^{ikx} - u_k^n(x) k^2 e^{ikx}] + V_{SL} [e^{ikx} u_k^n(x)] \quad (\text{A.8})$$

where $(u_k^n(x))''$ and $(u_k^n(x))'$ are respectively the second and first derivative of $u_k^n(x)$. Dividing through by e^{ikx} we find that

$$-\frac{\hbar^2}{2m^*} [(u_k^n(x))'' + 2(u_k^n(x))' ik - u_k^n(x) k^2] + V_{SL} u_k^n(x) = E^n(k) u_k^n(x). \quad (\text{A.9})$$

It is then relatively straightforward to discretise this equation into a matrix problem, where the solution is the set of eigenvalues and eigenvectors corresponding to $E^n(k)$ and $u_k^n(x)$ for a given value of k , remembering the boundary condition given in equation (A.5). In this case the problem was solved using the “eig” function in MATLAB[®].

The method outlined is not as accurate as analytic solutions such as the Kronig-Penney model [2] but is essentially identical assuming a small enough discretisation

step is used . This numerical method is advantageous in being easily adapted to different, and more complex potentials, compared to the reformulation of the Kronig-Penney model required to solve these problems.

Appendix B

Experimental measurement of current and the role of contacts

In this appendix, we consider the experimentally measured current in the circuit of the superlattice. In section 3.1, we assumed that the superlattice device (consisting of contact regions and the superlattice layers) is neutral. This assumption is justified if the response time of electrons in the contacts is small enough to screen any net charge increase in the superlattice layers. We can find the characteristic time scale of electrons to respond to perturbing potentials in the contacts by calculating the Fermi velocity. The Fermi energy, E_f , in the contacts is given by [2]

$$E_f = \frac{\hbar^2}{2m^*} (3\pi^2 n_0) \approx 10 \text{ meV}, \quad (\text{B.1})$$

where n_0 is the doping density of electrons in the contacts (see section 3.2). The corresponding Fermi velocity, v_f , is

$$v_f = \sqrt{\frac{2E_f}{m^*}} \approx 2.5 \times 10^5 \text{ m s}^{-1}. \quad (\text{B.2})$$

We define a typical response time of electrons in the contacts as l/v_f which is $\sim 10^{-13}$ s and \ll than the time scale of the charge domain motion ($\sim 10^{-10}$ s). Consequently, electrons in the contact will be able quickly to screen any net charge increase in the superlattice layers.

The charge neutrality of the superlattice device requires the field at the left- and right-hand edges of the device, F_0 , to be equal (see equation (3.12)). Therefore, the current measured by an ammeter placed in the circuit will be equal to

$$I_c = \sigma A F_0. \quad (\text{B.3})$$

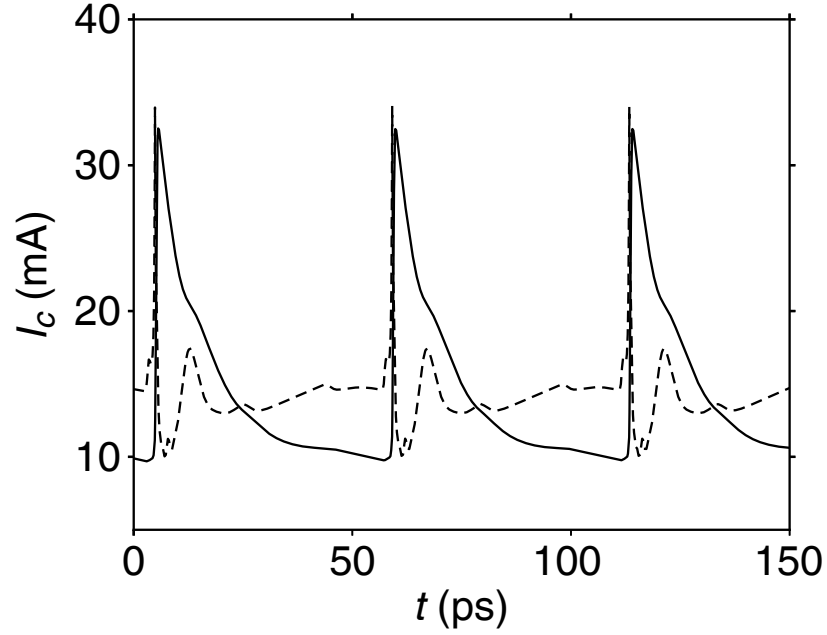


Figure B.1: Current oscillations in the circuit, $I_c(t)$ (solid line), and in the layers of the superlattice, $I(t)$, calculated when $\theta = 40^\circ$ for $V = 610$ mV and $B = 15$ T.

Figure B.1 compares $I_c(t)$ and $I(t)$ (as defined in equations (3.15) and (3.16)), when $B = 15$ T, $\theta = 40^\circ$, and $V = 610$ mV (see figure 3.5). The magnitude and fundamental frequency of the current oscillations are similar in both cases. However, we find that the size of the extra features in $I(t)$ (dashed curve), arising from the magnetic field-induced charge domains (see section 3.2.3), is diminished when we calculate I_c (solid curve). This is due to the screening effect of the wide contact regions, which could be reduced by changing the contact design (for example by reducing their length, l). It is important to note that, nevertheless, electrons in the active region of the device (the superlattice layers) do exhibit higher frequency oscillations, which could produce corresponding high-frequency electromagnetic radiation.

References

- [1] F. Bloch. Über die Quantenmechanik der Elektronen in Kristallgittern. *Zeitschrift für Physik*, 52:555–600, 1929.
- [2] C. Kittel. *Introduction to Solid State Physics*. Wiley, 2005.
- [3] N. W. Ashcroft and N. D. Mermin. *Solid State Physics*. W.B. Saunders Company, 1 edition, 1976.
- [4] E. Schrödinger. *Ann. Phys.*, 79:361–376, 1926.
- [5] E. Schrödinger. An undulatory theory of the mechanics of atoms and molecules. *Phys. Rev.*, 28:1049–1070, 1926.
- [6] S. M. McMurry. *Quantum Mechanics*. Prentice-Hall, 1996.
- [7] D. P. A. Hardwick, S. L. Naylor, S. Bujkiewicz, T. M. Fromhold, D. Fowler, A. Patanè, L. Eaves, A. A. Krokhin, P. B. Wilkinson, M Henini, and F. W. Sheard. Effect of inter-miniband tunneling on current resonances due to the formation of stochastic conduction networks in superlattices. *Physica E*, 32:285, 2006.
- [8] David P. A. Hardwick. *Quantum and semiclassical calculations of electron transport through a stochastic system*. PhD thesis, School of Physics and Astronomy, University of Nottingham, 2007.
- [9] M. Gustavsson, E. Haller, M. J. Mark, J. G. Danzl, G. Rojas-Kopeinig, and H. C. Nägerl. Control of interaction-induced dephasing of Bloch oscillations. *Phys. Rev. Lett.*, 100(8):080404, 2008.
- [10] L. Esaki and R. Tsu. Superlattice and Negative Differential Conductivity in Semiconductors. *IBM J. Res. Dev.*, 14:61, 1970.

-
- [11] R. Tsu. Applying the insight into superlattices and quantum wells for nanostructures: Low-dimensional structures and devices. *Microelectron. J.*, 38(10-11):959 – 1012, 2007.
- [12] H. T. Grahn. *Semiconductor superlattices: growth and electronic properties*. World Scientific, 1995.
- [13] L. Esaki and L. L. Chang. New transport phenomenon in a semiconductor "superlattice". *Phys. Rev. Lett.*, 33(8):495–498, Aug 1974.
- [14] A. Wacker. Semiconductor superlattices: a model system for nonlinear transport. *Phys. Rep.*, 357:1, 2002.
- [15] E. Schöll. *Nonlinear Spatio-temporal Dynamics and Chaos in Semiconductors*. Cambridge University Press, 2001.
- [16] L. L. Bonilla and H. T. Grahn. Non-linear dynamics of semiconductor superlattices. *Rep. Prog. Phys*, 68:577, 2005.
- [17] David Sherwood. *Effect of Stochastic Webs on Electron Transport in Semiconductor Superlattices*. PhD thesis, University of Nottingham, 2003.
- [18] T. M. Fromhold, A. Patanè, S. Bujkiewicz, P. B. Wilkinson, D. Fowler, D. Sherwood, S. P. Stapleton, A. A. Krokhin, L. Eaves, M Henini, N. S. Sankeshwar, and F. W. Sheard. Chaotic electron diffusion through stochastic web enhances current flow in superlattices. *Nature*, 428:726, 2004.
- [19] W. H. Press, S. A. Teukolsky, W. T. Vetterling, and B. P. Flannery. *Numerical recipes in C*. Cambridge University Press, 2nd edition, 1996.
- [20] Robin G. Scott. *Cold Atoms in Optical Lattices*. PhD thesis, University of Nottingham, 2003.
- [21] Sarah Naylor. *Stochastic Dynamics in Periodic Potentials*. PhD thesis, University of Nottingham, 2006.
- [22] Thomas E. Judd. *The Wave Mechanics of Cold Atoms*. PhD thesis, University of Nottingham, 2008.

-
- [23] T. Hartmann, F. Keck, H.J. Korsch, and S. Mossmann. Dynamics of Bloch oscillations. *New. J. Phys.*, 6, Jan 14 2004.
- [24] A. A. Ignatov, E. P. Dodin, and I. V. Shashkin. Transient response theory of semiconductor superlattices: connection with bloch oscillations. *Mod. Phys. Lett. B*, 5(16):1087–1094, 1991.
- [25] F. Beltram, F. Capasso, D. L. Sivco, A. L. Hutchinson, S. N. G. Chu, and A. Y. Cho. Scattering-controlled transmission resonances and negative differential conductance by field-induced localization in superlattices. *Phys. Rev. Lett.*, 64(26):3167–3170, Jun 1990.
- [26] C. Rauch, G. Strasser, K. Unterrainer, A. Wacker, and E. Gornik. Scattering and bloch oscillation in semiconductor superlattices. *Physica B: Condens. Matter*, 272(1-4):175 – 179, 1999.
- [27] J. B. Gunn. Properties of a Free, Steadily Travelling Electrical Domain in GaAs. *IBM Journal*, 10:300, 1966.
- [28] M. P. Shaw, V. V. Mitin, E. Schöll, and H. L. Grubin. *The physics of Instabilities in Solid State Electron Devices*. Plenum Press, New York, 1992.
- [29] M. Büttiker and H. Thomas. Current instability and domain propagation due to Bragg scattering. *Phys. Rev. Lett.*, 38(2):78–80, Jan 1977.
- [30] J. Kastrup, R. Klann, H. T. Grahn, K. Ploog, L. L. Bonilla, J. Galán, M. Kindelan, M. Moscoso, and R. Merlin. Self-oscillations of domains in doped GaAs-AlAs superlattices. *Phys. Rev. B*, 52(19):13761–13764, Nov 1995.
- [31] J. Kastrup, R. Hey, K. H. Ploog, H.T. Grahn, L. L. Bonilla, M. Kindelan, M. Moscoso, A. Wacker, and J. Galán. Electrically tunable GHz oscillations in doped GaAs-AlAs superlattices. *Phys. Rev. B*, 55(4):2476–2488, Jan 1997.
- [32] E. Schomburg, T. Blomeier, K. Hofbeck, J. Grenzer, S. Brandl, I. Lingott, A. A. Ignatov, K. F. Renk, D. G. Pavel’ev, Yu. Koschurinov, B. Ya. Melzer, V. M. Ustinov, S. V. Ivanov, A. Zhukov, and P. S. Kop’ev. Current oscillation in superlattices with different miniband widths. *Phys. Rev. B*, 58(7):4035–4038, Aug 1998.

-
- [33] A. Amann, K. Peters, U. Parlitz, A. Wacker, and E. Schöll. Hybrid model for chaotic front dynamics: From semiconductors to water tanks. *Phys. Rev. Lett.*, 91(6):066601, Aug 2003.
- [34] E. Schomburg, M. Henini, J. M. Chamberlain, D. P. Steenson, S. Brandl, K. Hofbeck, K. F. Renk, and W. Wegscheider. Self-sustained current oscillation above 100 GHz in a GaAs/AlAs superlattice. *Appl. Phys. Lett.*, 74:2179–2181, Apr 1999.
- [35] A. Patané, A. Ignatov, D. Fowler, O. Makarovskiy, L. Eaves, L. Geelhaar, and H. Riechert. Hot-electrons and negative differential conductance in GaAs_{1-x}n_x. *Phys. Rev. B*, 72(3):033312, Jul 2005.
- [36] W. J. Duffin. *Electricity and Magnetism*. McGraw-Hill Publishing Co., 4th edition, 1990.
- [37] J. Hizanidis, A. Balanov, A. Amann, and E. Schöll. Noise-induced front motion: Signature of a global bifurcation. *Phys. Rev. Lett.*, 96(24):244104, 2006.
- [38] B. J. Keay, S. Zeuner, S. J. Allen, K. D. Maranowski, A. C. Gossard, U. Bhattacharya, and M. J. W. Rodwell. Dynamic localization, absolute negative conductance, and stimulated, multiphoton emission in sequential resonant tunneling semiconductor superlattices. *Phys. Rev. Lett.*, 75(22):4102–4105, Nov 1995.
- [39] J. Inarrea and G. Platero. A.c. field assisted current in GaAs-AlGaAs superlattices. *Solid-State Electron.*, 40(1-8):295 – 298, 1996. Proceedings of the Seventh International Conference on Modulated Semiconductor Structures.
- [40] T. Schmidt, A. G. M. Jansen, R. J. Haug, K. v. Klitzing, and K. Eberl. Magnetic control of electric-field domains in semiconductor superlattices. *Phys. Rev. Lett.*, 81(18):3928–3931, Nov 1998.
- [41] B. Sun, J. Wang, W. Ge, Y. Wang, D. Jiang, H. Zhu, H. Wang, Y. Deng, and S. Feng. Current self-oscillation induced by a transverse magnetic field in a doped GaAs/AlAs superlattice. *Phys. Rev. B*, 60(12):8866–8870, Sep 1999.
- [42] F. Elsholz, A. Wacker, E. Schöll, M. Kast, G. Strasser, and E. Gornik. Magnetotransport through semiconductor superlattices. *Phys. Rev. B*, 63(3):033312, Jan 2001.

-
- [43] G. Yang, H. Meng, L.-F. Zhang, and S.-P. Zhou. The self-sustained current oscillation and the dynamics in superlattices under the action of electric and magnetic fields. *J. Appl. Phys.*, 103(12):123701, 2008.
- [44] C. J. Pethick and H. Smith. *Bose-Einstein Condensation in Dilute Gases*. Cambridge University Press, 2nd edition, 2008.
- [45] K. B. Davis, M. O. Mewes, M. R. Andrews, N. J. van Druten, D. S. Durfee, D. M. Kurn, and W. Ketterle. Bose-einstein condensation in a gas of sodium atoms. *Phys. Rev. Lett.*, 75(22):3969–3973, Nov 1995.
- [46] S. R. Wilkinson, C. F. Bharucha, K. W. Madison, Qian Niu, and M. G. Raizen. Observation of atomic wannier-stark ladders in an accelerating optical potential. *Phys. Rev. Lett.*, 76(24):4512–4515, Jun 1996.
- [47] T. M. Fromhold, A. A. Krokhin, C. R. Tench, S. Bujkiewicz, P. B. Wilkinson, F. W. Sheard, and L. Eaves. Effects of stochastic webs on chaotic electron transport in semiconductor superlattices. *Phys. Rev. Lett.*, 87(4):046803, Jul 2001.
- [48] E. Ott. *Chaos in Dynamical Systems*. Cambridge University Press, 2nd edition, 2002.
- [49] G. M. Zaslavsky. *Hamiltonian Chaos and Fractional Dynamics*. Oxford University Press, 2005.
- [50] A. A. Chernikov, R. Z. Sagdeev, D. A. Usikov, M. YU. Zakharov, and G. M. Zaslavsky. Minimal chaos and stochastic webs. *Nature*, 326:559, 1987.
- [51] A. A. Vasiliev, G. M. Zaslavsky, M. Y. Natenzon, A. I. Neishtadt, B. A. Petrovichev, R. Z. Sagdeev, and A. A. Chernikov. Attractors and stochastic attractors of motion in a magnetic-field. *Zh. Eksp. Teor. Fiz*, 94(10):170–187, Oct 1988.
- [52] R. Z. Sagdeev, D. A. Usikov, and G. M. Zaslavsky. *Nonlinear Physics*. Harwood Academic Publishers, 1988.
- [53] Chernikov A. A. Beloshapkin, V. V., M. Y. Natenzon, B. A. Petrovichev, R. Z. Sagdeev, and G. M. Zaslavsky. Chaotic streamlines in pre-turbulent states. *Nature*, 337(6203):133–137, Jan 12 1989.

-
- [54] G. M. Zaslavsky. *Weak Chaos and Quasi-Regular Patterns*. Cambridge University Press, 1991.
- [55] M. F. Shlesinger, G. M. Zaslavsky, and J. Klafter. Strange kinetics. *Nature*, 363:31, 1993.
- [56] P. K. Chia, L. Schmitz, and R. W. Conn. Stochastic ion behavior in subharmonic and superharmonic electrostatic waves. *Phys. Plasmas*, 3(5):1545–1568, MAY 1996.
- [57] C. F. F. Karney and A Bers. Stochastic ion heating by a perpendicularly propagating electrostatic wave. *Phys. Rev. Lett.*, 39(9):550–554, 1977.
- [58] S. A. Gardiner, J. I. Cirac, and P. Zoller. Quantum chaos in an ion trap: The delta-kicked harmonic oscillator. *Phys. Rev. Lett.*, 79(24):4790–4793, Dec 1997.
- [59] W. K. Hensinger, H. Haffner, A. Browaeys, N. R. Heckenberg, K. Helmerson, C. McKenzie, G. J. Milburn, W. D. Phillips, S. L. Rolston, H. Rubinsztein-Dunlop, and B. Upcroft. Dynamical tunnelling of ultracold atoms. *Nature*, 412(6842):52–55, July 2001.
- [60] D. A. Steck, W. H. Oskay, and M. G. Raizen. Observation of chaos-assisted tunneling between islands of stability. *Science*, 293(5528):274–278, July 2001.
- [61] R. G. Scott, S. Bujkiewicz, T. M. Fromhold, P. B. Wilkinson, and F. W. Sheard. Effects of chaotic energy-band transport on the quantized states of ultracold sodium atoms in an optical lattice with a tilted harmonic trap. *Phys. Rev. A*, 66(2):023407, Aug 2002.
- [62] P. Wilkinson and T. M. Fromhold. Chaotic ray dynamics in slowly varying two-dimensional photonic crystals. *Opt. Lett.*, 28(12):1034–1036, 2003.
- [63] D. Fowler, D. P. A. Hardwick, A. Patané, M. T. Greenaway, A. G. Balanov, T. M. Fromhold, L. Eaves, M. Henini, N. Kozlova, J. Freudenberger, and N. Mori. Magnetic-field-induced miniband conduction in semiconductor superlattices. *Phys. Rev. B*, 76(24):245303, 2007.

-
- [64] S. P. Stapleton, S. Bujkiewicz, T. M. Fromhold, P. B. Wilkinson, A. Patane, L. Eaves, A. A. Krokhin, M. Henini, N. S. Sankeshwar, and F. W. Sheard. Use of stochastic web patterns to control electron transport in semiconductor superlattices. *Physica D*, 199(1-2):166–172, Dec 1 2004. (Workshop on Trends in Pattern Formation, Dresden, Aug 25-Sep 19, 2003).
- [65] H. Goldstein, C. Poole, and J. Safko. *Classical Mechanics*. Addison Wesley, 3rd edition, 2002.
- [66] D. I. Kamenev and G. P. Berman. *Quantum Chaos: a Harmonic Oscillator in Monochromatic Wave*. Rinton, Princeton, New Jersey, 2000.
- [67] V. Ya. Demikhovskii, D. I. Kamenev, and G. A. Luna-Acosta. Quantum weak chaos in a degenerate system. *Phys. Rev. E*, 59(1):294–302, Jan 1999.
- [68] V. Ya. Demikhovskii, F. M. Izrailev, and A. I. Malyshev. Manifestation of arnol'd diffusion in quantum systems. *Phys. Rev. Lett.*, 88(15):154101, Apr 2002.
- [69] D. R. Fowler, A. V. Akimov, A. G. Balanov, M. T. Greenaway, M. Henini, T. M. Fromhold, and A. J. Kent. Semiconductor charge transport driven by a picosecond strain pulse. *Appl. Phys. Lett.*, 92(23):232104, 2008.
- [70] M. T. Greenaway, A. G. Balanov, E. Schöll, and T. M. Fromhold. Controlling and enhancing terahertz collective electron dynamics in superlattices by chaos-assisted miniband transport. *Phys. Rev. B*, 80(20):205318, 2009.
- [71] L. L. Bonilla. Theory of nonlinear charge transport, wave propagation, and self-oscillations in semiconductor superlattices. *J. Phys.: Condens. Matter*, 14:R341, 2002.
- [72] A. Amann, J. Schlesner, A. Wacker, and E. Schöll. Chaotic front dynamics in semiconductor superlattices. *Phys. Rev. B*, 65(19):193313, May 2002.
- [73] G. Schwarz and E. Schöll. Field Domains in Semiconductor Superlattices. *Phys. Stat. Sol. B*, 194:351, 1996.
- [74] E. Schöll. *Nonequilibrium Phase Transitions in Semiconductors*. Springer, Berlin, 1987.

-
- [75] C. P. Endres, H. S. P. Müller, S. Brünken, D. G. Paveliev, T. F. Giesen, S. Schlemmer, and F. Lewen. High resolution rotation-inversion spectroscopy on doubly deuterated ammonia, ND₂H, up to 2.6THz. *J. Mol. Struct.*, 795(1-3):242 – 255, 2006.
- [76] C. P. Endres, F. Lewen, T. F. Giesen, S. Schlemmer, D. G. Paveliev, Y. I. Koschurinov, V. M. Ustinov, and A. E. Zhucov. Application of superlattice multipliers for high-resolution terahertz spectroscopy. *Rev. Sci. Instrum.*, 78(4):043106, 2007.
- [77] M. Rini, R. Tobey, N. Dean, J. Itatani, Y. Tomioka, Y. Tokura, R. W. Schoenlein, and A Cavalleri. Control of the electronic phase of a manganite by mode-selective vibrational excitation. *Nature*, 449:72, 2007.
- [78] K. J. Ahn, F. Milde, and A. Knorr. Phonon-wave-induced resonance fluorescence in semiconductor nanostructures: Acoustoluminescence in the terahertz range. *Phys. Rev. Lett.*, 98(2):027401, 2007.
- [79] C. Thomsen, H. T. Grahn, H. J. Maris, and J. Tauc. Surface generation and detection of phonons by picosecond light pulses. *Phys. Rev. B*, 34(6):4129–4138, Sep 1986.
- [80] O. L. Muskens and J. I. Dijkhuis. High amplitude, ultrashort, longitudinal strain solitons in sapphire. *Phys. Rev. Lett.*, 89(28):285504, Dec 2002.
- [81] H.-Y. Hao and H. J. Maris. Study of phonon dispersion in silicon and germanium at long wavelengths using picosecond ultrasonics. *Phys. Rev. Lett.*, 84(24):5556–5559, Jun 2000.
- [82] T. Saito, O. Matsuda, and O. B. Wright. Picosecond acoustic phonon pulse generation in nickel and chromium. *Phys. Rev. B*, 67(20):205421, May 2003.
- [83] G. Tas and H. J. Maris. Electron diffusion in metals studied by picosecond ultrasonics. *Phys. Rev. B*, 49(21):15046–15054, Jun 1994.
- [84] A. Huynh, N. D. Lanzillotti-Kimura, B. Jusserand, B. Perrin, A. Fainstein, M. F. Pascual-Winter, E. Peronne, and A. Lemaître. Subterahertz phonon dynamics in acoustic nanocavities. *Phys. Rev. Lett.*, 97(11):115502, 2006.

-
- [85] J.-F. Robillard, A. Devos, and I. Roch-Jeune. Time-resolved vibrations of two-dimensional hypersonic phononic crystals. *Phys. Rev. B*, 76(9):092301, 2007.
- [86] V. K. Karavolas, M. J. Smith, T. M. Fromhold, P. N. Butcher, B. G. Mulimani, B. L. Gallagher, and J. P. Oxley. The effect of interface roughness scattering and background impurity scattering on the thermopower of a 2DEG in a Si MOSFET. *J. Phys.: Condens. Matter*, 2(51):10401–10410, 1990.
- [87] T. M. Fromhold, P. N. Butcher, G. Qin, B. G. Mulimani, J. P. Oxley, and B. L. Gallagher. Phonon-drag magnetothermopower oscillations in GaAs/As_xGa_{1-x}As heterojunctions. *Phys. Rev. B*, 48(8):5326–5332, Aug 1993.
- [88] B. A. Glavin, V. A. Kochelap, T. L. Linnik, K. W. Kim, and M. A. Stroscio. Generation of high-frequency coherent acoustic phonons in superlattices under hopping transport. i. linear theory of phonon instability. *Phys. Rev. B*, 65(8):085303, Jan 2002.
- [89] B. A. Glavin, V. A. Kochelap, T. L. Linnik, K. W. Kim, and M. A. Stroscio. Generation of high-frequency coherent acoustic phonons in superlattices under hopping transport. ii. steady-state phonon population and electric current in generation regime. *Phys. Rev. B*, 65(8):085304, Jan 2002.
- [90] A. J. Kent, R. N. Kini, N. M. Stanton, M. Henini, B. A. Glavin, V. A. Kochelap, and T. L. Linnik. Acoustic phonon emission from a weakly coupled superlattice under vertical electron transport: Observation of phonon resonance. *Phys. Rev. Lett.*, 96(21):215504, 2006.
- [91] P. M. Walker, A. J. Kent, M. Henini, B. A. Glavin, V. A. Kochelap, and T. L. Linnik. Terahertz acoustic oscillations by stimulated phonon emission in an optically pumped superlattice. *Phys. Rev. B*, 79(24):245313, 2009.
- [92] J. Bardeen and W. Shockley. Deformation potentials and mobilities in non-polar crystals. *Phys. Rev.*, 80(1):72–80, Oct 1950.
- [93] O Madelung. *Introduction to Solid-State Theory*. Springer-Verlag, 1978.
- [94] W.E. Bron. *Nonequilibrium Phonons in Nonmetallic Crystals*. North-Holland, 1986.

-
- [95] B. K. Ridley. *Quantum processes in semiconductors*. Oxford University Press, 4th edition, 1999.
- [96] Albert Rose. *Electron Phonon Interactions: A Novel Semiclassical Approach*. World Scientific, 1989.
- [97] D. D. Nolte, W. Walukiewicz, and E. E. Haller. Band-edge hydrostatic deformation potentials in iii-v semiconductors. *Phys. Rev. Lett.*, 59(4):501–504, Jul 1987.
- [98] R. Tsu and G. Döhler. Hopping conduction in a "superlattice". *Phys. Rev. B*, 12:680, 1975.
- [99] L. W. Couch II. *Digital and Analog Communication Systems*. Prentice-Hall Inc., 6th edition, 2001.
- [100] J. R. Hook and H. E. Hall. *Solid State Physics*. Wiley, 2nd edition, 2000.
- [101] S. Schmid, G. Thalhammer, K. Winkler, F. Lang, and J. Hecker Denschlag. Long distance transport of ultracold atoms using a 1d optical lattice. *New J. Phys.*, 8(8):159, 2006.
- [102] M. Schiavoni, F. R. Carminati, L. Sanchez-Palencia, F. Renzoni, and G. Grynberg. Stochastic resonance in periodic potentials: Realization in a dissipative optical lattice. *Europhys. Lett.*, 59:493–499, Aug 2002.
- [103] A. Browaeys, H. Haffner, C. McKenzie, S. L. Rolston, K. Helmerson, and W. D. Phillips. Transport of atoms in a quantum conveyor belt. *Phys. Rev. A*, 72(5):053605, 2005.
- [104] L. Fallani, C. Fort, J. Lye, and M. Inguscio. Bose-einstein condensate in an optical lattice with tunable spacing: transport and static properties. *Opt. Express*, 13(11):4303–4313, 2005.
- [105] T. Hyart, N. V. Alexeeva, J. Mattas, and K. N. Alekseev. Terahertz bloch oscillator with a modulated bias. *Phys. Rev. Lett.*, 102(14):140405, 2009.
- [106] T. Hyart, J. Mattas, and K. N. Alekseev. Model of the influence of an external magnetic field on the gain of terahertz radiation from semiconductor superlattices. *Phys. Rev. Lett.*, 103(11):117401, 2009.

REFERENCES

- [107] T. Hyart, A. V. Shorokhov, and K. N. Alekseev. Theory of parametric amplification in superlattices. *Phys. Rev. Lett.*, 98(22):220404, 2007.
- [108] R. G. Scott, A. M. Martin, T. M. Fromhold, S. Bujkiewicz, F. W. Sheard, and M. Leadbeater. Creation of solitons and vortices by bragg reflection of bose-einstein condensates in an optical lattice. *Phys. Rev. Lett.*, 90(11):110404, Mar 2003.